SCATTERING OF 14.1 MeV NEUTRONS IN Al, Cu AND Mo

HUSIN BIN WAGIRAN

Doctor of Philosophy

THE UNIVERSITY OF ASTON IN BIRMINGHAM

October 1987

THE UNIVERSITY OF ASTON IN BIRMINGHAM

SCATTERING OF 14.1 MEV NEUTRONS IN Al, Cu AND Mo

HUSIN BIN WAGIRAN

Doctor of Philosophy

October 1987

SUMMARY

The time of flight spectrometer based on the associated particle time of flight technique has been constructed in the present work to measure the elastic and non-elastic differential cross-sections of 14.1 MeV neutrons scattered from D-T fusion reactor blanket materials, Al, Cu and Mo. The 14.1 MeV neutrons were produced from $T(d,n)He^4$ reaction by accelerating the deuteron beam up to 140 keV using S.A.M.E.S type J electrostatic accelerator. The time origin of the neutron was determined by detecting the associated alpha-particles using NE102A thin plastic scintillator which provide 100% detection effeciency. A plastic scintillator NE102A mounted on a fast focused photomultiplier tube Philip 56 AVP was used in the neutron channel which provide 2.2 ± 0.2 ns time resolution at FWHM.

The angular distributions of 14.1 MeV neutrons scattered from the thin Al, Cu and Mo samples were measured in the angular range between 0° to 90°. The data are presented for elastic scattering and non-elastic neutrons scattering in the energy ranges (5-14) MeV in 3 MeV intervals. The differential inelastic cross-sections in Al to the sum of 0.84 and 1.04 MeV states are also presented. The differential elastic scattering cross-sections are compared to the results from ENDF-BIV and other published data. Legendre polynomial fits were produced and the integrated elastic cross-sections obtained from the fits were compared with the data of ENDF-BIV and others. The results of the differential elastic scattering cross-sections are compared to the prediction of earlier global optical models using optical model programme SCAT-2.

The differential cross-sections of 14.1 MeV neutrons scattered from thick sample of Al and Cu were measured at various thicknesses over the angular range between 0° to 90°. No similar measurements have been found to compare with the present work. The variation of measured cross-sections with sample thickness were found to follow the relationship $\sigma_x = \sigma_0 \exp(\alpha x)$. The constant parameter α obtained are compared with the previous measurements.

A Monte Carlo model was developed to predict the number of neutrons scattered from different sample thicknesses over the angular range between 0° to 350°. The number of scattered neutrons predicted from the model are compared with the experimental results.

Key words:Neutron/Elastic scattering/Cross-sections/Al, Cu and Mo.

ACKNOWLEDGEMENTS

I wish to express my sincere gratitude to Dr.P.N.Cooper for his constant guidance and supervision throughout the research work. I am also grateful to Dr.A.J.Cox for his supervision in the early phases of the research work.

My appreciation is also due to Mr.J.Phull and the members of Physics Workshop for their assistance in the early stages of the experimental work.

I also wish to record my appreciation of the University of Technology, Malaysia and the Public Services Department of Malaysia for their financial support.

Finally, I would like to note heartfelt appreciation to my wife, Norsiah, and my daughter, Zai, for their perseverance, moral support and encouragement throughout the period of research work.

Husin Bin Wagiran,
University of Aston in Birmingham.
October, 1987.

LIST OF CONTENTS

CHAPTER 4

EXPERIMENTAL PROCEDURE FOR ABSOLUTE DIFFERENTIAL CROSS-SECTION MEASUREMENT

CHAPTER 5

EXPERIMENTAL RESULTS

LIST OF TABLES

LIST OF FIGURES

CHAPTER 1

INTRODUCTION

1.1:INTRODUCTION.

Measurements of neutron cross-section such as neutron scattering cross-section for 14 MeV neutrons are important in a number of areas related to control thermonuclear reactor (CTR) design. The reaction which is considered to be the most favourable for nuclear fusion in CTR is

$$^{3}H + {}^{2}H \longrightarrow {}^{4}He + n + 17.6\ MeV$$

About 80% of the energy released per fusion corresponds to the 14 MeV neutrons leaving the plasma fuel. The plasma thus can be regarded as an isotropic source of 14 MeV neutrons. The plasma is surrounded by a number of blanket materials in order to convert 14 MeV neutrons to thermal energy and for breeding of tritium which is not present in nature. The blankets also have to provide for heat transport to external components of a thermal cycle designed to generate electrical power. In order to protect magnetic coils against radiation heating and damage, the blankets must also included a shielding zone. According to these principles a rough design of the blankets in CTR is shown in figure (1.1).

Deuterium which is necessary for fusion reaction in CTR occurs in nature with an abundance of 1 in 6500 atoms,

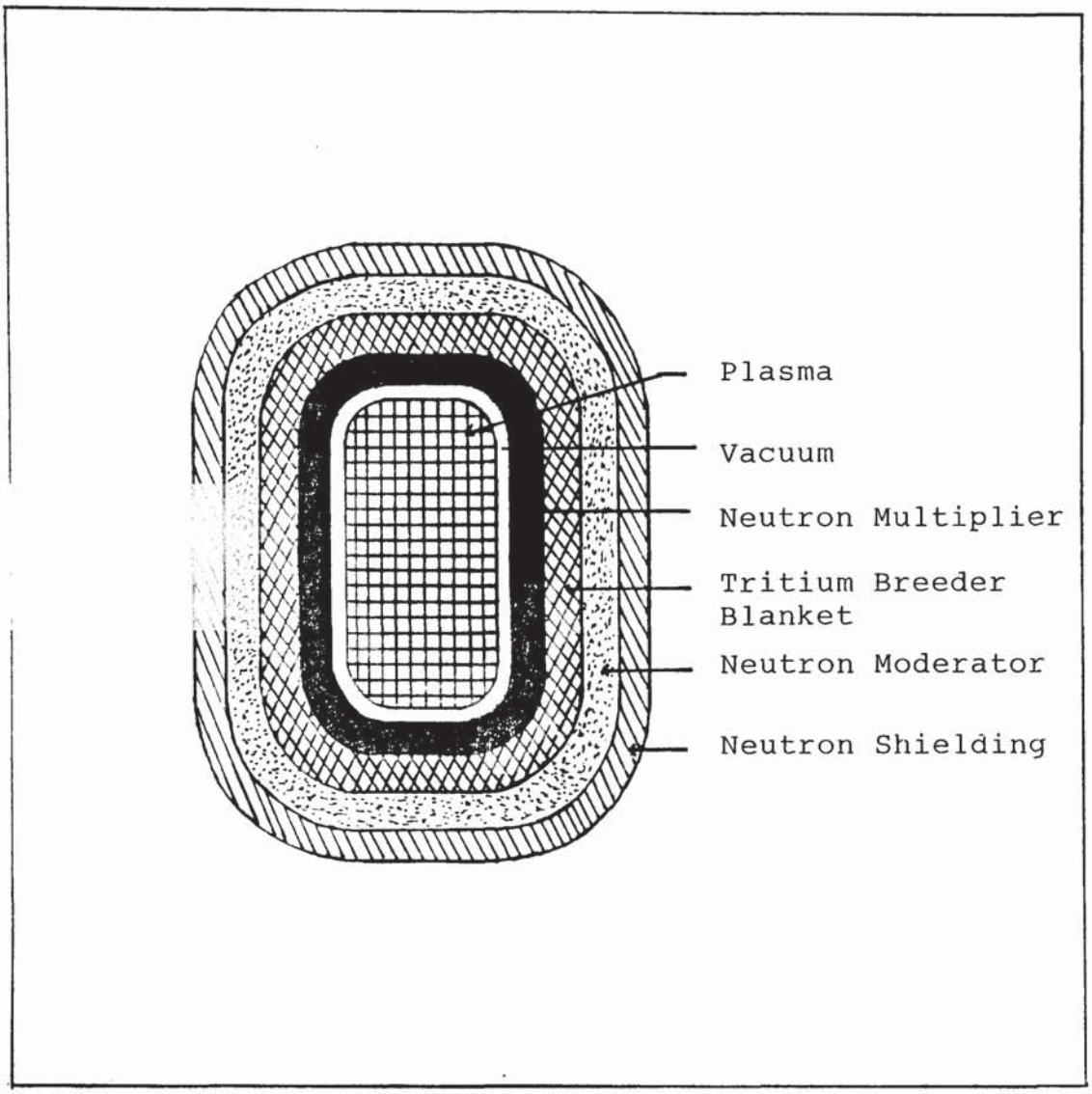

Figure (1.1):Conceptual design for Fusion Reactor.

while tritium which is radioactive with a half-life of 12.26 years has to be manufactured. Therefore, the breeder blankets have to be used to manufacture tritium. The only practical nuclear reactions which can be ultilised for this purpose are the neutron induced reaction with the two naturally occuring isotopes of lithium, i.e

$$^{7}Li + n \longrightarrow {}^{3}H + {}^{4}He + n \quad -2.5 \text{ MeV}$$

$$^{6}Li + n \longrightarrow {}^{3}H + {}^{4}He \quad +4.8 \text{ MeV}$$

In the design of the fusion reactor, the breeder blanket containing lithium will be used to manufacture tritium using 14 MeV neutrons from fusion reaction. The breeder blanket containing lithium surrounds the plasma volume. The 14 MeV neutrons interact with ^{7}Li producing tritium and less energetic neutron which may generate a further tritium from ^{6}Li reaction.

To enhance tritium breeding it is necessary to provide (n,2n) reactions in the breeder blanket. The (n,2n) reaction with large cross-section down to low energy is

$$^{9}Be + n \longrightarrow 2He^{4} + 2n$$

The other elements which can be used for neutron multiplication are Mo, Pb, Ta and W which have (n,2n)

cross-section in excess of 1 barn at 14 MeV neutron energy (1).

The plasma of 14 MeV neutrons with temperature about 10^8 K is separated from the structural materials by a vacuum layer. Therefore the vacuum wall is the most important part of the blanket. Because energy densities are highest in this region, the choice of materials for vacuum wall and structural materials are governed by several important criteria. The most important probably being the resistance against radiation damage and good mechanical properties at high temperature. It is generally believed that alloys should behave better than metals. The list thus should include basic alloys of Nb, Mo and W. Al and Cu are the materials that have to be considered in terms of economical point of view.

The kinetic energy of 14 MeV neutrons from fusion reaction has to be converted into heat to produced thermalised neutron spectrum. This can be achieved using moderator blanket which contain the materials with large elastic scattering cross-section and low atomic weight. According to fission reactor experience, graphite is the most favourable material and has proved to be efficient in moderating 14 MeV neutrons.

Finally, because of high energy gamma-rays produced from inelastic scattering and various capture processes, the biological shielding must have a high gamma-ray absorption cross-section as well as high thermal neutron

absorption cross-section. The choice is the materials such as lead, iron and concrete. In order to absorb the slow neutrons it is best to use ^{6}Li.

1.2:FAST NEUTRON SCATTERING.

The scattering of fast neutron with nuclei can be divided into two categories; elastic and inelastic scattering. In elastic scattering process the scattered neutron will emerge with a kinetic energy identical to its initial kinetic energy in the centre of mass system. In the laboratory system, the scattered neutron will emerge with a kinetic energy that depends on the scattering angle. However, in either system the sums of the kinetic energies of the neutron and the nucleus before and after the interaction are identical.

The elastic scattering interaction can be subdivided into to parts; shape elastic scattering and compound elastic scattering. The shape elastic occurs without the formation of a compound nucleus, while the compound elastic scattering comes from the formation of a compound nucleus and the subsequent emmision of the incident particle through the same channel.

In an inelastic scattering process, a fraction of the kinetic energy of the incident neutron is transfered to the target nucleus. A neutron of lower kinetic energy is then emitted, leaving the target nucleus in an excited state. The unstable nucleus usually emits one or more

gamma-rays to reach the ground state.

Inelastic scattering cannot occur unless the incident neutron has an energy higher than the energy of the first excited state of the target nucleus. This threshold energy is given by (2)

$$E_{th} = \frac{A + 1}{A} E_s \qquad (1\text{-}1)$$

where,

E_{th} = inelastic threshold energy,

E_s = the energy of a given excited state of the target nucleus,

A = the mass of the nucleus.

In many neutron-nucleus scattering interaction especially for medium and heavy nuclei, the scattered neutrons will have an anisotropic distribution at different angles of emission. To make such calculations, another type of cross-section which is angular dependent has to be introduced. This cross-section is called the differential cross-section $d\sigma/d\Omega(\theta)$, and is defined as the cross-section per unit solid angle at an angle θ to the incident neutron direction.

From the theoretical point of view, the neutron-nucleus scattering experiments are important source of information in the study of nuclear structure and nuclear reaction mechanism. It is necessary to measure these cross-sections for large number of nuclei

and at a sufficient number of energies so that the required data can be compared directly to the prediction of the nuclear models.

1.3:THE OPTICAL MODEL.

Optical model is the most successful method for interpreting the neutron-nucleus scattering cross-section for a large range of energies and mass numbers. In this model which was first proposed by Fernbach et al (3), the incident particles are not totally absorbed but partially absorbed and partially reflected or scattered by the target nucleus. The nuclear reaction is treated as a two-body problem in which an incident particle sees the nucleus as a limited region of complex potential of the form,

$$V(r) = V_R(r) + iW(r) + U_{so}(r) \qquad (1\text{-}2)$$

where,

$V_R(r)$ = the real central potential,

$W(r)$ = the imaginary potential,

and $U_{so}(r)$ = the spin-orbit potential.

The interaction potential is represented as a sum of a real potential, imaginary potential and spin-orbit potential. The real central potential which accounts for the scattering is always taken to have the form:

$$V_R(r) = V_o\ f(r,R_o,a_o) \qquad (1\text{-}3)$$

where $f(r,R_o,a_o) = [1 + \exp\ (r - R_o)/a_o]^{-1}$ which is called

Woods-Saxon form factor (4).

The imaginary part of the optical potential which is responsible for the absorption process in the nuclear reaction contains imaginary surface or/and imaginary volume potential. The imaginary form factor is usually assumed to be the Woods-Saxon for volume absorption and derivative Woods-Saxon for surface absorption.

The spin-orbit potential is used to explain the interaction of the nuclear reactions which depend on the spin of the nucleus.

The optical model has proven very successful to calculate differential elastic scattering cross-sections for various nucleus-particle interactions especially neutrons and protons at high energies. The foward peaking of neutron differential scattering cross-section at high energy where the experimental measurements cannot be done because of the experimental difficulties, can be predicted by this model. There are basically two types of analysis to determine the optical model parameters, i.e

(i) Single energy search. In this search a single set of data for one element at one energy is fitted. The optical parameters are adjusted systematically until a best fit is achieved between observed and calculated cross-section data.

(ii) Global search. In this search an average set of optical model parameters is sought to fit a number of angular distributions as a function of mass number or/and

energy.

As mentioned in section (1.2), the experimentally observed elastic scattering cross-section is divided into the shape elastic cross-section and compound elastic cross-section, i.e,

$$\sigma_E = \sigma_{S.E} + \sigma_{C.E} \qquad (1-4)$$

Because of this, the calculated differential cross-section is less than the observed value due to the present of compound elastic scattering. This feature can lead to difficulties in applying the optical model when compound elastic scattering is appreciable. The compound elastic scattering, however is appreciable only at the neutron energy below 5 MeV. If the neutrons of higher energy (say 10 MeV) were used, the possibility of compound elastic scattering would become very small, more nuclear levels being available for elastic scattering.

Many investigations have shown that the differential elastic, absorption and total cross-sections can be well fitted by the optical model with a complex potential with suitably adjusted parameters. A considerable number of computer programs are now available to determine optical parameters. An extensive analysis on elastic scattering of neutrons from nuclei was done by Perey and Buck (5) who used an energy independent non-local optical potential to fit the data from 1 to 25 MeV. An overall local neutron potential equivalent to

that of Perey and Buck has been derived by Wilmore and Hodgson (6) with different parameters. This set of optical potential which is energy dependent gives good agreement with experimental data for medium and heavy nuclei in the energy range 1 to 15 MeV.

A wide range of neutron data for nuclei with A > 40 and energies between 1 to 7 MeV was analyzed by Becchetti and Greenlees (7). Their model employed many nucleon-nucleus constrains based on the global proton-nucleus analysis for proton data between 10 to 40 MeV. El-Kadi et al (8) used this set of optical parameter on ^{63}Cu and ^{65}Cu and the prediction of the differential elastic cross-sections agree best for higher energies neutron.

Rapaport et al (9) reported three set of global optical model parameters based on fitting 11 MeV to 26 MeV neutron differential elastic scattering cross-sections for five nearly spherical nuclei between ^{40}Ca and ^{208}Pb. A smooth variation of the real radius parameter with mass number was investigated.

A number of other global parameter sets resulting from fitting such data over a wide range in energy and mass number have been published. For some reasons it is probably best to used parameter sets which have been determined systematically over a range of energies and mass numbers rather than use best fit parameters to a single angular distribution. This is because the

parameters obtained for a single angular distribution may be affected by systematic experimental errors. Because lack of experimental data available over a range of energies and mass numbers, a systematic establishment of the optical parameter set is difficult to obtain . Therefore, the experimental determination of differential scattering cross-sections over a large range of energies and mass numbers are strongly recommended.

1.4:THE RESEARCH PROGRAMME.

Nuclear data of interest in design of fusion reactor are neutron cross-sections, gamma-ray spectra and yield from radiative capture and inelastic scattering of neutrons. Existing data are mostly limited to fission reactor needs and not all the materials in fission reactor can be used in CTR. Neutron cross-section data at higher energies (say above 10 MeV) are poorly known. Therefore, a careful review of existing data and measurements of the important lacking data are strongly recommended.

In the present work, the measurements of differential scattering cross-sections at 14.1 MeV neutrons in aluminium, copper and molybdenum were carried out. Aluminium and copper are recommended as a structural materials in the fusion reactor. Therefore, the neutron scattering cross-sections for these elements may be needed for the study of radiation damage and for the radiative transmutation rate calculations.

Molybdenum has been considered as neutron multiplying materials constituent in the breeder blanket because of its high (n,2n) cross-section. It neutron scattering and various neutron cross-sections are important in tritium breeding ratio calculations for fusion reactor design.

The measurements of the differential scattering cross-sections were done using the associated particle time of flight spectrometer similar to those described by Janicki and Cox (10). A low energy, S.A.M.E.S, type J accelerator was used to provide 14.1 MeV neutrons from $T(d,n)He^4$ reaction. The design, construction and calibration of the spectrometer constituted one part of the reseach work.

From the literature survey under taken, it was found that the differential elastic scattering cross-sections for neutron energy around 14 MeV in aluminium have been measured by many workers. The earliest measurements were done by Coon et al (11) at neutron energy 14.5 MeV in the angular range between 5° to 150° using a ring geometry scatterer. The $T(d,n)He^4$ time of flight technique was adopted in their work and provided about 500 KeV energy resolution.

Pierre et al (12) measured differential elastic scattering cross-sections of 14 MeV neutrons over the angular range from 10^{o} to 138^{o} using a ring geometry and a plastic scintillator as detector. The time of flight

technique using $T(d,n)He^4$ reaction was also adopted in their work.

At the higher angles between 70° to 170° , the differential elastic scattering cross-sections of 14 MeV neutrons in aluminium have been measured by Yuasa (13). In his work, the neutrons generated by $T(d,n)He^4$ reactions were scattered by the disc-shaped scatterer, and counted by the (α-n) coincidence circuit with the resolving time of 4 ns.

Bonazzola et al (14) measured differrential cross-sections for elastic and inelastic scattering of 14.2 MeV neutrons in Al at foward angles between 26° to 90° . The measurements were done using a disc scatterer in the time of flight technique which provide a time resolution of 1.6 ns.

The latest measurements of the differential scattering cross-sections for 14 MeV neutrons in aluminium were done by Whisnant et al (15) in the angular range 20^o to 160^o using a neutron time of flight technique. Data were presented for elastic scattering and for inelastic scattering to the sum of the 0.84 and 1.01 MeV states, the 2.21 MeV state, and the sum of the 2.73, 2.98 and 3.00 MeV states.

In the case of copper, the differential elastic scattering cross-sections for 14 MeV neutrons were first measured by Coon (16) in the small angular range between 6^o to 50^o . Later on Coon et al (11) reported a new

measurements in large angular range between 5^{o} to 150^{o}.

An extensive study was done by El-Kadi et al (8) on the measurements of differential scattering cross-sections for 14 MeV neutrons from enriched samples of ^{63}Cu and ^{65}Cu. The data were presented for elastic scattering and for inelastic scattering to the combined group of first three states. The neutrons source were obtained from $D(d,n)He^{3}$ reaction by pulsed beam time of flight technique.

For molybdenum, the literature search revealed a limited number of elastic differential cross-section measurements for 14 MeV neutrons. The only measurement was reported by Strizhak et al (17) in the angular range between 15^{o} to 160^{o} using $T(d,n)He^{4}$ time of flight technique.

In the present work the angular distributions of scattered neutrons were investigated for various thicknesses of aluminium and copper samples. The thicknesses of the scattering samples used were up to 2 mean free path. For molybdenum sample only thin sample with 0.2 mean free path thickness was investigated.

The results of the differential elastic scattering cross-section for smallest sample thickness of aluminium, copper and molybdenum were compared to the predictions of the optical model using programme SCAT-2 (18).

In scattering cross-section measurements, as the sample thickness is increased, the probability of multiple

scattering is also increased. This results in an effective increase in the measured cross-section due to increase on the probability of neutron scattering interactions in the sample. Analysis of how the effective cross-section varies with thickness of sample is very complicated and simplifications have have to be made. One of the possible way to solve this problem is by Monte Carlo method. This method has been widely used in reactor core and blanket flux calculations. However, in using this method the accurated data of microscopic cross-sections are needed at various energies.

In this work, the differential scattering cross-sections were measured for different thicknesses of aluminium and copper samples. No such measurements have been done for these samples and it is hoped that these results will be usefull as a source of data to study the multiple scattering in the extanded sample.

In this work, a Monte Carlo simulation model was developed to study the multiple scattering process in the extanded samples. The model was capable of predicting the number of neutrons scattered from various thicknesses of the sample at all possible angles between 0° to 350° with 10° increments.

CHAPTER 2

THEORETICAL CONSIDERATIONS FOR THE ASSOCIATED PARTICLE TIME OF FLIGHT TECHNIQUE

2.1:INTRODUCTION.

Determination of neutron energy by the time of flight technique has been the most important approach in recent years. There are several different time of flight techniques for fast neutron spectroscopy. All of them are characterized by the measurement of time elapsed between the time of production of neutron at the target and the detection of neutron. The most useful method to measured the time different is by a time to pulse height converter whose pulse height output is directly proportional to the time different of the two pulses ariving at the converter input. This pulse height distribution can then be recorded on the multichannel analyzer.

Time of flight technique requires the establishment of two time signals, "start" and "stop", relating to neutron production and detection. The neutron source is normally produced by a nuclear reaction induced by ion bombardment. A pulsed beam of several nano-seconds duration causes a nuclear reaction in the target. The time of flight of the ejected neutron is measured over a distance of several metres and hence the energy of neutron is calculated. If the neutron source and detector are separated by a fixed distance d, known as the flight path,

then the time taken to travel this distance as a function of neutron energy is given by,

$$t = \frac{d}{v} = 72.298\ E_n^{-\frac{1}{2}}\ .d \quad \text{nsec.} \qquad (2\text{-}1)$$

where

E_n = the energy of neutron in MeV,

d = the flight path in metres.

Hence for a flight path of 1 metre, the time interval for neutron of energies in the range 0.5 MeV to 15 MeV is of the order of a few nano-seconds to 100 nano-seconds.

Equation (2-1) was derived for neutron energy in the non-relativistic region. The flight time up to 50 MeV neutron can be calculated with a small relativistic correction to an accuracy of better than 1 % (19). It is given by the equation

$$t = \frac{72.298}{E_n^{\frac{1}{2}}}\ d\ (\ 1 + 0.798\text{x}10^{-3}\ E_n)\ \text{nsec.} \qquad (2\text{-}2)$$

For neutron with energy of 14 MeV, the different between the relativistic and non-relativistic calculation of t/d is about 0.01 nano-second/metre.

The accuracy with which energy measurements are possible with the time of flight method is connected with the uncertainties Δt in flight time and Δl in the flight path. Since, the flight distance, d can be measured with high precision, the energy resolution is therefore

$$\Delta E_n = \frac{dE_n}{dt} \Delta t = 2 E_n \frac{\Delta t}{t} \qquad (2\text{-}3)$$

By inserting t from equation (2-1) to equation (2-3) the energy resolution is given by

$$\Delta E_n = 0.028 \frac{\Delta t}{d} E_n^{3/2} \text{ MeV} \qquad (2\text{-}4)$$

Various factors contribute to the time resolution Δt. These are

(i) The time spread due to the finite width of the neutron burst.

(ii) The time spread due to the finite thickness of the detector.

(iii) The time spread due to the variations in response time of the detector and electronics.

On the assumption that each factor leads to a Gaussian distribution, we may write,

$$\Delta t = \left[(\Delta t_P)^2 + (\Delta t_D)^2 + (\Delta t_E)^2 \right]^{1/2} \qquad (2\text{-}5)$$

where

Δt_P = the time spread due to the finite width of the neutron burst.

Δt_D = the time spread due to the finite thickness of the detector.

Δt_E = the time spread due to variations in response time of the detector and electronics.

The quantities Δt_P and Δt_D can be varied but as they are reduced the efficienccy of the system is decreased.

Δt_E is fixed chieftly by variation in response time of the detector. The rise time of the detector pulse is governed by the decay time of the scintillator and the transit time spread of the photomultiplier. In the proton-recoil detector the spread in response time is due largely to the continuous range of pulse amplitudes especially if large scintillator and light guide is used.

There are two types of measurement of energy distribution of neutrons emitted from the nuclear reaction which can be measured by the time of flight technique. These are,

(i) Measurement of gamma-ray production by inelastic scattering as the residual nucleus de-excited.

(ii) Direct measurement of the scattering of neutron energy and angular distribution.

These two types of measurement are important source of information in the study of nuclear structure and nuclear reaction mechanism.

2.2:THE PRINCIPLE OF THE TIME OF FLIGHT SPECTROMETER.

The basic problems involved in using time of flight technique can be divided into two parts,

(i) The production of a signal giving the time zero at the start of the flight of neutrons whose the energy is

to be measured.

(ii) The production of another signal corresponding to the end of its flight.

The time of production of neutron can be determined by two general methods, i.e,

(i) The pulsed beam method.

(ii) The associated particle method.

2.2.1:THE PULSED BEAM METHOD.

The pulsed beam method can be used for all reactions in which the neutrons are produced by nuclear reaction induced by ion bombardment. Therefore, a wide range of neutron energy can be covered by the use of different types of charged particles induced reactions with a suitable accelerator device.

In the pulsed beam method, the pulsed beam of particles is used to initiate the neutron emission. This can be achieved by modulating the beam of charged particles striking the target to produce short bursts of particles. The neutrons produced in short bursts are then be used to mark the beginning of the neutron flight time. The end of the flight path of neutrons is marked by a signal from the neutron detector.

The method used to produce short bursts of beam particles depends on the energy involved and the type of particle accelerator which is used. The most useful methods to produce short bursts of beam particles can be

devided into two categories, i.e,

(i) Beam Sweeping Method, and

(ii) Beam Bunching Method.

In the beam sweeping method, the beams are passed across a set of deflector plates. A high frequency, high voltage signal is supplied to the deflection plates to sweep the beam rapidly across an aperture infront of the target. A neutron bursts as small as 1 ns duration can be produced by this method. This method was first proposed by Cranberg and Levin (20) using a Van de Graaft accelerator to accelerate protons to produce neutrons from $T(p,n)He^3$ reaction. The accelerated protons were swept across the target by applying sinusoidal voltage of frequency 3.7 MHz to a pair of deflector plates. With this method neutron bursts of 2 ns duration were obtained.

The method discussed above is typically the post-acceleration beam pulsing type and generally restricted to ion beams with energy less than 2 MeV. For beams of higher energy the pre-acceleration technique is prefered. In this technique the beam is swept before it leaves the high voltage terminal of the accelerator. By this method, the duration of the neutron bursts obtained is comparably larger but a greater ion burst current can be produced and this reduces the background problems.

In the beam bunching method, the ion bursts are produced by bunching the beam after the beam was swept by either post or pre-acceleration techniques. The methods

for beam bunching can be made by a Mobley type-magnet (21) or Klystron buncher. Smith et at (22) employed the Molbey type-magnet to pulse the proton beams to produce neutrons from $^{7}Li(p,n)Be^{7}$ reaction. The pulsed ion beams of 10 to 15 ns duration were accelerated through a stabilized potential of the Van de Graaf. After acceleration, the beams burst passed through an electrostatic deflector driven by a radiofrequency oscillator kept in a synchronous phase with the beam burst. The phase was such that the burst was swept across the entrance face of a 90° time compression magnet. The magnet employed provided a time contraction of about 10 to 1 resulting in an about 1 ns ion burst at the neutron producing reaction.

Klystron bunching has been described by Stelson et al (23) for use with a Cockroft-Walton accelerator. The ion burst with 30 ns duration after being chopped with a frequency of 4.5 MHz was then velocity modulated in a Klystron tube to produce a neutron burst of less than 2ns duration.

2.2.2:THE ASSOCIATED PARTICLE METHOD.

The associated particle time of flight technique was first employed in neutron scattering experiment by O'Niel (24). This technique cannot be used when no particle or gamma-ray is emitted in association with neutron, i.e in the processes in which the neutron emission leaves the residual nucleus in the ground state.

In the associated particle method the start signal is taken from the detection of the associated particle or gamma-ray emitted from the neutron producing reaction. The associated particle or gamma-ray is directly related to the instant of neutron production and can be detected in a fixed solid angle by placing the detector as close as possible to the neutron source to obtain the maximum rate of coincidence. The target geometry must be carefully designed so that the associated radiations can escape the target.

As the time zero is obtained without the use of pulsed neutron source, the uncertainty in the neutron production time is only governed by time uncertainty of the detector and electronics and the associated particle path geometry. The time uncertainty of the detector and electronics depends mostly on the scintillator and photomultiplier employed. In recent years there have been considerable improvements in photomultipliers which introduce the possibilities of achieving minimum time resolution.

In the present work, the associated particle time of flight technique was employed. The reaction

$$T + d \longrightarrow n + {}^{4}He + 17.6 \text{ MeV}$$

was adopted to produce a 14.1 MeV neutron source. The S.A.M.E.S type J electrostatic accelerator was used to

accelerate a deuteron beam up to 140 keV on to a TiT target. The He^4 nucleus (alpha-particle) emitted with an energy of 3.5 MeV can provide a zero time signal for neutron time of flight measurement. The zero time signal obtained by alpha-particle detection is directly related to the instant of neutron production.

The solid angle subtended by alpha-particle detector at the tritium target defines a related solid angle into which the associated neutrons are emitted. The related position of the scattering sample and the alpha-particle detector was obtained from the kinematics of the $T(d,n)He^4$ reaction. This will be discussed in the following sections.

2.3:KINEMATICS OF THE $T(d,n)He^4$ REACTION.

The neutron source used in the present experiment was produced from $T(d,n)He^4$ reaction. A monoenergetic 14.1 MeV neutron will be produced by accelerating the deuteron beam up to 140 keV onto Tritium target. The alpha-particle produced in this reaction associated to the 14.1 MeV neutron has an energy of 3.5 MeV.

The Kinematics of the $T(d,n)He^4$ reaction can be represented in the laboratory and centre of mass system by the two body interaction as shown in figure (2.1).

From the conservation of momentum and energy, the following equation can be obtained.

$$Q = E_n\left(1 + \frac{M_n}{M_\alpha}\right) - E_d\left(1 - \frac{M_d}{M_\alpha}\right) - \frac{2}{M_\alpha}(M_n M_d E_n E_d)^{\frac{1}{2}} \cos\theta_n \quad (2\text{-}6)$$

where,

Q = the Q-value of the $T(d,n)He^4$ reaction,

M_n = mass of neutron,

M_α = mass of alpha-particle,

M_d = mass of deuteron,

E_n = energy of neutron in the laboratory system,

E_d = energy of deuteron in the laboratory system,

θ_n = the neutron emission angle in the laboratory system.

By rearranging equation (2-6), Benveniste and Zenger (25) relates the neutron energy E_n and the angles of emission θ_n in the laboratory system as,

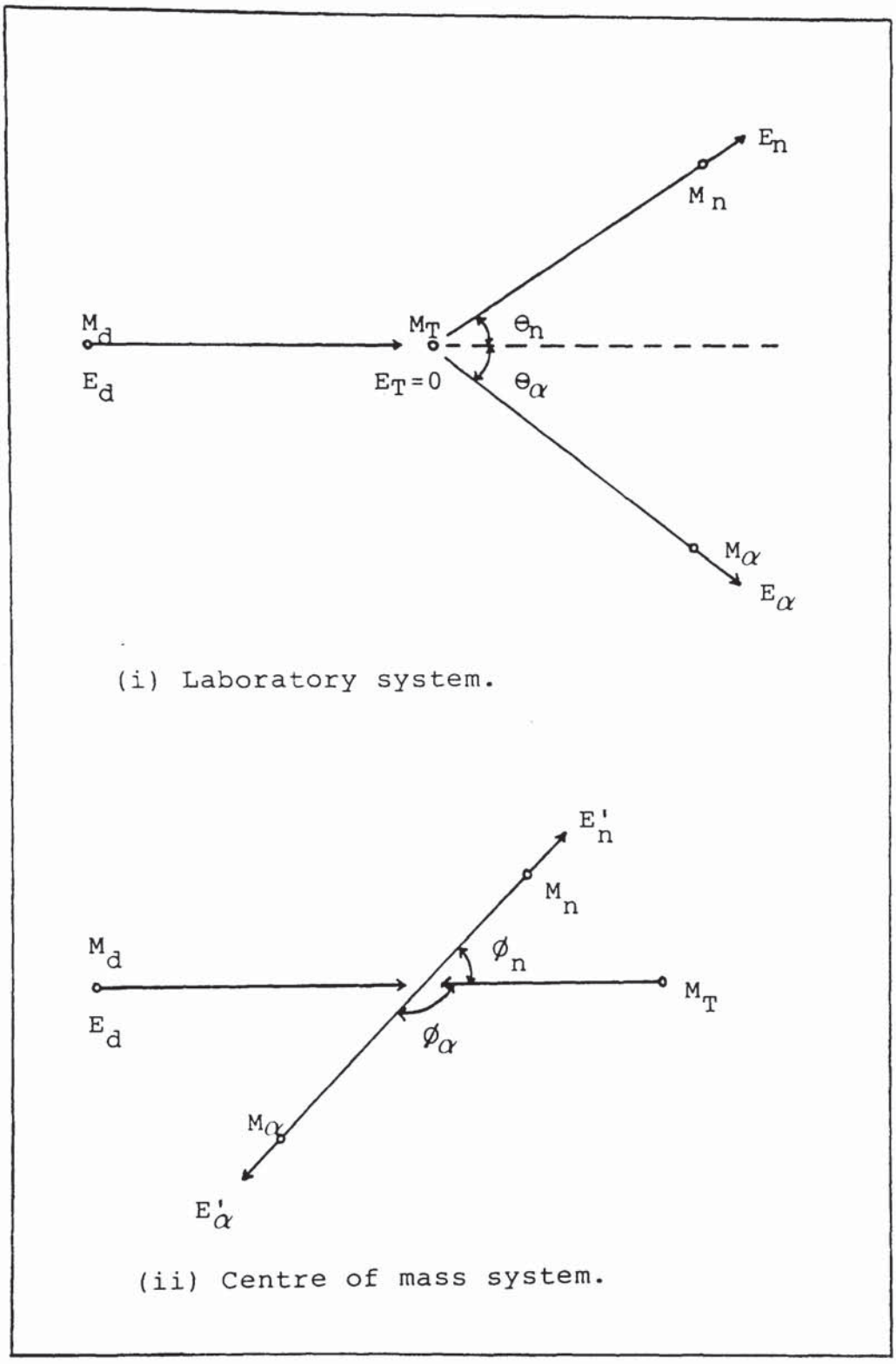

Figure (2.1):Representation of $T(d,n)He^4$ reaction in the laboratory and the centre of mass system

$$E_n = E_d \frac{M_n M_d}{(M_n + M_\alpha)^2} \left\{ 2 \cos^2\theta_n + \frac{M_\alpha (M_n + M_\alpha)}{M_d M_n} \left(\frac{Q}{E_d} + 1 - \frac{M_d}{M_\alpha} \right) \right.$$
$$\left. \pm 2 \cos\theta_n \left[\cos^2\theta_n + M_\alpha \frac{(M_n + M_\alpha)}{M_d M_n} \left(\frac{Q}{E_d} + 1 - \frac{M_d}{M_\alpha} \right) \right]^{\frac{1}{2}} \right\} \quad (2\text{-}7)$$

Based on the above equation, the energy of neutron at various angles of emission from different deuteron energies was calculated using computer programme written in BASIC as shown in Appendix A . Figure (2.2) shows the variation of neutron energies with angles in the laboratory system.

The target assembly used in the present work was designed to allow observation of the alpha-particles emitted at $\theta_\alpha = 90^\circ$ to the incident deuteron beam direction. Therefore, it was necessary to relate, in the laboratory system, the neutron emission angles associated with an alpha-particle detector centred at $\theta_\alpha = 90^\circ$. The following equation, given by Benveniste and Zenger (25), relates the neutron and alpha-particle angles in the laboratory system, i.e

$$\tan\theta_\alpha = \frac{\frac{1}{2}\sin^2\theta_n + \sin\theta_n (1/\gamma^2 - \sin^2\theta_n)^{\frac{1}{2}}}{-\sin^2\theta_n + \cos\theta_n (1/\gamma^2 - \sin^2\theta_n) - M_\alpha/M_n} \quad (2\text{-}8)$$

where

$$\frac{1}{\gamma^2} = \frac{M_\alpha}{M_n} \left(\frac{M_d + M_T}{M_d} \right) \left(\frac{M_T}{M_d + M_T} + \frac{Q}{E_d} \right) \quad (2\text{-}9)$$

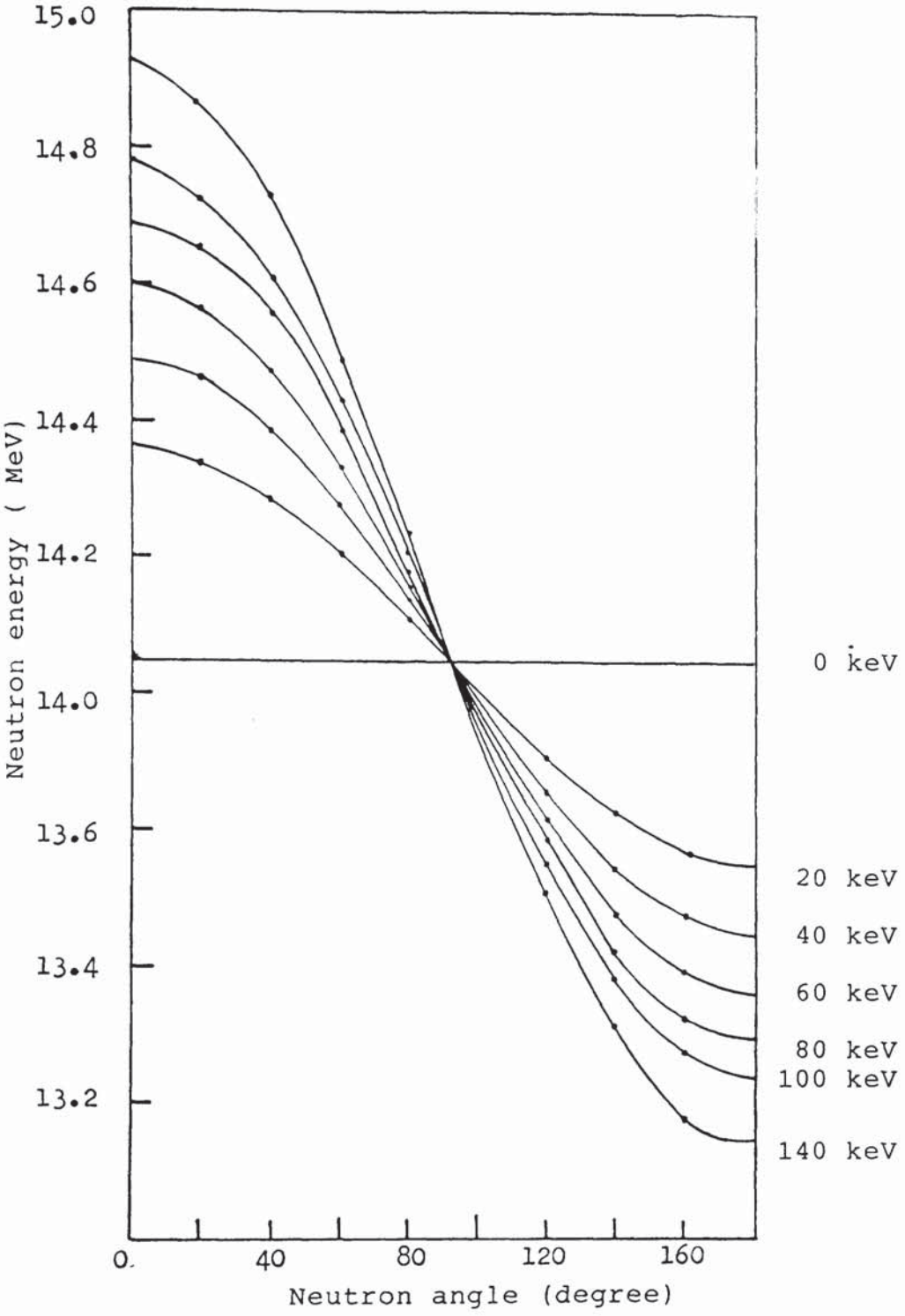

Figure (2.2):Variation of neutron energy with angle from $T(d,n)He^4$ reaction at various deuteron energies.

Using equation (2-8) and (2-9), the angular relationship between neutron and alpha-particle was calculated by a computer programme written in BASIC (Appendix A).

In the present work, the solid angle of alpha-particle detector was defined by a 11mm x 19mm rectangular aperture in an aluminium plate. This aperture subtended a semi-angle of 3.5° in the horizontal and 6° in the verticle directions at the target with detector to target centre distance of 90mm. Figure (2.3) shows the relationship between neutron and alpha-particle angles in the angular range interest for deuteron energies from 0 to 140 keV. The figure shows that the alpha-particle detected at $90^{\circ} \pm 3.5^{\circ}$ defined a neutron beam over the angular range $\theta_n = 78.5^{\circ}$ to $\theta_n = 93.5^{\circ}$. In this angular range, the neutron yield is not uniform since the $T(d,n)He^4$ reaction cross-section is a function of deuteron energy and the energy range of deuterons producing neutron varies with θ_n. For example, from figure (2.3), at $\theta_n = 80^{\circ}$, the neutron yield as defined by alpha-particle detector is produced only by deuteron interactions with energies from 90 keV to 140 keV and at $\theta_n = 85^{\circ}$, neutron can be produced by deuteron with energies from 10 to 140 keV. The details of the neutron yield produced from $T(d,n)He^4$ reaction will be discussed in the following section.

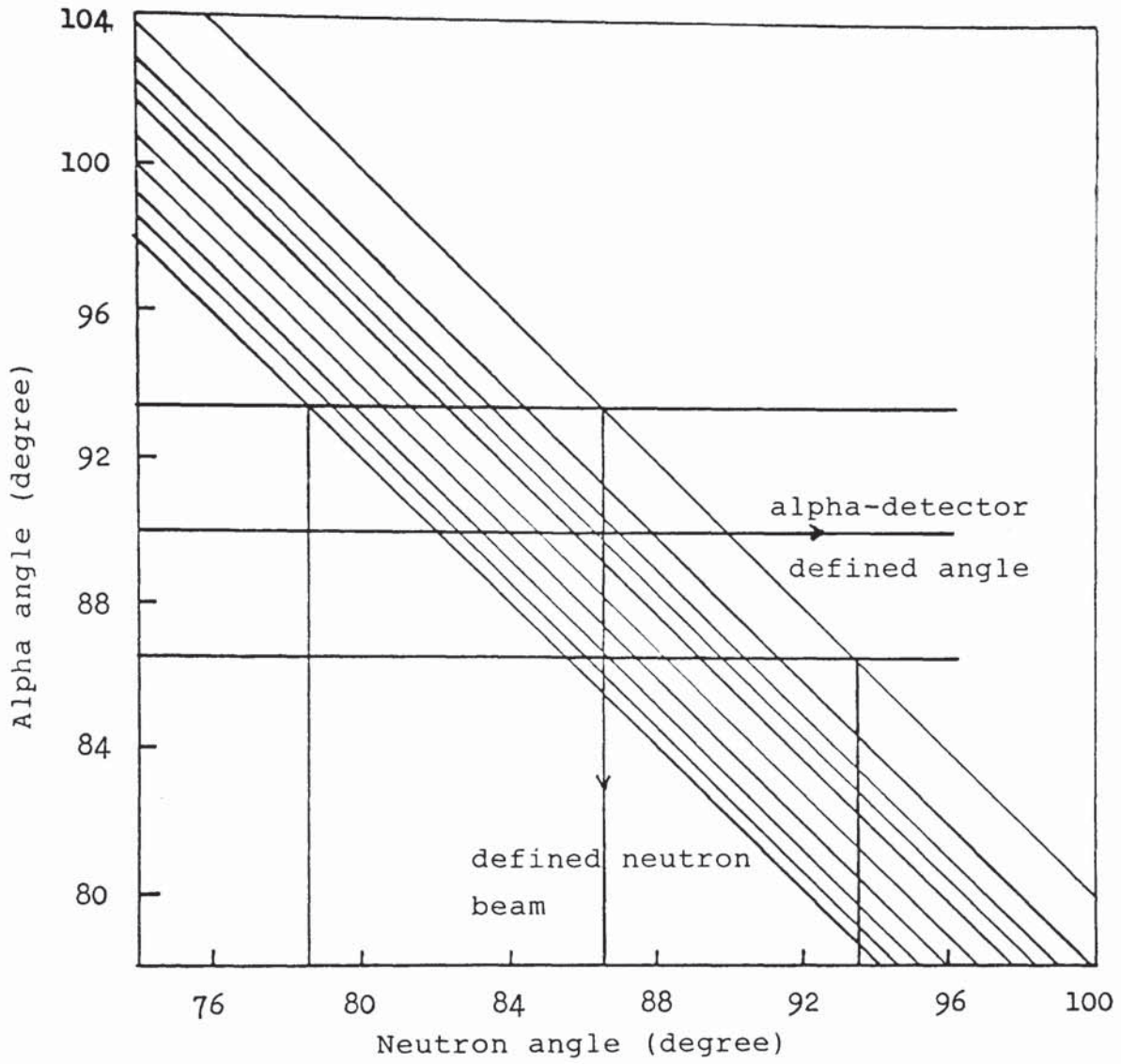

Figure (2.3):Relationship between alpha and neutron angles at various incident deuteron energies in the laboratory system.

2.4: THE NEUTRON YIELD FROM $T(d,n)He^4$ REACTION.

To determine the neutron beam profile, i.e the relative neutron yield over the angular range from θ_n = 78.5° to 93.5°, the variation of neutron yield with deuteron energy must be calculated.

The total "thick" target yield of neutrons per incident deuteron is given by

$$Y(E) = \int_0^E \frac{n\,\sigma(E)\,dE}{dE/dx(E)} \qquad (2\text{-}10)$$

where,

n = the number of tritium atom per cm^3 in the target,

$\sigma(E)$ = the $T(d,n)He^4$ reaction cross-section at deuteron energy E,

dE/dx(E) = the rate of energy loss of deuteron in the target.

The above expression assumed that the incident particle flux is constant throughout the target. This is a good approximation as only a very small fraction of deuteron beam interacts with tritium target.

Since the angular dependence of the differential cross-section for $T(d,n)He^4$ reaction is isotropic in the centre of mass system up to 200 keV (26,27), the total yield of neutrons per incident deuteron energy per unit solid angle, at a neutron emission angle θ_n is given by

$$Y(E,\theta_n) = \int_0^E 4\pi n \frac{\frac{d\sigma}{d\Omega'}(E)\ \frac{d\Omega'}{d\Omega}(\theta_n,E)}{\frac{dE}{dx}(E)} dE \qquad (2\text{-}11)$$

where,

$\frac{d\sigma}{d\Omega'}(E)$ = the differential cross-section per unit solid angle at deuteron energy E,

$\frac{d\Omega'}{d\Omega}(\theta_n,E)$ = the anisotropy factor.

In order to calculate the neutron yield, each term in equation (2-11) must be known. This will be discussed in the following sections.

2.4.1. THE NUMBER OF TRITIUM ATOM IN TiT TARGET.

The target foil used in this work was type TRT31 from Radiochemical Center, Amersham plc and consisted 1.09 mg per cm^2 layer ($\sim$ 2200 nm thickness) of tritiated titanium on copper backing. The number of tritium atom in TiT target is obtained by the following expression (28),

$$n = \frac{N \rho_{TiT} \times 6.02 \times 10^{23}}{A_{TiT}} \qquad (2\text{-}12)$$

where, A_{TiT} = mass of TiT target,

$\rho_{TiT} = \frac{48 + 3N}{48} \times \rho_{Ti} \times 0.85$ is the density of the TiT target,

N = tritium loading factor.

In this calculations a loading factor of one was assumed. However, it is possible to imagine a surface layer lacking in tritium atoms compared with the inside depth of the target. Gunnersen and James (28) have investigated the distribution of tritium atom in the TiT target. They found that the concentration peak of tritium is never less than 300 nm below the surface, and there is very little tritium contained in upper surface layer of about 50 nm, or in the lower one-third of the TiT material.

By assuming a loading factor of one tritium per titanium atom throught the thickness of the target, the density of the target is then,

$$\rho_{TiT} = \frac{48 + 3}{48} \rho_{Ti} \times 0.85 = 4.1 \text{ g/cm}^3$$

where,

$$\rho_{Ti} = 4.54 \text{ g/cm}^3 .$$

The factor 0.85 arises from the 15% expansion which the titanium lattice undergoes during tritiation.

The number of tritium atom per cm^3 is then

$$n = \frac{1 \times \rho_{Ti} \times 6.02 \times 10^{23}}{A_{TiT}} = 4.84 \times 10^{22} \text{ atoms/cm}^3$$

2.4.2:THE DIFFERENTIAL CROSS-SECTION FOR $T(d,n)He^4$ REACTION.

The differential cross-section for the production of neutron from $T(d,n)He^4$ reaction has been found to be isotropic in the centre of mass system by Allen and Poole (26) and Argo et al (27) up to at least 200 keV deuteron energies. Conner et al (29) have measured for deuteron energies between 10 keV to 1730 keV and Arnold et al (30) for 7.5 keV to 120 keV deuteron energy range. The values obtained are fairy good agreement between the various authors (26,29,30).

For the purpose of the neutron yield calculation, the values of the differential cross-section for the $T(d,n)He^4$ reaction were taken from Liskin and Poulsen (31) for deuteron energies up to 140 keV. Figure (2.4) shows the 0^0 centre of mass differential cross-section versus deuteron energy up to 200 keV.

2.4.3:THE ANISOTROPY FACTOR.

The anisotropy factor $d\Omega'/d\Omega$ is required to convert the centre of mass differential cross-section to the laboratory system. Anisotropy factor is defined by ratio of the solid angle in the centre of mass system and the laboratory system, into which the neutron is scattered and given by,

$$\frac{d\Omega'}{d\Omega} = \frac{\text{Sin } \theta_n \, d\theta_n}{\text{Sin } \phi_n \, d\phi_n} \qquad (2\text{-}13)$$

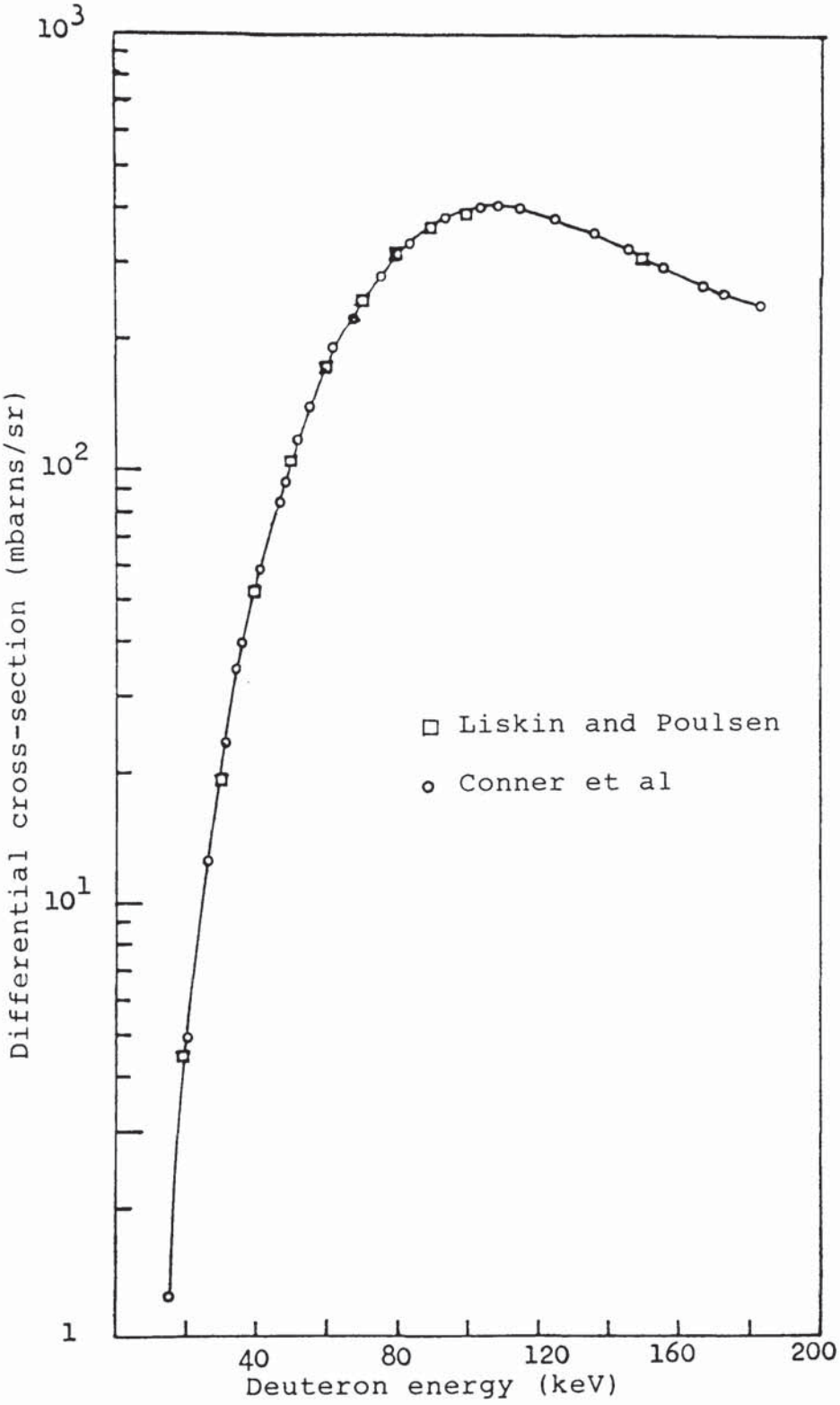

Figure (2.4): 0° centre of mass differential cross-section for $T(d,n)He^4$ reaction versus deuteron energy.

where

$d\Omega'$ = the element of solid angle in the centre of mass system,

$d\Omega$ = the element of solid angle in the Laboratory system,

Θ_n = the neutron emission angle in the Laboratory system,

ϕ_n = the neutron emission angle in the center of mass system.

Benveniste and Zenger (25) gave the relationship between Θ_n and ϕ_n as

$$\text{Cos } \phi_n = - \gamma \text{Sin}^2 \Theta_n + \text{Cos}(1 - \gamma^2 \text{Sin}^2 \Theta_n)^{\frac{1}{2}} \qquad (2\text{-}14)$$

where γ was defined previously in equation (2-9).

Differentiating equation (2-14) and rearranging give

$$\frac{d\Omega'}{d\Omega} = \frac{\gamma \left[\text{Cos } \Theta_n + (1/\gamma^2 - \text{Sin}^2 \Theta_n)^{\frac{1}{2}}\right]^2}{(1/\gamma^2 + \text{Sin}^2 \Theta_n)^{\frac{1}{2}}} \qquad (2\text{-}15)$$

The anisotropy factor is plotted against the neutron angle for deuteron energies between 0 to 140 keV are shown in figure (2.5). For neutron emitted between $\Theta_n = 78.5^\circ$ to $\Theta_n = 93.5^\circ$, the anisotropy factor is a slowly varying function of deuteron energy and it can be considered as a contant to within 1% with the value unity.

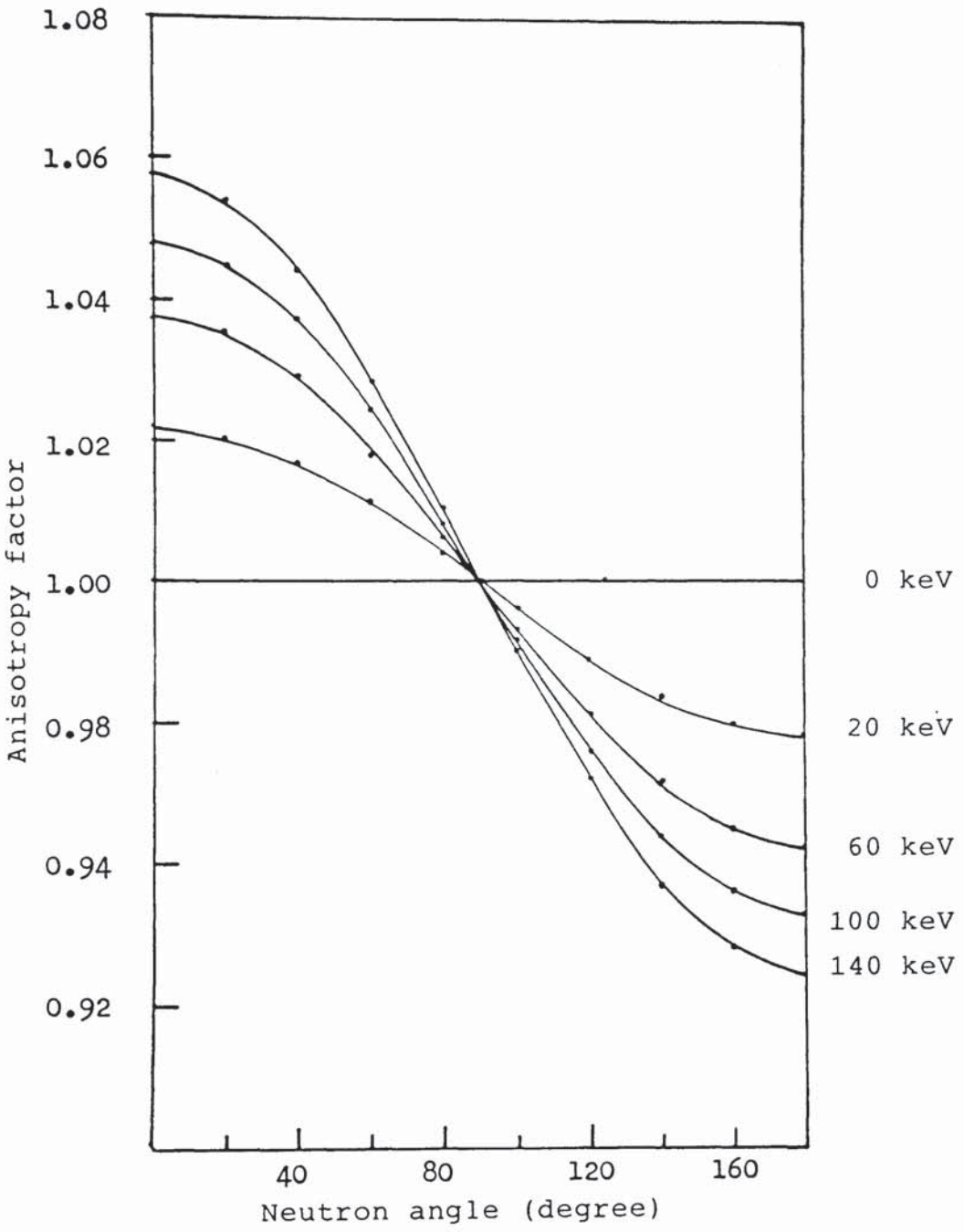

Figure (2.5):The neutron anisotropy factor versus neutron angle at various deuteron energies.

2.4.4:THE RATE OF ENERGY LOSS OF DEUTERON IN TiT TARGET.

In order to calculate the neutron yield over the energies of deuterons from the incident energy E down to the point where all their energy is absorbed, the rate of energy loss, (dE/dx) of deuteron in TiT target are required at various deuteron energies up to 140 keV. There are no available experimental data on the rate of energy loss of deuteron in TiT target for the required energy range. However, Gunnersen et al (28) and Benveniste and Zenger (25) used the values of (dE/dx) of deuterons in titanium and tritium to calculate the rate of energy loss in TiT target. The following equation has been used.

$$\frac{dE}{dx}(E) = \frac{48}{3 + 3N}\left[\frac{dE}{dx}(E)\right]_{Ti} + \frac{3N}{48 + 3N}\left[\frac{dE}{dx}(E)\right]_{T} \qquad (2\text{-}16)$$

where

$\left[\frac{dE}{dx}(E)\right]_{Ti}$ = the rate of energy loss of deuteron in titanium for deuteron energy E,

$\left[\frac{dE}{dx}(E)\right]_{T}$ = the rate of energy loss of deuteron in tritium for deuteron energy E,

N = the tritium loading factor.

Because of the lack of data available on the rate of energy loss of deuteron in titanium, the rate of energy loss was derived from the proton data (25,28). By assuming that the rate of energy loss is a function only

on the velocity of the particle, the value of (dE/dx) of deuterons are simply obtained by doubling the energy scale, i.e,

$$\left[\frac{dE}{dx}(E)\right]_{p(E)} = \left[\frac{dE}{dx}(E)\right]_{d(2E)} \qquad (2\text{-}17)$$

where,

$\left[\frac{dE}{dx}(E)\right]_{p(E)}$ = the rate of energy loss of proton,

$\left[\frac{dE}{dx}(E)\right]_{d(2E)}$ = the rate of energy loss of deuteron.

Warshaw (32) has measured the rate of energy loss of proton in Al, Cu, Ag and Au in the energy range 50 keV to 350 keV. Benveniste and Zenger (25) and Gunnersen et al (28) calculated the values of (dE/dx) of proton in titanium by interpolating with respect to $A^{-\frac{1}{2}}$ between Warshaw's experimental curves for proton in Al and in Cu. This curve has then been extrapolated back to origin to obtain the lower energy loss values.

In the present calculation, the rate of energy loss of deuteron in titanium was taken from Gunnersen et al (28). Figure (2.6) shows the variation of the rate of energy loss of deuteron in titanium with deuteron energy up to 140 keV.

The rate of energy losses of deuterons in tritium gas have been published by Reynolds et al (33) for deuteron energy range 60 keV to 700 keV. These measurements agree with some energy loss measurements made

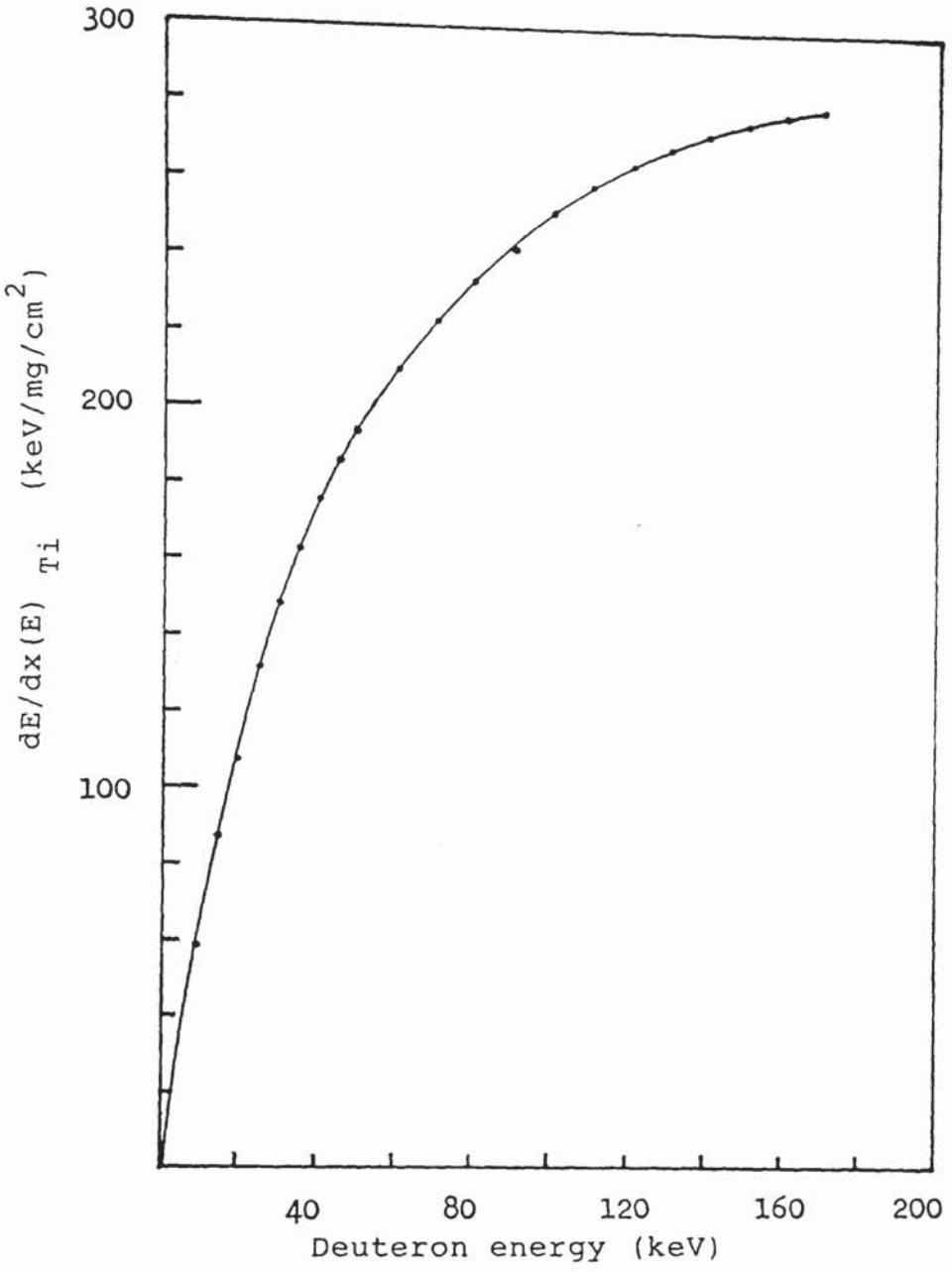

Figure (2.6):The rate of energy loss of deuteron in titanium.

by Philips (34) for 20 keV to 160 keV deuterons in tritium. For the purpose of the calculations, the rate of energy losses of deuteron in tritium were taken from Philip's works. The rate of energy loss of deuteron in tritium versus deuteron energy is plotted and shown in figure (2.7).

Combining the data of figures (2.6) and (2.7), the rate of energy losses of deuteron in TiT target at various deuteron energies were calculated from equation (2-16). The results are presented in table (2.1) and plotted as shown in figure (2.8).

Gunnersen et al (28) have measured experimentally the rate of energy loss of deuteron in TiT target for a limited deuteron energy range between 40 keV to 120 keV. The data obtained are higher than the values calculated from the obove method. However, the shape of the curves are still the same as shown in figure (2.8).

With all the informations discussed in sections 2.4.1 to 2.4.4, the neutron yield as a function of deuteron energy can be calculated. As we are only interested in the line shape the constant $4\pi n$ in equation (2-11) is set to unity. Therefore, the neutron yield per unit solid angle per incident deuteron energy, at angle θ_n , from deuterons in the energy interval E to dE is obtained using equation (2-11) and it gives,

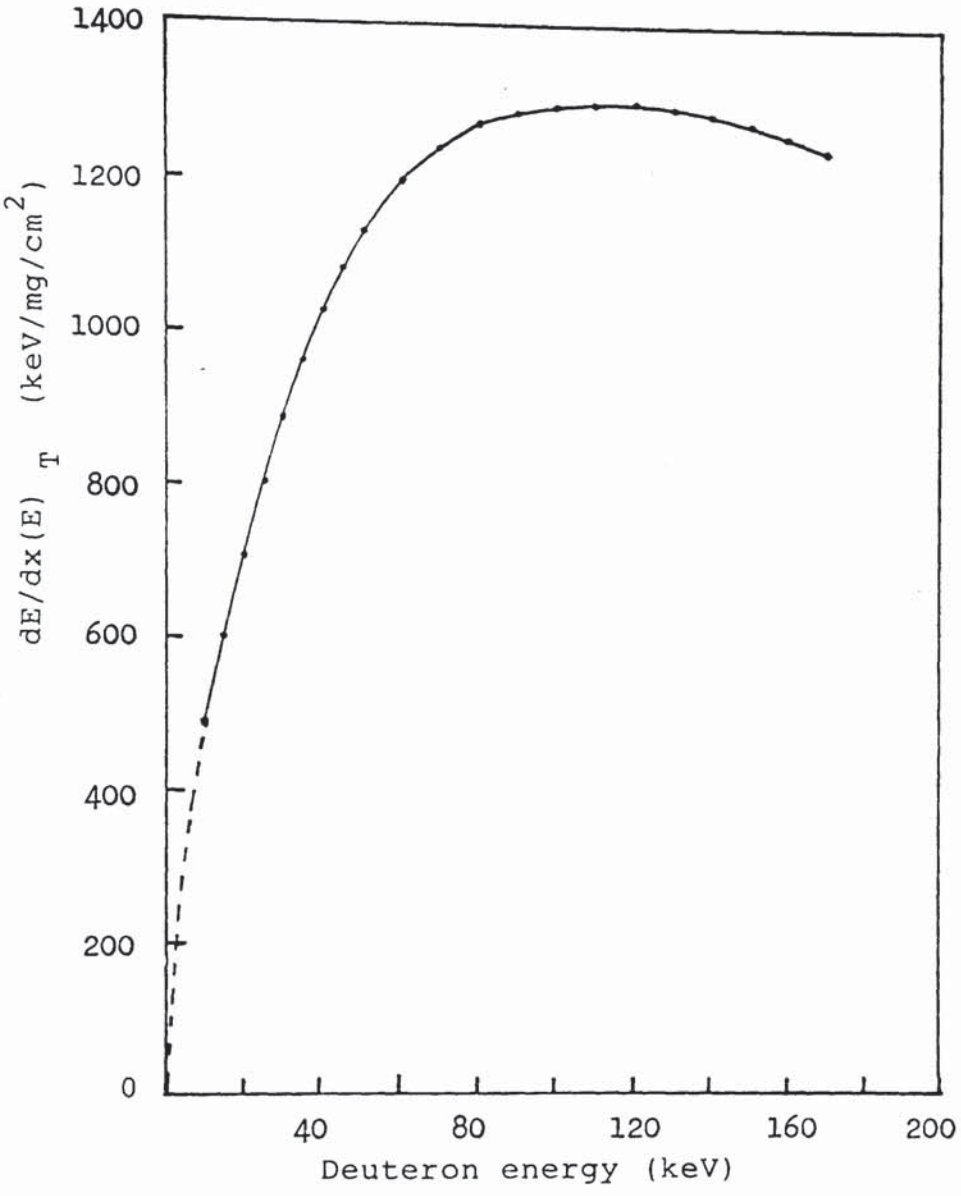

Figure (2.7):The rate of energy loss of deuteron in tritium.

Table (2.1):The rate of energy loss of deuteron in titanium, tritium and tritiated titanium.

E (MeV)	$[dE/dx(E)]_T$ keV/mg/cm²	$[dE/dx(E)]_{Ti}$ keV/mg/cm²	$[dE/dx(E)]_{Ti_xT}$ keV/mg/cm²
10	490	59	84.4
15	600	88	118.1
20	704	108	143.1
25	802	132	171.4
30	890	149	192.6
35	960	163	209.8
40	1023	177	226.8
45	1081	187	239.6
50	1128	193	247.9
60	1183	210	267.2
70	1238	223	282.7
80	1268	233	293.9
90	1281	242	303.1
100	1290	252	313.1
110	1294	260	320.8
120	1295	265	325.6
130	1288	269	328.9
140	1281	273	332.3
150	1270	276	334.5
160	1251	278	335.2
170	1231	280	336.9

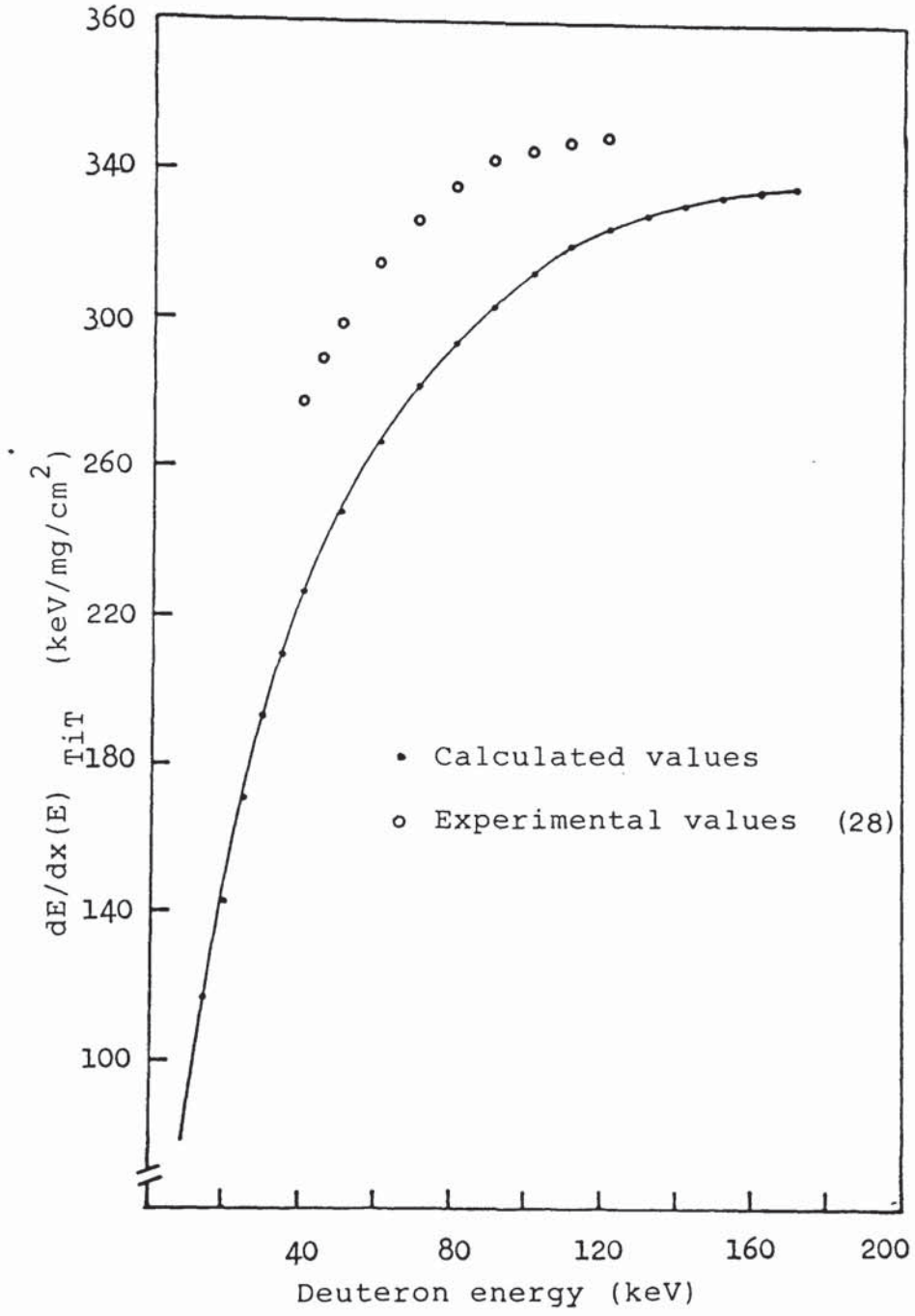

Figure (2.8):The rate of energy loss of deuteron in Tritiated titanium target.

$$Y(\theta_n,E) \propto \frac{\frac{d\sigma}{d\Omega'}(E) \cdot \frac{d\Omega'}{d\Omega}(E,\theta_n) \cdot dE}{\left[\frac{dE}{dx}(E)\right]_{TiT}} \qquad (2\text{-}18)$$

Applying numerical integration to equation (2-18) the neutron yield per unit solid angle per incident deuteron energy was obtained from expression

$$Y(\theta_n,E) = \sum_{\Delta E=10} \frac{\frac{d\sigma}{d\Omega'}(E) \cdot \frac{d\Omega'}{d\Omega}(E,\theta_n) \cdot \Delta E}{\left[\frac{dE}{dx}(E)\right]_{TiT}} \qquad (2\text{-}19)$$

The calculations were done in 10 keV energy steps and resulting the neutron production curve as shown in figure (2.9). The anisotropy factor $\frac{d\Omega'}{d\Omega}$ was taken as a constant with value unity.

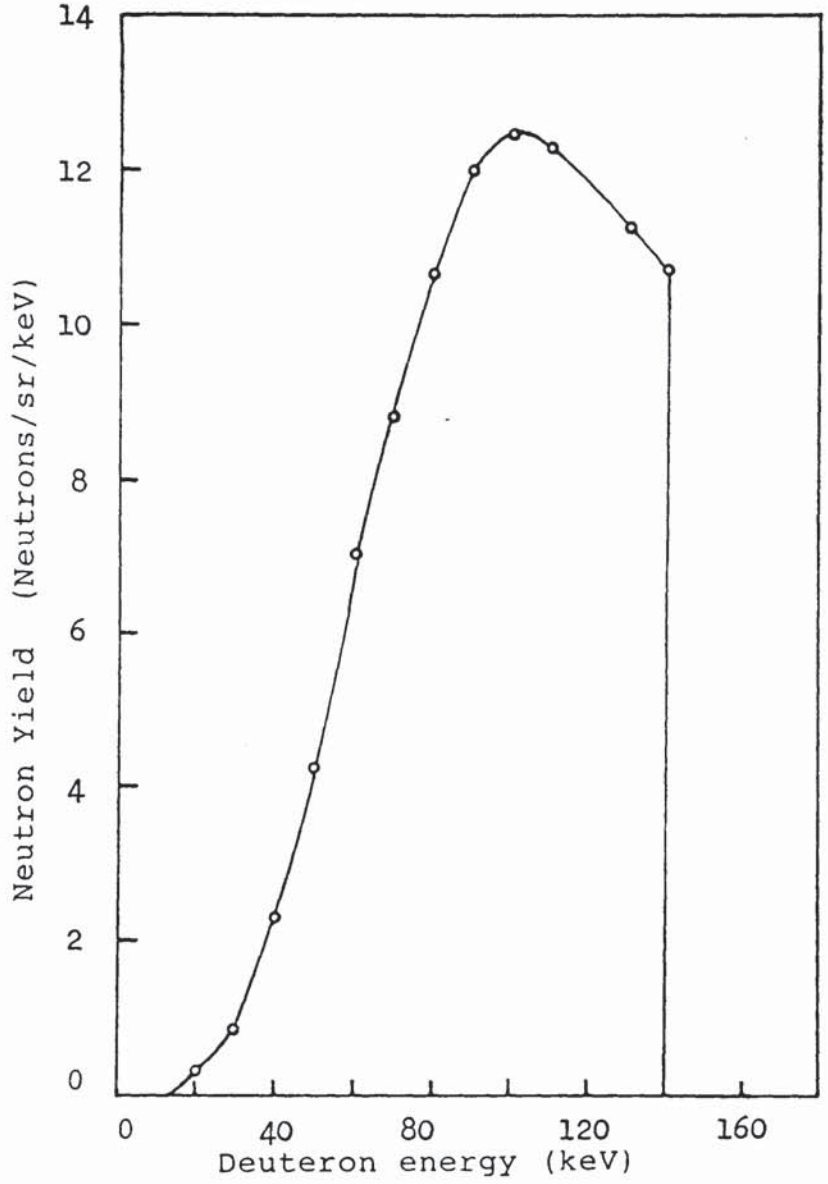

Figure (2.9):Neutron yield from $T(d,n)He^4$ reaction as a function of deuteron energy.

2.5:THE NEUTRON BEAM PROFILE.

The neutron yield at each angle θ_n is called the neutron beam profile and can be calculated using the information of figures (2.3) and (2.9). The figures show that the neutron angle varies with deuteron energy (figure 2.3) and the relative neutron yield varies with deuteron energy (figure (2.9).

The total neutron output was given by the area under the neutron production curve (figure 2.9), i.e

$$A_T = \int_0^{E=140\text{keV}} Y(\theta_n, E)\, dE \qquad (2\text{-}20)$$

By considering the specific case of neutron emitted at angle $\theta_n = 86.5^\circ$, the fraction of neutrons with associated alpha-particle was given by

$$F = \frac{\int_{E_1}^{E_2} Y(\theta_n, E)}{A_T} dE \qquad (2\text{-}21)$$

where

E_1 = lower limit for deuteron energy,

E_2 = upper limit for deuteron energy.

The value of $\int_{E_1}^{E_2} Y(\theta_n, E)\, dE$ is the area under the neutron production curve between deuteron energy E_1 to E_2. For example, from figure (2.3) at $\theta_n = 80^\circ$ the emitted neutrons having detected associated alpha-particles, are only produced by deuterons in the energy interval 140 keV to 90 keV. The area under the curve of figure (2.9) in

the energy interval E = 140 keV to 90 keV is propotional to neutron yield for this deuteron energy interval. Thus the neutron yield at each angle θ_n , as defined by alpha-particle detector was calculated.

The calculated neutron beam profile over the angular range $\theta_n = 78.5^\circ$ to $\theta_n = 93.5^\circ$ defined by the 90 $\pm 3.5^\circ$ alpha-particle detector is shown in figure (2.10) and tabulated in table (2.2).

The FWHM of the neutron beam profile is 7° and it is centred at 83.5° to the incident deuteron beam direction. This angle was chosen as the 0° neutron scattering angle in the practical arrangement.

There are two main assumptions have been made in the calculation of neutron beam profile. These are

(i) The tritium loading factor was taken to be constant throughout the thickness of the target and has a value of unity. The rate of energy loss of deuteron in TiT target depends on loading factor (equation 2.16). However, Benveniste et al (35) showed that a change of a factor of 3 in loading factor will yield a only 10 % change in dE/dx . Since the energy dependence of dE/dx is a very weak function of loading factor, the loading factor can be expected to have unimportant influence in the calculation of neutron beam profile.

(ii) The angular straggling of deuteron and alpha-particle in the target was negligible in the calculation. This effect has been discussed in detail

Table (2.2):Numerical values for calculating the neutron beam profile

Neutron angle(Θ_n)	Deuteron energy (keV)		$\int_{E_1}^{E_2} Y(\Theta_n,E)\,dE$	$F = \int \frac{Y(\Theta_n,E)}{A_T}\,dE$
	lower limit(E_1)	Upper limit(E_2)		
78.5°	140	140	0	0
78.8°	130	140	110	0.011
79.1°	120	140	226	0.224
79.4°	110	140	348	0.346
79.7°	100	140	473	0.470
80.1°	90	140	596	0.592
80.5°	80	140	712	0.707
80.8°	70	140	812	0.806
81.3°	60	140	890	0.884
81.7°	50	140	945	0.938
82.2°	40	140	978	0.971
82.6°	30	140	995	0.988
83.5°	20	140	1006	0.999
84.3°	10	140	1007	1.000
85.5°	0	140	1007	1.000
85.8°	0	130	897	0.891
86.1°	0	120	781	0.776
86.4°	0	110	659	0.654
86.7°	0	100	534	0.530
87.1°	0	90	411	0.408
87.5°	0	80	295	0.293
87.8°	0	70	195	0.194
88.3°	0	60	117	0.116
88.7°	0	50	62	0.062
89.2°	0	40	29	0.029
89.6°	0	30	12	0.012
90.5°	0	20	1	0.001
91.5°	0	10	0	0.000
94.0°	0	0	0	0.000

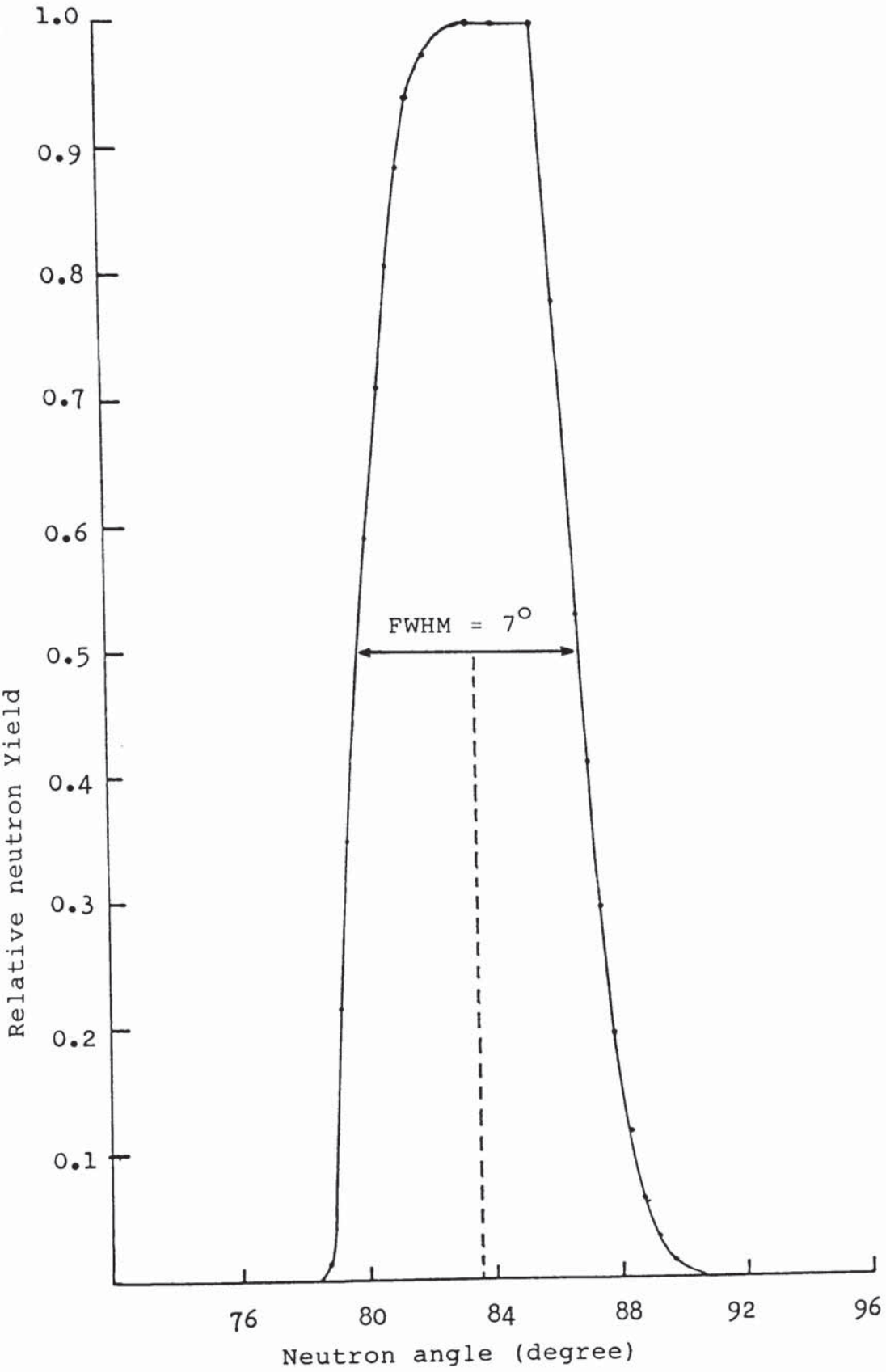

Figure (2.10):The neutron beam profile.

with particular emphasis on its effect on the neutron beam profile by Connel (36).

Figure (2.11) (2.12) show the angular relationship of alpha-particle detector and scattering sample arrangement in the horizontal and verticle directions respectively.

In the preceding calucations of the neutron-alpha relationship a point source was considered. In practice an approximation to a point source was obtained by limiting the dimension of the deuteron beam at the target. In this work a copper aperture plate with dimension of 10mm x 1mm was used.

In the horizontal direction the neutron beam was defined by alpha-particle detector aperture centered at θ_α = 90° and subtending angle of 7° at the reaction point defined by 11 mm alpha-particle aperture. The neutron beam was centered at 83.5° and subtending angle of 12° at the total width of the neutron beam profile of figure (2.10). In the verticle direction the neutron beam was defined by alpha-particle detector aperture of 19 mm width centered at θ_α = 90°. The area of the sample irradiated by the neutrons beam was estimated as 4.2 cm x 4.2 cm.

2.6:THE NEUTRON LINE SHAPE.

The neutron source produced at a given angle of emission has an energy spread due to the various energies

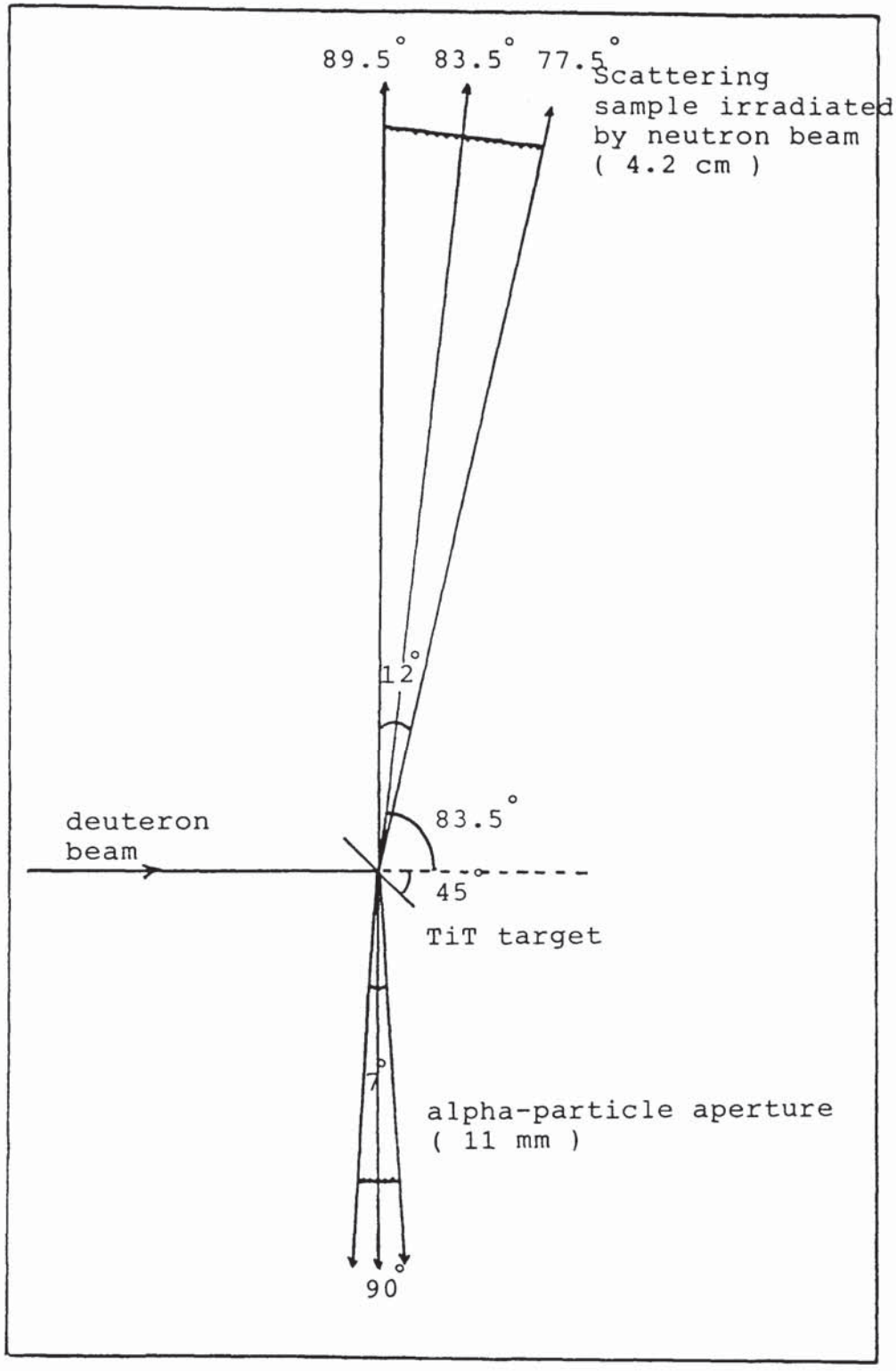

Figure (2.11):Neutron beam at horizontal direction defined by 11 mm alpha-particle aperture.

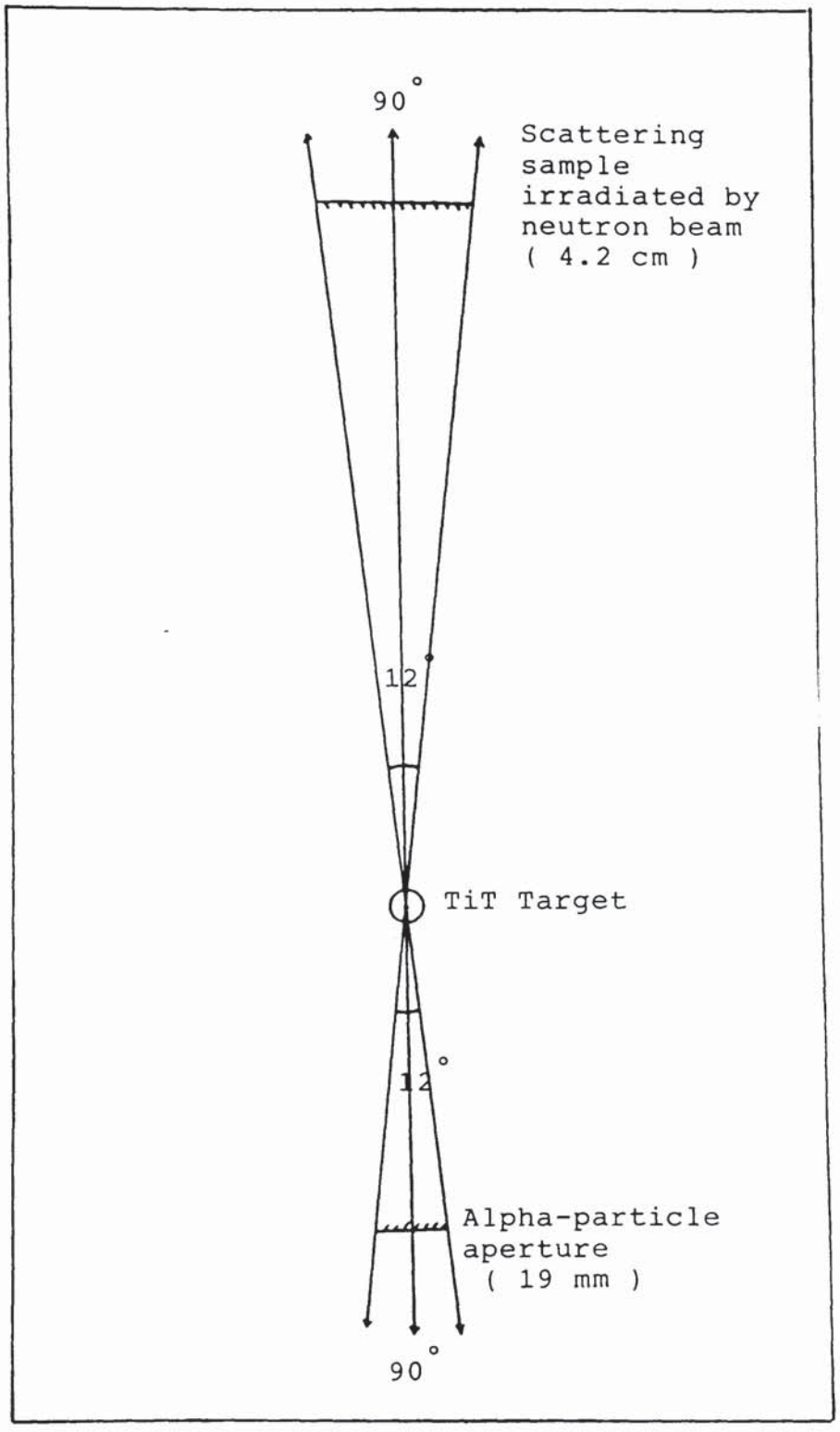

Figure (2.12):Neutron beam in verticle plane defined by 19 mm alpha-particle aperture.

of deuteron inducing reaction inside the target. In practice the energy spread is possibly caused by three effects,

(i) The solid angle of the alpha-particle detector with respect to the target,

(ii) The scattering of deuterons and alpha-particles inside the target,

(iii) The $T(d,n)He^4$ reactions occur at different deuteron energies, owing to the energy loss of the deuterons inside the target.

The energy distribution of neutron at an angle θ_n is refered as neutron line shape and can be theoretically calculated using equation (2-7) and (2-18). The y-axis of the neutron line shape is propotional to the neutron yield and it is given by equation (2-18). The x-axis of the line shape i.e the neutron energy as a function of neutron angle θ_n and deuteron energy E is given by equation (2-7).

The neutron line shape was evaluated using equation (2-18) and (2-7) for deuterons energy range from 0 to 140 keV for neutron angles of 90° , 83.5° and 80° . The neutron line shape for these angles are shown in figure (2.13). The figures show that the energy spread of neutron increases as the angle decreased. For angle θ_n = 83.5° the energy spread is about 100 keV with the neutron peaked at En = 14.1 MeV.

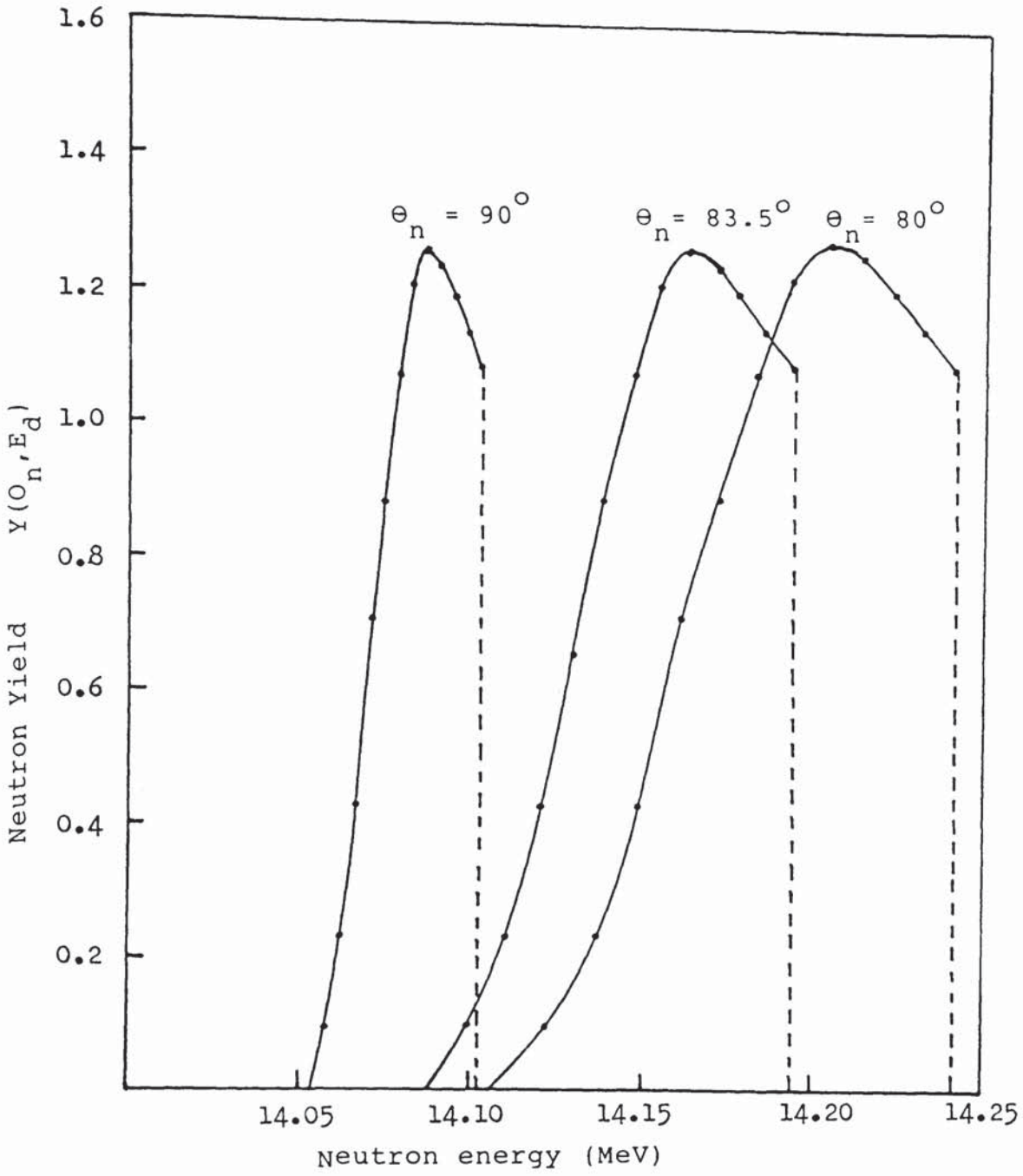

Figure (2.13):The neutron line shape for different values of neutron angle.

CHAPTER 3

DESCRIPTION OF THE EXPERIMENTAL APPARATUS

3.1:THE EXPERIMENTAL ARRANGEMENT FOR THE ASSOCIATED PARTICLE METHOD.

3.1.1:THE S.A.M.E.S ACCELERATOR.

The low energy, S.A.M.E.S, type J accelerator was used in this work to produce an incident deuterons beam. The deuterons beam bombard a tritiated titanium target to produce 14 MeV neutrons.

The electrostatic voltage generator output can be varied continuosly from 0 to 160 kV. From the manufacturer's specification, the generator could deliver 2 mA at 150 kV with stability of about 1 %.

The deuteron gas was supplied to the quartz ion source bottle through a thermally activated palladium leak and a discharge was excited by a 100 MHz R.F oscillator to produce deuteron ions. The ions were extracted using a variable potential from 0 to +6 kV above the extraction canal potential (top terminal potential). To increase the extracted beam the ions were concentrated at the entrance of the extraction canal by a magnetic field produced by a coil located at the base of the ion source bottle. The ions were focussed by an electrostatic lens supplied with 0 to -45 kV potential relative to the exit canal by an oil-immersed Cockroft-Walton generator situated inside the

high voltage terminal of the accelerator. The cross-sectional diagram of the accelerator is shown in figure (3.1).

The S.A.M.E.S accelerator, target assembly and detectors are placed in a shielded room as shown in figure (3.2). The accelerator was operated from control panel which was shielded behind a concrete wall 65 cm thick.

3.1.2:THE BEAM TUBE AND TARGET ASSEMBLY.

The deuterons beam were passed through a beam tube 45 cm long and 10 cm diameter to the tritiated titanium (TiT) target. The pumping system of the accelerator maintained the high vaccum in the accelerator, beam tube and target assembly. The preasure in the system can be reduced to about 10^{-6} torr in the absence of an ion beam. A gate valve was fixed between the accelerator and the beam tube in order to separate these two parts if necessary. A small aperture with dimension of 10 mm x 1 mm was fixed at 12.5 cm behind the target to define the deuteron beam.

A small tritiated titanium target supplied by Amersham International Plc. was used and contained 0.78 Ci tritium per cm^3 absorbed in a titanium layer of 1.09 mg per cm^2 thickness. The target is 25.4 mm in diameter supported on a copper backing with thickness of 2.54 mm and 28.6 mm diameter.

The target was clamped onto a circular copper disc

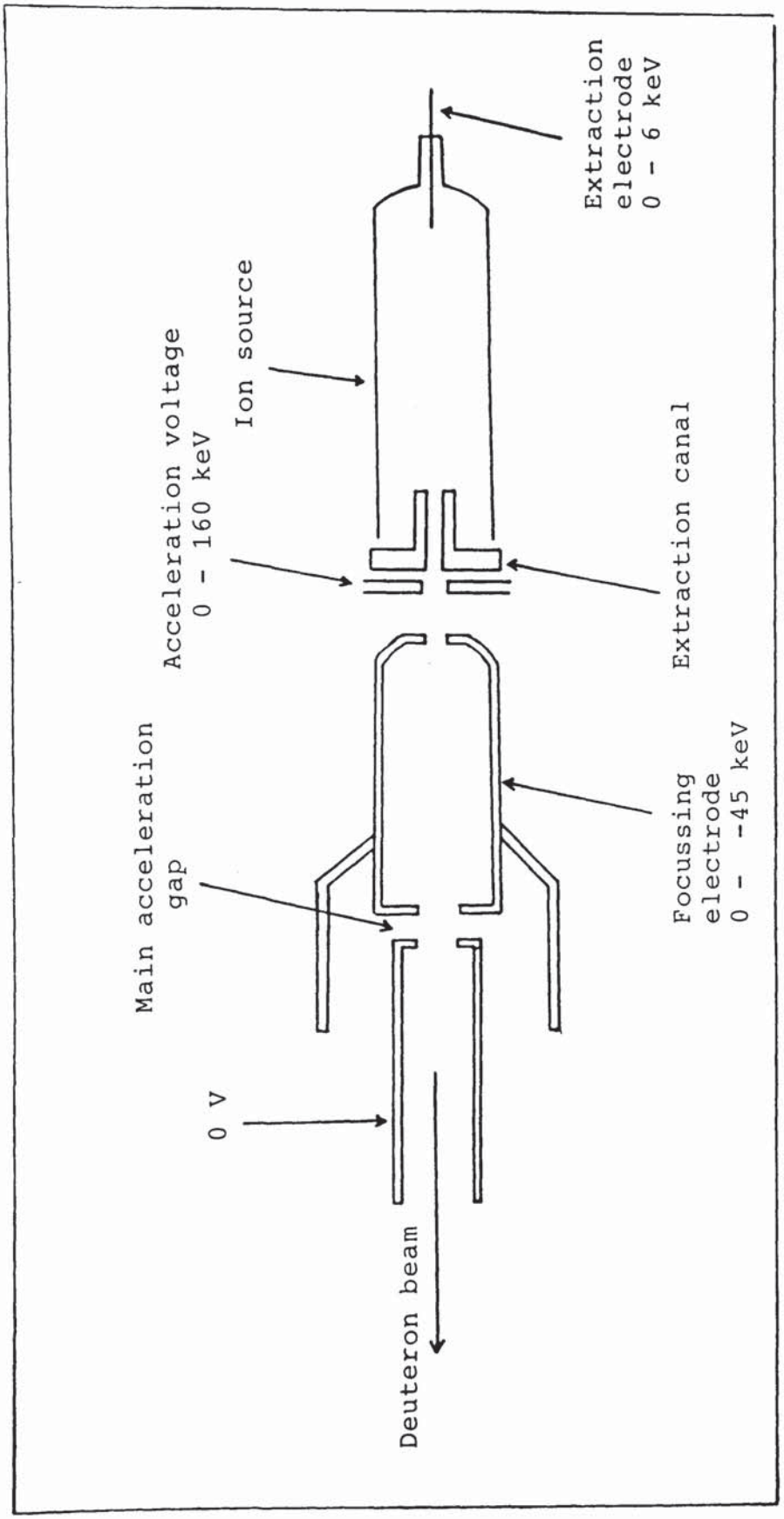

Figure (3.1): The cross-sectional diagram of the S.A.M.E.S ion source and focusing and acceleration electrodes.

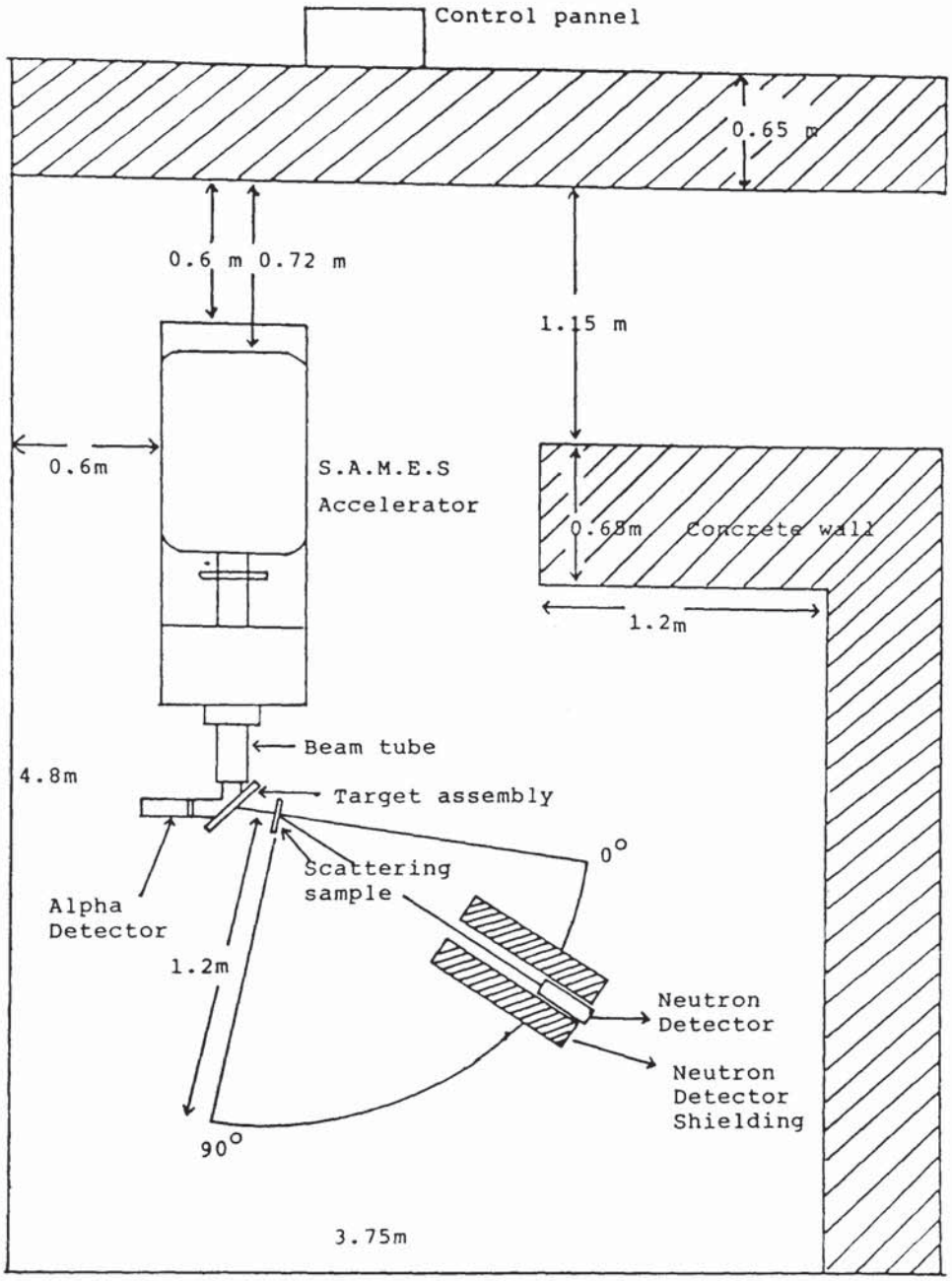

Figure (3.2):The position of the accelerator in the experimental room.

with outer diameter of 13 cm and 1.5 cm thickness and was water cooled. In order to reduce the area of the target exposed to the vaccum system and so to keep it clean, a circular aperture with diameter of 1 cm was placed infront of the target such that the 1 cm x 1 mm beam was incident in the diameter of the aperture. The cross-sectional diagram of the target assembly is shown in figure (3.3).

The alpha-particle detector was positioned at 90^{o} with respect to the incident deuteron beam and 90 mm distance from the tritiated titanium target. A rectangular aperture with dimensions 19 mm in vertical and 11 mm in horizontal directions was fixed at the end of the detector window in order to define the solid angle of the detected alpha-particles. The arrangement of the target assembly and beam tube is shown in figure (3.4).

3.1.3:THE SAMPLE POSITION AND ARRANGEMENT.

From the neutron beam profile (figure 2.10), the most intense neutrons were emitted at angle $\theta_n = 83.5^{o}$ from the deuteron beam direction, associated with the alpha-particle emission at $\theta_\alpha = 90^{o}$ to the deuteron beam direction. In this work the scattering sample was positioned normal to this angle with a distance 20 cm from the tritiated titanium target.

Two sample geometries, cylindrical and flat plate, can be used with the present experimental arrangement. In this sample geometry, the sample is made in the form of a

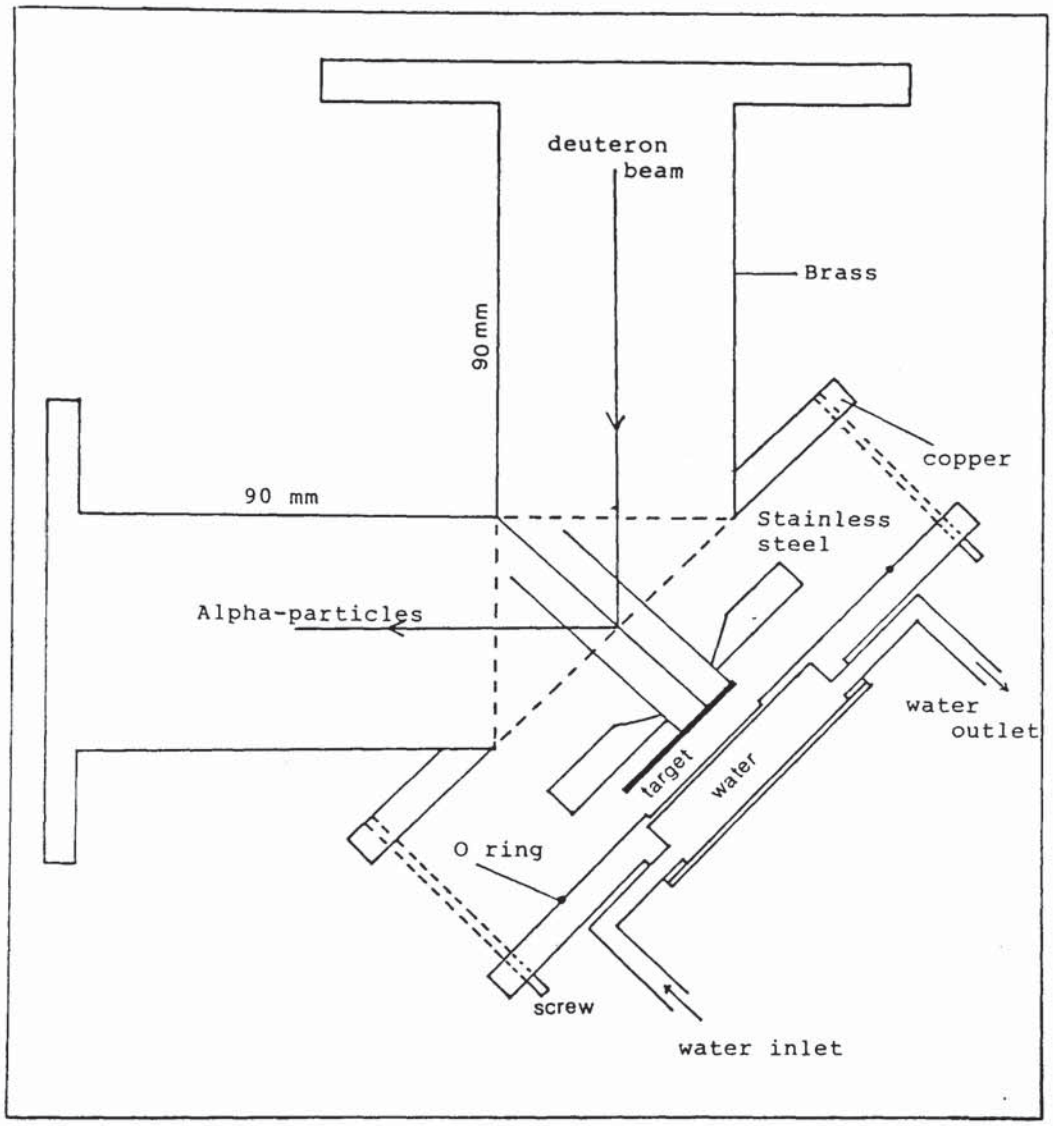

Figure (3.3):The cross-sectional diagram of the target assembly.

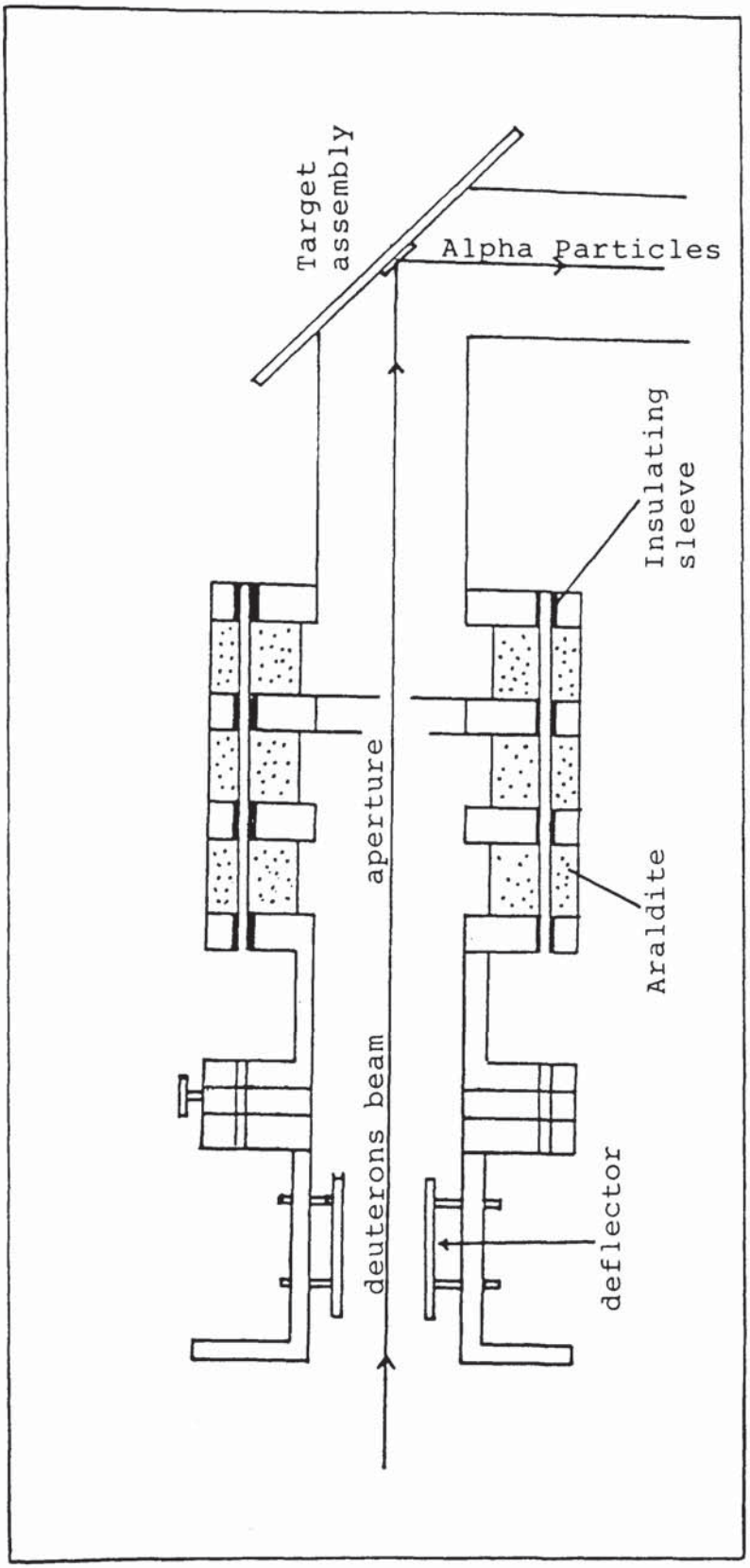

Figure (3.4): The target assembly and the beam tube.

rectangular slab of material. In order to reduce the multiple scattering, usually a thin flat plate sample is used.

One of the advantages of the flat plate sample is that, the sample can be made wider, to subtend completely the defined neutron beam. This cannot easily be done with cylindrical sample which needs a pencil beam. The area of the sample irradiated by neutrons beam was 4.2 cm x 4.2 cm, limited by alpha-particle detector aperture. The flight path of the neutron was measured from the centre of the sample to the neutron detector window and has a distance of about 1.2 m. By rotating the neutron detector, the angular distributions of scattered neutrons can be obtained at foward angles up to 90° . The sample was placed on the sample holder made from steel and fixed to the floor.

A massive shield was used around the detector to reduce the background radiations of scattered neutrons. A shadow bar of paraffin wax was placed between the sample and neutron detector to stop the direct beam of neutron scattered from the sample.

3.2:NEUTRON DETECTOR.

3.2.1:INTRODUCTION.

Neutrons are different from the other types of radiation since their interaction for detection are with nuclei of the detecting material rather than with atomic electrons. The neutron is an uncharged particle, and it cannot therefore be directly detected by observing the ionization produced. Detection of fast neutrons is generally based on scattering or charged particle emitting reactions with nuclei where the energy is transferred from the neutron to charged particles and the latter are detected via ionization. The nuclear reactions which are suitable for neutron detection should yield only charged particle in their ground states. Otherwise, the energy determination is ambiguous. This limits the reactions to $^{3}He(n,p)^{3}H$ and $^{6}Li(n,\alpha)^{3}H$. The $^{10}B(n,\alpha)^{7}Li$ reaction which is often used in slow neutron works, leads mainly to the first excited state in ^{7}Li. Generally these reactions are limited to neutrons of lower energies such that the energy released cannot be confused with elastic scattering.

In the fast neutron detection, the detection based on the scattering process is widely used. In this process, the neutron energy is transfered to the charged particles and the amount of the energy transfered depends on the scattering angle and the mass of the scatterer. The maximum energy transfer decreases as the mass of the

scatterer increases. Therefore, the most widely used method of fast neutron detection is based on the neutron-proton scattering. Neutrons are elastically scattered by all nuclei, but the energy transfer to the recoil nucleus is maximum for neutron-proton scattering.

There are three advantages of using recoil protons for fast neutron detection (37). These are

(i) The energy of the recoil protons is much higher than any other recoil nucleus,

(ii) The neutron-proton scattering cross-section is high,

(iii) Up to 20 MeV, the neutron-proton scattering has isotropic angular distribution in the centre of mass coordinate system.

The energy of the recoil nucleus can be calculated from the energy and linear momentum conservation. In the laboratory coordinate system, the recoil energy is given by,

$$E_r = \frac{4\ A}{(1+A)^2}\ E_n\ \mathrm{Cos}^2\theta_n \qquad (3\text{-}1)$$

where

E_n = the energy of the incident neutron,

E_r = the energy of the recoil nucleus,

A = the mass of the scatterer,

θ_n = the scattering angle of the recoil nucleus in the laboratory coordinate system.

The recoil nucleus will have maximum energy in a head-on collision i.e for $\theta_n = 0^\circ$ and hence,

$$(E_r)_{max} = \frac{4A}{(1+A)^2} E_n \qquad (3\text{-}2)$$

Equation (3-2) shows that the maximum fractional energy transfer decreases as the mass of the scatterer increases.

For neutron-proton scattering, equation (3-1) become

$$E_p = E_n \cos^2 \theta_n \qquad (3\text{-}3)$$

where, $0^\circ < \theta_n < 90^\circ$

E_p = the energy of the recoil proton.

In collision with hydrogen (A=1) the neutron can transfer all of its energy in a head-on collision. This trend explains why the materials containing hydrogen atoms are normally used in recoil detectors especially for fast neutron detection.

The neutron elastic scattering cross-section from hydrogen is high and its energy dependence is well known (38,39,40,41). Figure (3.5) shows the variation of neutron total cross-section with energy (41). A good approximation to the hydrogen scattering cross-section is the simple formula suggested by Marion and Young (42) for energy range up to 20 MeV as,

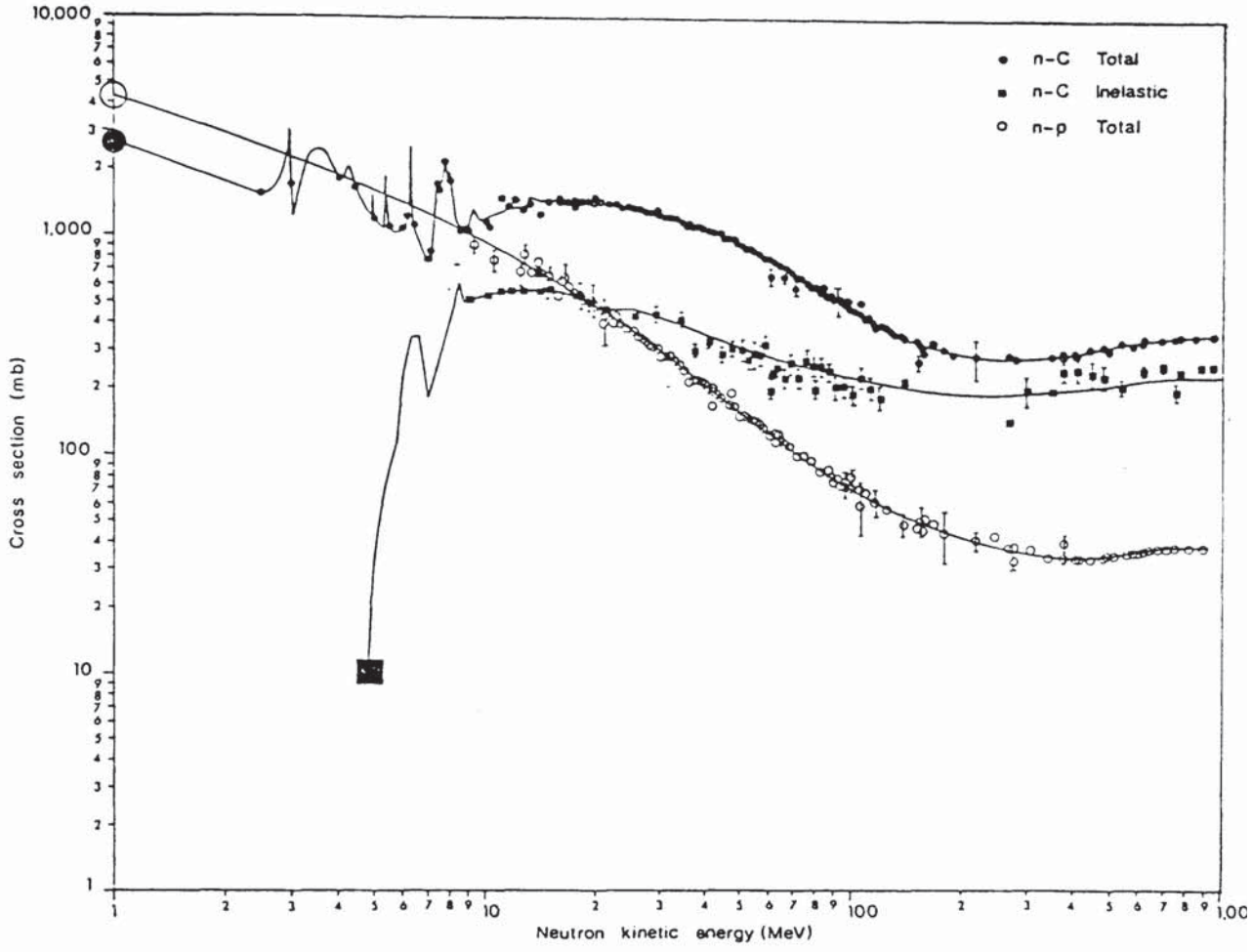

Figure (3.5):The n-C total, n-C inelastic and n-p total cross-sections versus neutron energy.

$$\sigma_s(E_n) = \frac{4.83}{E_n^{\frac{1}{2}}} - 0.578 \quad \text{barns} \qquad (3\text{-}4)$$

where,

E_n = the neutron energy in MeV.

Most fast neutron detectors use organic material which contained hydrocarbon molecules and the neutron-carbon scattering has to be considered too. Figure (3.5) shows the neutron-carbon cross-section at various energies (41). The graphs show that only elastic scattering on carbon occurs below 5 MeV, while at 10 Mev the inelastic scattering amounts to about 22 %.

One of the easiest ways to use proton recoil in the detection of fast neutron is through the application of a hydrogen containing scintillator. Organic scintillators containing principaly hydrogen and carbon are the most convenient means of obtaining a high concentration of hydrogen and hence a high detection efficiency. Successful applications have been reported using organic scintillator such as anthracene, stilbene, plastic and organic liquids. The recoil protons produce scintillators can be detected using a photomultiplier tube. The plastic scintillator NE102A manufactured by Nuclear Enterprise was employed in the present work.

3.2.2:PLASTIC SCINTILLATOR NE102A.

Many different plastic scintillators are commercially available with a hydrogen to carbon ratio as

given by the manufacturers of around 1.2. Plastic scintillator can be found with a good selection of standard sizes of rods, cylinders and flat sheets. Because the material is relatively inexpensive, plastics are often the only practical choice, if the large volume solid scintillator are needed.

In the present work a plastic scintillator type NE102A with 50.8 mm thickness and 50.8 mm radius manufactured by Nuclear Enterprises was used. The light output pulse from NE102A scintillator had a rise time of about 1 ns and exponential decay with a time constant of about 2.4 ns. Thus, NE102A is practically suitable for the fast neutron time of flight experiment designed in the present work.

The properties of the plastic scintillator NE102A are given by manufacturer as follow,

Density = 1.032 gm cm^{-3}

Refractive index = 1.581

Wave-length of maximum emission = 425 nm

Hydrogen-carbon ratio = 1.104.

In the time of flight experiments the thickness of the scintillation detector results in a time uncertainty due to the variation in flight times to different detection points within the scintillator. The time uncertainty dt can be found by the relation,

$$dt = \frac{L}{(2E_n/m)^{\frac{1}{2}}} \qquad (3\text{-}5)$$

where,

L = the thickness of detector,

m = neutron mass,

E_n = the neutron energy incident on the detector.

For 14 MeV neutron, the time uncertainty for L = 5.08 cm thickness of NE102A scintillator was calculated to be about 1 ns.

3.2.3:NEUTRON DETECTOR EFFICIENCY.

In nuclear spectroscopy studies where neutrons have to be detected, the knowledge of the neutron detector efficiency is very important. In fast neutron cross-section experiments using time of flight technique, it is usual to detect neutrons having a range of energy spread over several MeV. Theoretical papers and some experimental investigations have shown that neutron detection efficiency of organic scintillators may vary considerably with energy and is particularly sensitive near the detector threshold (43-50). Therefore, it was necessary to compute and check by experimental measurement, the efficiency of the neutron detector used in the present work as a function of incident neutron energy.

In general, the efficiency of an organic scintillator is defined as the ratio of the number of recoil protons to the number of incident neutrons i.e

$$\epsilon(E_n) = \frac{N_p}{N_o} \qquad (3\text{-}6)$$

where

N_p = the number of recoil proton produced in the scintillator,

N_o = the number of incident neutron at energy E_n.

In practice, this efficiency cannot be used directly to convert from observed counting rate to neutron flux because it is ordinarily not possible to count all recoil protons.

The detection efficiency of a device based on the recoil protons or other recoil nuclei can be calculated from the scattering cross-section. By assuming that only one kind of nucleus is present in the scintillator, the intrinsic efficiency is given by

$$\epsilon(E_n) = 1 - \exp\left(- n\sigma_s(E_n) \cdot L \right) \qquad (3\text{-}7)$$

where,

n = the number of target nuclei per unit volume,

$\sigma_s(E_n)$ = the neutron scattering cross-section of the nuclei,

L = the path length through the detector for incident neutron.

Elastic scattering is the only neutron interaction with hydrogen nuclei. For neutron energies below 20 MeV it is considered to be isotropic in the centre of mass

system (51).

In organic scintillators, carbon appears in combination with hydrogen and therefore equation (3-7) cannot be used to calculate the efficiency of such detectors. However, the efficiency of the scintillator consisting entirely of carbon and hydrogen can be calculated quite easily under assumption that only single (n-p) scattering occurs. Defining L to be the lenght of the scintillator, the number of recoil protons corresponding to initial (n-p) collisions is given by (52),

$$N_p(E_n, L) = N_o \cdot n_H \cdot \sigma_H(E) \cdot L \cdot f(aL) \qquad (3-8)$$

where

N_o = the number of neutron flux at energy E_n,

n_H = the number of hydrogen atom per cm^3 of scintillator,

$\sigma_H(E_n)$ = the neutron-proton scattering cross-section at neutron energy E_n.

$$a(E_n) = n_H \cdot \sigma_H(E_n) + n_C \cdot \sigma_C(E_n) \qquad (3-9)$$

where

n_C = the number of carbon atom per cm^3 of scintillator,

$\sigma_C(E_n)$ = the neutron-carbon total cross-section at energy E_n.

$$f(aL) = [1 - \exp(-a(E_n) \cdot L)] / a(E_n) \cdot L \qquad (3-10)$$

which allows for the attenuation of the neutron beam in passing through the scintillator. In this approximation, scattering by hydrogen following scattering by carbon is neglected.

It is possible to calculate the efficiency of the neutron detector by equation (3-8) if the values of n_H, n_C and σ_H, σ_C are known. For plastic scintillator NE102A the value of n_H and n_C are quoted by the manufacturer as

$$n_H = 5.25 \times 10^{22} \text{ atoms/cm}^3,$$

$$n_C = 4.75 \times 10^{22} \text{ atoms/cm}^3.$$

The total neutron-proton cross-section has been measured by many workers (53,54,55,56). Swartz et al (38) gave an analytical expression for the neutron-proton cross-section as,

$$\sigma_H(E_n) = 5.603\pi \left[(1 + 7.417E_n) + 0.1105\, E_n^2 \right]^{-1} + 0.8652\pi \left[(1 - 0.2427E_n + 0.0028\, E_n^2 \right]^{-1} \quad (3\text{-}11)$$

where E_n is the neutron energy expressed in MeV and $\sigma_H(E_n)$ is the cross-section in barns. The values obtained using this formula were within -0.3% to -1% with the values evaluated from ENDF-B4 and UKNDL (57).

Gammel (58) gave the following formula to calculate total neutron-proton cross-section as a function of neutron energy,

$$\sigma_H(E_n) = 3\pi \left[1.206E_n + (-1.86 + 0.9415E_n + 0.0001306E_n^2)^2 \right]^{-1} + \pi \left[1.206E_n + (0.4223 + 0.13E_n^2)^2 \right]^{-1} \quad (3\text{-}12)$$

For the purpose of the efficiency calculation, the neutron-proton cross-sections were evaluated using

equation (3-11) and the neutron-carbon cross-sections were taken from ENDFB-4 (59). The efficiency obtained by applying equation (3-8) to a 5.08 cm thickness of NEIO2A plastic scintillator at various neutron energies between 1 MeV to 14 MeV are tabulated in table (3.1) and shown in figure (3.6).

3.2.4:NEUTRON DETECTOR EFFICIENCY WITH DOUBLE SCATTERING.

Equation (3-8) only applicable to calculate the efficiencies of the scintillator under assumption that only single scattering events were considered. This single (n-p) scattering is the most probable event when the thin scintillator is used. For large scintillator it was possibly happen that recoil protons can be produced by neutrons, which have already been scattered one or more times by carbon or by hydrogen. It was shown that the single (n-p) scattering is dominated by neutron interaction with hydrogen nuclei in the scintillator at energies less than 12 MeV and at higher energies interaction with carbon become increasingly important (60). Since the scintillator can be considered as a mixture of hydrogen and carbon atoms, the most probable interactions of fast neutrons with these nuclei to be considered in the 0.02 MeV to 15 MeV energy range are (46)

a) elastic scattering on hydrogen nuclei,

b) elastic scattering on carbon nuclei,

c) inelastic scattering on carbon nuclei,

Table (3.1):Numerical values for calculating the efficiencies of neutron detector efficiencies at various neutron energies.

E_n MeV	$n_H\sigma_H$ cm^{-1}	$n_C\sigma_C$ cm^{-1}	$n_H\sigma_{H1}$ cm^{-1}	$n_C\sigma_{C1}$ cm^{-1}	$\epsilon_1(E_n)$ %	$\epsilon_2(E_n)$ %
1.0	0.2236	0.1221	0.2441	0.1330	51.51	65.17
2.0	0.1525	0.0807	0.1671	0.0831	45.37	52.92
3.0	0.1196	0.0618	0.1321	0.0758	39.70	45.05
4.0	0.0994	0.0912	0.1105	0.1211	32.35	38.65
5.0	0.0852	0.0560	0.0954	0.0998	30.89	34.77
6.0	0.0747	0.0489	0.0840	0.0527	28.15	31.47
7.0	0.0662	0.0437	0.0751	0.0427	25.80	28.60
8.0	0.0596	0.0688	0.0678	0.0304	22.24	26.15
9.0	0.0541	0.0551	0.0618	0.0486	21.06	24.00
10.0	0.0494	0.0547	0.0567	0.0380	19.49	22.25
11.0	0.0454	0.0570	0.0523	0.0323	17.98	20.68
12.0	0.0421	0.0593	0.0486	0.0247	16.68	19.33
13.0	0.0390	0.0617	0.0453	0.0353	15.51	18.06
14.0	0.0364	0.0636	0.0423	0.0392	14.50	16.96

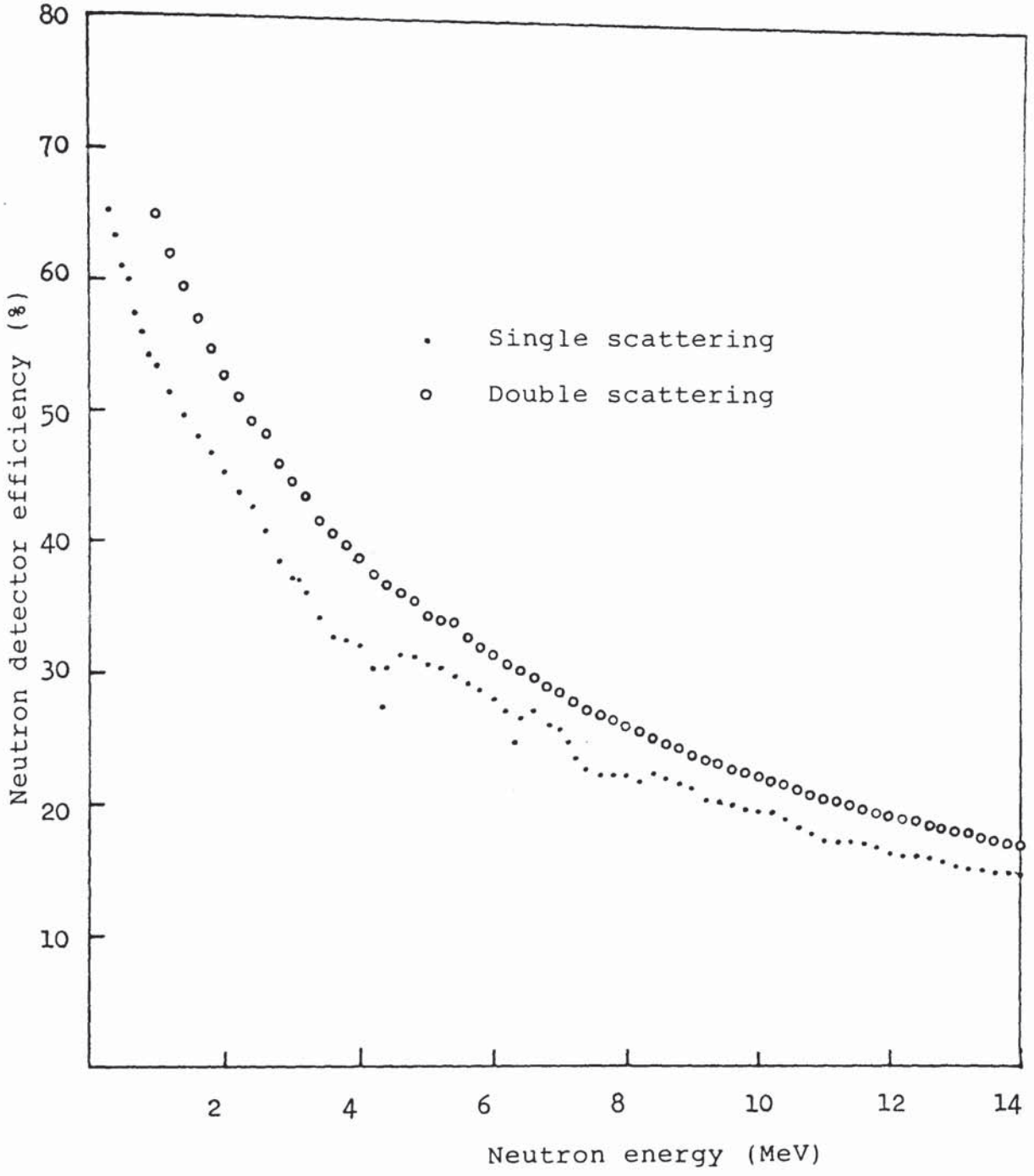

Figure (3.6):Calculated neutron detector efficiency for various neutron energies.

d) the reaction $^{12}C(n,n')C^{*} \longrightarrow 3\alpha$,

e) the reaction $^{12}C(n,\alpha)^{9}Be$.

The correction due to these effects is difficult to calculate and requires a Monte-Carlo type calculation (46,48,49). However, the contribution of second scattering events can be estimated as follow,

3.2.4.1:SCATTERING BY CARBON AND HYDROGEN.

In the presence of carbon in the scintillator as well as hydrogen atoms, the scattered neutron may still undergo a hydrogen scattering after a carbon scattering and before escaping from the scintillator. The number of neutrons scattered once by carbon in a scintillator of length L is given by,

$$N_C(E_n,L) = N_o \cdot n_C \cdot \sigma_C(E_n) \cdot L \cdot f(aL) \qquad (3\text{-}13)$$

all terms are defined as equation (3-8).

The incident neutron may lose between 0 to 28% of it energy after scattering with carbon nuclei and this can be estimated quite easily by equation (3-1). Therefore, the maximum energy of a subsequent recoil proton will vary between 100% and 72% of the original energy. Swartz et al (52) and Tome (61) estimated the average recoil energy as $0.85\ E_n$.

The number of recoil protons corresponding to neutrons scattered once from carbon and then colliding with a proton is given by

$$N_{pc}(E_1, L, L_1) = N_C \cdot n_H \sigma_{H1}(E_n) \cdot L_1 \cdot f(a, L_1) \qquad (3\text{-}14)$$

where

L_1 = some characteristic distance that the scintillator presents to the neutrons after they have been once scattered from the carbon,

$\sigma_{H1}(E_1)$ = the cross-section for average energy of neutron i.e $E_1 = 0.85E_n$,

$a_1 = n_H \cdot \sigma_{H1}(E_1) + n_C \cdot \sigma_{C1}(E_1)$ for average neutron energy i.e $a_1 = a(E_1)$

The total number of recoil protons is $N_p(E_n, L) + N_{pc}(E_1, L, L_1)$ where $N_p(E_n, L)$ is the number calculated from equation (3-8) for single neutron-proton scattering only. Thus, if every recoil protons were detected, the theoretical value for the absolute efficiency of the scintillator including double scattering would be given by

$$\epsilon_2(E_n, L, L_1) = (N_p + N_{pc})/N_o \qquad (3\text{-}15)$$

From equation (3-8) and (3-14) and rearranging, equation (3-15) can be written as

$$\epsilon_2(E_n, L, L_1) = \epsilon_1 \cdot (E_n, L) [\, 1 + N_{pc}/N_p \,] \qquad (3\text{-}16)$$

By assuming $L_1 = L/2$, Swartz et al (52) calculated the efficiency of a stilbene scintillator with 12.7 mm thickness and obtained a good agreement with the experimental results within 0.25%. Jackson et al (43)

used L = 2 cm to calculate the efficiency of a cylindrical NE218 scintillator of 12.7 cm diameter and 7.62 cm thickness. This distance corresponds to the distance a 1.0 MeV neutron beam would travel in the scintillator before being reduced to slightly less than half its original intensity.

In the present work, the efficiency of the detector as a function of neutron energy up to 14 MeV was calculated by considering the effect of double scattering from carbon and hydrogen. The average energy of recoil proton was taken to be $0.85E_n$ and $L_1 = L/2$, same as Swartz (52) works. The cross-section data for carbon and hydrogen were taken from reference (59) and (38) respectively.

Numerical data useful for calculating ϵ_2 are given in table (3.1). Applying equation (3-16), the values of ϵ_2 for NE102A plastic scintillator with 5.08 cm thickness at various neutron energies from 0 to 14 MeV was obtained and is shown in figure (3.6).

3.2.4.2:DOUBLE SCATTERING FROM HYDROGEN.

Protons may also be produced by neutron having two or more collisions with hydrogen in the scintillator. In double scattering from hydrogen, two recoil protons are produced at the same instance of time. These events are recorded as a single event, with an apparent energy would be the sum of the two proton energies if the response of

the efficiency were linear. These events can be effectively be negleted since it will only serve to increase the detector pulse hight corresponding to the initial collision. However, double scattering from hydrogen does result in a distortion of the output pulse hight spectrum of the scintillator. The pulse hight spectrum to be expected under this assumption has been calculated by Segal et al (62) and Swartz et al (38). They found that the approximate calculation for the number of recoil protons produced in double scattering by hydrogen is

$$N_{2H}(E_n, L, L_1) = 2\, N_p \cdot \epsilon_1(E_n, L_1) \qquad (3\text{-}17)$$

The factor 2 arises from the fact that ϵ_1 varies approximately as $E^{-\frac{1}{2}}$, so that a neutron scattered once from hydrogen has a higher chance of being scattered again.

3.2.5:ENERGY DISTRIBUTION OF RECOIL PROTONS.

In the neutron-proton scattering, the energy of the recoil proton in the laboratory system is represented by equation (3-3). In the centre of mass coordinate system, for incoming neutron with energy E_n, the energy of the recoil proton can be deduced from the conservation of momentum and energy to give the following relationship,

$$E_p = \frac{1}{2} E_n (1 - \text{Cos } \phi) \qquad (3\text{-}18)$$

where,

ϕ = the scattering angle of the neutron in the centre of mass system.

Consider now, the way in which the recoil energies of proton are distributed. Firstly defined $\sigma(\phi)$ as the differential scattering cross-section in the centre of mass system, then, by definition, the probability that the neutron will be scattered into $d\phi$ about ϕ is

$$P(\phi)\ d\phi = 2\pi \text{Sin } \phi\ d\phi\ \frac{\sigma(\phi)}{\sigma_s} \qquad (3\text{-}19)$$

where,

σ_s = the total scattering cross-section integrated over all angles.

Let $p(E_p)dE_p$ represent the probability of creating a recoil proton with energy in dE_p about E_p where,

$$P(E_p)\ dE_p = P(\phi)\ d\phi \qquad (3\text{-}20)$$

then, equation (3-20) can be written as follow

$$P(E_p) = 2\pi \mathrm{Sin}\ \phi \ \frac{\sigma(\phi)}{\sigma_s} \ \frac{d\phi}{dE_p} \qquad (3\text{-}21)$$

If we differentiate equation (3-18) we get

$$dE_p = \frac{E_n}{2} \ \mathrm{Sin}\ \phi \ d\phi \qquad (3\text{-}22)$$

Now, evaluting $d\phi/dE_p$ from equation (3-22) and subtitute to equation (3-21), gives

$$P(E_p) = \frac{\sigma(\phi)}{\sigma_s} \ \frac{4\pi}{E_n} \qquad (3\text{-}23)$$

For most neutron energies less than 20 MeV the neutron-proton scattering is nearly isotropic in the centre of mass system. By this assumption the differential cross-sections for neutron-proton scattering can be considered as a constant with the value of $\sigma_s/4\pi$. Therefore, for proton-neutron scattering, the expected proton recoil energy distribution is a simple rectangle, i.e

$$P(E_p) \ \alpha \ \frac{1}{E_n} \quad \text{where} \quad 0 < E_p < E_n \qquad (3\text{-}24)$$

$$= 0 \quad \text{where} \quad E_p > E_n$$

Figure (3.7) shows the proton recoil energy distribution for proton-neutron scattering.

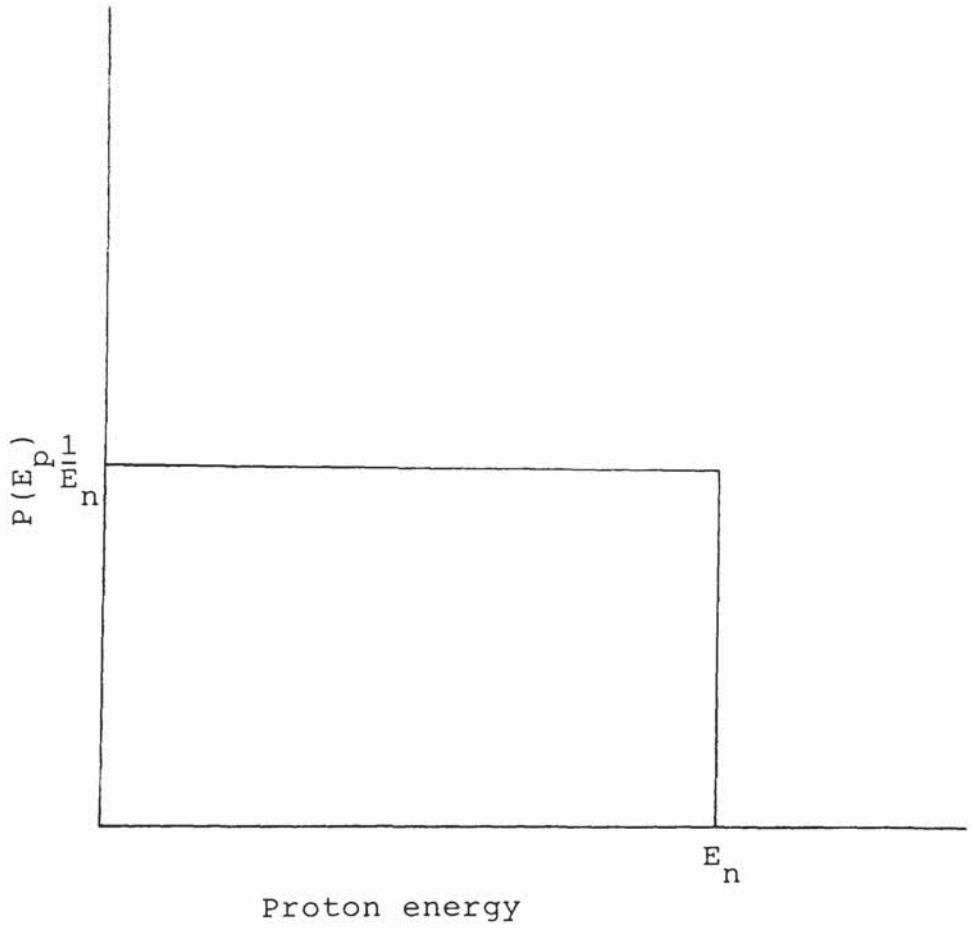

Figure (3.7):Energy distribution of recoil protons produced by monoenergetic neutrons.

3.2.6:RESPONSE OF THE ORGANIC SCINTILLATOR.

In the organic scintillator, neutral radiations such as gamma-rays and neutrons are detected if they produce respectively recoil electron or recoil nuclei within the scintillator material. The charged particles produced will then generate ionization. A relatively small fraction of the ionization energy loss by a charged particle in a scintillator is converted into fluorescent light energy. The remainder is dissipated non-radiatively primarily in the form of lattice vibrations or heat (63). The fraction of the charged particle energy which is converted into fluorescent light energy depends on the type and its energy. Electrons generate more light than do heavy particles (e.g proton) of equal energy when stopped in the organic scintillator and have linear response for electron energies above 125 keV (63,64,65). Protons and heavier particles have non-linear response particularly at higher energies (63,64). Figure (3.8) shows the scintillation response of plastic scintillator NE102A at various energies for protons and electrons (65). The figure shows at energies of a few hundred keV the response to proton is smaller by a factor of ten compared with the light yield of equivalent energy electron. At higher energies the discrepancy is less but the proton response is always below the electron response.

Since the scintillation response to protons is non-linear with respect to their energies, an expression

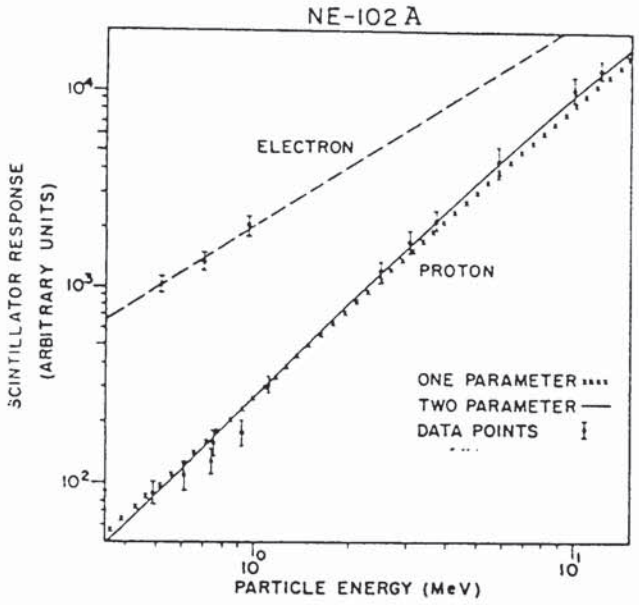

Figure (3.8):The response of NE102A plastic scintillator to electrons and protons.

is needed to relate the response with energy. Birks (63) in describing the scintillation process in organic scintillator, expressed in differential form the scintillation response S with respect to range r, as

$$\frac{dS}{dr} = \frac{A\left(\frac{dE}{dr}\right)}{1 + kB\left(\frac{dE}{dr}\right)} \qquad (3\text{-}25)$$

where

$\frac{dS}{dr}$ = the fluorescence light energy emitted per unit path length,

$\left(\frac{dE}{dr}\right)$ = the specific energy loss for the charged particle,

A = the scintillation efficiency,

kB = a constant for a given scintillator.

B is a constant which when multiplied by (dE/dr) gives the specific density of ionized and excited molecules along the particle track, and k is a quenching parameter. Swartz and Owen (52) calculated the response of stilbene to protons for values of kB equal to 0.010 and 0.012 mg cm^{-2} keV^{-1} versus proton energy as part of their description of the process of detecting neutrons by the recoil of protons in organic scintillator.

In order to match experimental data more closely, other formulae for (dS/dr) have been proposed by a number

of authors. Wright (66) attributing the effect to a different mechanism obtains,

$$\frac{dS}{dr} \propto \log \left(1 + a \left(\frac{dE}{dr} \right) \right) \qquad (3\text{-}26)$$

where a is a constant.

Gooding et al (67) have measured the value of a to be (0.025 ± 0.002) mg cm^{-2} MeV^{-1} for NE102A plastic scintillator.

An extensive analysis of the response of a number of organic scintillators has been carried out by Croun and Smith (65). Their analysis are based largely on the data of Smith et al (64) and used the empirical formula suggested by Chou (68) i.e

$$\frac{dS}{dr} = \frac{A \left(\frac{dE}{dr} \right)}{1 + kB \left(\frac{dE}{dr} \right) + C \left(\frac{dE}{dr} \right)^2} \qquad (3\text{-}27)$$

where C is treated as an empirical fitted parameter. Equation (3-27) approaches equation (3-25) for small value of (dE/dr).

There have been several other theoretical studies of organic scintillators which have yielded formulae for (dS/dr) (69,70,71). These formulae also reduced to equation (3-25) for small value of (dE/dr).

In the present work where the plastic scintillator

type NE102A was used, the calculation based on the Birk's formula was done. In order to avoid dependence on specific unit for S, it is convenient to represent the scintillator output by the variable P = S/A, hence equation (3-25) can be written as

$$\frac{dP}{dE} = \frac{1}{A}\frac{dS}{dE} = \frac{1}{1 + kB\left(\frac{dE}{dr}\right)} \qquad (3\text{-}28)$$

where the unit P and E are identical.

For electrons (dE/dr) is sufficiently small that equation (3-28) reduces to

$$\frac{dP}{dE} = 1 \qquad (3\text{-}29)$$

or

$$P = E_e$$

This is in agreement with the observed linearity of the scintillation response for electrons.

For proton, however, the values of (dE/dr) is large. By integrating equation (3-28), the pulse height of proton for a given proton energy E can be obtained as

$$P = \int_0^{E=E_p} \frac{1}{1 + kB\left(\frac{dE}{dr}\right)}\, dE \qquad (3\text{-}30)$$

The specific energy losses at various proton energies are required for the calculation. Many

investigations have been carried out to obtain the specific energy losses of proton in organic scintillator. For energy range between 1 to 150 MeV, Gooding and Pugh (67) represented the range-energy curve for $CH_{1.105}$, which is the composition of the plastic scintillator NE102A, by a power law of the following form

$$\frac{dE}{dr} = 16.94\ r^{-0.448} \qquad (3\text{-}31)$$

where the range r is in g/cm^2 and energy in MeV. This relationship was derived from the range energy curve for NE102A determined by Rich and Madey (72) by interpolating between C, CH and CH_2.

The specific energy losses of protons in various organic scintillators have been computed by Croun and Smith (65). They used the following formula to compute the specific energy losses for proton.

$$\frac{dE}{dr} = \frac{4\pi e^2}{m_o v^2} (N_H \cdot B_H + N_C \cdot B_C) \qquad (3\text{-}32)$$

where

e = the electron charge,

m_o = the electron rest mass,

v = velocity of the particle,

B_H = the atomic stopping number for hydrogen,

B_C = the atomic stopping number for carbon,

N_H = the number of hydrogen atoms/g,

N_C = the number of carbon atoms/g.

In their calculation, the atomic stopping number for hydrogen and carbon were taken from the data published by Hirschfelder and Magee (73).

In the present calculation, the specific energy losses of proton in NE102A scintillator were taken from Croun and Smith (65). The values for proton energies up to 14 MeV are tabulated in table (3.2) and plotted as shown in figure (3.9).

Based on the Birk's formula, the value of constant kB for plastic scintillator has been measured by many workers. Evans and Bellamy (74) have found the value of kB to be 1.0×10^{-2} g cm^{-2} MeV^{-1} for proton energies between 1.2 MeV to 14 MeV. The value of kB obtained was in good agreement between experimental data and the theoretical approach where they assumed that (dE/dr) for protons in NE102A scintillator was the same as that in CH. The same value of kB was obtained by Gettner and Selove (75) in their analysis for proton energies below 2.3 MeV. For higher proton energies between 28 MeV to 148 MeV, the value of kB has been measured by Gooding and Pugh (67) with the value of 1.32×10^{-2} g cm^{-2} MeV^{-1} . Croun and Smith (65) obtained the value of kB for plastic scintillator NE102A as 1.31×10^{-2} g cm^{-2} MeV^{-1} . Their analysis were based on the experimental data of Smith et al (64) for proton in the energy range from 0.35 MeV to 15.0 MeV.

Table (3.2):Numerical values for calculating the Pulse Height of Proton in Plastic Scintillator NE102A.

E MeV	(dE/dr) keV/mg/cm	(dP/dE)	Area under the energy range	Pulse height P(Mev)
0.5	386.7	0.2055	0.0550	0.0550
1.0	238.1	0.2957	0.1235	0.1785
1.5	180.8	0.3561	0.1625	0.3410
2.0	148.4	0.4025	0.1885	0.5295
2.5	127.0	0.4405	0.2110	0.7405
3.0	110.3	0.4755	0.2310	0.9715
3.5	97.3	0.5068	0.2455	1.2170
4.0	88.1	0.5316	0.2590	1.4760
4.5	79.0	0.5587	0.2720	1.7480
5.0	73.7	0.5757	0.2825	2.0305
5.5	68.1	0.5949	0.2925	2.3230
6.0	62.5	0.6154	0.3025	2.6255
7.0	55.5	0.6431	0.6275	3.2530
8.0	50.1	0.6662	0.6540	3.9070
9.0	45.3	0.6882	0.6810	4.5880
10.0	41.9	0.7074	0.6960	5.2840
11.0	38.9	0.7199	0.7110	5.9950
12.0	36.3	0.7338	0.7255	6.7205
13.0	34.0	0.7463	0.7400	7.4605
14.0	32.1	0.7570	0.7500	8.2105

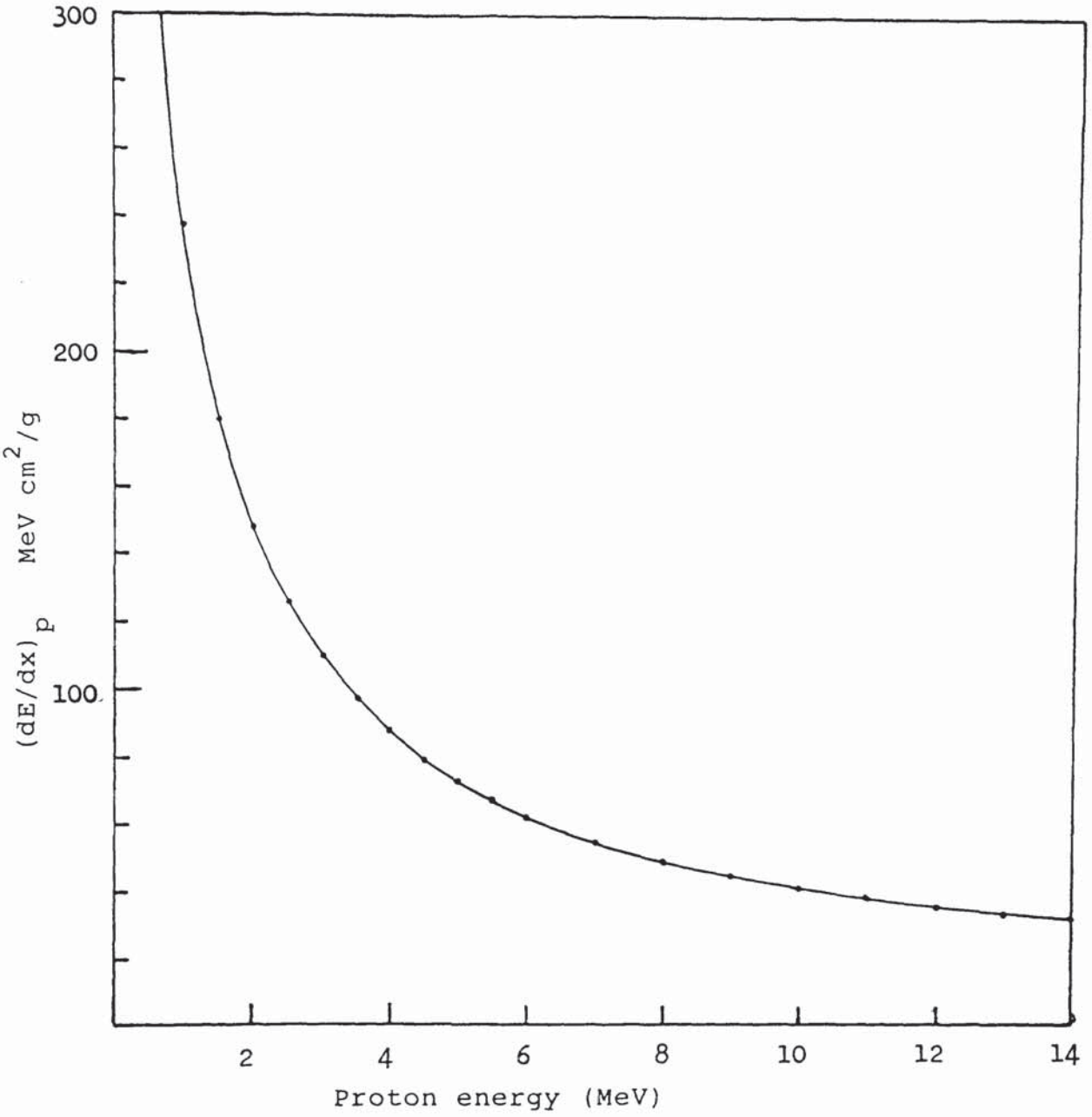

Figure (3.9):The specific energy loss of proton versus proton energy for NE102A scintillator.

As we are interested in proton energies between 1 MeV to 14 MeV, the value of kB = 1.0×10^{-2} g cm^{-2} MeV^{-1} proposed by Evans and Bellamy was taken in the present calculation. Using the data in table (3.2) for (dE/dr) and kB = 1.0×10^{-2} g cm^{-2} MeV^{-1} to equation (3-28), the values of (dP/dE) at various proton energies were calculated for NE102A plastic scintillator, giving the curve shown in figure (3.10).

The pulse height of proton P at various proton energies can be calculated from equation (3-30) using the numerical integration. The pulse height of proton P become,

$$P = \sum_{E=0}^{E=E_p} \frac{1}{1 + kB\left(\frac{dE}{dr}\right)} \Delta E \qquad (3\text{-}33)$$

Using the 0.5 MeV energy steps, the area under the (dP/dE) versus dE curve were traced for E = 0 to E = E_p. The results of the calculation are tabulated in table (3.2) and presented in figure (3.11).

If the number of recoil protons with energies between E and E + dE is written as dN = N(E)dE, and the scintillator output between P and P + dP as dN = N(P)dP, then the two spectra are related by

$$N(E) = N(P)\frac{dP}{dE} \qquad (3\text{-}34)$$

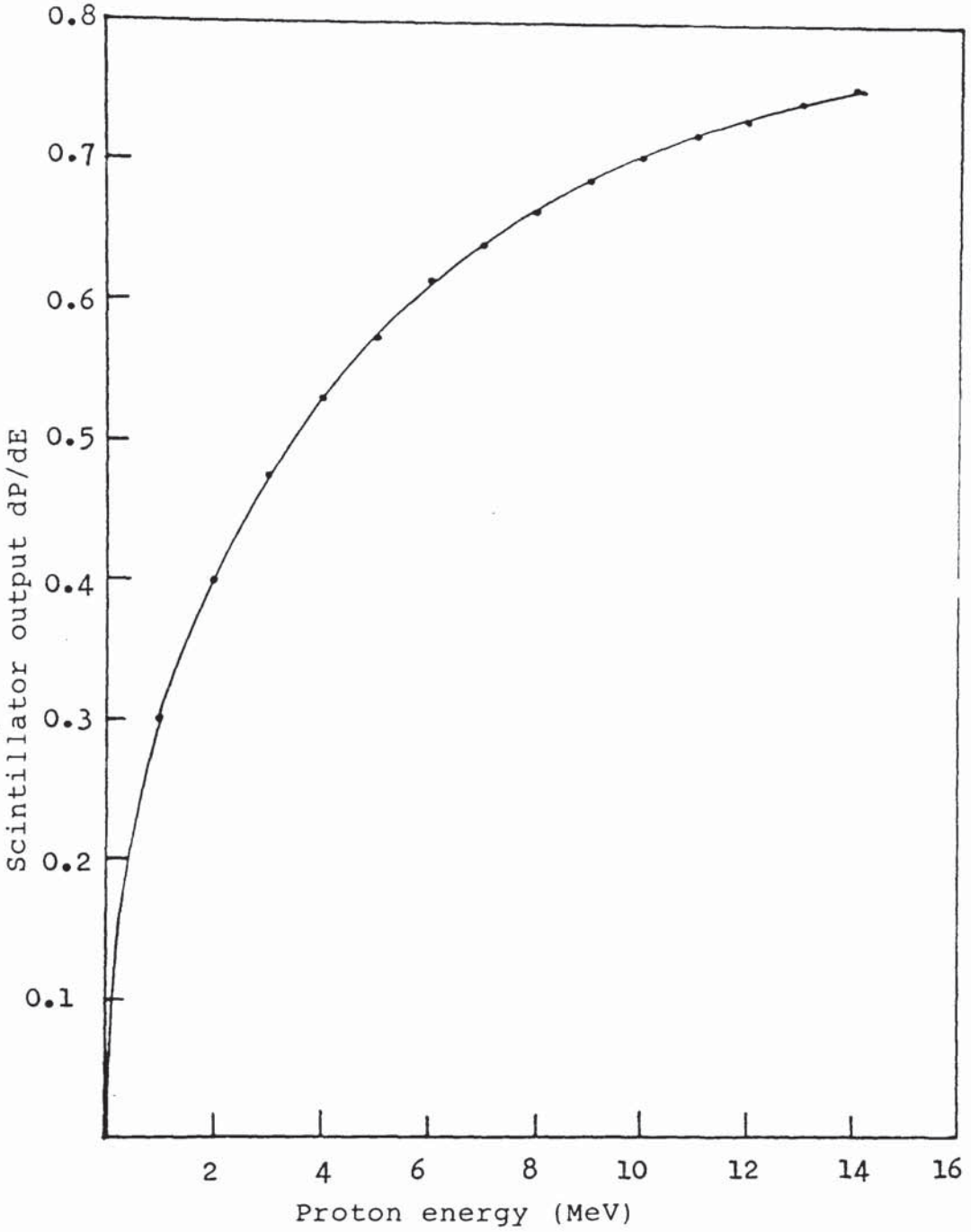

Figure (3.10):The scintillator output dP/dE versus proton energy for NE102A plastic scintillator.

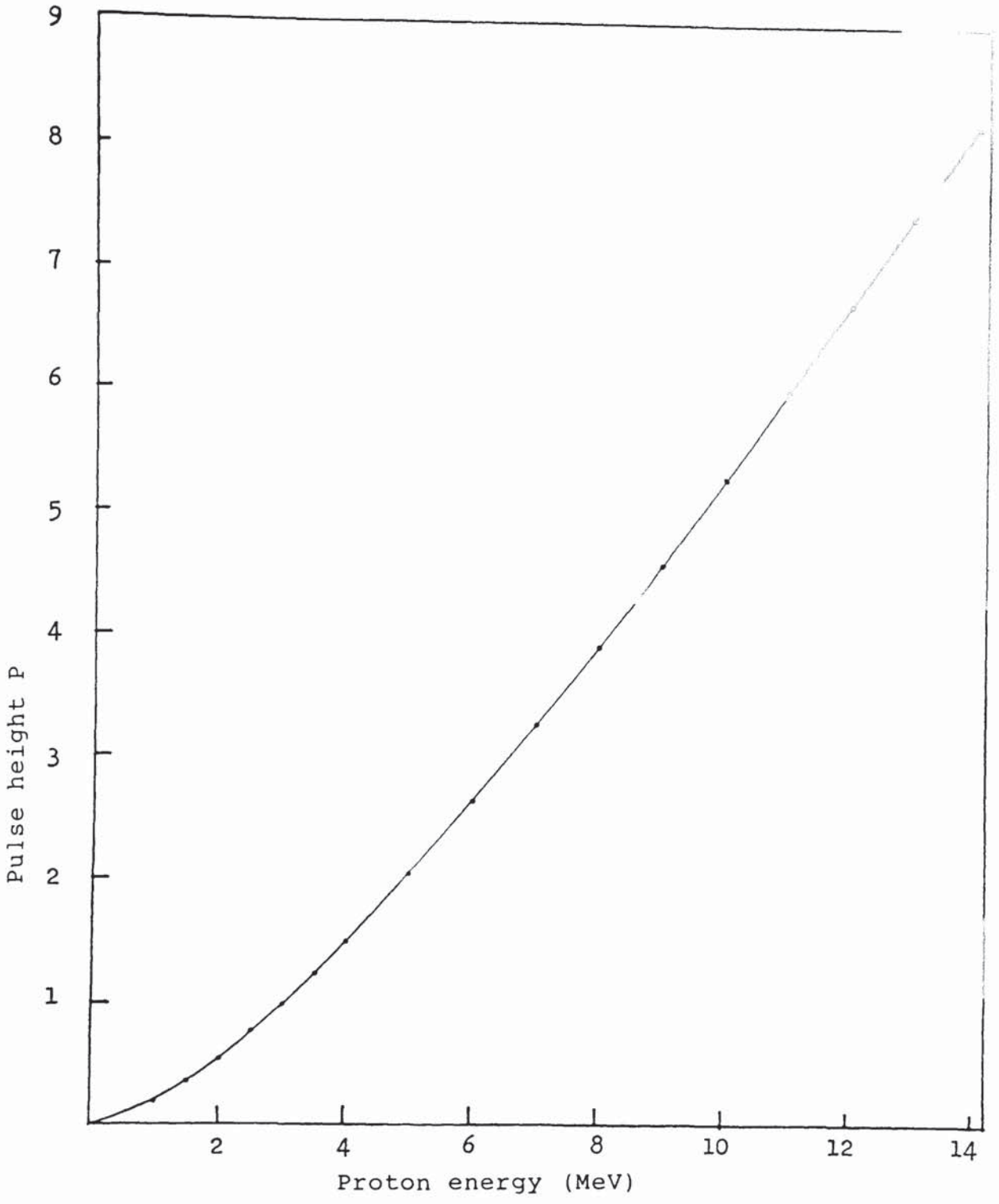

Figure (3.11):The pulse height of proton versus proton energy for NE102A plastic scintillator.

This relationship results in the requirement that the area under the two spectra be the same. For simplicity, N(E) was taken as one and therefore equation (3-35) become

$$N(P) = \frac{dE}{dP} \qquad (3\text{-}35)$$

Using equation (3-35) and the data from table (3.2), the pulse height spectrum for recoil protons produced by 14 MeV neutron in NE102A plastic scintillator were calculated and shown in figure (3.12). In practice the pulse height spectrum will be distorted as shown with dashed line. This distortion is due to the statistical fluctuation in the scintillator output and the photomultiplier tube.

3.2.7:NEUTRON DETECTOR EFFICIENCY WITH DISCRIMINATOR.

The theoretical values for absolute efficiency discussed in sections 3.2.3 and 3.2.4 were calculated without introducing any discrimination or bias level setting. This was called "zero bias" efficiency. In the actual experimental measurement however, there are some pulses arising from lower energy neutrons, gamma-rays and noise pulses that arise spontanously in the counting system. These pulses have to be eliminated from the spectrum by setting the pulse shape discriminator at a certain level. Detector pulse heights below this level

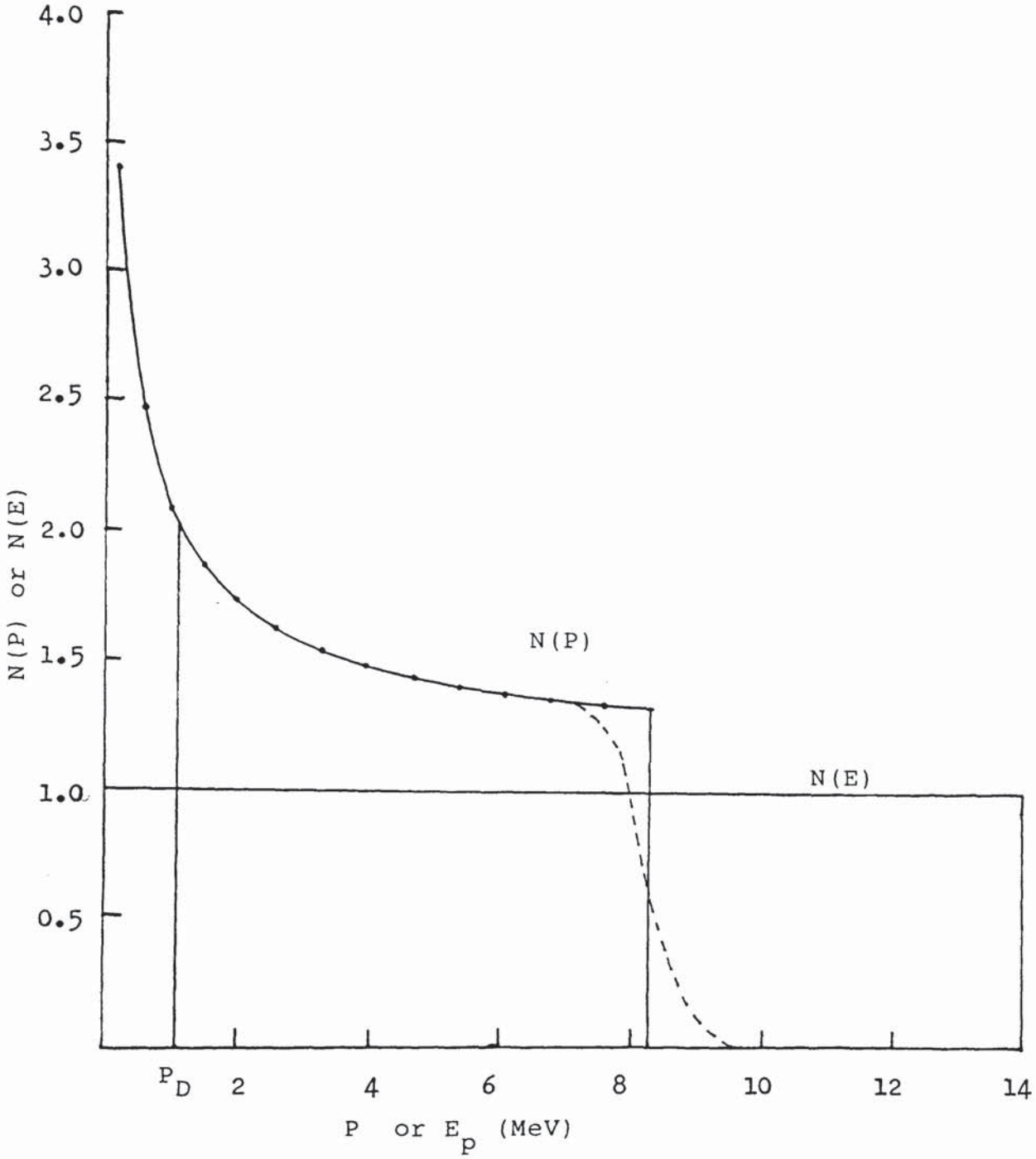

Figure (3.12):The pulse height spectrum of proton and proton recoil energy spectrum for NE102A plastic scintillator.

will not be observed by the detector due to this bias level set. The detector with a finite discrimination level will always have a somewhat lower efficiency particulaly at low neutron energies because some recoil events will inevitably be eliminated in the discriminator process.

In order to calculate the effect of bias level setting on the detector efficiency, it is necessary to know the relation between the neutron energy and its corresponding recoil proton pulse height spectrum. By assuming that the pulse height spectrum due to neutrons of energy E_n is rectangular shape, Jackson et al (43) used the following formula to calculate the efficiency of NE218 liquid scintillator with a discriminator level setting i.e,

$$\epsilon_d(E_n) = [1 - (\frac{B}{E_n})] \frac{(N_p + N_{pc})}{N_o} \qquad (3\text{-}36)$$

where B is the effective neutron energy corresponding to the bias level. In their analysis, the value of B was chosen to give the best available fit to the experimental values.

Mubarakmand and Anwar (76) obtained the efficiency curve of NE102A scintillator for 2 MeV bias from the zero bias curve through the relation,

$$\epsilon_d(\text{2 MeV bias}) = \epsilon_{do}(\text{zero bias})(1 - \frac{2}{E_n}) \qquad (3\text{-}37)$$

where

ϵ_d = the efficiency for 2 MeV bias level setting,

ϵ_{do} = the zero bias efficiency,

E_n = the energy of the incident neutron.

In the present work, the efficiency with discriminator setting for NE102A plastic scintillator was calculated using the pulse height spectrum in figure (3.12). Defining P_D to be the discrimination level, the detector efficiency for 14 MeV neutron is given by

$$\epsilon(14) = \epsilon_1(14) \times \frac{(A_{14} - A_D)}{A_T} \qquad (3\text{-}38)$$

where

$\epsilon_1(14)$ = the efficiency of 14 MeV neutron without discrimination,

A_{14}-A_D = the area under the pulse height spectrum between ordinate P_D and P_{14},

P_D = the discrimination level,

P_{14}= pulse height due to 14 MeV proton,

A_T = the total area under pulse height spectrum.

Taken from the same graph of pulse height spectrum, the efficiency for neutron of energy E_n is then given by

$$\epsilon(E_n) = \epsilon_1(E_n) \times \frac{(A_E - A_D)}{A_T} \times \frac{14}{E_n} \qquad (3\text{-}39)$$

where $(A_E - A_D)$ is the area under the pulse height spectrum between P_D and P_E, and P_E is the pulse height due to proton energy E.

The discriminator level in an organic scintillator detector is usually chosen by measuring the Compton edge of a gamma-ray source. Because of the low atomic number of the constituents of organic scintillators, there is a low probability of photoelectric absorption; therefore, light pulses arising from incident gamma-rays are produced by the recoil electrons in Compton scattering. It can be seen in the gamma-ray spectrum taken from organic scintillator where only the Compton edges are distinguishable. Because the relation of light pulse height to electron energy is consider linear (77), a gamma-ray source with known energy is often used to calibrate the energy scale of the detector output. The discrimination level is fixed by setting the discriminator at certain value to reject pulses due to gamma-rays from specific source.

In the present work, the discrimination level was determined using Co^{60} gamma-rays which emit two gamma-rays with energies 1.17 MeV and 1.33 MeV. Gamma-rays interact with plastic scintillator to produce Compton electrons with energies ranging up to a maximum value given by

$$E_e\,(\max) = \frac{E_\gamma}{1 + \dfrac{m_o c^2/2}{E_\gamma}} \qquad (3\text{-}40)$$

where

E_γ = the gamma-ray energy in MeV,

m_o = the rest mass of electron,

c = the velocity of light.

For a gamma-ray with energy 1.33 MeV, the maximum energy of the Compton recoil electron was calculated using equation (3-40) as 1.116 MeV. As mentioned in section (3.2.6), the pulse height of electron is given by equation (3-28) as

$$\frac{dP}{dE_e} = 1 + kB \left(\frac{dE_e}{dr}\right) \quad . \qquad (3\text{-}41)$$

At electron energy 1.116 MeV, the value of (dE /dr) of electron in organic scintillator is negligibly small. Therefore, the pulse height due to electrons is given by

$$P = E_e \qquad (3\text{-}42)$$

Hence, a 1.116 MeV electrons produces a pulse of amplitude P = 1.116 MeV. From the pulse height spectrum of proton (figure 3.11) it was found that a pulse height of amplitude P = 1.116 MeV corresponds to the proton energy of 3.33 MeV. Therefore, the method chosen for derterminig the discrimination level with Co^{60} gamma-rays as a reference, resulted in the rejection of pulses due to neutrons with energy less than 3.33 MeV.

After determining the bias condition at P = 1.116 MeV the neutron detector efficiencies were calculated by counting the area under the pulse height spectrum in the

energy range of interest. Applying equation (3-39), the efficiecncy of neutron detector at various neutron energies up to 14 MeV using the zero cutt-off efficiency from figure (3.6) is plotted and shown in figure (3.13).

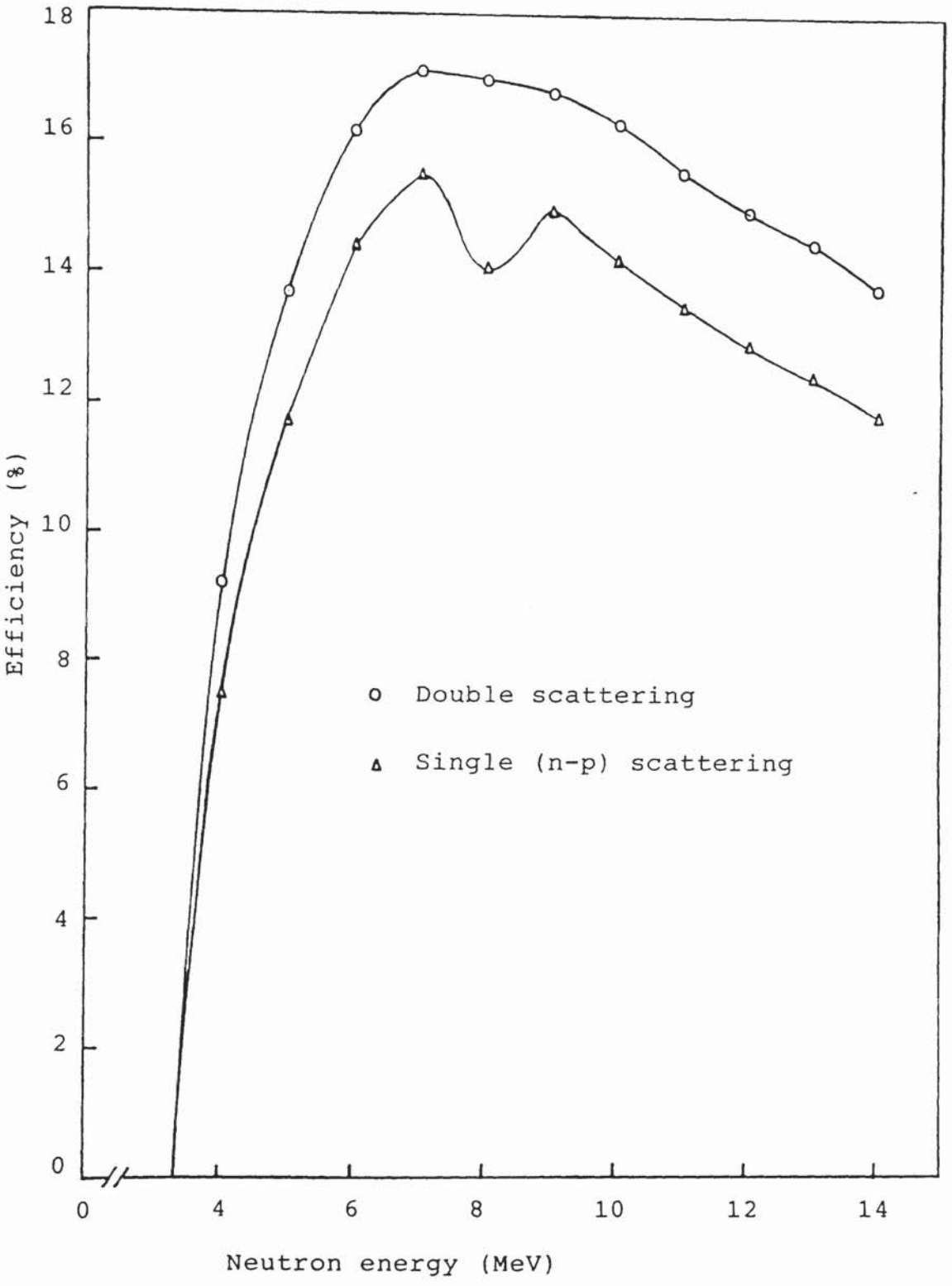

Figure (3.13):The calculated efficiency of NE102A plastic scintillator with discriminator set at 3.33 MeV

3.2.8:NEUTRON DETECTOR SHIELDING.

In neutron scattering experiment, it is necessary to shield the detector from neutrons other than those which are scattered by the sample at the particular angle of observation. As the plastic scintillator detector is sensitive to gamma-rays, adequate detector shielding againts gamma-radiation is also required. In the present experiment, there are two main sources of background neutrons and gamma-rays produced by the source, i.e

(i) Indirect neutrons and gamma-rays scattered from the surrounding materials in the laboratory,

(ii) Direct flux from neutron source.

Therefore, in order to prevent these two types of background radiations , two kinds of shielding have to be used, i.e,

(i) A massive shielding collimator surrounding the detector,

(ii) A shadow bar shielding for direct neutrons.

3.2.8.1:SHIELDING MATERIALS.

Any detector designed for neutron counting must obviously be shielded against external sources of background neutrons to enhence its signal to background ratio. Because fast neutrons are involved in the present experiment, effective shielding must be employed to attenuate fast neutrons without causing activity of the

shielding materials. This can be done by the following requirements

(a) Moderate the fast neutrons,

(b) Absorb slow neutrons,

(c) Absorb the secondary penetrating radiations e.g gamma-ray.

a) Fast neutron moderator.

The most effective moderators to slow down the fast neutrons to low energies are elements with low atomic number. Hydrogen-containing materials such as water and paraffin wax are the most useful neutron moderator. As shown in figure (3.5) the neutron-hydrogen cross-section is relatively high but decreases as the energy increases. At high neutron energies, the neutron-proton cross-section is dominated by the elastic scattering process. Therefore, hydrogen does not produce any secondary gamma-rays in reactions with fast neutrons. Only at thermal neutron energy, neutrons captured by hydrogen produce a single gamma-ray of energy 2.23 MeV from the $^{1}H(n,\gamma)H^{2}$ with a cross-section of 335 mbarns at 0.0253 eV (78).

Because of the difficulties of the construction of a suitably shaped leak proof water tank, paraffin wax is usully preferred as a major component of most fast neutron shields. In using paraffin wax, neutron-carbon scattering has to be considered. As shown in figure

(3.5), only elastic scattering on carbon occurs below 5 MeV, while at high energies the inelastic processes become increasingly important. The inelastic (n,γ) reaction with carbon-12 produces 4.43 MeV gamma-rays, but cross-section for this reaction is very much less than for elastic scattering by hydrogen and carbon.

b) Absorption of slow neutrons.

The moderated energy neutrons can be eliminated through an approprite capture reaction. Therefore, the second component of the shielding should contain the materials with high neutron absorption cross-section at low neutron energy. The materials should also produce stable reaction products in their reaction with slow neutron, or if the unstable products are produced, they should decay without the emission of penetrating gamma-rays.

The materials which have large capture cross-section with slow neutron are cadmium, boron and lithium. Because many gamma-rays are emitted in neutron capture process with cadmium, therefore, boron and lithium are the only practical choice for slow neutron shielding.

The capture reaction of slow neutron with boron occurs with ^{10}B and is given by the following reaction

$$^{10}_{5}B + ^{1}_{0}n \longrightarrow \begin{cases} ^{7}_{3}Li + \alpha + Q \ (2.79\ MeV) \ \text{(ground state)} \\ ^{7}_{3}Li^{*} + \alpha + Q \ (2.31\ MeV) \ \text{(excited state)} \end{cases}$$

^{10}B has an isotopic abundance of 19.7% in natural boron. The cross-section for the obove reaction is 3840 barns for 0.025 eV neutrons and has a 1/v variation as shown in figure (3.14) (79). The majority (94%) of the capture reaction in ^{10}B leads to an excited state in the ^{7}Li product nucleus, which subsequently decays by the emission of 0.48 MeV gamma-ray with half life of about 10^{-13} sec.

For lithium the capture cross-section for slow neutron occurs with ^{6}Li i.e

$$^{6}_{3}Li + {}^{1}_{0}n \longrightarrow {}^{4}_{2}He + {}^{3}_{1}H + \quad Q = 4.78 \text{ MeV}.$$

The reaction proceeds directly to the ground state of the product nuclei and therefore no gamma-rays are emitted. The unstable tritium decays by low energy beta-emission (18 keV end point energy) with a 12.26 years half life to helium-3 without gamma-ray emission.

Lithium-6 has an isotopic abundance of only 7.4% in natural lithium. The neutron capture cross-section for lithium-6 is about 945 barns for 0.025 eV neutron and has a 1/v variation as shown in figure (3.14). The graph shows that the neutron capture cross-section for lithium-6 is always smaller than boron-10 at energies below 200 keV. Because of the above disadvantages, boron is the most practical choice for slow neutron shielding. Generally, because of constructional reasons, boron is usually used in form of compound typically boric oxide.

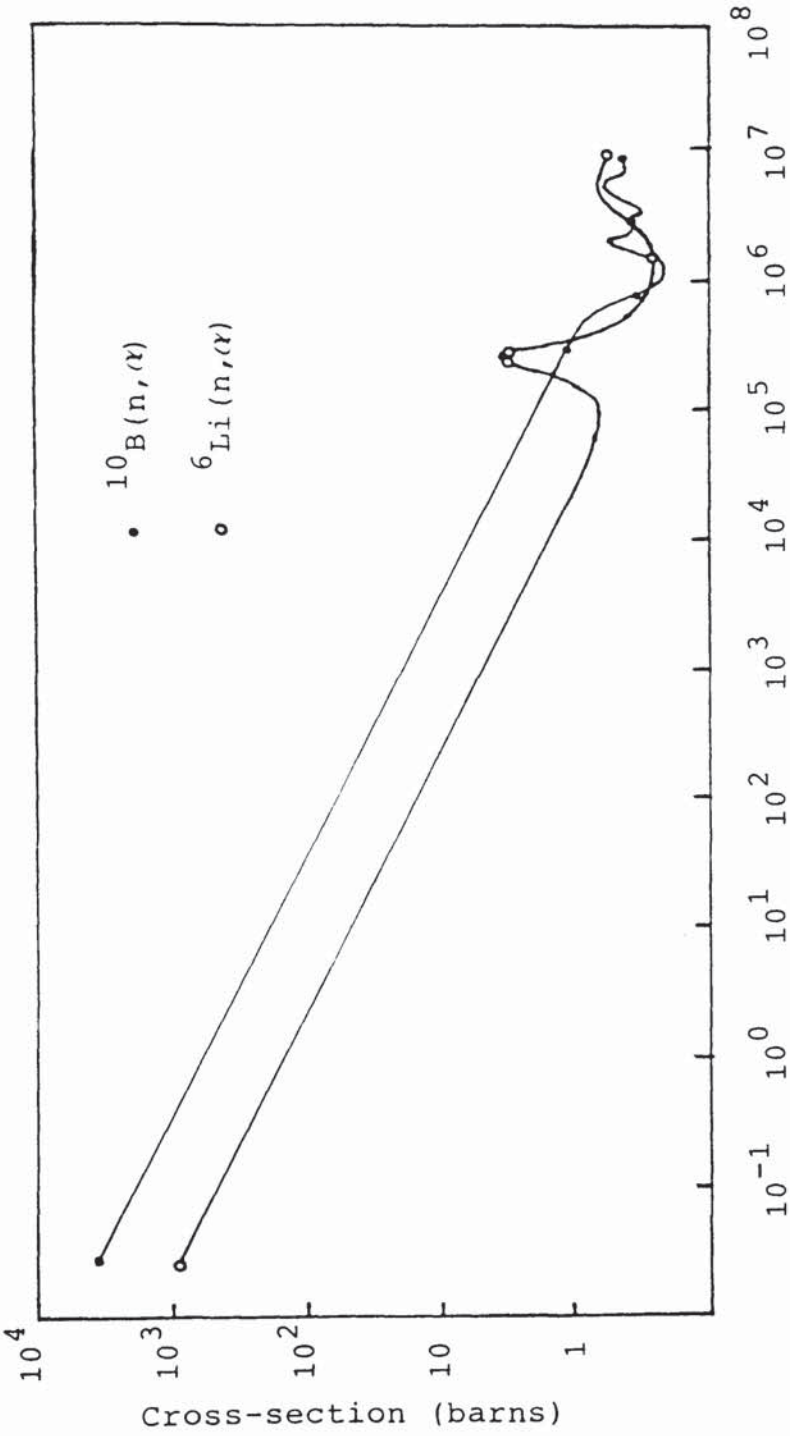

Figure (3.14): Cross-section versus neutron energy for $^{10}B(n,\alpha)$ and $^{6}Li(n,\alpha)$ reactions.

c) Asorption from the secondary penetrating radiation.

The detector should be shielded from gamma-rays produced by reactions in the shielding materials and the general gamma-rays background from the surrounding materials in the laboratory. Therefore, the innermost part of the shielding should contain gamma-ray absorbing material. Materials with high atomic number are the most effective shielding materials for gamma-rays. Because of its high density and large atomic number, lead is the most widely used material for the construction of detector shields. With its high density a few cm of lead will provide a large reduction in the background gamma-rays.

3.2.8.2:SHIELDING DESIGN FOR NEUTRON DETECTOR.

The neutron detector shielding which has been used so far and which has given reasonably satisfactory performance was designed by Connel (36). The cross-sectional diagram of the shielding is shown in figure (3.15).

In order to moderate the undesired background neutrons the outermost part of the shield was the moderator material. The moderator consisted of paraffin wax with a thickness of 150 mm at the side of the neutron detector and about 300 mm infront of the detector. A thickness of 200 mm of paraffin wax is considered enough to absorbed most high energy neutrons (80).

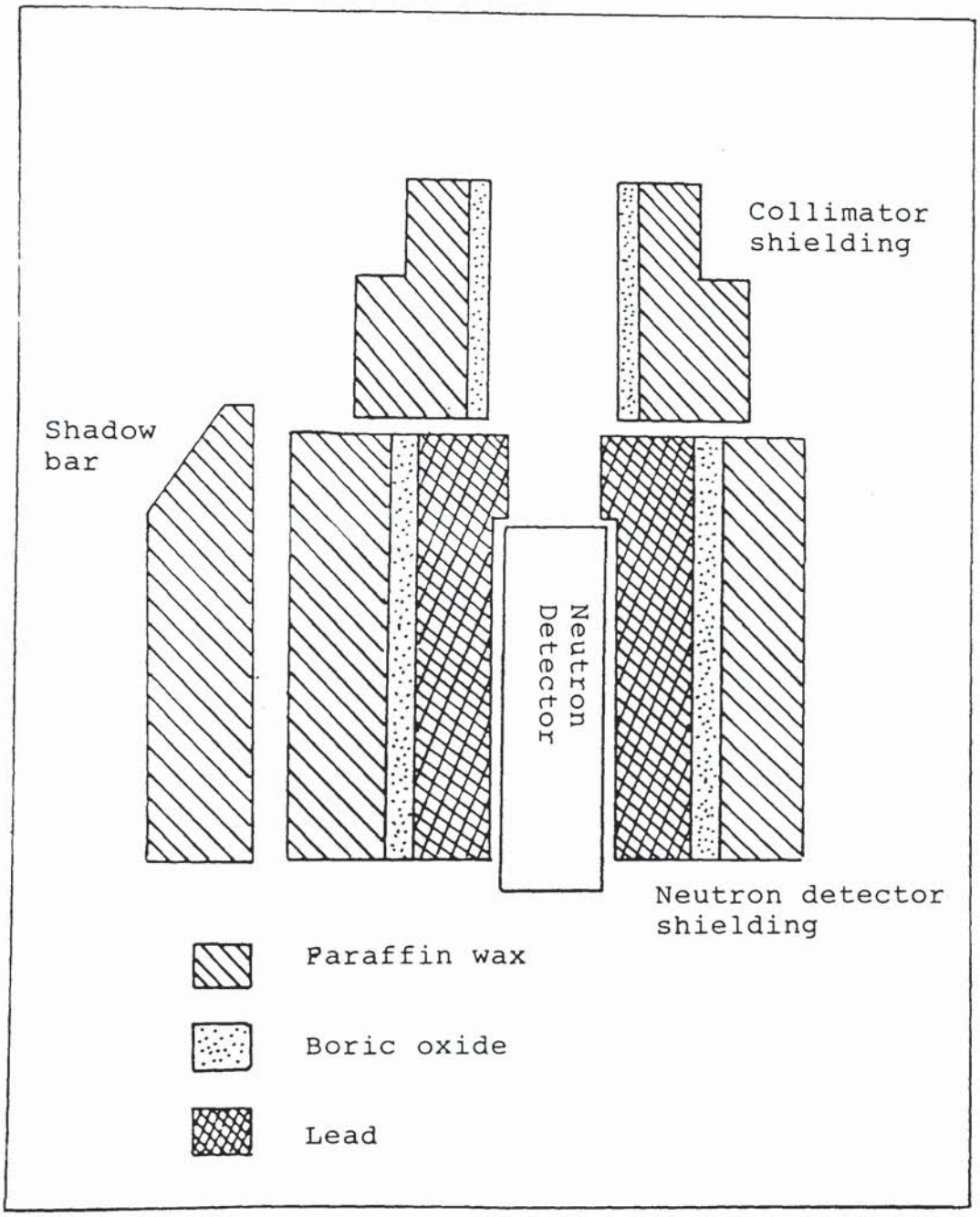

Figure (3.15):The cross-section of the neutron detector shielding, collimator shielding, and shadow bar shield.

In order to absorb the slow neutrons by capture reaction, the shield also contained a lining boric oxide powder with thickness of 15 mm packed into a sealed double walled cylinder with an effective density of 1200 kg m^{-3}. Connel (36) has shown that the thickness of 15 mm of boric oxide absorbs 100% of a neutron flux up to a neutron energy of about 1 eV.

Finally, the innermost part of the detector shielding is the lead gamma-ray shield with thickness 55 mm at the side of the detector and has a maximum thickness of 125 mm infront of the detector. Connel (36) had calculated the half thickness values of lead at various gamma-ray energies by the simple exponential absorption law. He found that the 3.5 MeV gamma-rays are the most penetrating with the half thickness of 15 mm. Therefore, a minimum thickness of 55 mm of lead is adequate to absorb the gamma-ray background from the reactions in the shielding materials and general gamma-rays background.

In order to reduce the background radiation entering the detector, a collimator shield was placed infront of the detector. The collimator shield also contained a lining of boric oxide powder into a sealed double walled cylinder and had a thickness of 15 mm to absorb all incident thermal neutrons.

3.2.8.3:SHADOW BAR SHIELDING.

In the scattering experiment using time of flight technique, neutron detector has to be shielded from the direct flux of the neutron source. This can be done by placing a shadow bar shield between scattering sample and the neutron detector.

The shadow bar shields are normally made from a heavy metal such as copper, iron and tungsten or from hydrogenous materials. However, by using a heavy metal as a neutron shadow bar shield, hard gamma-rays are generally produced by nonelastic processes, therefore hydrogenous materials are prefered in our type of experiment. Hydrogen can provide on average a 50% energy degradation per elastic collision. Materials suitable for shadow bars have been investigated by Hopkins et al (81). They found that for neutrons above 6 MeV, materials in order of merit were tungsten, copper, iron, lead and polythene. For lower neutron energies polythene was the most efficient for shadow bar shield.

The shadow bar shield must be sufficiently massive and long to attenuate the direct neutron beam. A shadow bar made from paraffin wax with dimension $60x20x20\ cm^3$ is used in the present work as shown in figure (3.15).

3.3:ALPHA-PARTICLE DETECTOR.

3.3.1:THE CHOICE OF ALPHA-PARTICLE DETECTOR.

In the associated particle method the instant of neutron production from $T(d,n)He^4$ reaction was monitored by the detection of alpha-particle counts. As 3.5 MeV alpha-particle is emitted at 90° from the deuteron beam direction, a suitable alpha-detector should be chosen to detect the particles for this particular energy.

There are two types of alpha-particle detector which have to be considered at present application. These are semiconductor detector and organic scintillator detector which have the following properties as required in the present works, i.e

(i) an excellent alpha-particle detection efficiency,

(ii) a fast rise time of less than 10 ns to enable accurate timing,

(iii) a low efficiency for neutrons and gamma-rays,

(iv) less sensitive to radiation damage.

The type of semi-conductor detectors which are commonly used to detect alpha-particles from $T(d,n)He^4$ reaction is silicon surface barrier detector. Such detector has shown very good energy resolution and linearity, coupled with a fast rise time and compact size. It has relatively low sensitive to both neutrons and gamma-rays. In silicon surface barrier detector, fast neutrons are detected mainly by (n,p) and (n,α) reactions

on Si^{28}. However Dearnaley and Whitehead (82) have shown that the efficiency of silicon surface barrier detector to fast neutron is exceptionally low with the magnitude of about 10^{-6} to 10^{-5} for 14 MeV neutron. The detection of gamma-rays by silicon surface barrier detector is based on the Compton scattering events but because of the very thin sensitivity region, the efficiency is relatively low.

The main disadvantage in using a surface barrier detector was the small amplitude of the output pulse. The detector would require a high gain, wide band amplifier to generate an adequate timing pulse. Because of this difficulty, the plastic scintillator detector is the best possible choice to be used in the present work.

The plastic scintillator detector used was type NE102A manufactured by Nuclear Enterprises plc. It is readily available in thin sheet of 0.5 mm thickness and 3.81 x 3.81 cm^2 dimension, thus having a low neutron detection efficiency. The gamma-rays detection efficiency is low due to the low values of mass number constituents in organic material. The response of plastic scintillator to neutrons and gamma-rays has been discussed in section (3.2.6).

In the $T(d,n)He^4$ reaction the alpha-particles emitted at 90^o to the deuteron beam direction have an energy of 3.5 MeV. The range-energy curve for alpha-particle in plastic scintillator NE102A given by the manufacturer is shown in figure (3.16). The figure

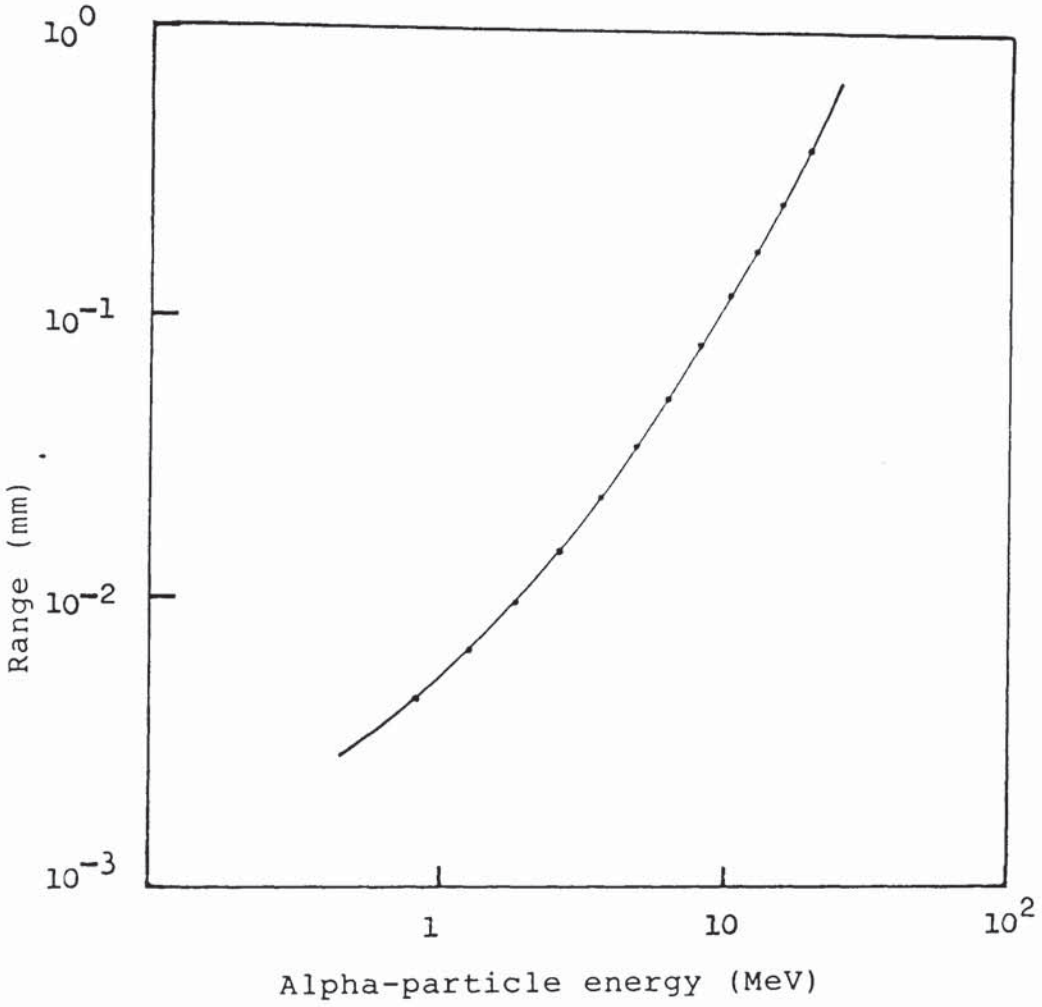

Figure (3.16):Range energy curve of alpha-particle in NE102A scintillator.

indicates a range of 2.5×10^{-3} cm for 3.5 MeV alpha-particle. Since the thickness of the scintillator used was 5×10^{-2} cm, hence the 100% efficiency is easily achieved for alpha-particle detection. The efficiency of the plastic scintillator with thickness of 5×10^{-2} cm was estimated using equation (3-8) and giving the value of 1.87×10^{-3} for 14 MeV neutrons. Hence, the background of neutrons introduced a negligible error in the alpha-particle detection.

The plastic scintillator NE102A was used with a Philips 56 AVP Photomultiplier tube mounted through a perspex light guide of 70 mm thickness. The photomultiplier and light guide used will be discussed in the next chapter.

Figure (3.17) shows the alpha-particle detector arrangement. The detector is at a distance of 90 mm from the target and is positioned at 90^{o} with respect to the incident deuteron beam direction. An O ring vacuum seal was attached between perspex light guide and the target assembly flange to ensure good vacuum condition. The base flange of the alpha-detector system was insulated from the target assembly using insulating spacer of polyethelene and nylon bolts. This was done to keep the detector system at earth potential because the potential will rise in the target assembly under deuteron bombardment.

The solid angle of the alpha-particle detector was defined by a 11 mm x 19 mm rectangular aperture in an

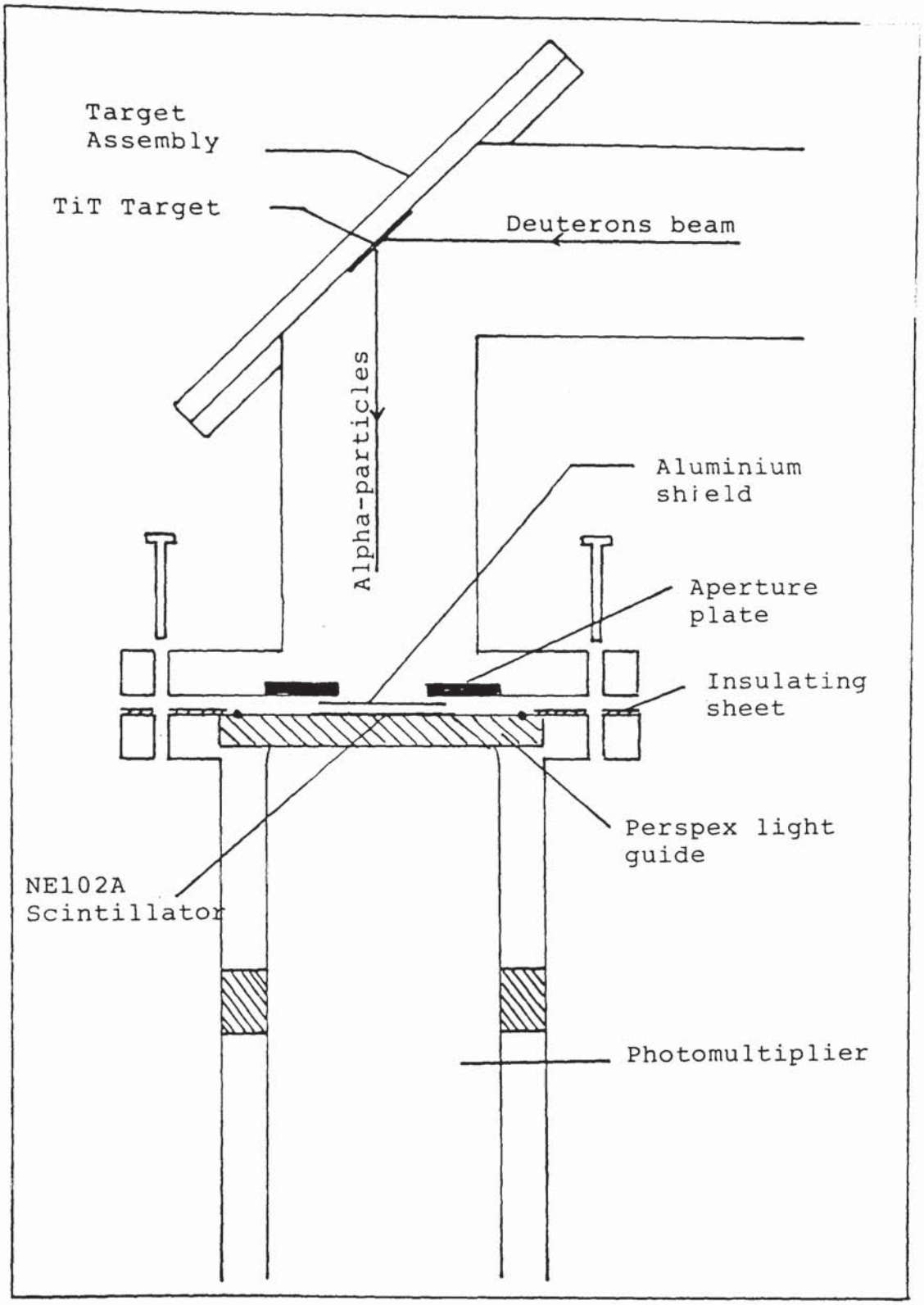

Figure (3.17):The alpha-particle detector arrangement.

aluminium plate which was positioned infront of the scintillator. The detector subtended a semi-angle of 3.5^{o} in the horizontal and 6^{o} in the verticle directions at the target with detector-target centre distance of 90 mm.

3.3.2:ALPHA-DETECTOR SHIELDING.

There are two sources of radiation constituted a low energy background in the detection system of alpha-particles. These are beta-particles emitted by the decay of tritium target and deuterons scattered by the target.

Tritium is unstable isotope and decays by emitting beta-particles with a 12.3 years half-life to He^{3} , and have maximum energy of 18.6 keV. The deuteron background results from scattering of primary beam through 90^{o} by the target atoms into alpha-detector and has an energy less than 140 keV. In order to eliminate these background radiations from alpha-particle detection system an aluminium foil shield was used in the present application. The thickness of the aluminium shield should be chosen so that deuterons and beta-particles will be stopped but allow the 3.5 MeV alpha-particles to pass through the detector. This can be estimated by considering the range of beta-particles, deuterons and alpha-particles in aluminium.

The range-energy data show that the range of 18.6

keV beta-particles in aluminium is 2×10^{-4} cm (42). There are no available experimental data in the range of deuterons in aluminium. However, using the proton data, the range of deuteron in aluminium can be calculated from equation (2-17). Using the proton data published by Warshaw (32) the range of deuteron in aluminium for 140 keV deuteron energy was calculated as 2.0×10^{-4} cm.

To stop all the beta-particle and deuterons reach the detector, an aluminium foil with thickness of 4.4×10^{-4} cm was chosen. This thickness allows alpha-particle to reach the detector as the range of 3.5 MeV alpha-particle in aluminium which was calculated by Baynham (83) using Bethe's formula as 11×10^{-4} cm. The aluminium foil shield was held on the top of the scintillator using a non-drying imersion oil.

3.4 :ADDITIONAL REACTIONS AFFECTING THE DETECTION OF ALPHA PARTICLES FROM $T(d,n)He^4$ REACTION.

In section (3.3.2), the deuterons and beta-particles which are expected to reach into alpha-particle detector were shielded by an aluminium foil. However, it is possibly happen that any nuclear reaction as well as $T(d,n)He^4$ reaction, which produced either neutrons or alpha-particles will be detected by alpha-particle detector. The two reactions which could possibly occur in or near the target and detected by alpha-particle detector are

(i) $H^2 + H^2 \longrightarrow n + He^3$ (+3.27 MeV)

(ii) $He^3 + H^2 \longrightarrow p + He^4$ (+18.3 MeV)

Reaction (i) will possibly occured in the beam tube near the target when the accelerated deuterons beam react with deuterons which have been loaded up on the beam tube or aperture in the beam tube. This reaction produces neutron and become a secondary source of neutron in our system. In order to estimate the amount of error effected by this reaction, we have to consider the cross-section for both $D(d,n)He^3$ and $T(d,n)He^4$ reactions. The cross-sections for both reactions are shown in figure (3-18) taken from reference (31). The figure shows that the cross-section for $D(d,n)He^3$ reaction is very much smaller than that $T(d,n)He^4$ reaction particularly at low energy deuteron. For example for deuteron energy 140 keV, the cross-section for $D(d,n)He^3$ reaction is something like 100 times smaller than that $T(d,n)He^4$ reaction and the different is decreased as the energy increased. Therefore, as the energy of deuteron beam was accelerated only up to 140 keV, the neutron yield from $D(d,n)He^3$ reaction is relatively small and will introduce negligible error in the alpha-particle detection.

From the kinematics of nuclear reaction the neutron produced from $D(d,n)He^3$ reaction has an energy ranging up to about 3 MeV by bombarding with deuteron energies up to 140 keV. This low energy neutron will not be detected by neutron detector because the neutron discriminator was set

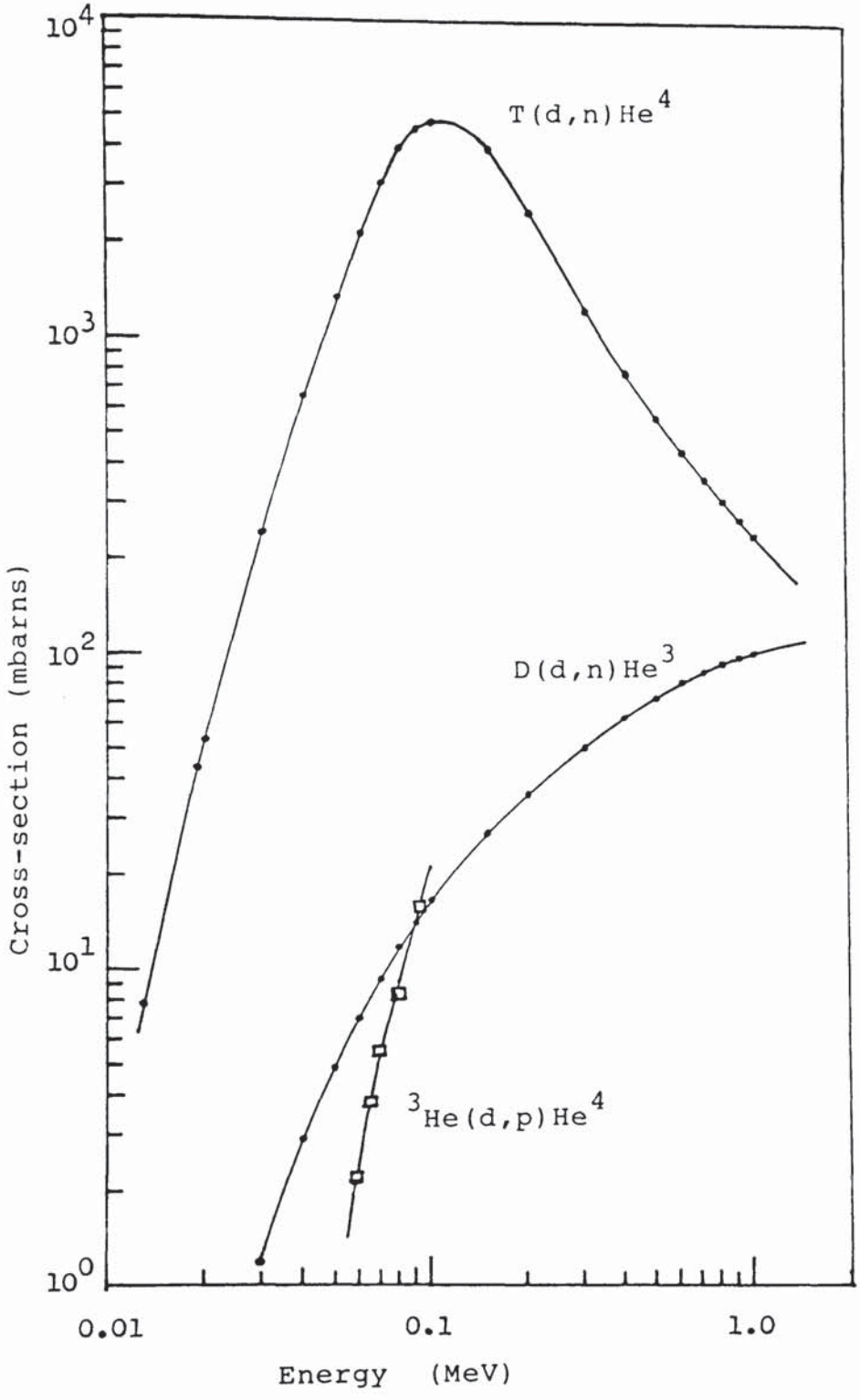

Figure (3.18):The cross-section for T(d,n)He^4, D(d,n)He^3 and T(d,p)He^4 reactions.

so that the only neutron with energies above 3.33 MeV will allow into the detection system (see section 3.2.7).

Tritium is unstable isotope and decays by beta-emission to He^3 . The He^3 atoms will produce $^3He(d,p)He^4$ reaction under deuterons bombardment. The alpha-particle produced by this reaction is very similar to that of the alpha-particle from $T(d,n)He^4$ reaction and will possibly cause trouble because its can easily be detected by alpha-particle detector. However, as shown in figure (3.18), the cross-section for $^3He(d,p)He^4$ reaction is much smaller compared to that the $T(d,n)He^4$ reaction at lower deuteron energies. Therefore, if one avoids high energy deuteron the effects from $^3He(d,p)He^4$ reaction can be neglected. Using a new targets can further reduce the amount of He^3 available for $^3He(d,p)He^4$ reaction.

There will be some deuterons in a used target due to the ion beam. Therefore, the $D(d,n)He^3$ reaction can occur and the He^3 released might be mistaken for an alpha-particle in a plastic scintillator. The proton with energy 3.66 MeV at 90° produced from $^3He(d,p)He^4$ reaction also introduces the same effect.

CHAPTER 4

EXPERIMENTAL PROCEDURE FOR ABSOLUTE DIFFERENTIAL CROSS-SECTION MEASUREMENT

4.1:DETECTION SYSTEM ARRANGEMENT AND CALIBRATION.

The physical arrangement for the scintillator and its incooperation with the photomultiplier tube are important design considerations. In the following sections the scintillator/photomultiplier assembly and the relevant associated electronics calibration will be discussed.

4.1.1:THE PHOTOMULTIPLIER TUBE.

In the radiation detection and spectroscopy using scintillator detectors, the weak light output of scintillator pulses have to be converted into corresponding electrical signals. This can be achieved using a photomultiplier tube where light signals of a few hundred photons can be converted into usable current pulses without adding a large amount of random noise to the signal.

In the present work the photomultiplier tube employed in the neutron detector was Philip 56 AVP which has a rise time of about 2 ns and was adequate for the present experiment. The block diagram of the photomultiplier tube is shown in figure (4.1). The

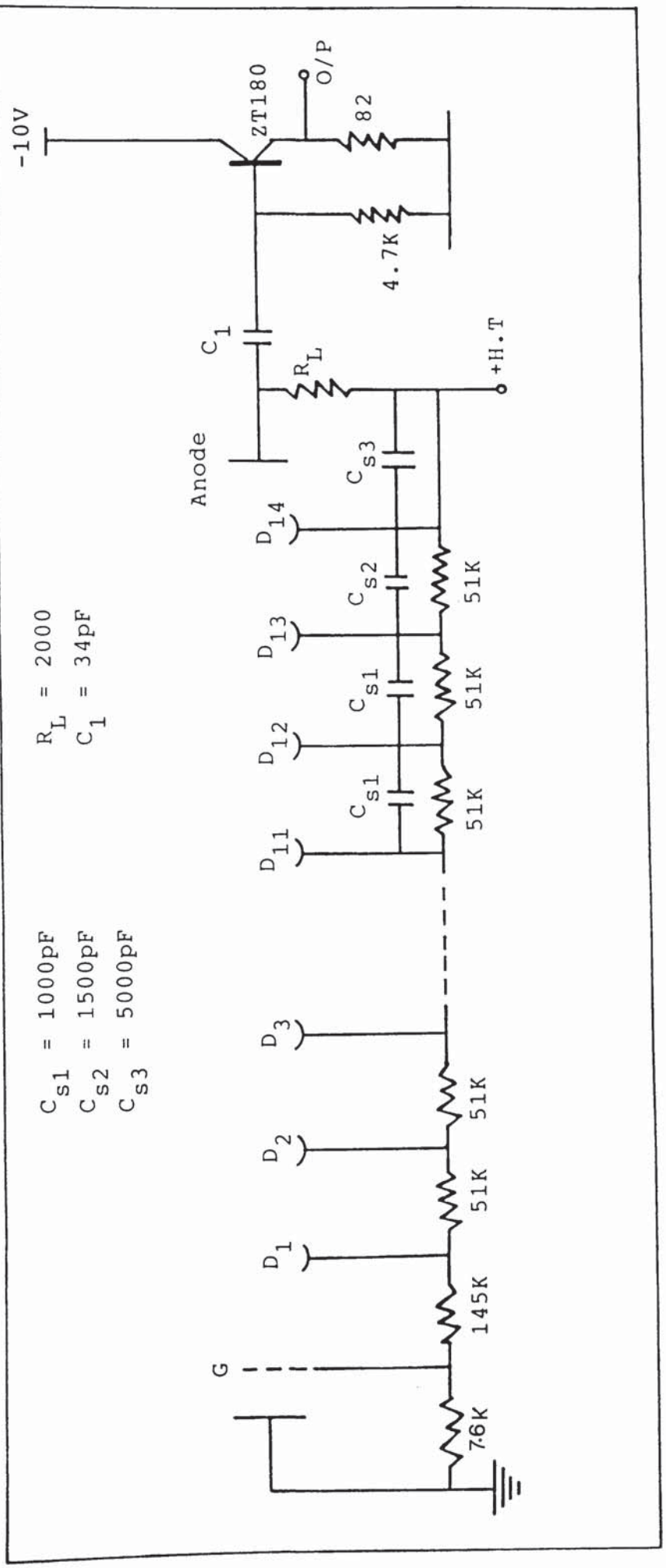

Figure (4.1): The photomultiplier dynode chain and emitter follower for neutron detector.

cathode of the photomultiplier tube is a thin coating of photoelectric material which converts photons from scintillator to electrons. The electrons are attracted to the dynode by a potential provided by a resistive voltage divider. The cathode of the photomultiplier tube is grounded and the divider string supplies successively increasing positive voltages to each dynode down the multipling string. The d.c current through the chain was 2.3 mA for operating voltage of 2.0 kV.

The Philip 56 AVP photomultiplier tube has 14 stages of amplification giving a gain of approximately 10^8 when operated at 2.0 kV. This high gain eliminated the need for futher amplification of the output pulse.

For efficient photoelectron collection, the voltage between photocathode and first dynode was made several times greater than dynode to dynode voltage differences by connecting a higher value resistor.

The four capacitors were included across the last four dynode chain resistors in order to help hold these later dynode voltages at a constant value throughout the pulse. These stabilizing capacitors were needed because of the high pulse current in the later stage of the tube. The capacitor supplies the current lost from the dynode during the pulse and is recharged by the divider string current during the period between pulses.

The load capacitor R_L and H.T blocking capacitor were chosen so that the resulting anode circuit time

constant had a suitable magnitude and duration.

In the present work a long coaxial cable was used in order to connect the output of the photomultiplier tube to the neutron discriminator. In order to avoid any signal reflection in this cable, the anode signal of the photomultiplier was matched into the cable through an emitter follower. The block diagram of the emitter follower is shown at the base of the photomultiplier dynode chain circuit.

The electron emitted from the photocathode and dynodes have a low average energy and are quite sensitive to magnetic fields. Even the influence of the earth's magnetic field is sufficient to deflect electrons away from their normal path. Since the neutron detector was moved around the sample, the movement of the photomultiplier relative to the earth's magnetic field can disturb the trajectories of these electrons. This results in changes in the gain of the photomultiplier. To eliminate this effect a thin cylinder of mu-metal which fitted closely around the photomultiplier tube was employed. The position of the mu-metal is shown in figure (4.3).

A similar type of photomultiplier was used for alpha-particle detector. Here, the cathode of the photomultiplier was held at a negative potential, while the anode was held at a zero potential. The dynode resistor chain for the alpha-particle detector is shown in

figure (4.2).

The alpha-particle detector was fixed at 90° to the deuteron beam direction. Therefore mu-metal was not employed in the alpha-particle photomultiplier tube.

4.1.2:PERSPEX LIGHT GUIDE.

In many applications a material known as a light guide has been used to match a photomultiplier tube directly to one face of a scintillator. This material guides the light from scintillator by total internal reflection and also serves to spread the light more uniformaly over the cathode. Idealy the light guide used for this purpose should be transparent and have the same refractive index as the scintillator. The surfaces of the light guide are highly polished and often surrounded by a reflective wrapping to reflect back some of the light which would have escaped. Lucite or perspex with an index of refraction 1.49 to 1.51 is the most widely used material, and can easily be formed into complex shapes.

In this work a light guide was necessary to make an efficient optical coupling between 10 cm diameter of scintillator used in neutron detector and 5 cm diameter of photomultiplier tube. A perspex light guide of 7 cm thickness was employed covering from the scintillator to the cathode of the photomultiplier tube. Any light guide whose cross-sectional area decreases from scintillator to photomultiplier tube will result in some light loss (79).

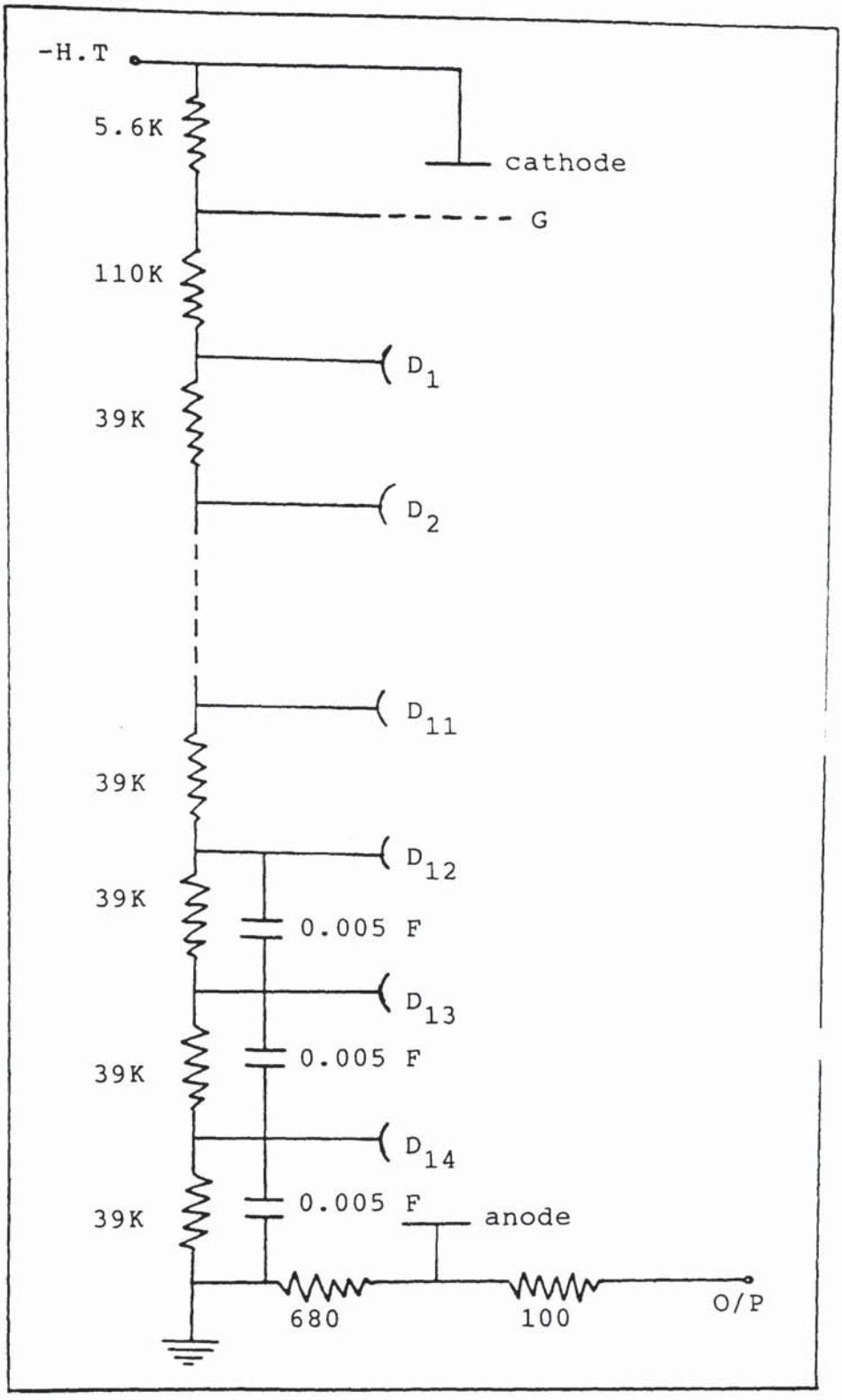

Figure (4.2):The photomultiplier dynode chain for alpha detector.

However if the cross-sectional area is maintained constant and sharp bends are avoided, the light guide can theoretically transmit all the light that enters within the acceptance angle at the input end.

In the installation of the light guide, it is necessary to ensure good optical contact between scintillator and photomultiplier tube in order to minimize the amount of reflection at the interfaces. The contact between scintillator and perspex light guide was made using NE 580 optical cement which has a refractive index close to that of NE102A plastic scintillator (n = 1.581). Optical contact between light guide and the photomultiplier tube was obtained by using a non-drying immersion oil. Figure (4.3) shows the scintillator-photomultiplier assembly.

4.1.3.SETTING THE NEUTRON DISCRIMINATOR LEVEL.

A ^{60}Co gamma-ray source was used to set the discriminator level of the neutron detector by determining the position of the Compton edge of the 1.33 MeV gamma-ray energy. In section (3.2.7) it was mentioned that a pulse of amplitude of 1.116 MeV produced from 1.33 MeV gamma-ray energy corresponds to a proton energy of 3.33 MeV. Therefore, setting up the discriminator with ^{60}Co gamma-rays as a reference resulted in the rejection of pulses due to neutrons with energy less than 3.33 MeV.

In this work the discriminator used in the neutron

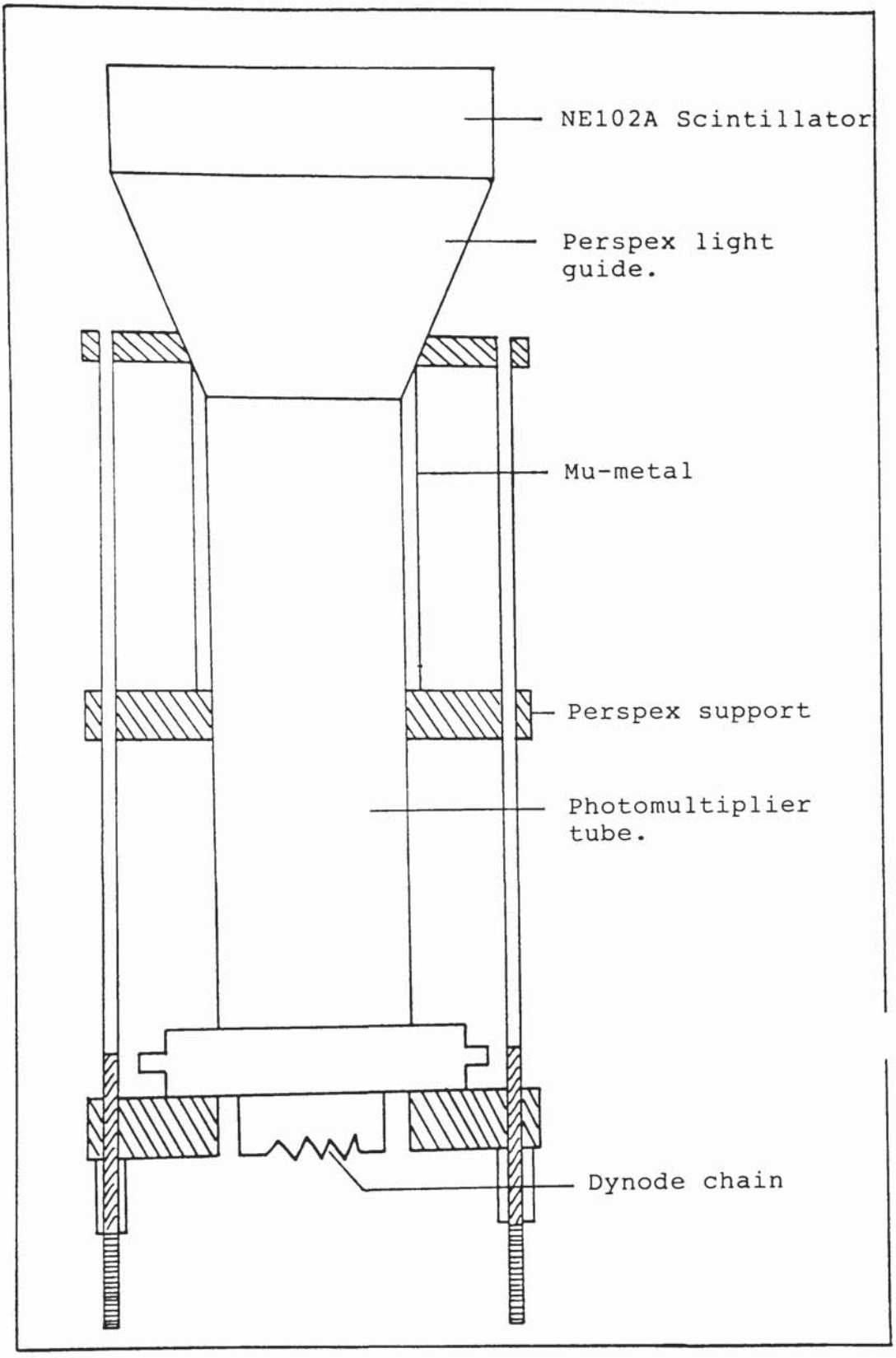

Figure (4.3):The scintillator-photomultiplier assembly.

line was the ORTEC 463 Constant Fraction Discriminator. The block diagram for measuring the discriminator level is shown in figure (4.4). The anode output of the photomultiplier was fed by a long coaxial cable via emitter follower into a NE4681 Scaler. The small ^{60}Co gamma-ray source was placed close in front of the detector. The count for a time interval of 1 minute was noted as a function of the discriminator level with 4 mV increments. The difference in the number of counts in 4 mV interval was calculated and plotted against intervals of discriminator setting as shown in figure (4.5). This histrogram represents the Compton spectrum of the ^{60}Co gamma-ray.

Various authors (77,84,85) give different opinions about the position of the Compton electron edge on the Compton distribution. Flynn et al (77) indicated that the channel number at which the Compton edge falls to one-half of it plateau value, is in fact, consistently (4 ± 1)% above the maximum Compton electron energy. Knock et al (85) stated that the peak of the Compton distribution was (4.9 ± 1.7)% below the Compton edge while the half-height was (11.7 ± 3.4)% above the Compton edge. However the channel location of the half-maximum on the Compton distribution was certainly dependent upon the resolution of the detector, photomultiplier tube and electronics of the spectrometer.

In the present work the Compton edge of ^{60}Co

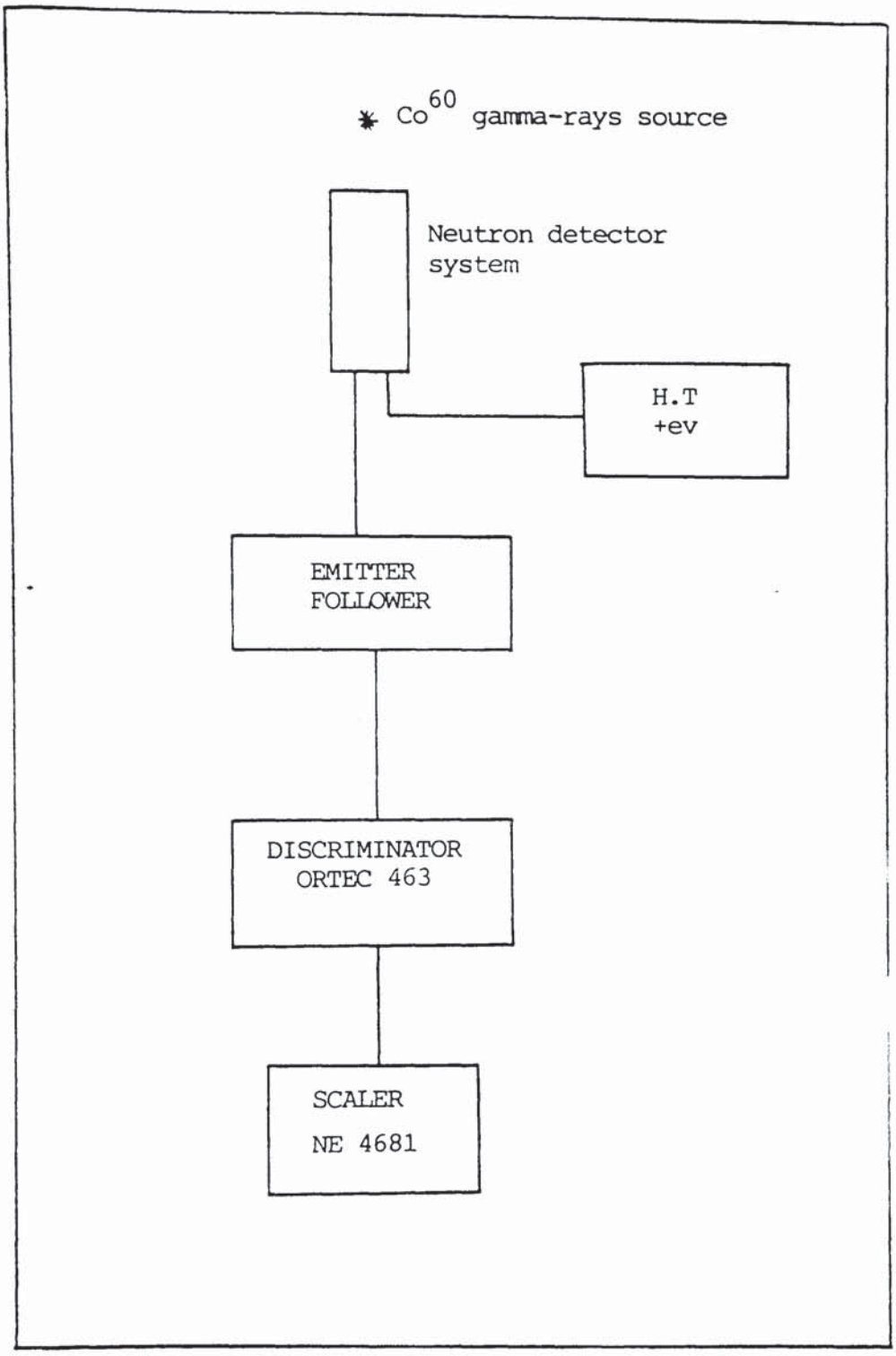

Figure (4.4):The block diagram of the electronics used to set the neutron discriminator level.

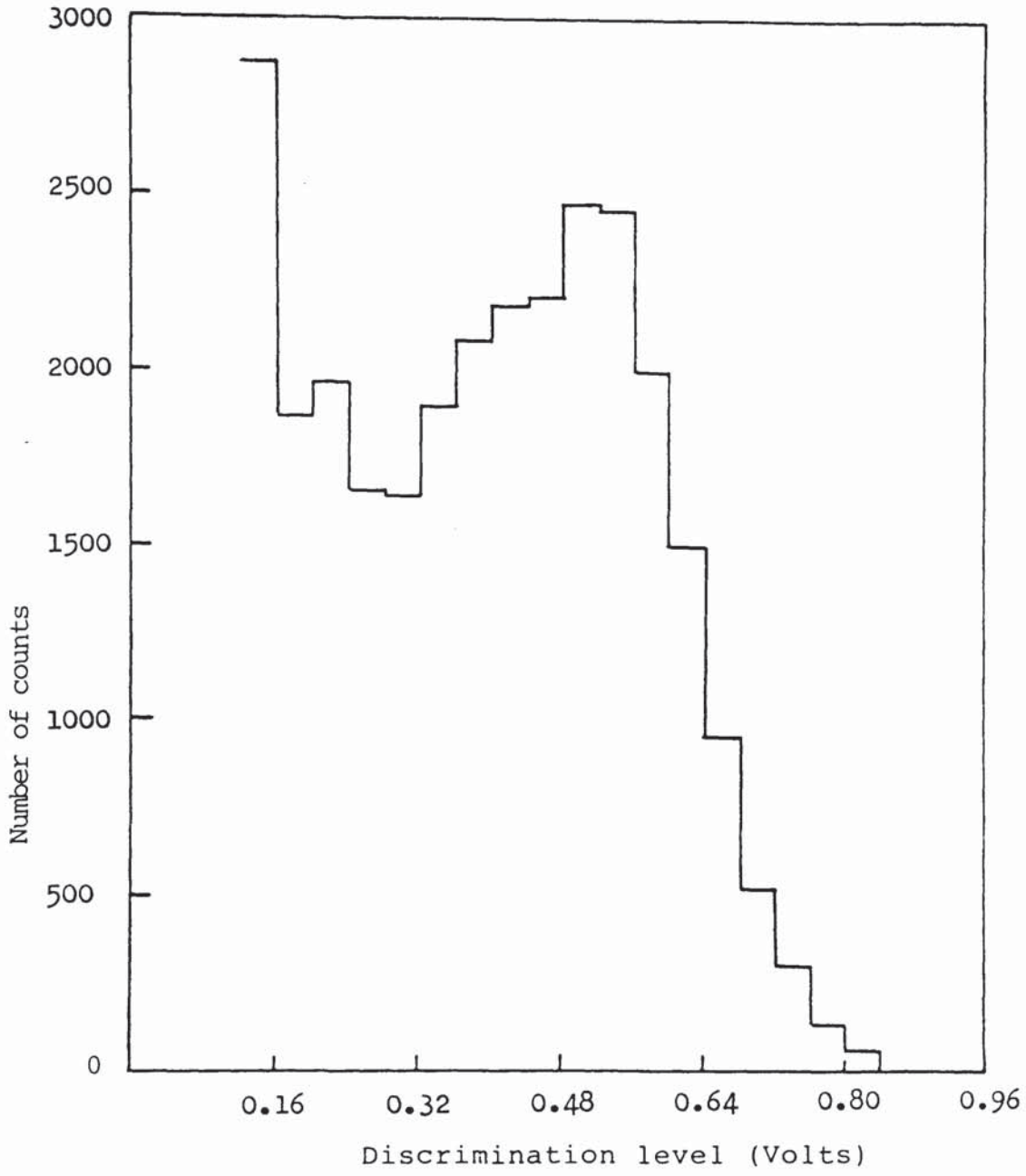

Figure (4.5):Compton spectrum for Co^{60} gamma-ray source

gamma-rays was chosen at a point where the count rate fell to one-half of its peak value. This value was determined as the discriminator level setting for the experiment.

4.1.4:SETTING THE ALPHA DISCRIMINATOR LEVEL.

In order to eliminate the undesired pulses below 3.5 MeV from the alpha-particle detection system, a 100 MHz discriminator ORTEC 436 was used. The block diagram for setting the discriminator level is shown in figure (4.6). The detector output pulse was amplified using the linear amplifier ORTEC 485. The negative discriminator pulses provided suitable gating pulses for the linear gate. As the discriminator level was increased, the linear gate was not open, hence the pulses below the discriminator level were blocked from the multichannel analyzer.

The pulse height spectrum of 3.5 MeV alpha-particle produced from $T(d,n)He^4$ reaction is shown in figure (4.7). The discriminator level as determined by the above method is shown in the figure.

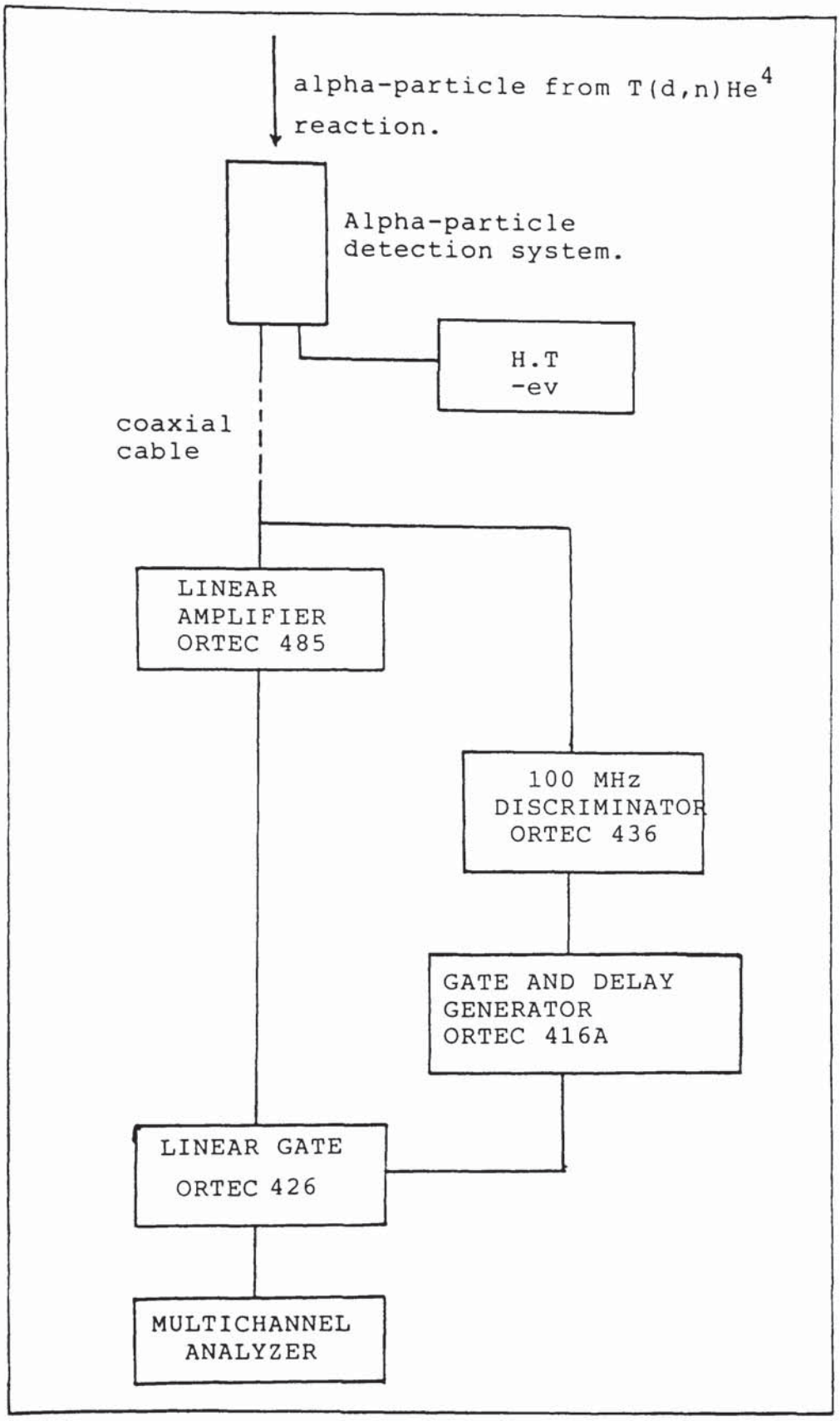

Figure (4.6):The block diagram of the electronics used to set the alpha-particle discriminator level.

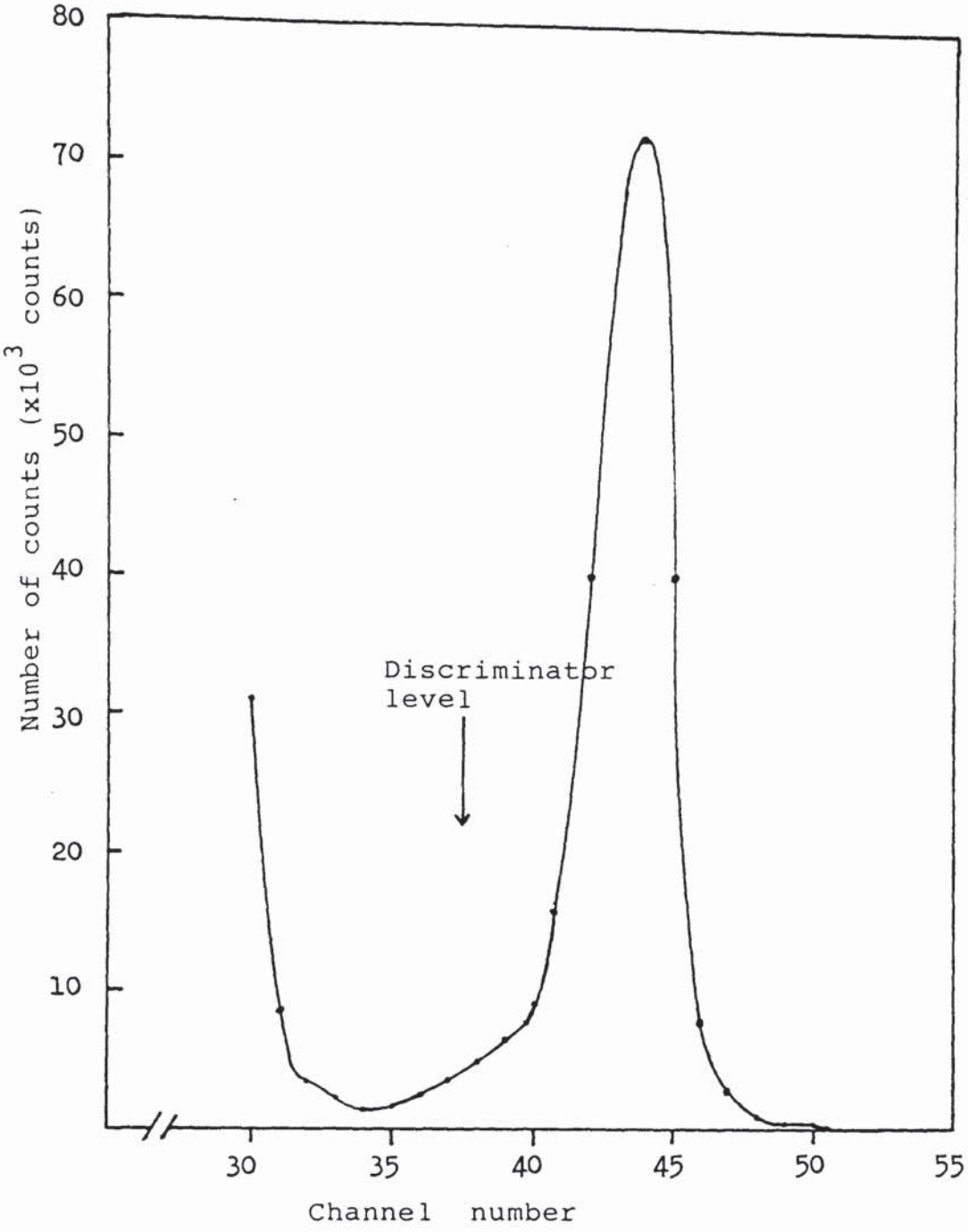

Figure (4.7):The alpha-particle pulse height spectrum from T(d,n)He^4 reaction.

4.2:THE ELECTRONICS OF THE ASSOCIATED PARTICLE TIME OF FLIGHT TECHNIQUE.

The electronics of the associated particle time of flight technique apparatus consists of fast timing circuits for the start and stop signal; a time to pulse height converter with a multichannel analyzer. The block diagram of the electronics used is shown in figure (4.8).

The time to pulse height converter is used to produce output pulses that are linearly proportional to the time delay between pairs of pulses fed successively to the start and stop signal. The time to pulse height converter used in this experiment was ORTEC 447 and the full scale time range made adjustable and had a variable time conversion range between (0-50) ns, (0-250) ns and (0-500) ns.

The anode pulses of the neutron photomultiplier was fed into a long coaxial cable through an emitter follower circuit. The emitter follower provides a suitable drive into the coaxial cable. The coaxial cable from the fast negative output of the anode of neutron photomultiplier tube was connected into the input of the constant fraction discriminator ORTEC 463. The constant fraction discriminator was set so that the only pulses whose amplitudes are higher than the threshold level can be accepted. The pulse at the discriminator output was then fed into the start of the time to pulse height converter.

The anode output of the alpha-particle

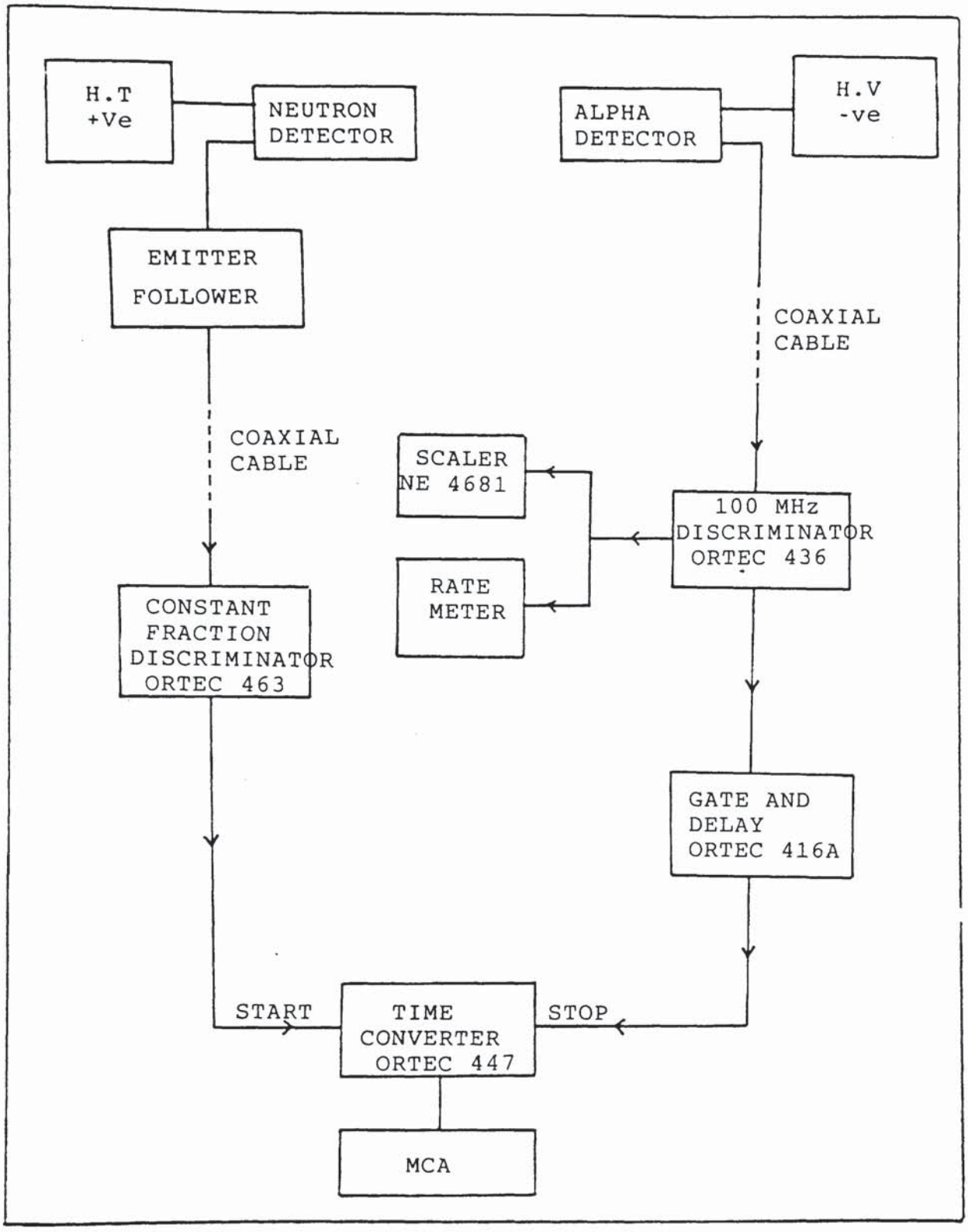

Figure (4.8):The block diagram of the electronics used in the associated particle time of flight technique.

photomultiplier tube was fed into a 100 MHz discriminator system ORTEC 436 through a long coaxial cable. The negative output of the discriminator was fed into a gate and delay generator ORTEC 416. The delayed signal was then be used to stop the time converter.

The output of the time converter was connected to the multichannel analyzer to collect the coincidence spectrum. The total number of alpha-particles was obtained by connecting the positive of the 100 MHz discriminator into a scaler NE 4681 and a ratemeter was also used as a guide to maintain constant output level.

4.3:THE SPECTROMETER PERFORMANCE.

4.3.1:TIME RESOLUTION OF THE SPECTROMETER.

By setting up the neutron and alpha discriminator level, the absolute time resolution of the spectrometer was tested by observing the direct neutron beam at θ_n = 83.5° using the electronics setup as described in section (4.2). Before the actual measurement was done, subsequent adjustments were made to give optimum time resolution and background condition.

The time resolution of the spectrometer was determined at the full width of the peak at half maximum amplitude (FWHM). It was found that the time resolution of the spectrometer depended on the repetition rate in the alpha channel (neutron yield) where the time resolution

increased from 2.0 ns at 30 kCount sec^{-1} to 3.0 ns at 100 kCount sec^{-1}. Therefore, in order to ensure the stability of the time resolution in the spectrometer, it was necessary to maintain a constant yield in the alpha channel throughout the experimental measurements.

By considering the background condition as well as the measurement time, the repetition rate of 55 kCount sec^{-1} was chosen to be used throughout the experimental measurements. The coincidence spectrum for a repetition rate of 55 kCount sec^{-1} was taken as shown in figure (4.9). The optimum time resolution was obtained as 2.2± 0.2 ns FWHM and the full width at 1/10 maximum was found to be 4.1 ± 0.4 ns.

In the associated particle time of flight technique the time resolution contributions in the neutron spectrum may be associated with three types of timing process:

(i) The time spread due to the finite neutron energy spread.

(ii) The time spread due to the variations in response time of neutron in the detector.

(iii) The time spread due to the variations in response time associated with the photomultiplier tube and the electronic equipment.

The neutron energy spread in the $T(d,n)He^4$ reaction has been discussed in section (2.6). It was shown that at $\theta_n = 83.5^\circ$ the neutron energy spread was about 100 keV with the most intense neutrons peaked at E_n

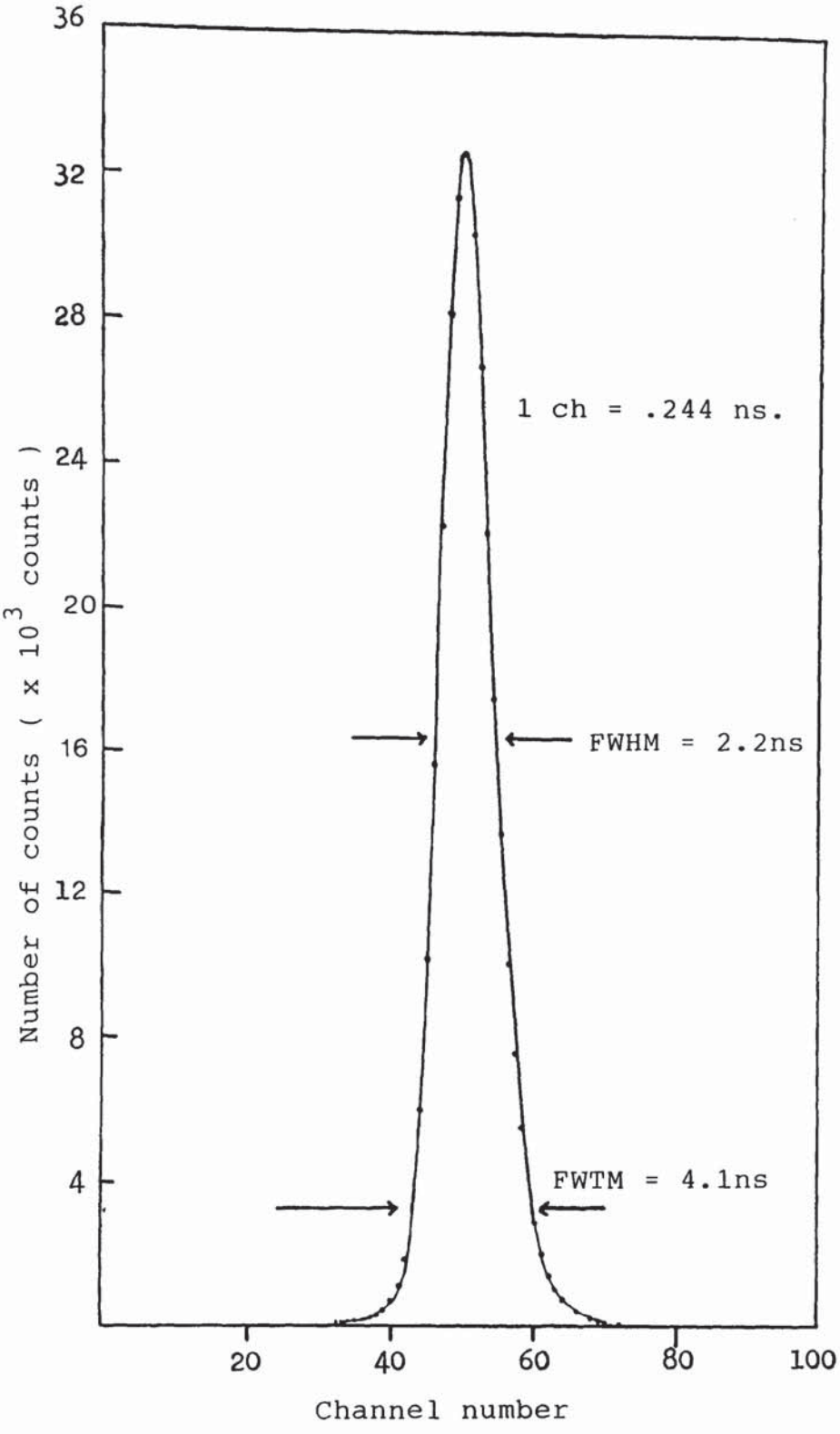

Figure (4.9):The time spectrum taken from direct neutron beam at $\theta_n = 83.5^{\circ}$.

= 14.1 MeV. The spread of neutron energy is possibly due to the following effects,

(a) The solid angle of alpha-particle detector with respect to the target.

(b) The scattering of deuterons and alpha-particle inside the target.

(c) The $T(d,n)He^4$ reactions occur at different deuteron energies, owing to the energy loss of the deuterons inside the target.

The spread due to the variations in response time of neutrons in scintillator detectors have been discussed by Moszynski et al (86). They stated that the process of nuclear radiation detection in the scintillator leads to several sources of time uncertainty and it can be summarized as follow,

(a) The energy transfer from the detected nuclear particles to the optical level in the scintillator.

(b) The finite decay time of light emitting states in the scintillator and the light yield of the scintillator as a function of the energy of the detected radiation.

(c) Variation of the time of light collection from the scintillator at the photocathode.

The processes stated above refer to the properties of the scintillator and they are reflected in the shape and intensity of the light pulse. However, if large scintillator is used the light collection process

influences significantly the light pulse shape (87,88). Self-absorption and re-emission processes are considered to increase the decay time constant of scintillator.

In the present work a perspex light guide was used in order to match the scintillator to the photomultiplier tube. The use of light guide will increase the spread in response time due to the fluctuations of the photon collection time on the photochathode.

The time resolution contributions in the photomultiplier tube have been discussed in details by Moszynski et al (86). The time resolution capabilities of photomultipliers are associated with,

(a) The variation of the transit time of electrons travelling from the photocathode to the anode. The dispersion of the electron transit time in a photomultiplier is considered due to the following sources of time uncertainty,

(i) The variation of the transit time of photoelectrons between a photocathode and a first dynode due to the different in initial velocity and emission angle of photoelectrons.

(ii) The variation of the transit time of photoelectrons emitted from different points of the photocathode.

(iii) The transit time spread from the secondary electrons between dynodes.

(b)The sensitivity of photocathode and the efficiency

of photoelectron collection on the first dynode. These characteristics will determined the numbers of photoelectrons released from the photocathode.

(c) Spread in gain of the electron multiplier which increases the pulse height distribution of output pulses.

The time spread in the electronic equipment is contributed by the intrinsic time resolution of the electronics, stability, time variation of time pick-off units and effect of electronic noise.

The minimum time resolution of 2.2 ns obtained from this spectrometer is due to the contributions to the time fluctuations from various causes as discussed above.

The energy resolution of the spectrometer can be estimated using equation (2.4). For 14 MeV neutron with Δt = 2.2 ns, the energy resolution was found to be 2.7 MeV.

4.3.2:THE BACKGROUND SUBTRACTION.

As the experimental measurements were done in the experimental area surrounded by concrete walls, the neutron detector shielding discussed in section (3.2.8) was essential. The block diagram of the experimental arrangement is shown in figure (4.10).

The coincidence spectrum of each sample was accumulated with the pulse height analyzer in the "ADD" mode for a fixed number of alpha-particle counts. The background radiations were subtracted by removing the sample and pulse height analyzer was set in the "SUB"

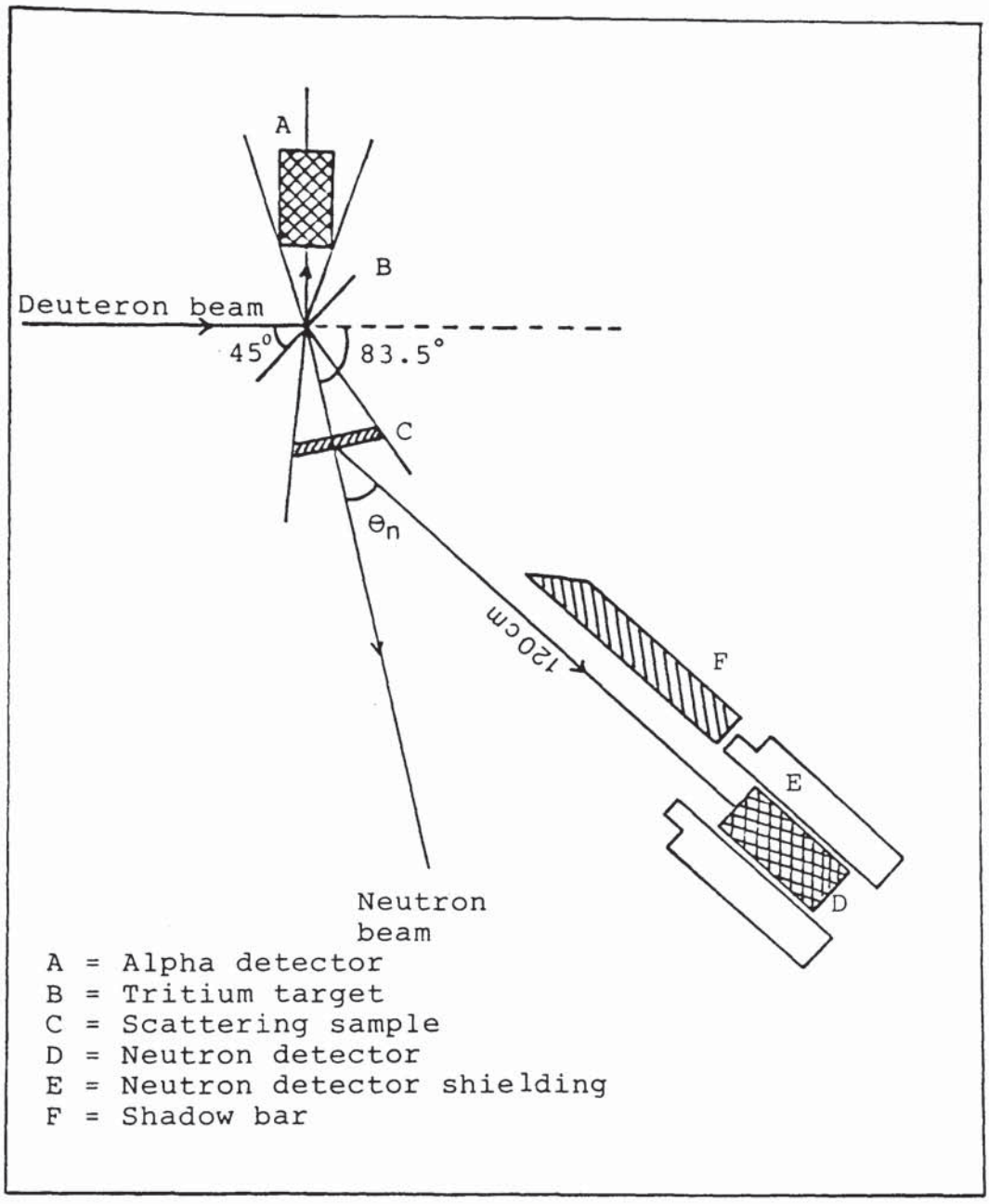

Figure (4.10):The experimental arrangement of the associated particle time of flight technique.

mode. The subtraction was done with the same number of alpha-patricle counts.

The total error of the number of counts σ_N in the coincidence spectrum was calculated by

$$\sigma_N = \left[\sum (\sigma_{Ni})^2 \right]^{\frac{1}{2}} \qquad (4\text{-}1)$$

Where,

$$\sigma_{Ni} = (A_i + B_i)^{\frac{1}{2}} \qquad (4\text{-}2)$$

A_i = the number of counts in "ADD" mode for i th channel,

B_i = the number of counts in "SUB" mode for i th channel.

4.4:MEASUREMENT OF THE ABSOLUTE DIFFERENTIAL CROSS SECTION

4.4.1:THE CROSS-SECTION OF NUCLEAR REACTION.

The probability of occurance of a particular collision process such as elastic scattering of a particle through a certain angle is conveniently expressed as a cross-section. The total cross-section σ_T of a nucleus is a measured of the reaction probability for all interaction processes; elastic and non-elastic processes.

Consider a parallel beam of n_o neutrons per cm^2 incident normally on a slab of material of thickness x containing N nuclei perunit volume as shown in figure (4.11). If the probability of any collision processes is determined by an area σ_T ascribed to each centre then for a single incident particle, the chance of collision in passing through the thin element dx of area A is given by

$$\frac{N\ A\ dx\,\sigma_T}{A} = N\,\sigma_T\,dx \qquad (4\text{-}3)$$

If each interaction removes the particle from the beam, then the change in intensity dn is described by the equation

$$-\frac{dn}{n} = N\,\sigma_T\,dx \qquad (4\text{-}4)$$

where the negative sign means that the intensity n decreases as the thickness x increases. Assuming $n = n_o$

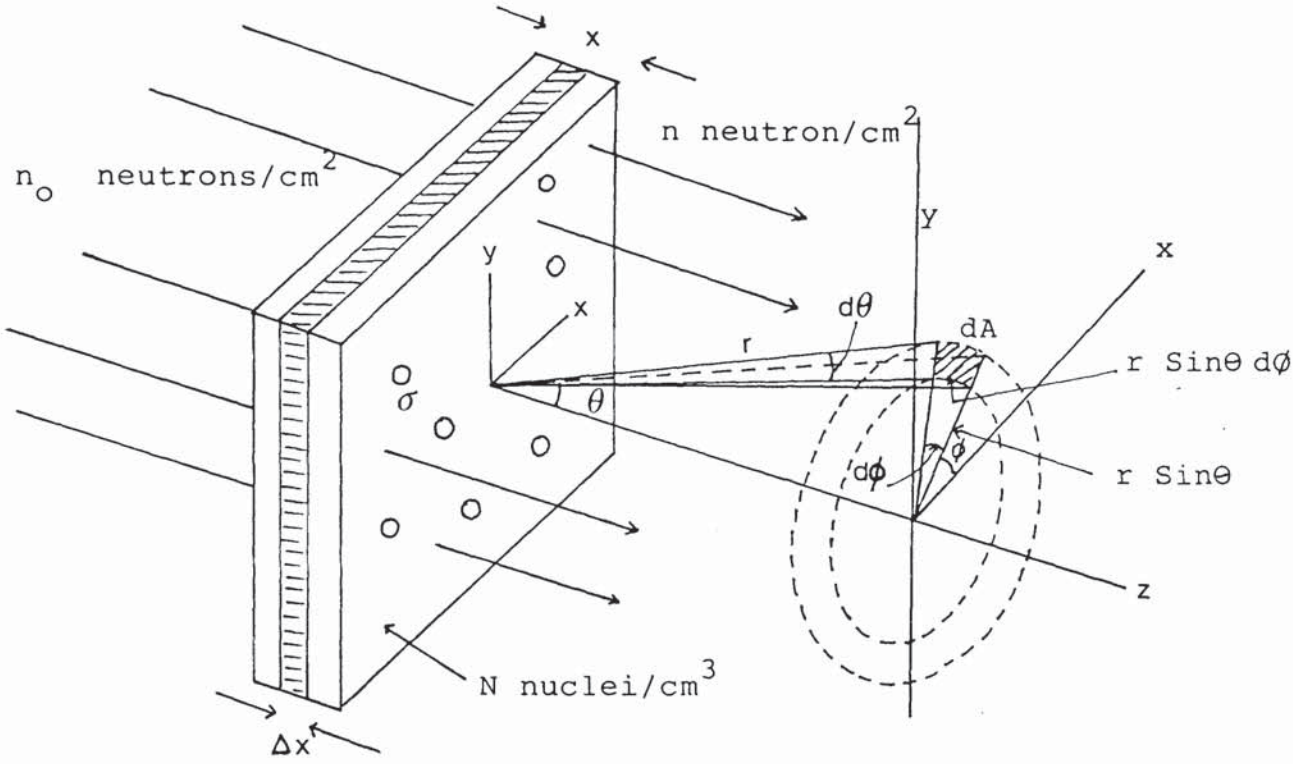

Figure (4.11):The concept of cross-section and the elements of the calculation of the solid angle $d\Omega$.

at t = 0 and integrating equation (4.4) gives the following equation

$$n = n_o e^{-N\sigma_T x} \qquad (4\text{-}5)$$

The number of interactions in the sample per unit time is then given by

$$n_o - n = n_o (1 - e^{-N\sigma_T x}) \qquad (4\text{-}6)$$

If we are only concerned with the neutron elastic scattering process, the total number of neutrons, N_e produced from the neutron elastic scattering is given by

$$N_e = n_o (1 - e^{-N\sigma_T x}) \frac{\sigma_e}{\sigma_T} \qquad (4\text{-}7)$$

where σ_e is the neutron elastic scattering cross-section.

4.4.2:THE DIFFERENTIAL CROSS-SECTION.

In many nuclear reactions, it was found that the outgoing particles will have an anisotropic distribution at different angle of emission. To make such calculations, another type of cross-section which is angular dependent, has to be taken into account. This cross-section is called the differential cross-section and is defined as the cross-section per unit solid angle.

The differential cross-section which is measured of the probability of radiation being emitted into an element

of solid angle $d\Omega$ at an angle Θ to the incident beam direction is given by

$$d\sigma = \sigma(\Theta)\, d\Omega \qquad (4\text{-}8)$$

The quantity $\sigma(\Theta)$ is measured in barns per steradian.

By integrating the differential cross-section over a solid angle Ω, the reaction cross-section is obtained as

$$\sigma = \int \sigma(\Theta)\, d\Omega \qquad (4\text{-}9)$$

The solid angle is given by

$$d\Omega = \frac{\text{Area}}{(\text{distance})^2} = \text{Sin}\ \Theta\ d\Theta\ d\phi \qquad (4\text{-}10)$$

The total solid angle is

$$\Omega = \int_{\Omega} d\Omega = \int_0^{2\pi}\int_0^{\pi} \text{Sin}\ \Theta\ d\Theta\ d\phi = 4\pi \qquad (4\text{-}11)$$

The total reaction cross-section σ over 4π solid angle can be found by combining equations (4-9) and (4-10) i.e

$$\sigma = \int_{4\pi} \sigma(\Theta)\, d\Omega = \int_{\phi=0}^{2\pi}\int_{\Theta=0}^{\pi} \sigma(\Theta)\ \text{Sin}\ \Theta\ d\Theta\ d\phi \qquad (4\text{-}12)$$

If the differential cross-section is independent of azimuth ϕ, about the incident beam direction, the ϕ integration gives 2π and

$$\sigma = 2\pi \int_0^{\pi} \sigma(\theta) \, \text{Sin}\, \theta \, d\theta \qquad (4\text{-}13)$$

where,

$\sigma(\theta) = d\sigma/d\Omega(\theta)$ is the differential cross-section.

If we are only concerned with the differential elastic scattering, the total number of elastically scattered neutron in solid angle $d\Omega$ and an angle θ is given by

$$N_e(\theta) = n_o \left[1 - \exp\left(-n\sigma_T x\right) \right] \frac{d\sigma}{d\Omega}(\theta) \frac{\Delta\Omega}{\sigma_T} \qquad (4\text{-}14)$$

where

n_o = the total number of incident neutrons on the sample.

$1 - \exp(-n\sigma_T x)$ = the fraction of the neutron beam interacting in the sample

σ_T = the total cross-section of neutron for the sample.

$d\sigma/d\Omega(\theta)$ = the differential elastic scattering cross-section for neutron on the solid angle $d\Omega$,

$\Delta\Omega$ = the solid angle.

Thus the neutron differential elastic scattering cross-section can be written as,

$$\frac{d\sigma}{d\Omega}(\theta) = \frac{N_e(\theta)\sigma_T}{n_o\left[1 - \exp\left(-n\sigma_T x\right)\right] . \Delta\Omega} \qquad (4\text{-}15)$$

In the absolute measurement of the differential

cross-section, the neutron detector counts have to be corrected for the detector efficiency to obtain the absolute neutron yield. By considering the efficiency of the detector $\epsilon(E_n)$, equation (4-15) become,

$$\frac{d\sigma}{d\Omega}(\Theta) = \frac{N_e(\Theta) \cdot \sigma_T}{n_o \, [1 - \exp(-n\sigma_T x)] \cdot \epsilon(E_n) \cdot \Delta\Omega} \qquad (4\text{-}16)$$

4.4.3:CORRECTIONS APPLIED TO THE DIFFERENTIAL CROSS-SECTION FORMULA.

In the actual experimental measurement, several factors have to be considered to calculate the differential cross-section using equation (4-16). The correction factors arise due to the geometrical arrangement of the target assembly and the angular spread of the neutron beam. These are discussed in the following sections.

4.4.3.1:ALPHA MONITOR BACKGROUND CORRECTION.

In this experiment, an alpha-particle scintillation detector was used to determine the total number of neutrons produced from $T(d,n)He^4$ reaction. Since the detector is also sensitive to both neutrons and gamma-rays, the alpha counts have to be corrected from the background radiations. The background radiations may be expected from two sources, i.e

(i) Background due to the detection of fast neutrons and radiations promptly emitted from the fast neutrons interaction with the materials of the target assembly.

(ii) Background due to the detection of gamma-rays and beta-particles resulting from the activation of the target assembly.

The background radiations from the fast neutrons and prompt radiations can be estimated by monitoring the

count-rate of the alpha-particle detector with an aluminium shield. It was shown by Baynham (83) that 0.02 mm of aluminium would stop 3.5 MeV alpha-particle. Therefore, using an aluminium plate with thickness 1mm as a shielding is sufficient to stop the 3.5 MeV alpha-particle. Aluminium also has low 14 MeV neutron reaction cross-sections and with small thickness, it only can produce a small amount of secondary radiations. Therefore by placing 1mm aluminium shield in front of the scintillator, only fast neutrons and radiations promptly emitted from the interaction of the target assembly will be detected by alpha-particle detector. With the same target current, the count-rate of alpha-particle detector is then noted without aluminium shield. The measurement was repeated for various target current to estimate the accuracy of the final results.

The difference between these two count-rates is estimated as the background correction due to this effect. The correction factor due to this effect was found to be

$$F_1 = 0.945 \pm 0.004.$$

The background due to the detection of radiations resulting from the activation of the target assembly can be estimated by measuring the alpha-particle count-rate immediately after switching off the deuteron beam, after the accelerator was run for a long time. The correction for this effect was estimated about 2% of the total

number of neutrons.

4.4.3.2:CORRECTION DUE TO THE ABSORPTION OF NEUTRONS IN THE TARGET ASSEMBLY.

The neutron beam from the $T(d,n)He^4$ reaction must pass through the materials in the target assembly before leaving the target assembly. The intensity of the defined incident neutron beam on the scattering sample was reduced due to the neutron elastic scattering and non-elastic reactions in escaping the target assembly. Due to this effect, the number of neutrons incident on the scattering sample should be corrected.

To estimate the correction factor due to this effect, the thickness and the cross-section of the materials in the target assembly where the neutrons have passed through should be considered. As discussed in section (3.1.2), the target assembly used in this work was made from copper and was water cooled. The 14 MeV neutron must pass through about 2.975 mm thickness of copper and 10 mm of water before leaving the target assembly. Using the cross-section data for copper (89) and H_2O (36), the fraction of the source neutrons escaping from the target can be calculated by the following formula,

$$F_2 = \exp - [\Sigma_{Cu} \cdot x_{Cu} + \Sigma_{H_2O} \cdot x_{H_2O}] \qquad (4\text{-}17)$$

where,

Σ_{Cu} = the macroscopic cross-section of copper,

x_{Cu} = the thickness of copper,

$\Sigma_{H_2O} = n_{H_2O} (2 \times \sigma_H + \sigma_O)$ = the macroscopic cross-section of water.

x_{H_2O} = the thickness of water.

The cross-section data used in this calculation are presented in table (4.1).

Table (4.1)

The total cross-section of Cu,H and O at 14 MeV neutron.

element	thickness (mm)	(barns)
Cu	2.98 ± 0.03	2.90 ± 0.06
H_2O O	10.00 ± 0.03	1.523 ± 0.002
H_2O H		0.646 ± 0.014

The correction factor F_2 was calculated as

$F_2 = 0.846 \pm 0.002$.

4.4.3.3:CORRECTION FOR SCATTERED NEUTRONS FROM THE SAMPLE.

The correction for scattered neutrons from the scattering sample is important in the cross-section measurements. This correction depends on the sample thickness and the detector angle to the neutron beam direction. In the present experiment, the sample was

positioned at right angles to the neutron beam direction. The scattered neutrons escaping at small scattering angle have minimum thickness of the sample to penerate, while neutron scattered at 90° have a maximum thickness to penetrate into the sample.

In order to estimate the correction due to this effect, consider the sample of thickness x_o positioned in the most intense part of the neutron beam of intensity ϕ_o, with the detector placed at an angle θ_n to the neutron beam direction (figure 4.12). A reduction of the neutron intensity will occur after traversing a thickness dx due to the interaction of neutrons within the sample. The fractional decrease in intensity is given by

$$-\frac{d\phi}{\phi_o} = n\,\sigma_T\,dx \qquad (4\text{-}18)$$

where,

n = the number of nuclei perunit volume of the scattering sample,

σ_T = the total cross-section of 14 MeV neutron in the scattering sample.

The intensity of neutrons transmitted through the sample of thickness x_o was obtained by integrating equation (4-18) and gives,

$$\phi(x_o) = \phi_o\, e^{-n\sigma_T x_o} \qquad (4\text{-}19)$$

Therefore, for neutrons traversing different paths

in the thick sample, the different values of $\phi(x_o)/\phi_o$ will be obtained. By dividing the sample into slices of 0.5 cm thickness and by drawing the sample-detector geometry, the path length of the neutron beam traveling in the sample at specific angle θ_n was estimated. The path length of each slice for specific angle was averaged and the fractional average of scattered neutron is then given by

$$C = \frac{\phi(x_o)}{\phi_o} = \frac{1}{N} \sum_{\Delta x=0.5}^{\Delta x=x_o} e^{-n \sigma_T \Delta x} \qquad (4\text{-}20)$$

where,

N = the total number of 0.5 cm slice in the sample,

Δx = the average neutron path in the sample.

The same procedure was then repeated separately for each thickness of the sample for each angle in the angular range studied. For the purpose of the calculation, the total neutron cross-sections of the samples under investigation were taken from BNL 325 (1). For fixed incident neutron energy, the total cross-section is nearly constant for fairly high mass number samples because the scattered neutron energy changes little as the angle is varied from 30^o to 90^o.

Figure (4.12) illustrates the sample geometry used to measure the path length of the scattered neutrons.

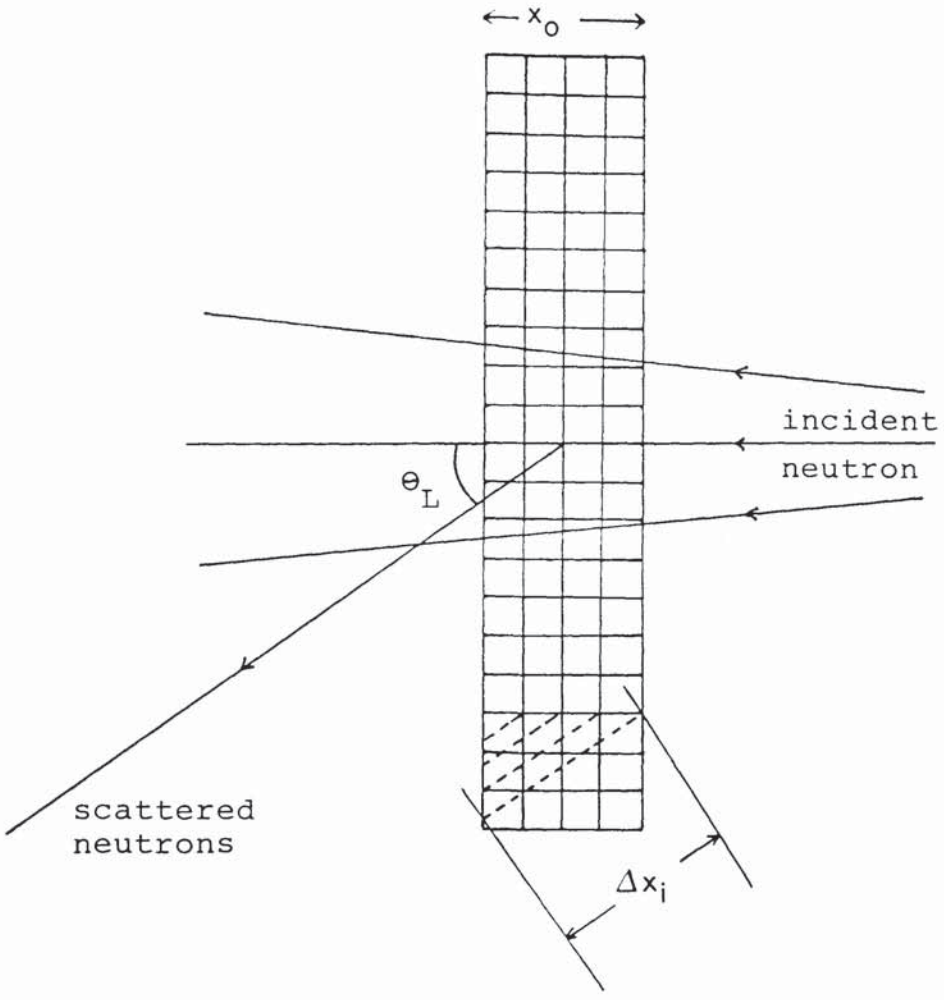

$$\Delta x = \frac{1}{N} \sum_{i=1}^{x_o} \Delta x_i$$

Figure (4.12):The sample geometry used to measure the path length (Δx) of the scattered neutrons from the sample.

4.4.3.4:SAMPLE THICKNESS CORRECTION.

Equation (4-16) used for calculating the differential cross-section was derived by assuming that a narrow parallel beam of neutrons is incident normally onto a uniform scattering sample. However, from the neutron beam profile (section 2.5), it was found that the neutron beam diverges from a point over an angular range of 12^{o} . Since the sample thickness varies with the angular range of the neutron beam, therefore, it was necessary to find the average of the weighted thickness of the scattering sample.

The weighted average thickness of the sample can be calculated by equation,

$$\bar{x} = \frac{\sum_i f_i x_i}{\sum_i f_i} \qquad (4\text{-}21)$$

where,

x_i = the sample thickness which depends on the neutron emission angle θ_n as shown in figure (4-13),

f_i = the weighting fraction, proportional to the area under the neutron beam profile curve in the 1^{o} interval denoted by i,

$\sum f_i$ = the total area under the neutron beam profile.

The weighted average sample thickness was evaluated using the neutron beam profile in figure (2.10). The neutron beam profile was divided up into 1^{o} intervals and the area under the curve was measured to calculate the

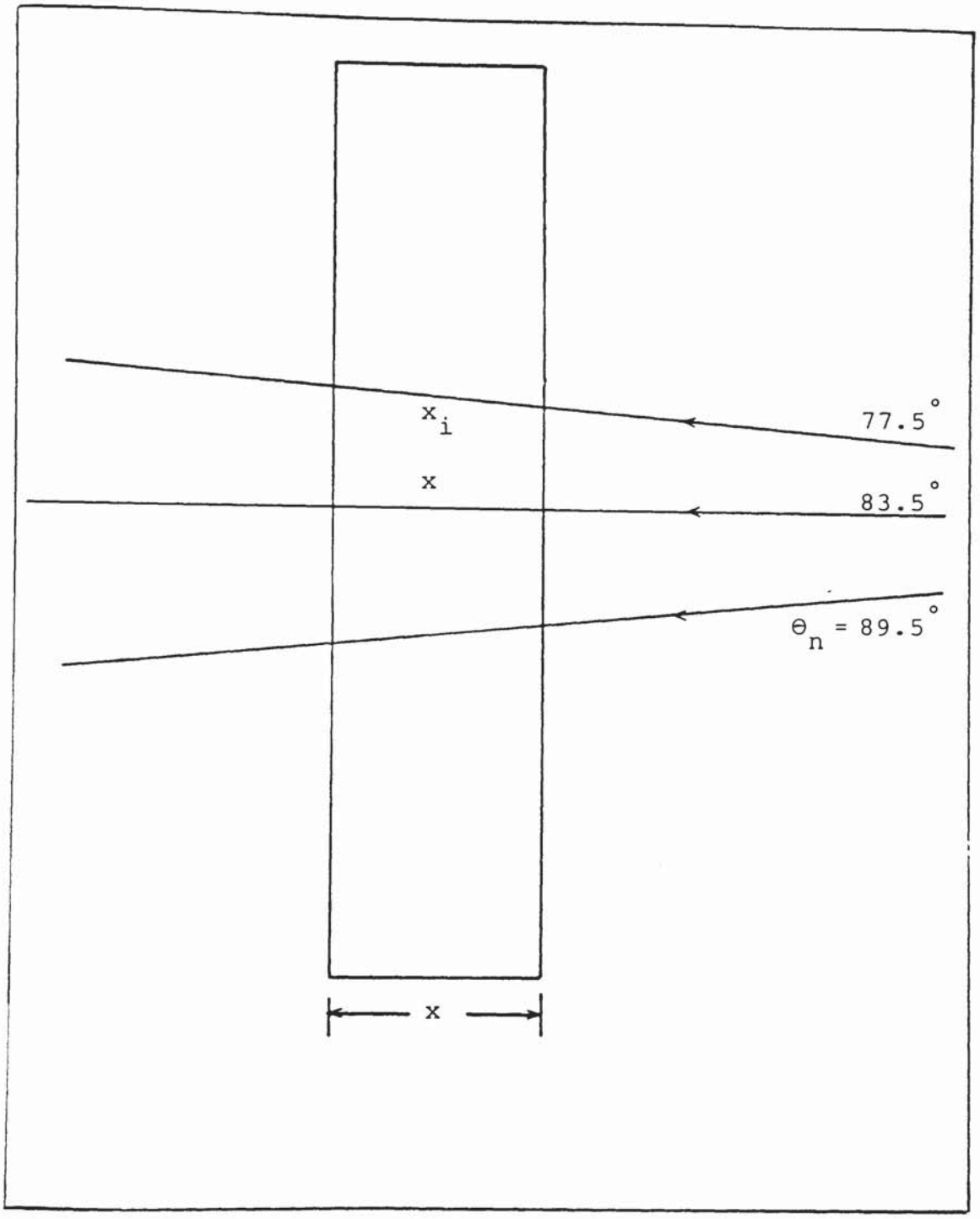

Figure (4.13):Calculation of the weighted sample thickness.

fraction of f_i . The weighted sample thickness was found to be

$$\bar{x} = x\ (\ 1.006 \pm 0.005)\ cm$$

where x is the actual sample thickness.

4.4.3.5:THE SOLID ANGLE.

By assuming a point source of neutron scattered from the sample, the solid angle subtended by neutron detector is given by

$$\Delta\Omega = \frac{A_D}{R^2} \text{ stradian} \qquad (4\text{-}22)$$

where,

A_D = the area of the neutron detector,

R = the distance between sample and detector.

4.4.4:FORMULA FOR DIFFERENTIAL CROSS-SECTION.

BY considering all the above correction factors, the differential scattering cross-section is calculated by equation

$$\frac{d\sigma}{d\Omega}(\Theta_L) = \frac{N_e(\Theta_L)\cdot\sigma_T}{n_o\cdot\epsilon(E_n)\cdot[1-\exp(-n\sigma_T\bar{x})]\cdot F_1\cdot F_2\cdot C\cdot\Delta\Omega} \qquad (4\text{-}23)$$

4.5 :DETERMINATION OF THE NUMBER OF COUNTS IN THE NEUTRON SPECTRA.

The neutron energy spectrum obtained in this experiment consists of a primary peak for neutron elastic scattering and secondary peaks for neutron inelastic scattering at the lower energy side. The peak position of the spectrum is used to determined the energy of the scattered neutron while the number of counts is determined from the area under the neutron profile. If the complicated effects of the background continuum and peak tailing are not significant or can be subtracted, the neutron profile can be represented by a Gaussian distribution. Since the neutron spectrum obtained in this work already had the background radiations subtracted the Gaussian function distribution can be represented to be used to determined the peak area under the neutron profile.

For the purpose of the peak area determination the accurate determination of Gaussian parameters such as positions, width, peak height and area of the peak are required. The calculation of this parameter are normally performed by a least squares method (79,90,91). The least squares fitting is made by minimizing the quantity called χ^2.

$$\chi^2 = \frac{1}{N} \sum_{i=1}^{N} \left[\frac{Y_i - Y(x_i)}{(\Delta Y_i)} \right]^2 \qquad (4\text{-}24)$$

where,

Y_i = the measured values at i th channel X_i ,

ΔY_i = the error due to Y_i ,

$Y(X_i)$ = the predicted values,

N = the number of channel.

More detail of the Gaussian fitting is illustrated in Appendix B together with the Computer Programme written in BASIC.

In order to examine the validity of the present method, a typical fitting of neutron spectra at 14 MeV scattered from Carbon was performed as shown in figure (4.14). The results obtained are listed in table (4.2).

Table (4.2)

The Gaussian parameters obtained from the fitting of neutron spectrum scattered from carbon

Reaction	Peak height	Area	σ	FWHM ns	χ^2
Q=0	317	3616	4.55	2.6	0.11
Q=4.43MeV	76	579	3.02	2.0	0.05

Because the data near the edge of the peak are subject to non-Gaussian distortions, the fit was done to the data points that lie at more than halfway up to the

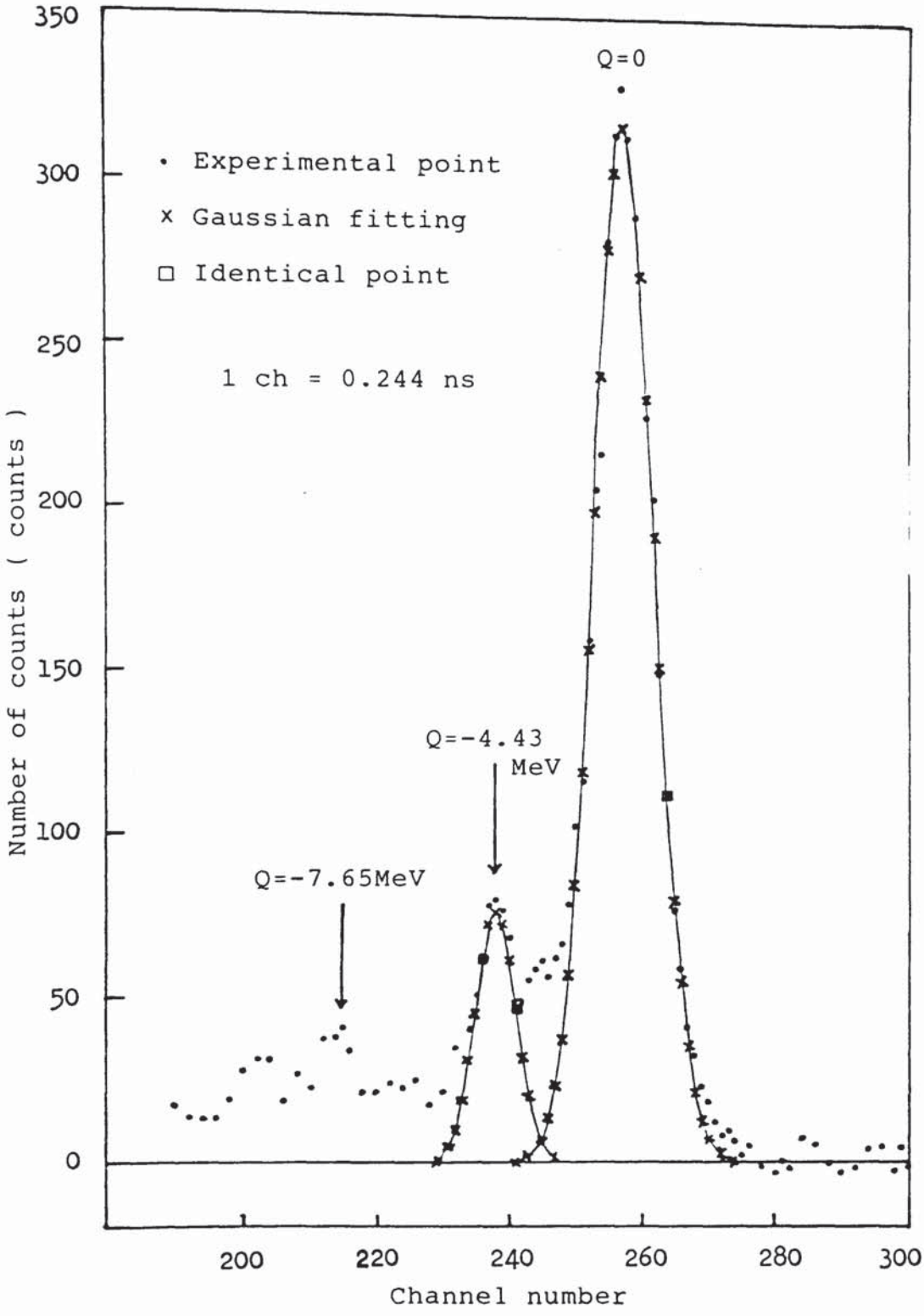

Figure (4.14):Time of flight spectrum of C^{12} at 14.1 MeV neutrons at scattering angle 30°.

peak.

For neutron spectrum obtained from scattered neutrons by aluminium, copper and molybdenum, the fitting was done to the data points at the right hand side of the spectrum up to the neutron peak because the left hand side of the spectrum included a contribution from the inelastic peaks of the exicited states. Using this procedure it was possible to strip off the contribution of the inelastic scattered neutrons in the elastic peak. A typical fitting of neutron spectra scattered from molybdenum is shown in figure (4.15) and the parameters obtained by this method are tabulated in table (4.3).

Table (4.3)

The Gaussian parameters obtained from the fitting of neutron spectrum scattered from molybdenum

Reaction	Peak height	Area	σ	FWHM ns	χ^2
Q = 0	260	1658	2.5	2.6	0.03

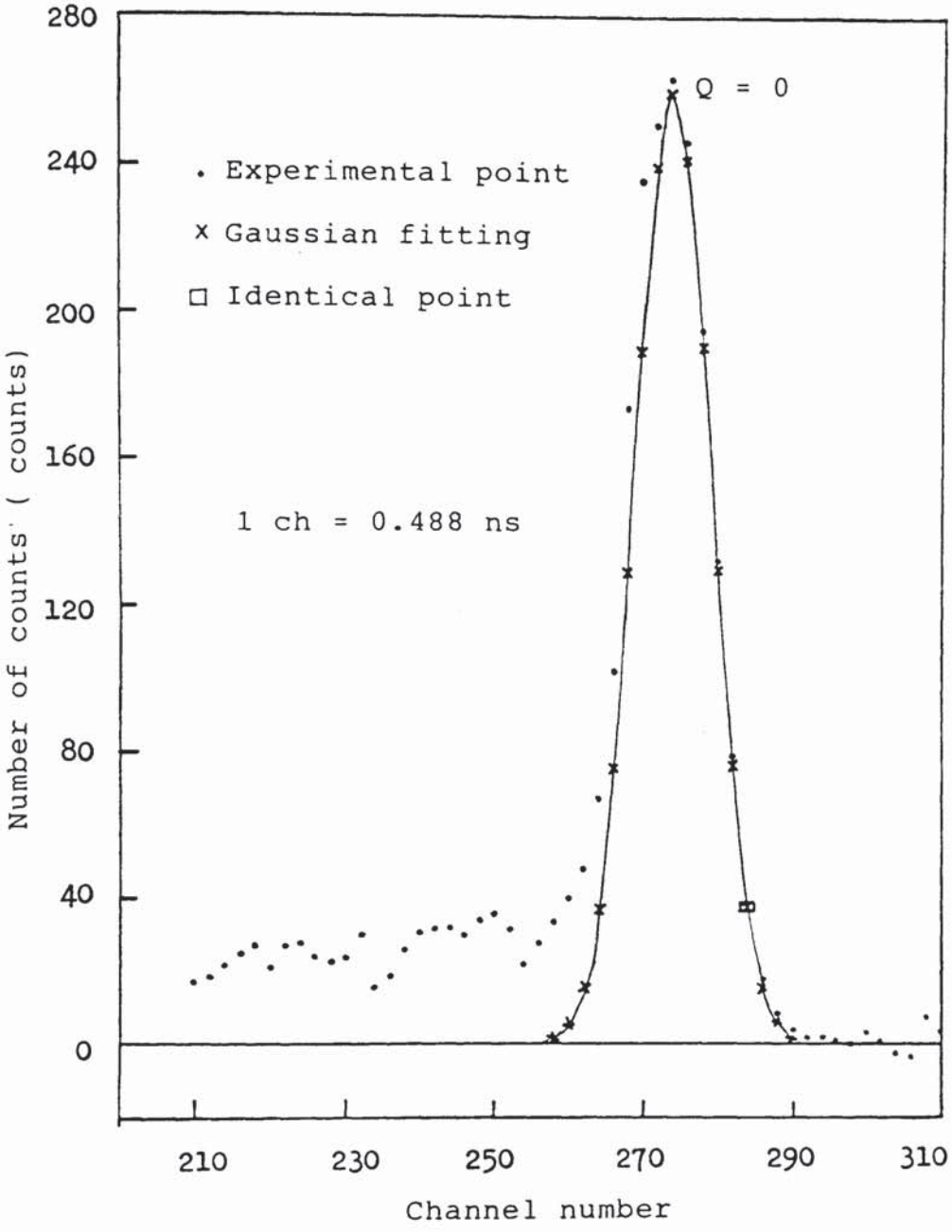

Figure (4.15):Time of flight spectrum of molybdenum at 14.1 MeV neutrons at scattering angle 35°.

4.6:NEUTRON DETECTOR EFFICIENCY MEASUREMENT.

The theoretical values for the absolute efficiency of the scintillation detector used in the present work were evaluated in sections (3.2.3) and (3.2.4). It is necessary to check and compare the theoretical values of the neutron detector efficiency by experimental measurements in order to provide the actual figure of the efficiency. In this work the neutron detector efficiency was measured experimentaly by two methods, i.e

(i) Absolute method

(ii) Relative method

4.6.1:THE ABSOLUTE DETECTOR EFFICIENCY MEASUREMENT.

In the absolute efficiency measurement, the accurate knowledge of the neutron flux is required. In the $T(d,n)He^4$ reaction adopted in the present work, the neutron flux produced from the reaction was measured by detecting the alpha-particles. Therefore, it is possible to determine the efficiency of the neutron detector by comparing the number of counts encounted in the neutron detector to the number of neutron indicated by the alpha-particle detector count.

The detector was placed close to the direct neutron beam at $\Theta_n = 83.5^{\circ}$ with a distance of 25 cm. Using the same electronic setup to that in the main experimental measurements (figure 4.8), the efficiency of the neutron detector was calculated by the following formula,

$$\epsilon = \frac{n_c}{n_o} \frac{d\Omega_\alpha}{d\Omega_n} \qquad (4\text{-}25)$$

where,

n_c = the total number of coincidences i.e the total counts under the neutron peak.

n_o = the total number of incident neutrons defined by alpha-particle detector,

$d\Omega_\alpha$ = the solid angle subtended by alpha detector aperture,

$d\Omega_n$ = the solid angle subtended by neutron detector.

The efficiency of neutron detector at 14.1 MeV was measured to be (9.96 ± 0.30) %. The error was mainly due to the statistical error in the neutron detector counts.

4.6.2:THE RELATIVE DETECTOR EFFICIENCY MEASUREMENT.

In the relative efficiency measurement, a standard sample with known differential elastic scattering cross-section can be used with the associated particle time of flight technique. The $^{1}H(n,n)H^{1}$ differential cross-section is useful standard because of the simple scattered neutron spectrum. However, carbon often appears in combination with hydrogen in the hydrogenous materials which made the neutron spectrum more complicated. ^{12}C has an accurately known differential cross-section making it suitable as a standard in the detector efficiency

measurement. The wide separation (4.43 MeV) of the ground state and the first exited state make C^{12} the better choice.

In this work, the relative efficiency of the neutron detector at energy lower than 14.1 MeV was determined by measuring the number of scattered neutron from carbon at detection angles of 30° and 80°, representing neutron energies 13.79 MeV and 12.28 MeV respectively. The carbon scatterer was in form of a flat plate of graphite with dimension of 15 cm x 20 cm and 1.0 cm thickness, gave a minimum multiple scattering contribution. The experimental arrangement and the electronics setup were similar to those in the main experiment in order to minimize some of the systematic errors.

Alternate runs were done with carbon scatterer positioned normal to the direct neutron beam, and without carbon scatterer in the subtraction mode in order to correct the background from direct neutrons beam and the other background radiations. Figure (4.14) shows the time spectrum of carbon scattered at 30°.

Using the correction factors discussed in section (4.4.3), the efficiency of the neutron detector was calculated using equation,

$$\epsilon(E_n) = \frac{N_e(\Theta) \cdot \sigma_T}{n_o \cdot F_1 \cdot F_2 \cdot C \cdot [1-\exp(-n\sigma_T \bar{x})] \cdot d\sigma/d\Omega(\Theta)} \quad (4\text{-}26)$$

where,

$d\sigma/d\Omega\ (\theta)$ = the differential elastic scattering cross-section for carb n at angle θ in the laboratory system,

σ_T = the carbon total cross-section.

The other terms are as previously defined.

For the purpose of the relative efficiency calculation, the neutron total and differential elastic scattering cross-section data for ^{12}C were taken from from ENDF-B4 (59). Figure (4.16) shows the differential elastic cross-section for 14 MeV neutrons on carbon in the centre of mass system.

The differential cross-section in the centre of mass system was converted into the laboratory system by the following formula,

$$\sigma(\theta_L) = \frac{(1 + \gamma^2 + 2\gamma \cos \theta_C)^{3/2}}{1 + \gamma \cos \theta_C} \sigma(\theta_C) \qquad (4\text{-}27)$$

where,

$$\theta_C = \theta_L + \sin^{-1}(\gamma \sin \theta_L) \qquad (4\text{-}28)$$

θ_C = centre of mass angle,

θ_L = laboratory angle,

$\sigma(\theta_C)$ = differential cross-section for elastic scattering in the centre of mass system,

$\sigma(\theta_L)$ = differential cross-section for elastic scattering in the laboratory system,

$\gamma = (M_1/M_2)$; M_1 is the mass of incident neutron

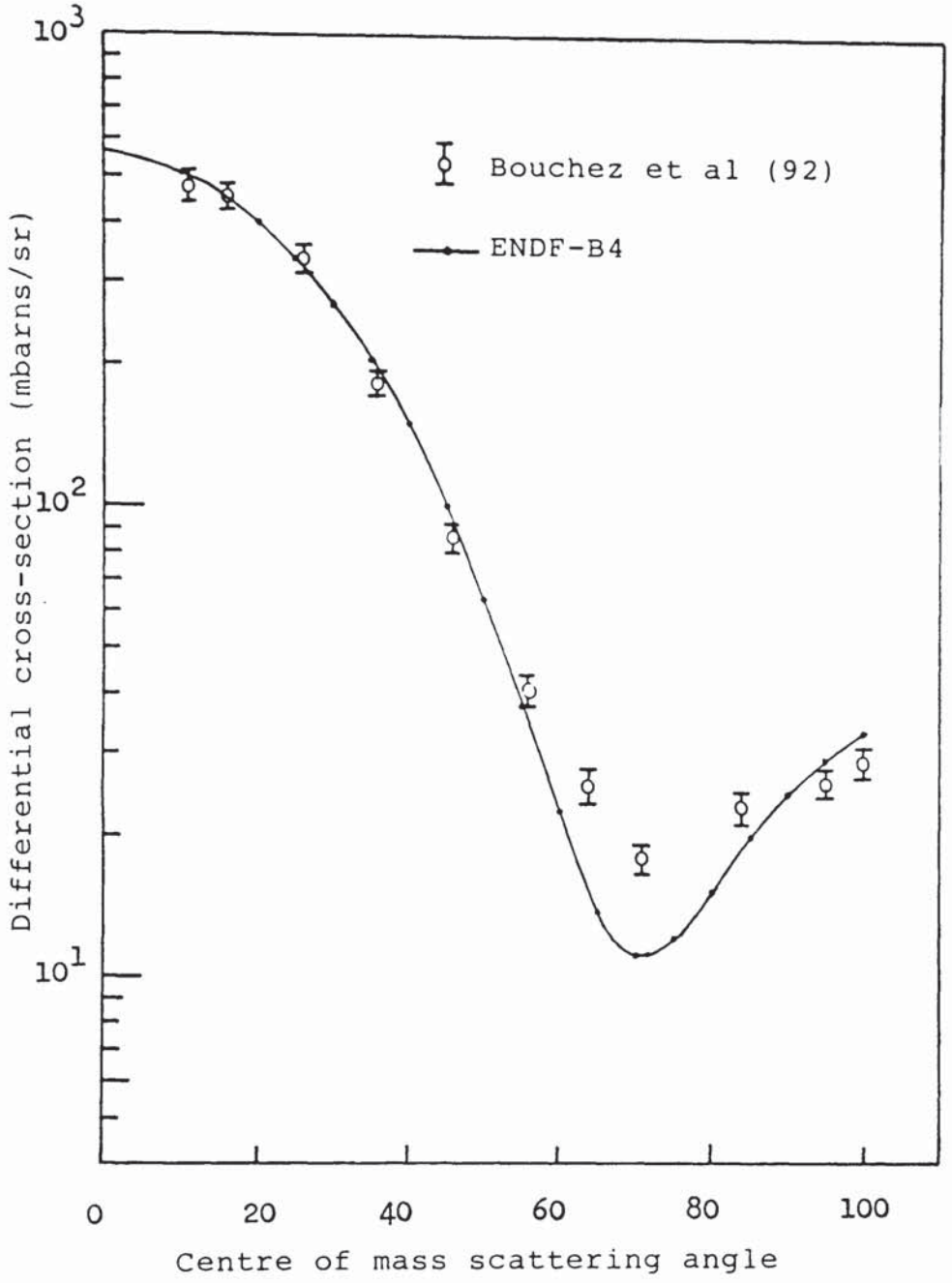

Figure (4.16):(n-C) differential cross-section as a function of scattering angle at 14.1 MeV neutrons in the centre of mass system.

and M_2 is the mass of the target nucleus.

Jasim (93) had measured experimentaly the efficiency of the neutron detector NE102A plastic scintillator for neutron energies 10.20 MeV, 8.20 MeV and 5.76 MeV using $^{1}H(n,n)H^{1}$ reaction from water scattered from 14.1 MeV at angles 30°, 40° and 50°. The results obtained are tabulated in table (4.4) together with the present experimental results.

table (4.4)

Neutron detector effociencies

Scatterer	Θ_L°	E_n (MeV)	$\epsilon(E_n)$ %	Author
Direct beam	0	14.10	9.96 ± 0.30	Present Work
C^{12}	30	13.97	9.80 ± 0.63	Present work
C^{12}	80	12.28	9.98 ± 1.11	Present work
H_2O	30	10.20	10.20 ± 0.29	Jasim (93)
H_2O	40	8.20	9.80 ± 0.30	Jasim (93)
H_2O	50	5.76	8.20 ± 0.30	Jasim (93)

Jasim (93) represented the neutron detector efficiency as a function of neutron energy by a polynomial fitting to his experimental data yielding equation,

$$\epsilon(E_n) = 8.66 \times 10^{-4} E_n^{3} f_2 - 7.78 f_1 \qquad (4\text{-}29)$$

where,

$$f_1 = 8.23 - 4.84\ E_n + E_n^2 \qquad (4\text{-}30)$$

$$f_2 = 937.159 - 48.708\ E_n + E_n^2 \qquad (4\text{-}31)$$

The neutron detector efficiency was plotted as a function of neutron energy as shown in figure (4.17). The figure shows that the present efficiency measurements are in good agreement with the data obtained from equation (4.28).

The errors contributed in the present measurements were calculated for each term in equation (4-26). The contributed errors for each term are tabulated in table (4.5).

Table (4.5)

Experimental errors for calculation of the detector efficiencies using equation (4-26)

Parameter	Estimate error (%)
$n_e(\Theta)$	4 to 10
σ_T	4.6
F_1	0.4
F_2	0.25
$\Delta\Omega$	0.8
$\bar{x}$	0.5
exponential	0.7

The experimental measurements of the neutron

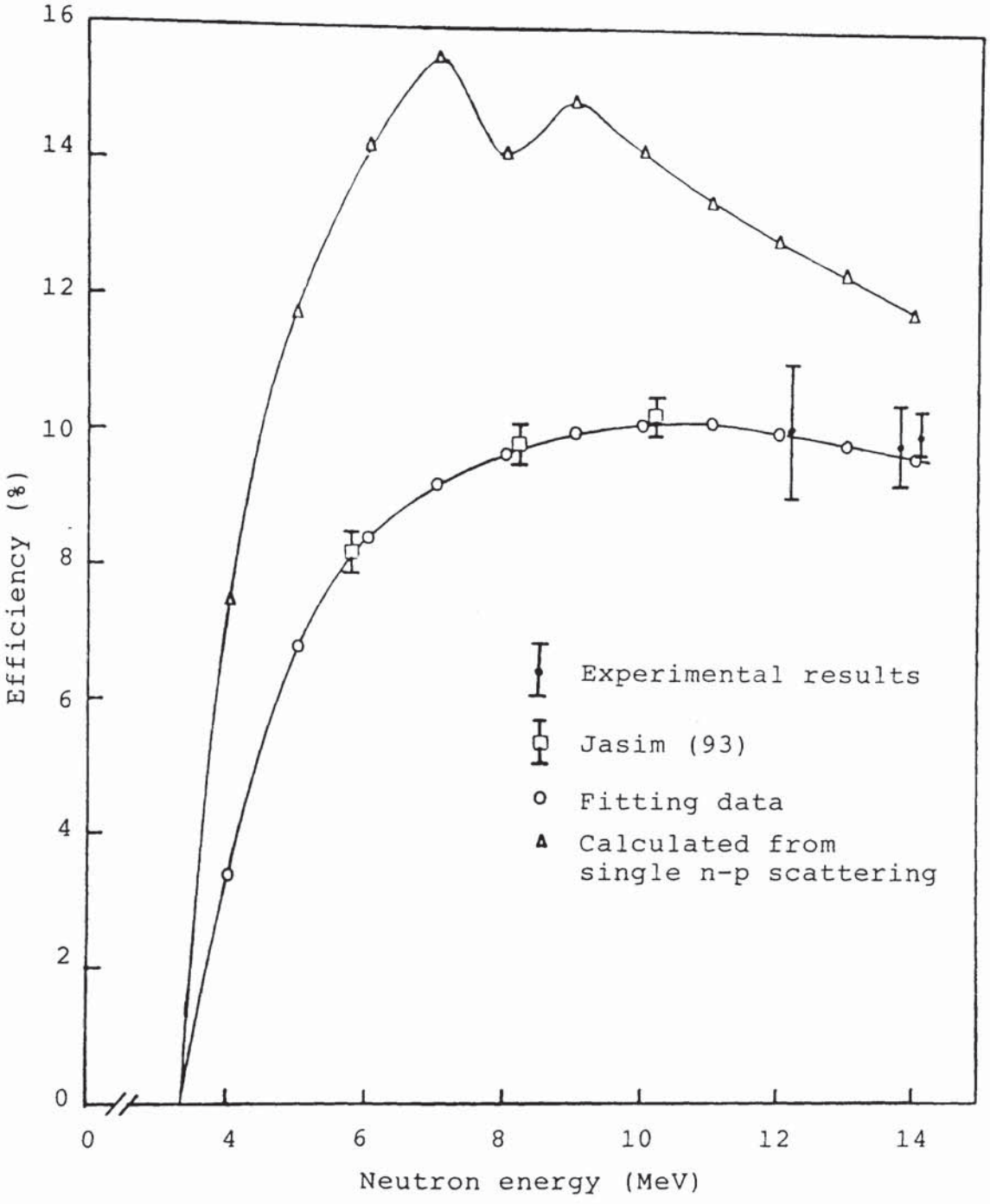

Figure (4.17):Neutron detector efficiency versus neutron energy.

detector efficiency are compared to the theoretical efficiency calculation based on the single scattering from hydrogen as shown in figure (4.17). There are some disagreement between two curves where the theoretical efficiencies are always higher than that the experimental measurements. This disagreement is possibly caused by the following factors,

(i) The theoretical efficiencies calculation was done without considering the existance of the light guide in the detector system. As discussed in section (4.1.2), the perspex light guide with 70 mm thickness was employed in order to match between 10 cm diameter of scintillator and 5 cm diameter of photomultiplier tube. The cross-sectional area of the light guide decreased from scintillator to photomultiplier tube and will result in some light loss and this reduced the detector efficiency. Because the scintillator and the light guide were not covered with a reflector, it might some light loss before reaching the cathode of the photomultiplier. In other words, the perspex light guide does not realy transmit light like a true light guide that uses total internal reflection.

(ii) The discrimination level of the neutron detector was set by determining the position of the Compton edge from the Co^{60} gamma-rays source where the half-height of the Compton peak was chosen to determine the bias setting. As discussed in section (4.1.3), there

is no such standard procedure to determine the position of the Compton electron edge on the Compton distribution. Therefore, it might be an error in determining the bias setting in the present experiment.

(iii) Some light loss in the photomultiplier tube especialy in the photocathode will also reduce the efficiency of the detection system.

The experimental measurements of the neutron detector efficiency were chosen to be used in the calculation of the differential cross-section. For the fixed incident neutron energy, the efficiency of the neutron detector are nearly constant for fairy heavy atoms in the scatterer because the scattered neutron energy changes little as the angle is varied from 30° to 90° . Therefore, the efficiency measured by the absolute method was used to calculate the differential scattering cross-sections for aluminium, copper and molybdenum.

CHAPTER 5

EXPERIMENTAL RESULTS

5.1:RESULTS FOR ALUMINIUM SAMPLE.

5.5.1:BACKGROUND OF THE SAMPLE.

The scattering samples of aluminium consist of Al^{27} isotope with 100 % abundance. Six different thicknesses of aluminium sample inform of flat plate geometry were investigated. The thicknesses and the dimensions of the samples used in the present work are listed in table (5.1).

Table (5.1)

Dimensions of the aluminium samples used in the present work

Sample Dimension (cm^2)	Sample Thickness	
	(cm)	m.f.p at 14 MeV
20 x 15	2.54	0.267
20 x 15	3.81	0.400
20 x 15	7.62	0.800
20 x 15	11.43	1.200
20 x 15	15.24	1.600
20 x 15	19.05	2.000

The experimental measurements of the differential cross-section were done using the electronic setup discussed in section (4.2) and the experimental arrangement as shown in figure (4.10). The time spectra were taken with the sample in position and the sample was removed for background subtraction for the same number of alpha counts. The sample-detector distance used in these measurements was 120.5 cm.

The typical time spectra of 14 MeV neutrons for scattering angles 30^{0}, 70^{0}, and 90^{0} in the laboratory system scattered from different thicknesses of aluminium sample are shown in figures (5.1), (5.2) and (5.3) respectively. The spectra mainly consist of a primary peak for neutron elastic scattering and secondary peaks for neutron inelastic scattering for the excited states of aluminium. The energy level diagram of Al^{27} is presented in figure (5.4).

The left hand side of the aluminium spectra is not well separated due to very close separation (0.844 MeV) between the ground state and the first excited state of the nuclei. However, using the Gaussian shape of elastic peak, the contribution of the inelastic scattered neutrons can be eliminated. The method of Gaussian fitting was discussed in section (4.5).

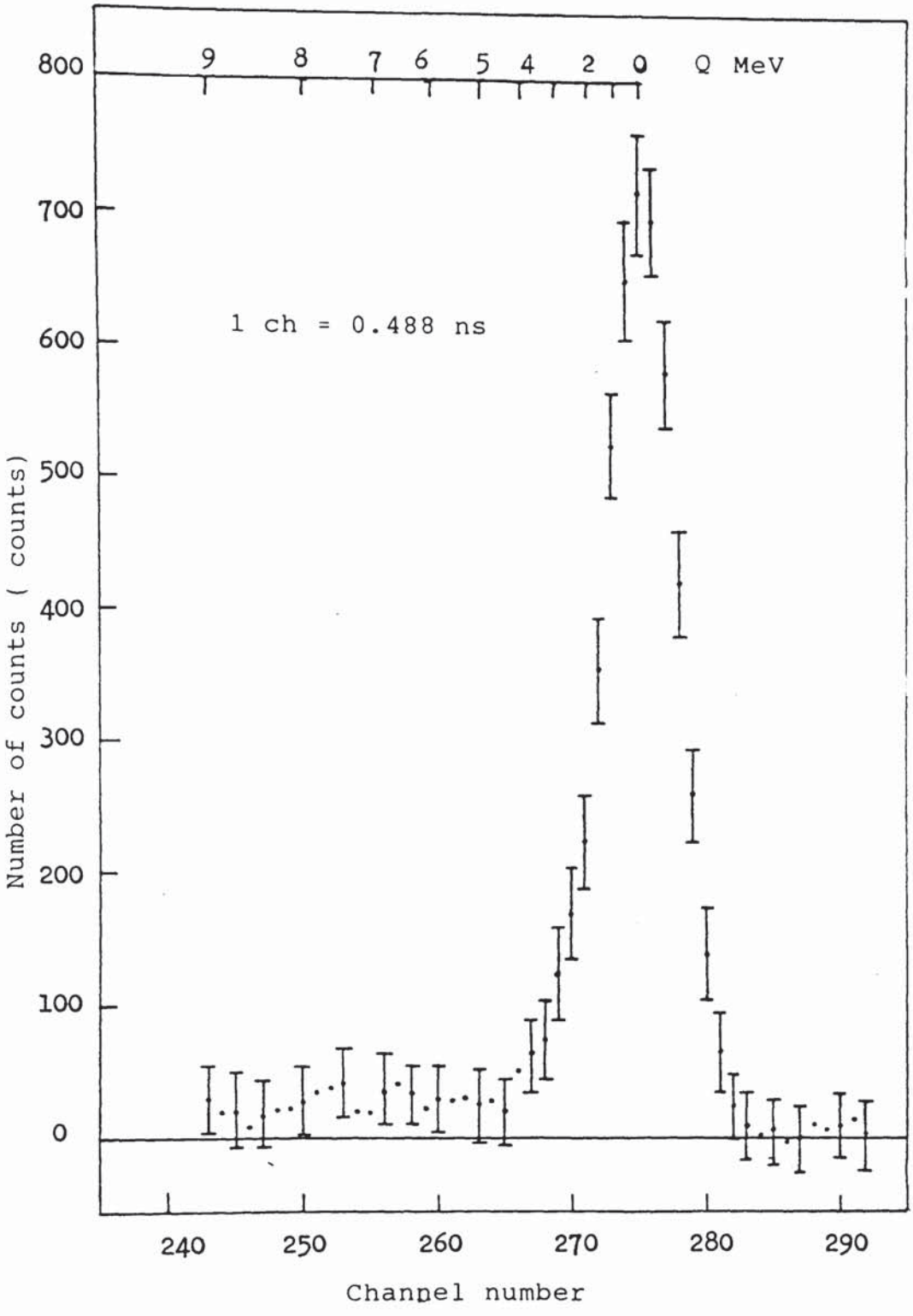

Figure (5.1):The time of flight spectrum of 14.1 MeV neutrons at 30° scattered from 2.54 cm thickness of aluminium.

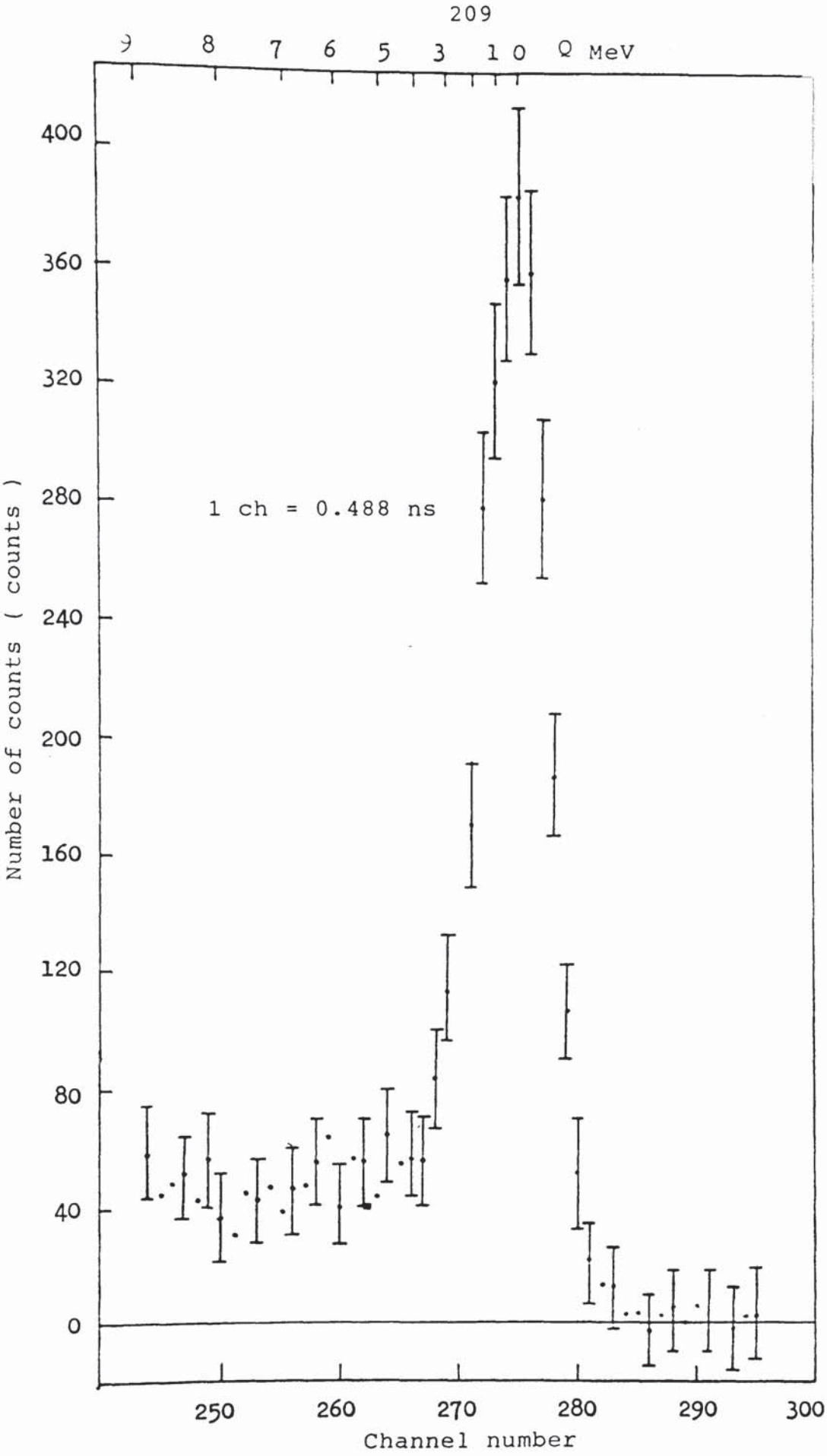

Figure (5.2):The time of flight spectrum of 14.1 Mev neutrons at 70° scattered from 11.43 cm thickness of aluminium.

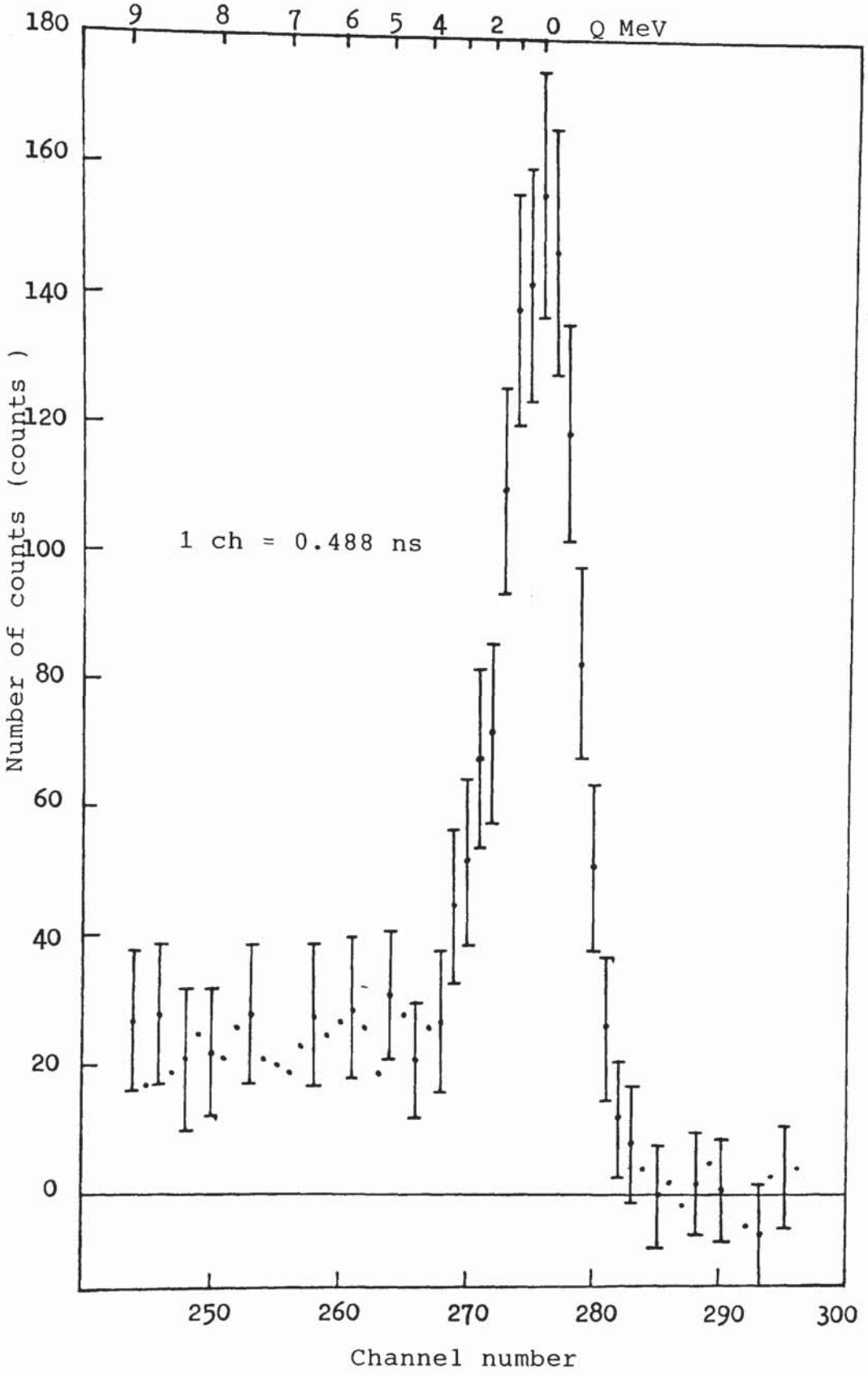

Figure (5.3):The time of flight spectrum of 14.1 MeV neutrons at 90° scattered from 15.24 cm thickness of aluminium.

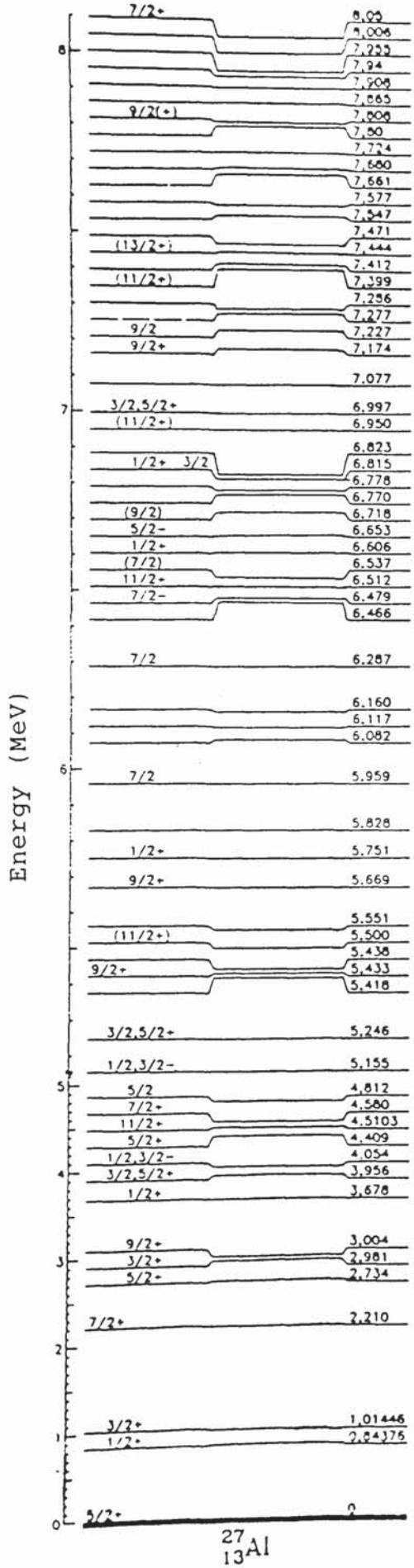

Figure (5.4): Energy level diagram of $^{27}_{13}Al$

5.1.2:EXPERIMENTAL DIFFERENTIAL ELASTIC CROSS-SECTION RESULTS.

Aluminium differential elastic scattering cross-sections for each sample thickness in the angular range between 30^{o} to 90^{o} were calculated using equation (4-23). The results in the laboratory system are tabulated in table (5.2).

Table (5.2)

Aluminium differential cross-sections for elastic scattering of 14.1 MeV neutrons in the laboratory system

θ (degree)	x (cm)	λ (m.f.p)	$d\sigma/d\Omega(\theta)$ mbarns/sr
30	2.54	0.267	138 ± 10
	3.81	0.400	184 ± 10
	7.62	0.800	208 ± 10
	11.43	1.200	238 ± 13
	15.24	1.600	257 ± 15
	19.05	2.000	282 ± 19
40	2.54	0.267	11 ± 4
	3.81	0.400	13 ± 3
	7.62	0.800	16 ± 3
	11.43	1.200	19 ± 3
	15.24	1.600	24 ± 3
	19.05	2.000	26 ± 4
50	2.54	0.267	20 ± 3
	3.81	0.400	27 ± 3
	7.62	0.800	24 ± 3
	11.43	1.200	29 ± 3
	15.24	1.600	32 ± 4
	19.05	2.000	34 ± 4
60	2.54	0.267	44 ± 4
	3.81	0.400	46 ± 4
	7.62	0.800	53 ± 4
	11.43	1.200	61 ± 4
	15.24	1.600	67 ± 5
	19.05	2.000	81 ± 6

Table (5.2):Continued

O (degree)	x (cm)	λ (m.f.p)	d /d (O) mbarns/sr.
70	2.54	0.267	43 ± 5
	3.81	0.400	45 ± 4
	7.62	0.800	49 ± 4
	11.43	1.200	61 ± 5
	15.24	1.600	66 ± 5
	19.05	2.000	77 ± 6
80	2.54	0.267	23 ± 5
	3.81	0.400	24 ± 4
	7.62	0.800	27 ± 3
	11.43	1.200	32 ± 3
	15.24	1.600	35 ± 3
	19.05	2.000	43 ± 4
90	2.54	0.267	15 ± 6
	3.81	0.400	15 ± 4
	7.62	0.800	19 ± 3
	11.43	1.200	21 ± 3
	15.24	1.600	27 ± 3
	19.05	2.000	28 ± 3

The errors indicated in the differential cross-sections were calculated by considering the errors in each term of the equation (4-23). The total error was mainly contributed from the counting statistic error on the number of neutrons scattered from the sample and it varies for different scattering angles and for different sample thicknesses. The errors estimated for each term of equation (4-23) are listed in table (5.3).

Table (5.3)

Experimental errors in the calculations of the differential elastic and inelastic scattering cross-sections in aluminium.

Factor	Estimated error (%)
F_1	0.4
F_2	0.3
$\Delta\Omega$	0.8
$\epsilon(E_n)$	0.3
$\bar{x}$	<1.0
$1-\exp(-n\sigma_T x)$	0.8 - 4.8
n_e	$(A_i + B_i)^{\frac{1}{2}}$
σ_T	2.3

The differential elastic cross-section data obtained from the experiment as a function of the laboratory scattering angle can be expressed in the form of a Legendre polynomial expansion (95),

$$\frac{d\sigma}{d\Omega}(\theta_L) = \sum_{l=0}^{l_{max}} a_l \; P_l \; (\cos \theta_L) \qquad (5\text{-}1)$$

where,

$$a_l = \frac{\sigma_{int}}{4\pi} (2l + 1) f_l \qquad (5\text{-}2)$$

$P_l (\cos\theta_L)$ = the l th Legendre polynomial in term of variable,

θ_L = the laboratory scattering angle,

σ_{int} = integrated scattering cross-section,

f_l = the l th Legendre polynomial coefficient.

The details of the Legendre polynomial expansion are illustrated in appendix C together with the computer programme written in FORTRAN.

The results for the differential elastic scattering cross-section were fitted with Legendre polynomial expansions which are shown as the smooth curves in figure (5.5). The Legendre polynomial coefficients are given in table (5.4).

Table (5.4)

Legendre polynomial coefficients for elastic scattering of 14.1 MeV neutrons from aluminium.

a_l	sample thickness (cm)					
	2.54	3.81	7.62	11.43	15.24	19.05
a_0	90.80	123.35	136.48	161.82	157.43	173.99
a_2	262.45	396.66	435.17	517.46	437.30	512.82
a_4	319.83	492.90	537.01	643.84	572.50	621.52
a_6	269.00	405.21	436.50	530.98	452.57	498.77
a_8	70.94	139.84	146.02	186.37	118.57	121.33
a_{10}	-	27.45	20.91	38.90	-	-

The maximum coefficients of order l_{max} were obtained by minimizing χ^2 defined as,

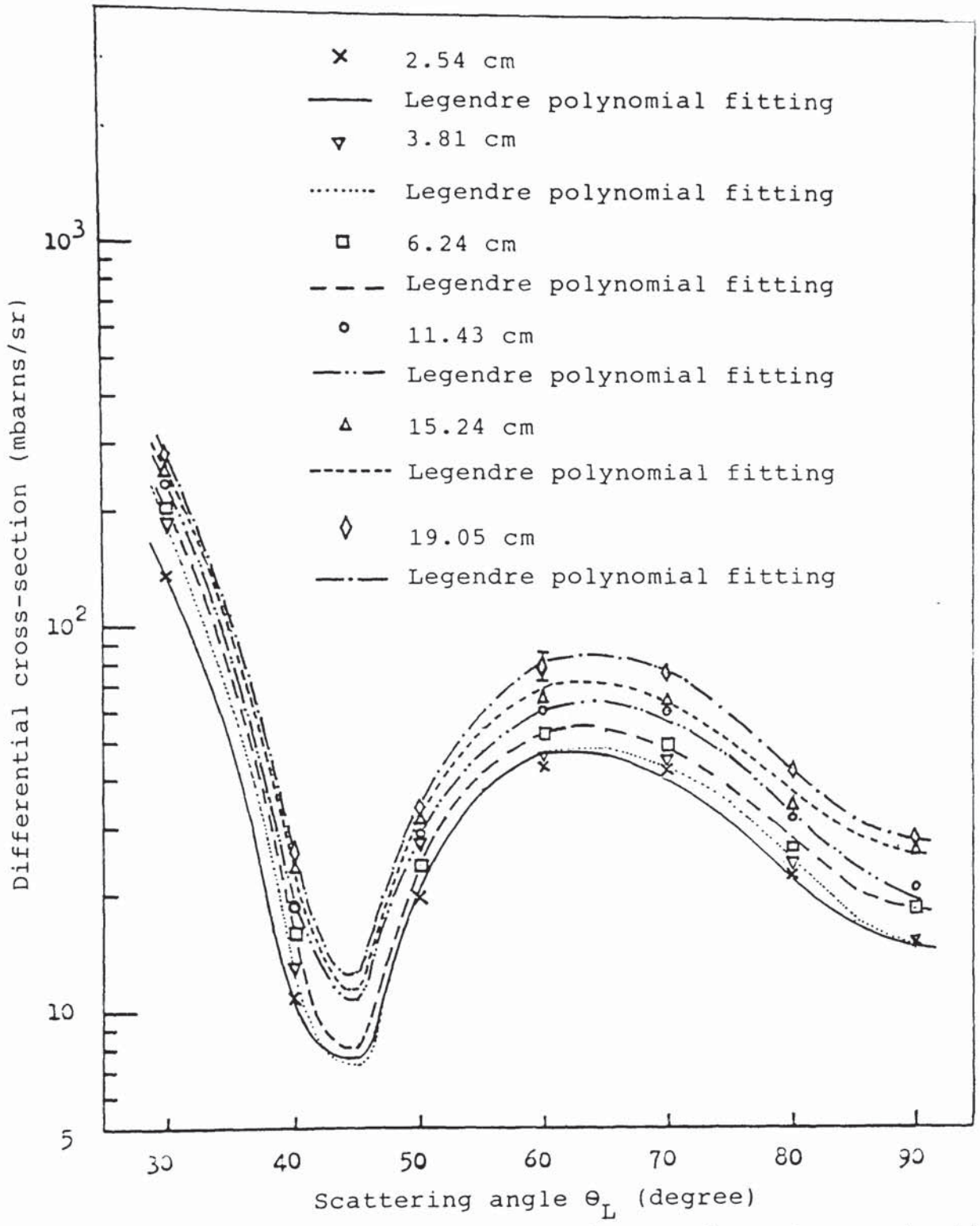

Figure (5.5):Angular distributions of neutron elastic scattering at 14.1 MeV neutrons for different thicknesses of aluminium.

$$\chi^2 = \frac{1}{N} \sum^{N} \left\{ \frac{\left[\frac{d\sigma}{d\Omega}(\theta)\right]_{exp} - \left[\frac{d\sigma}{d\Omega}(\theta)\right]_{cal}}{\left[\frac{d\sigma}{d\Omega}(\theta)\right]_{exp}} \right\}^2 \qquad (5\text{-}3)$$

where,

$\left[\frac{d\sigma}{d\Omega}(\theta)\right]_{exp}$ = the experimental differential cross-section,

$\left[\frac{d\sigma}{d\Omega}(\theta)\right]_{cal}$ = the calculated differential cross-section,

$\left[\frac{d\sigma}{d\Omega}(\theta)\right]_{exp}$ = the error of the differential cross-section,

N = the number of data fitted.

The best fitting for the aluminium differential elastic cross-section data were obtained by specifing only even terms in the polynomial.

The integrated elastic scattering cross-section between 30° to 90° angular range can be calculated by equation;

$$\sigma_{int} = \int_{\pi/6}^{\pi/2} \frac{d\sigma}{d\Omega}(\theta)\, d\Omega \qquad (5\text{-}4)$$

The solid angle $d\Omega$ is defined as,

$$d\Omega = 2\pi \sin\theta\, d\theta \qquad (5\text{-}5)$$

Therefore, equation (5-4) can be written as,

$$\sigma_{int} = \int_{\pi/6}^{\pi/2} \frac{d\sigma}{d\Omega}(\theta) \text{ Sin } \theta \, d\theta \qquad (5\text{-}6)$$

Using the numerical integration, the integrated elastic scattering cross-section becomes,

$$\sigma_{int} = 2\pi \sum_{i=\pi/2}^{i=\pi/2} \frac{d\sigma}{d\Omega}(\theta)_i \text{ Sin } \theta_i \quad \Delta\theta \qquad (5\text{-}7)$$

In the present work, the integrated elastic scattering cross-sections for each thickness of aluminium sample were calculated using equation (5-7) with 5^o intervals by trapezoidal method. The differential cross-section data were taken from the Legendre polynomial fitting. Table (5.5) shows the integrated elastic scattering cross-sections for six different thicknesses of aluminium.

Table (5.5)

The calculated integrated elastic scattering cross-sections between 30^o to 90^o angular range for different thicknesses of aluminium in the laboratory system

Sample thickness (cm)	σ_{int} (30^o-90^o) mbarns/sr
2.54	177 ± 9
3.81	192 ± 8
7.62	219 ± 7
11.43	257 ± 8
15.24	288 ± 9
19.05	329 ± 10

5.1.3:THE VARIATION OF THE DIFFERENTIAL ELASTIC CROSS-SECTION WITH SAMPLE THICKNESS.

Due to the effect of multiple scattering of the incident neutrons in the sample, the measured differential elastic scattering cross-sections for each scattering angle increased with increasing sample thickness as shown in table (5.2). The effective increase in the differential cross-section indicated an increase of the probability of the neutron scattering interactions in the sample with increasing sample thickness.

The variation of the differential cross-section of 14.1 MeV neutrons as a function of the sample thickness of iron had been studied by Anvarian et al (96) and Jasim (93) for lithium and lead samples. They represented the variation of the differential cross-sectian with sample thickness in an equation of exponential form;

$$\left[\frac{d\sigma}{d\Omega}(\theta)\right]_t = \left[\frac{d\sigma}{d\Omega}(\theta)\right]_o . e^{\alpha t} \qquad (5\text{-}8)$$

where,

$\left[\frac{do}{d\Omega}(\theta)\right]_t$ = the measured differential cross-section, for thickness t at scattering angle θ ,

$\left[\frac{do}{d\Omega}(\theta)\right]_o$ = the differential cross-section at a scattering angle θ as the sample thickness approaches zero,

α = a constant,

t = the sample thickness in unit of mean free path.

Equation (5-8) can be represented as a straight line by taking the logarithm;

$$\log_e \left[\frac{d\sigma}{d\Omega}(\Theta)\right]_t = \log_e \left[\frac{d\sigma}{d\Omega}(\Theta)\right]_t + \alpha\, t \qquad (5\text{-}9)$$

By using the least square method, the constant α can be determined.

In the present work the aluminium differential elastic scattering cross-section data for each scattering angle, for six different thicknesses of aluminium sample were fitted using a least squares fitting programme as shown in appendix D. The values of constant α obtained from the fitting for each scattering angle are shown in table (5.6). From the table, it is shown that the values of α are nearly constant for each scattering angle in the angular range studied. The average value of constant α was determined as,

$$\alpha = 0.36 \pm 0.08 \ (\text{m.f.p})^{-1}$$

Figure (5.6) shows the variation of the $\log_e\left[\frac{d\sigma}{d\Omega}(\theta)\right]$ as a function of mean free path thickness for each scattering angle. The solid lines appear in the figure were plotted using the average value of α.

Table (5.6)

The values of α obtained from the least square fitting for each scattering angle

angle (deg)	α (m.f.p)$^{-1}$
30	0.33 ± 0.04
40	0.45 ± 0.12
50	0.33 ± 0.08
60	0.34 ± 0.05
70	0.33 ± 0.06
80	0.35 ± 0.08
90	0.37 ± 0.11

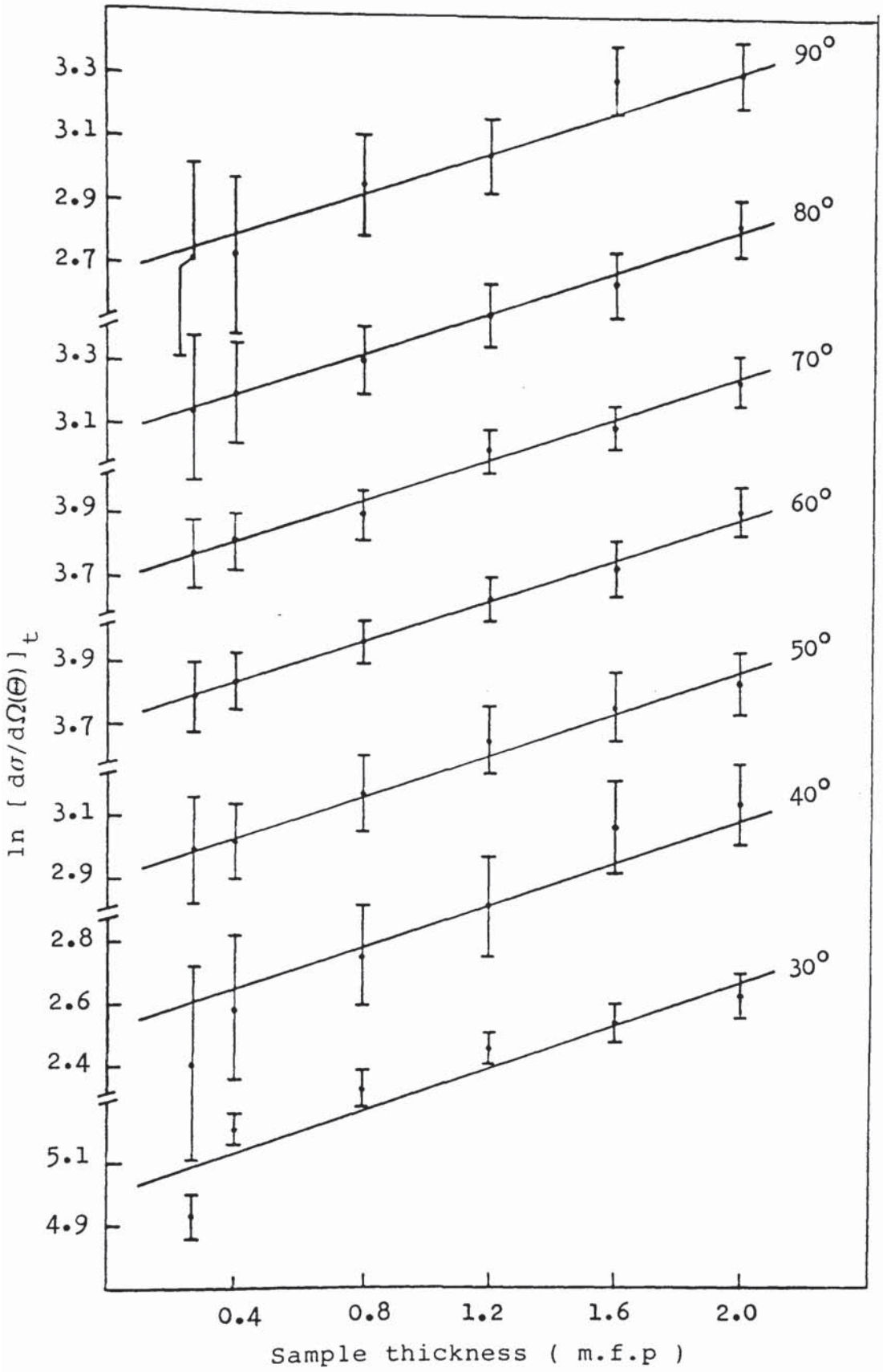

Figure (5.6):The variation of the aluminium differential elastic cross-section as a function of sample thickness at various scattering angles.

5.1.4:EXPERIMENTAL RESULTS FOR ALUMINIUM DIFFERENTIAL INELASTIC CROSS-SECTION.

The differential inelastic scattering cross-sections corresponding to the combined groups of 0.844 MeV and 1.041 states for aluminium samples were calculated using equation (4-23). The number of counts in the neutron inelastic peaks of 0.844 MeV and 1.041 MeV states were determined after subtracting the contribution of the Gaussian peak of the neutrons elastic scattering. The results are tabulated in table (5.7).

Table (5.7)

Aluminium differential inelastic cross-sections of 14.1 MeV neutrons for combined groups of 0.844 MeV and 1.041 MeV states in the laboratory system.

θ (deg)	Thickness (cm)	$d\sigma/d\Omega(\theta)$ (mbarns/sr)
30	2.54	4.8 ± 1.9
	3.81	4.9 ± 1.7
	7.62	6.5 ± 1.6
	11.43	6.3 ± 1.6
	15.24	8.1 ± 1.8
	19.05	8.2 ± 1.9
40	2.54	3.8 ± 0.7
	3.81	3.1 ± 0.6
	7.62	2.5 ± 0.6
	11.43	3.8 ± 0.6
	15.24	3.9 ± 0.6
	19.05	5.3 ± 0.7

Table (5.7):Continued.

Θ (deg)	Thickness (cm)	dσ/dΩ(Θ) (mbarns/sr)
50	2.54	3.5 ± 0.8
	3.81	3.5 ± 0.7
	7.62	4.4 ± 0.7
	11.43	4.4 ± 0.7
	15.24	3.9 ± 0.7
	19.05	4.3 ± 0.7
60	2.54	4.4 ± 1.1
	3.81	4.5 ± 1.0
	7.62	5.4 ± 1.0
	11.43	5.3 ± 1.0
	15.24	7.1 ± 1.0
	19.05	7.7 ± 1.1
70	2.54	2.8 ± 1.1
	3.81	3.9 ± 1.0
	7.62	4.2 ± 1.0
	11.43	5.4 ± 1.0
	15.24	5.5 ± 1.0
	19.05	6.8 ± 1.1
80	2.54	1.9 ± 0.9
	3.81	2.7 ± 0.9
	7.62	2.6 ± 0.7
	11.43	3.8 ± 0.8
	15.24	4.2 ± 0.7
	19.05	4.1 ± 0.8
90	2.54	1.8 ± 0.9
	3.81	1.9 ± 0.8
	7.62	2.0 ± 1.0
	11.43	2.6 ± 0.7
	15.24	2.5 ± 0.7
	19.05	3.0 ± 0.7

The experimental errors were calculated by considering each term in equation (4-23) as listed in table (5.3).

The experimental results for aluminium differential inelastic cross-section for each thickness

were fitted with Legendre polynomial expansion of equation (5-1). The best fitting terms of the polynomial were obtained by specifying only even terms in the polynomial. The polynomial coefficients for each sample thickness are tabulated in table (5.8).

Table (5.8)

Legendre polynomial coefficients for neutrons inelastic scattering of combined groups of 0.844 MeV and 1.041 MeV states at various sample thicknesses.

x (cm)	coefficients				
	a_0	a_2	a_4	a_6	a_8
2.54	4.065	5.781	4.315	5.312	1.577
3.81	3.543	1.466	-	-	-
7.62	4.033	2.145	-	-	-
11.43	4.672	1.579	-	-	-
15.24	5.124	2.328	-	-	-
19.05	5.846	2.842	-	-	-

Figure (5.7) shows the variation of the aluminium differential inelastic cross-section for combined groups of 0.844 MeV and 1.041 MeV states with scattering angle for various sample thicknesses.

The integrated inelastic scattering cross-sections for these excited states were calculated using equation

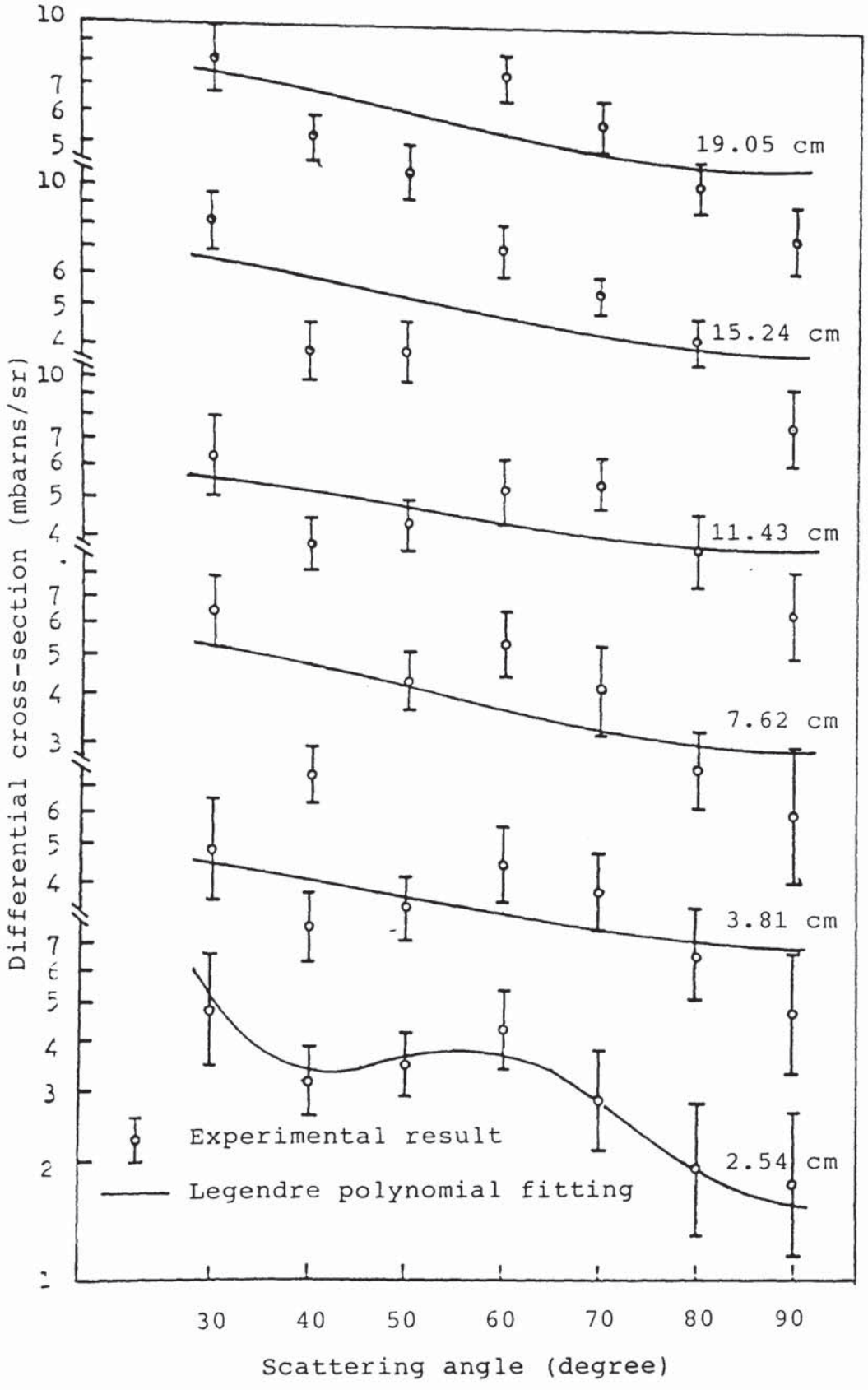

Figure (5.7): Angular distributions of neutron inelastic scattering cross-section for combined groups of 0.84 MeV and 1.04 MeV states for different thicknesses of aluminium.

(5-7) for 30° to 90° angular range. The results obtained for each sample thickness are tabulated in table (5.9).

Table (5.9)

The calculated integrated inelastic cross-sections between 30° to 90° angular range in the laboratory system for combined groups of 0.844 MeV and 1.041 MeV states for various thicknesses of aluminium.

Thickness (cm)	$\int_{\pi/6}^{\pi/2} \frac{d\sigma}{d\Omega}(\theta) \cdot d\Omega$
2.54	16 ± 2
3.81	18 ± 2
7.62	20 ± 2
11.43	24 ± 2
15.24	26 ± 2
19.05	30 ± 2

The individual peaks of the excited states of the neutrons inelastic scattering in aluminium are difficult to resolve because of the poor resolution of the spectrometer. Because of this, only angular distributions of neutrons in different energy ranges were calculated. The results for energy ranges E > 11 MeV, (11-8) MeV and (8-5) MeV for various thicknesses are tabulated in table (5.10).

Table (5.10)

Aluminium differential cross-sections for energy ranges E > 11 MeV, (11-8) MeV and (8-5) MeV for various thicknesses in the laboratory system.

θ^o	sample thickness (cm)	$d\sigma/d\Omega(\theta)$ mbarns/sr.		
		E > 11 (MeV)	(11-8) (MeV)	(8-5) (MeV)
30	2.54	164 ± 9	13 ± 3	18 ± 4
	3.81	207 ± 10	14 ± 2	18 ± 3
	7.62	237 ± 11	13 ± 2	23 ± 2
	11.43	268 ± 14	23 ± 2	27 ± 2
	15.24	296 ± 17	20 ± 2	29 ± 2
	19.05	324 ± 21	26 ± 2	32 ± 3
40	2.54	17 ± 4	9 ± 3	13 ± 4
	3.81	20 ± 2	10 ± 2	12 ± 2
	7.62	22 ± 2	12 ± 1	20 ± 2
	11.43	27 ± 2	12 ± 2	21 ± 2
	15.24	33 ± 3	15 ± 2	24 ± 2
	19.05	38 ± 3	15 ± 2	25 ± 2
50	2.54	26 ± 3	10 ± 2	12 ± 2
	3.81	31 ± 2	10 ± 1	16 ± 2
	7.62	33 ± 2	12 ± 1	21 ± 2
	11.43	38 ± 3	13 ± 1	21 ± 2
	15.24	40 ± 3	16 ± 2	28 ± 2
	19.05	45 ± 4	17 ± 2	25 ± 2
60	2.54	53 ± 3	10 ± 2	14 ± 2
	3.81	56 ± 3	10 ± 1	16 ± 2
	7.62	67 ± 4	12 ± 1	21 ± 2
	11.43	72 ± 4	13 ± 1	24 ± 2
	15.24	82 ± 5	15 ± 2	26 ± 2
	19.05	97 ± 7	19 ± 2	30 ± 3

Table (5.10):Continued.

θ^o	sample thickness (cm)	$d\sigma/d\Omega(\theta)$ mbarns/sr.		
		E > 11 (MeV)	(11-8) (MeV)	(8-5) (MeV)
70	2.54	50 ± 4	10 ± 2	16 ± 3
	3.81	54 ± 3	10 ± 1	13 ± 2
	7.62	59 ± 3	12 ± 1	22 ± 2
	11.43	74 ± 4	12 ± 1	22 ± 2
	15.24	77 ± 5	15 ± 2	29 ± 2
	19.05	91 ± 6	18 ± 2	30 ± 3
80	2.54	28 ± 3	7 ± 2	11 ± 3
	3.81	30 ± 3	6 ± 2	10 ± 2
	7.62	33 ± 2	7 ± 1	11 ± 1
	11.43	40 ± 3	8 ± 1	12 ± 2
	15.24	40 ± 3	11 ± 1	18 ± 2
	19.05	51 ± 4	11 ± 1	20 ± 2
90	2.54	19 ± 4	5 ± 3	6 ± 3
	3.81	20 ± 3	5 ± 2	7 ± 2
	7.62	25 ± 2	5 ± 1	7 ± 2
	11.43	26 ± 2	6 ± 1	10 ± 1
	15.24	34 ± 3	7 ± 1	11 ± 1
	19.05	36 ± 3	8 ± 1	11 ± 1

The differential scattering cross-sections for each energy range were plotted as a function of laboratory scattering angle corresponding to different sample thicknesses as shown in figures (5.8) through to (5.10). The smooth lines represent the Legendre polynomial fitting to the cross-section data for each sample thickness.

The integrated cross-sections for each energy range were calculated in the angular range between 30^o to 90^o using the same procedure as before. The results are tabulated in table (5.11).

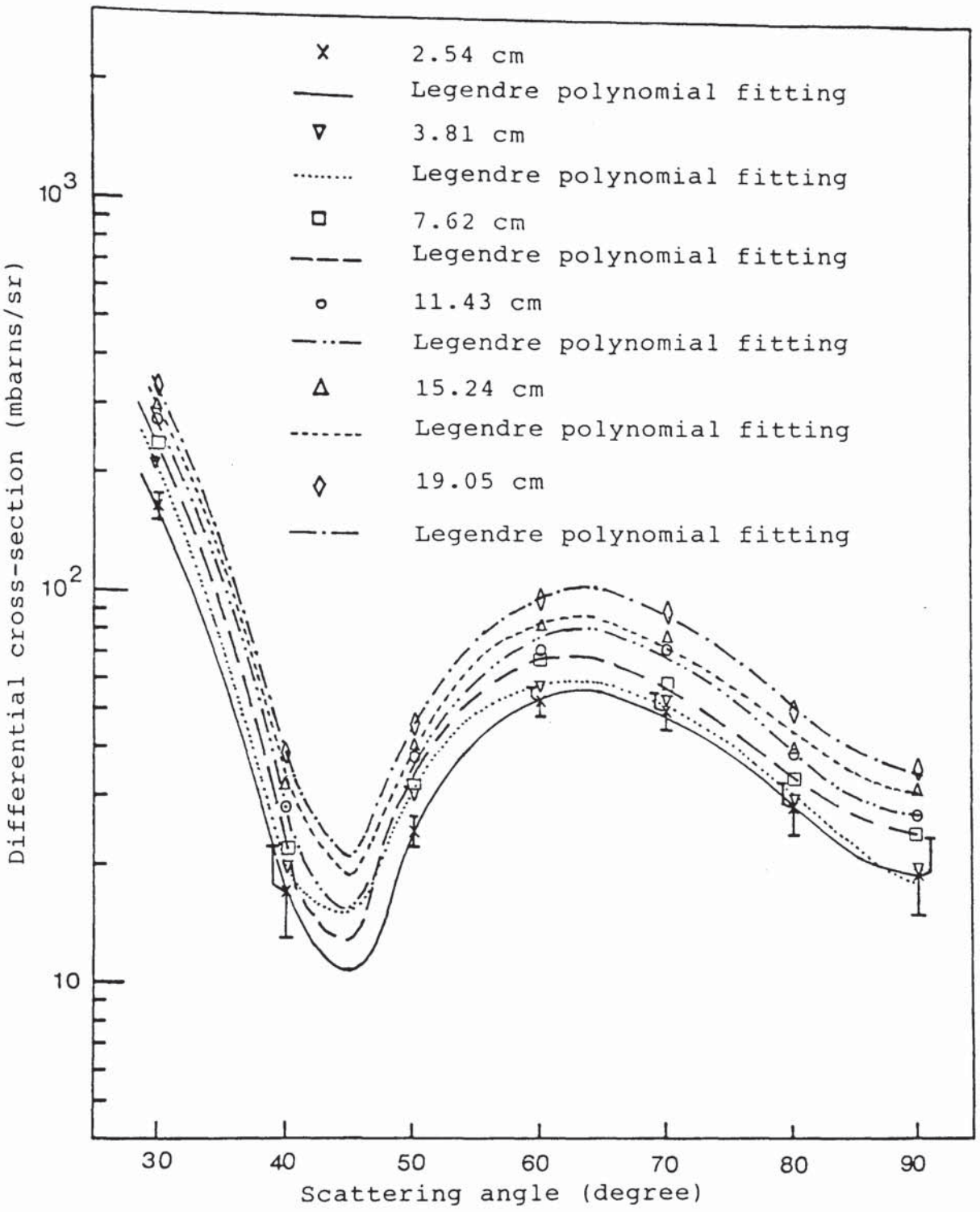

Figure (5.8):Angular distributions for the energy range E > 11 MeV at 14.1 MeV neutrons for different thicknesses of aluminium.

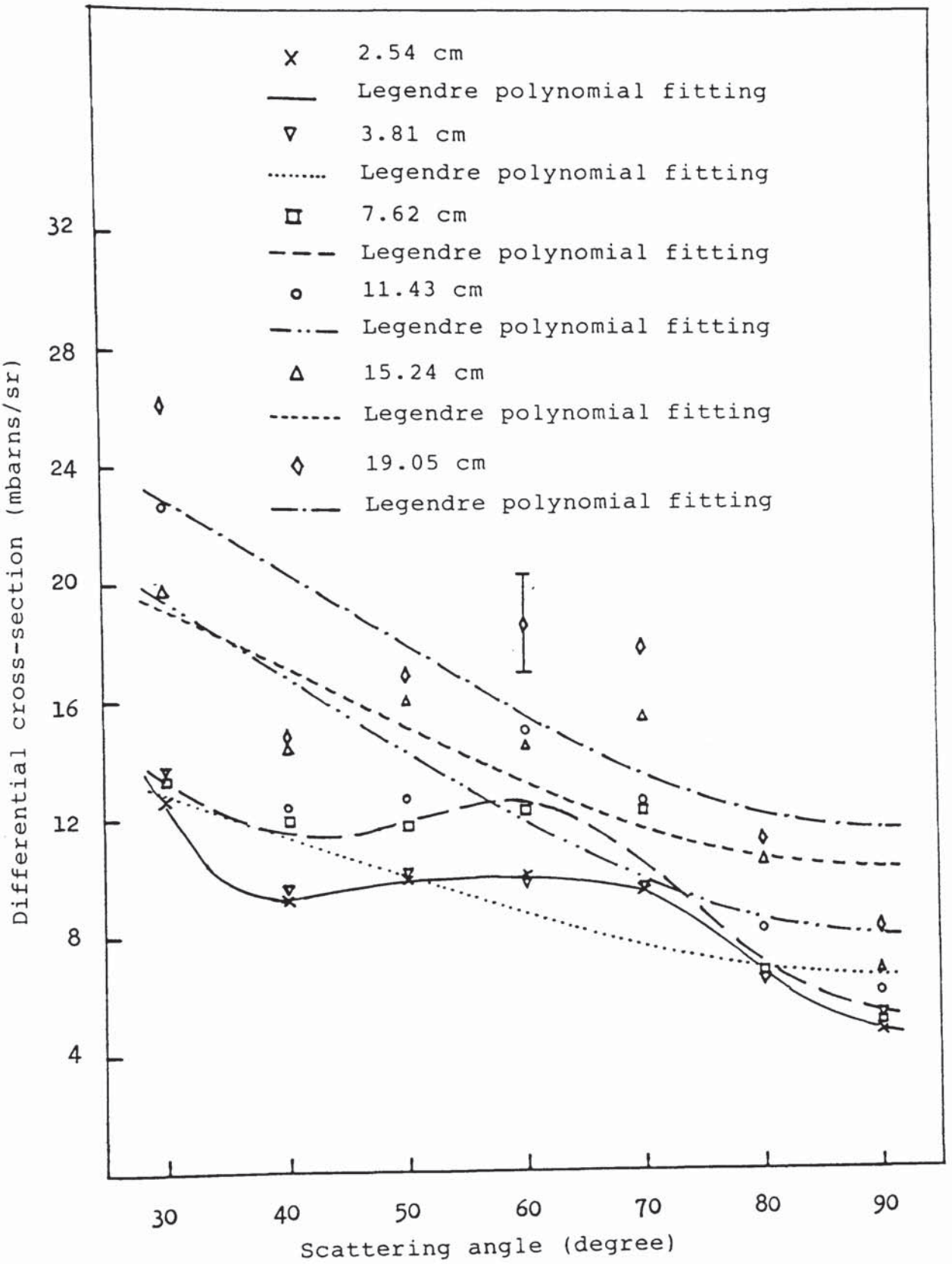

Figure (5.9):Angular distributions for the energy range (11-8) MeV at 14.1 MeV neutrons for different thicknesses of aluminium.

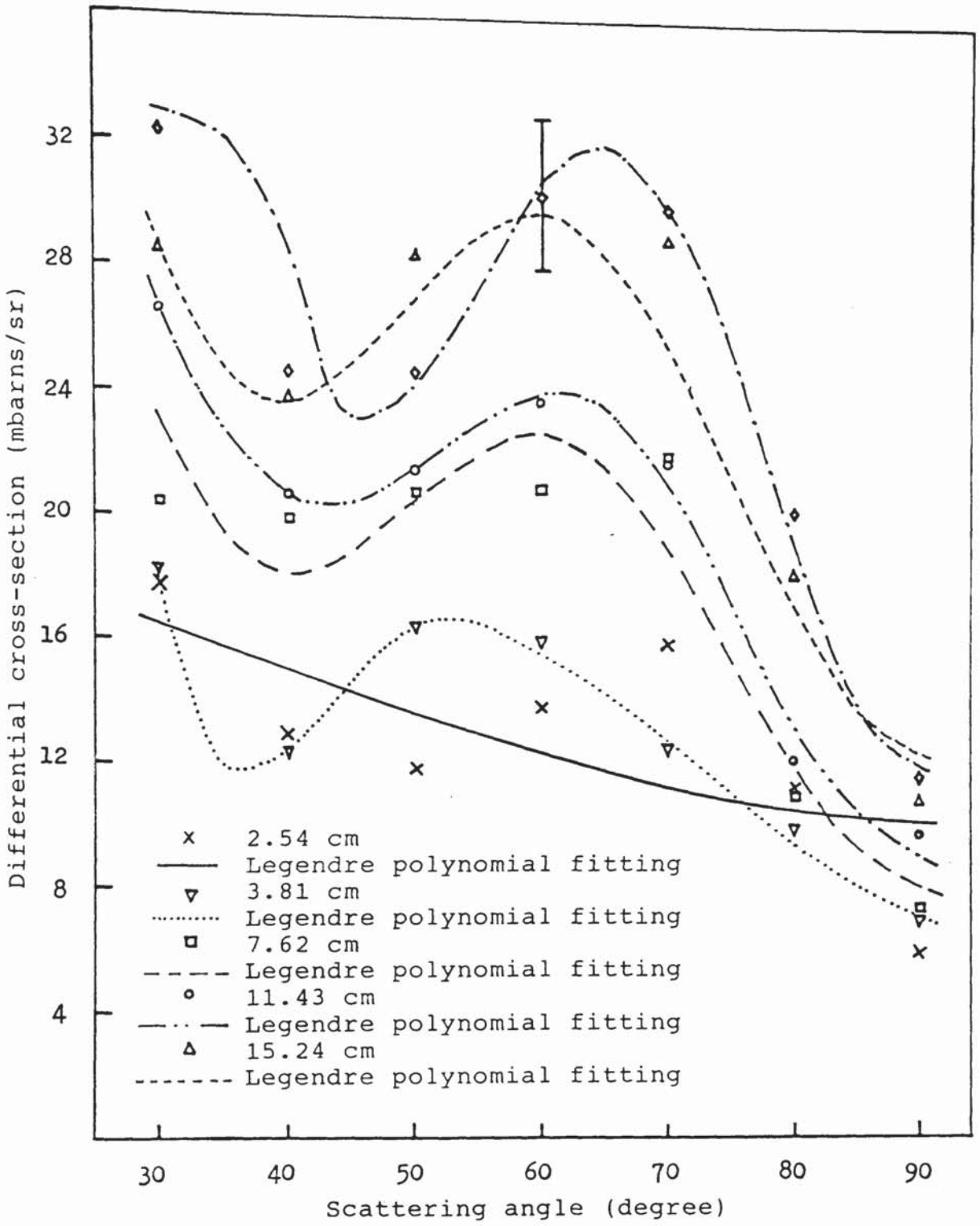

Figure (5.10):Angular distributions for the energy range (8-5) MeV at 14.1 MeV neutrons for different thicknesses of aluminium.

Table (5.11)

Aluminium integrated cross-sections in the angular range 30° to 90° for different energy ranges and different sample thicknesses.

sample thickness (cm)	$\int_{\pi/6}^{\pi/2} d\sigma/d\Omega(\theta)\, d\Omega$ mbarns		
	E > 11 (MeV)	(11-8) (MeV)	(8-5) (MeV)
2.54	214 ± 7	47 ± 4	67 ± 5
3.81	238 ± 6	47 ± 3	69 ± 4
7.62	271 ± 6	57 ± 2	94 ± 3
11.43	314 ± 7	65 ± 3	103 ± 4
15.24	346 ± 9	73 ± 3	127 ± 4
19.05	400 ± 11	84 ± 3	134 ± 4

5.1.5:THE VARIATION OF THE DIFFERENTIAL INELASTIC CROSS-SECTION WITH SAMPLE THICKNESS.

The experimental results for the differential inelastic cross-section for combined groups of 0.844 MeV and 1.041 MeV states and for energy ranges E > 11 MeV, (11-8) MeV and (8-5) MeV were fitted as a function of sample thickness using the least squares method discussed in section (5.3.1). The values of constant α obtained from the fitting for each angle and for different energy ranges are tabulated in table (5.12). Figures (5.11) through to (5.14) show the variation of the differential

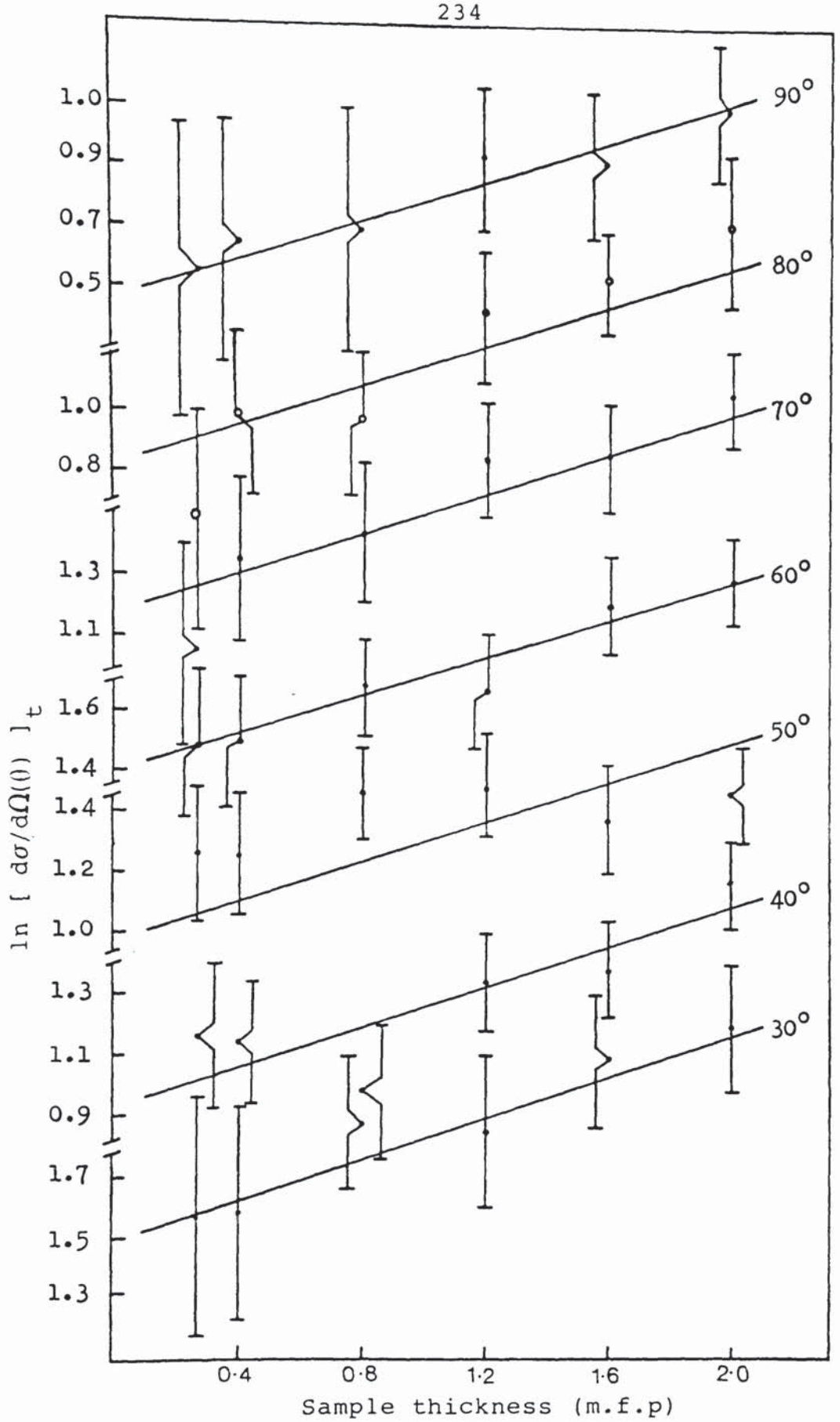

Figure (5.11):The variation of the aluminium differential inelastic cross-section for combined groups of 0.84 MeV and 1.04 MeV states as a function of sample thickness at various scattering angles.

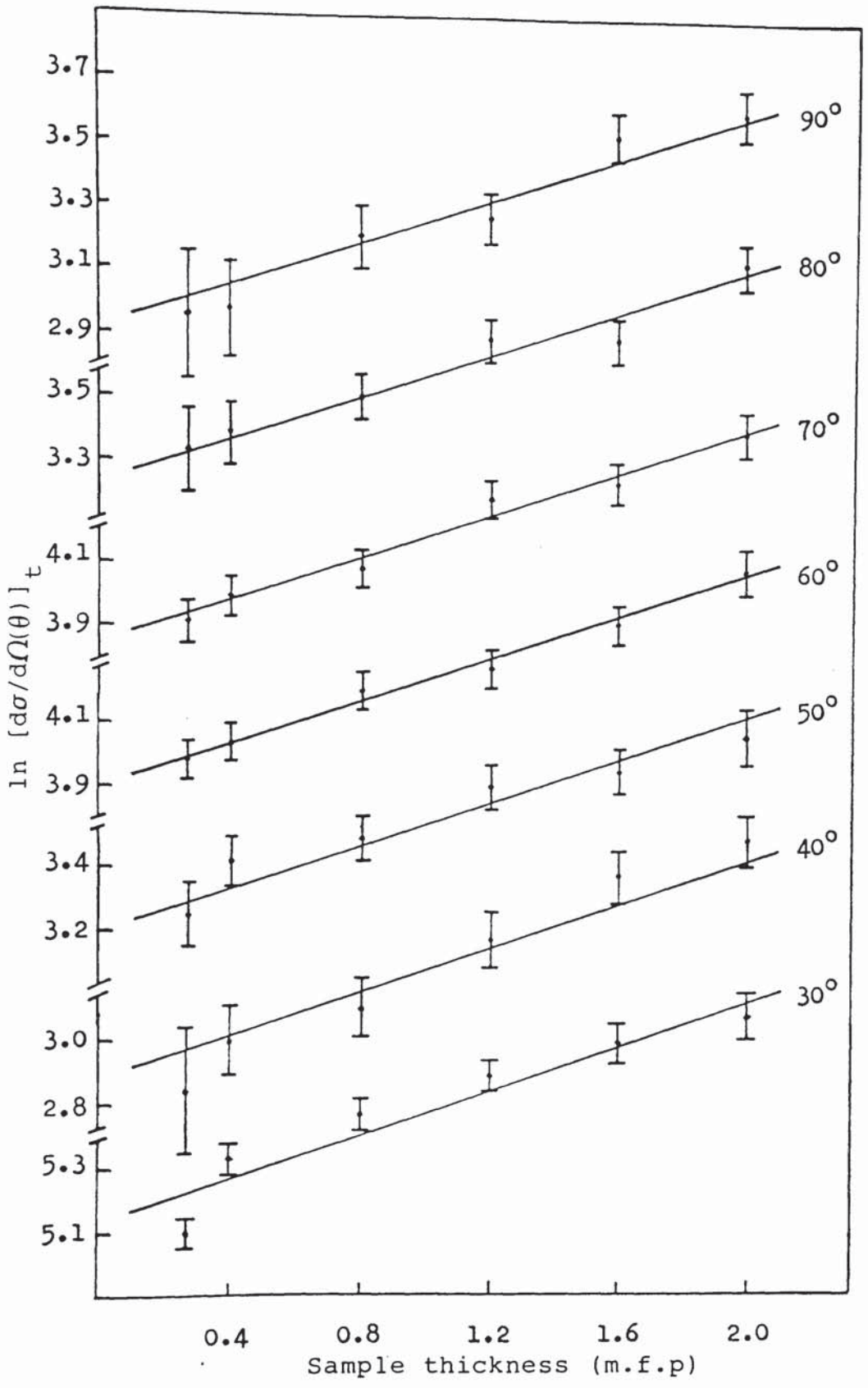

Figure (5.12):The variation of the aluminium differential cross-section for energy range E > 11 MeV as a function of sample thickness at various scattering angles.

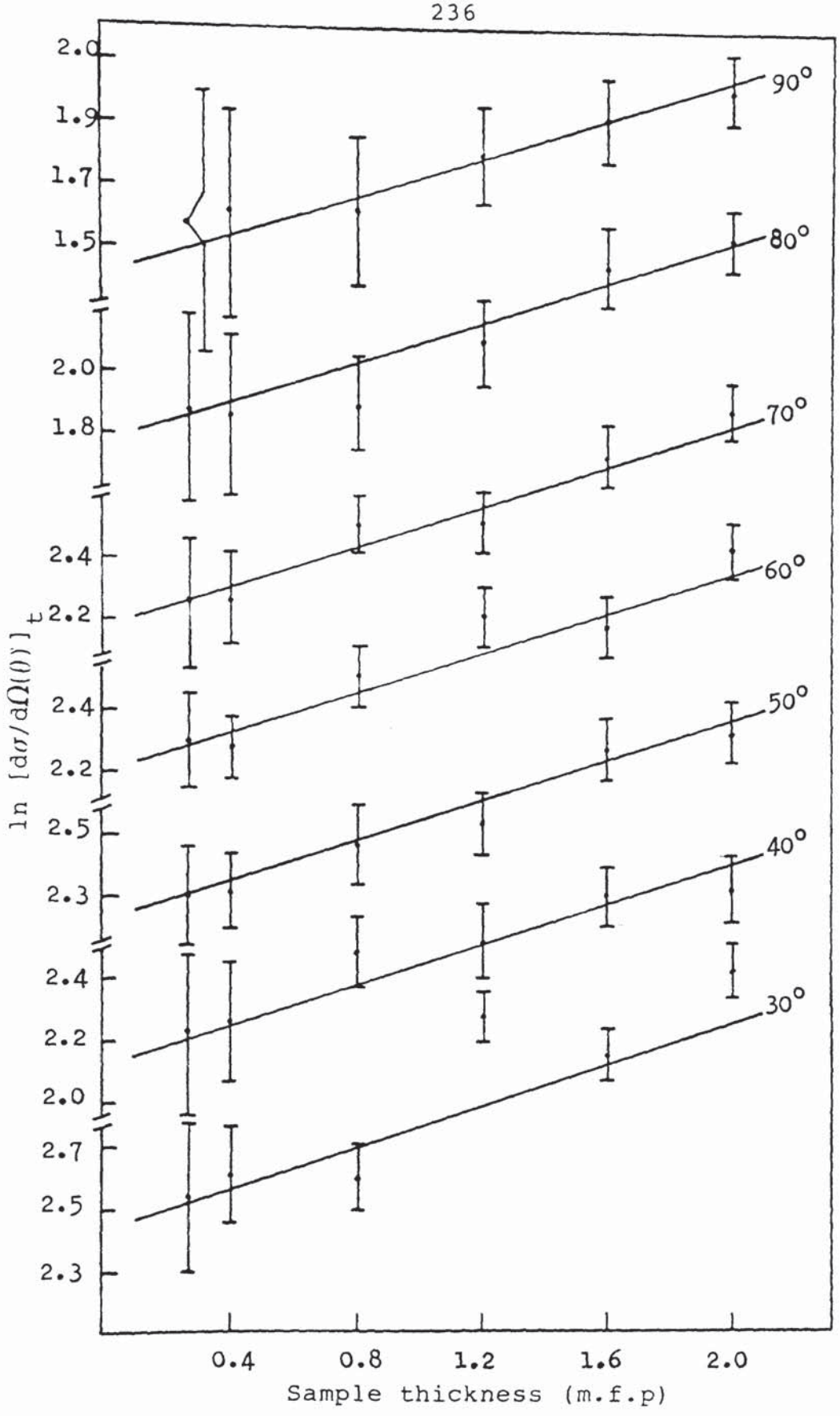

Figure (5.13): The variation of the aluminium differential cross-section for energy range (11-8) MeV as a function of sample thickness at various scattering angles.

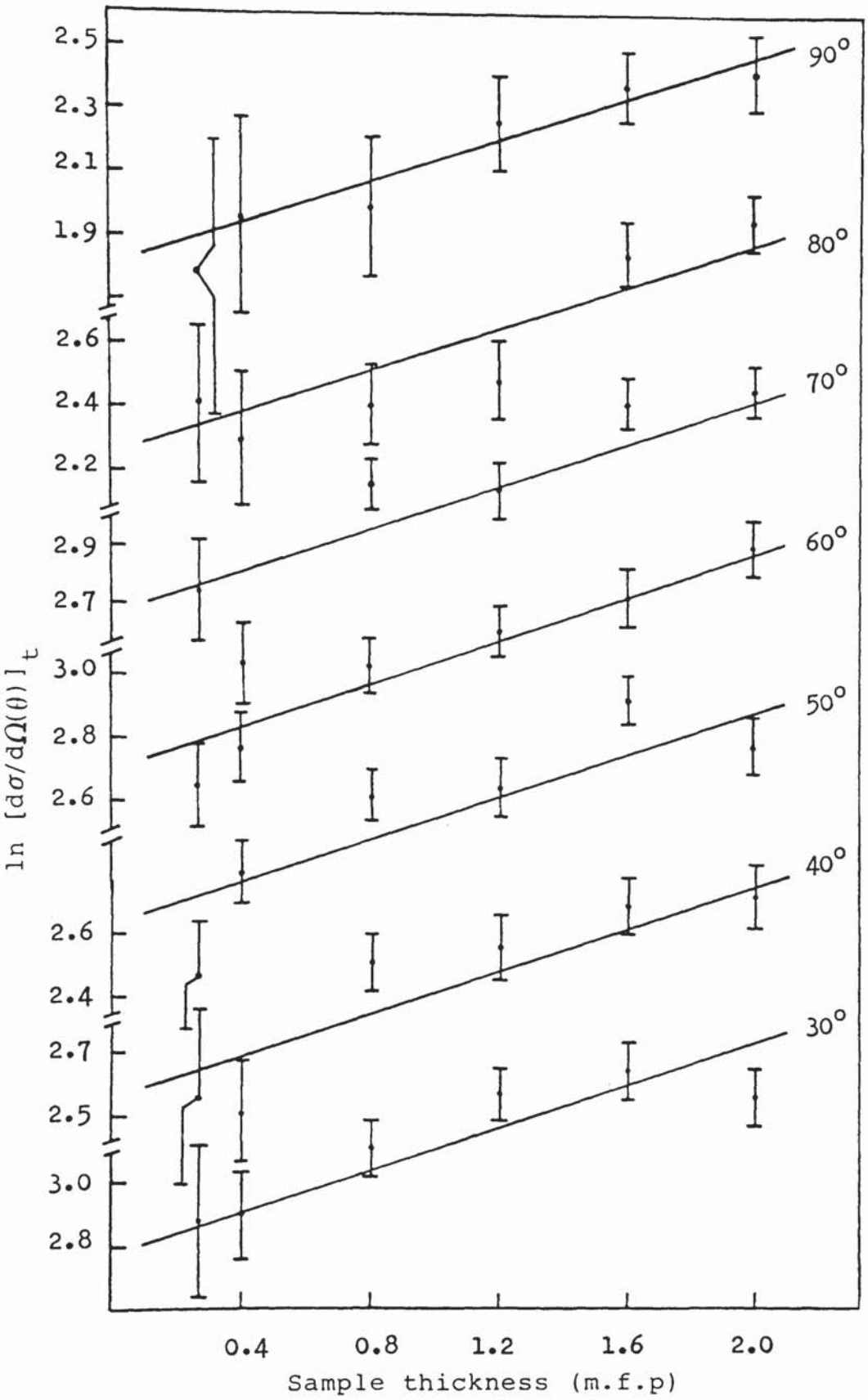

Figure (5.14):The variation of the aluminium differential cross-section for energy range (5-8) MeV as a function of sample thickness at various scattering angles.

cross-section with the thickness in term of mean free path. Each figure gives the variation for different scattering angles. The solid lines in each figure were plotted using the average value of α.

Table (5.12)

The values of constant α obtained from least squares fit to the experimental data for inelastic groups of 0.844 MeV and 1.041 MeV and for energy ranges E > 11 MeV, (11-8) MeV and (8-5) MeV.

angle (deg)	(n,n') 0.84,1.04MeV	E > 11 MeV	(8-11) MeV	(5-8) MeV
30	0.35 ± 0.18	0.35 ± 0.05	0.41 ± 0.08	0.32 ± 0.07
40	0.33 ± 0.12	0.44 ± 0.03	0.24 ± 0.10	0.32 ± 0.08
50	0.09 ± 0.12	0.29 ± 0.04	0.33 ± 0.08	0.33 ± 0.07
60	0.33 ± 0.12	0.33 ± 0.02	0.35 ± 0.07	0.40 ± 0.07
70	0.39 ± 0.15	0.34 ± 0.02	0.36 ± 0.08	0.41 ± 0.07
80	0.39 ± 0.19	0.32 ± 0.03	0.39 ± 0.11	0.47 ± 0.10
90	0.29 ± 0.23	0.31 ± 0.06	0.36 ± 0.15	0.32 ± 0.14
α_{av}	0.31 ± 0.16	0.34 ± 0.04	0.35 ± 0.10	0.37 ± 0.09

The average value of constant α for aluminium sample was found as,

$$\alpha_{Al} = 0.34 \pm 0.10 \quad (m.f.p)^{-1}.$$

5.1.6:EXPERIMENTAL RESULTS FOR THIN ALUMINIUM SAMPLE.

5.1.6.1:RESULTS FOR ELASTIC SCATTERING CROSS-SECTION.

The measurements of the differential cross-section for thin sample of aluminium were made in the angular range 30^{o} to 90^{o} with 5^{o} increments. The calculations were done using equation (4-23) and the data were converted to the centre of mass system using equations (4-27) and (4-28).

The results of the angular distribution of elastic scattered neutrons from thin sample of aluminium were tabulated in table (5.13) together with the results of other published data. Figure (5.15) gives a comparison of the present data with other measurements for scattering angles between 30^{o} to 90^{o} in the centre of mass system. From the figure, it appears that the present results for elastic scattering are in good agreement with previous measurements of Bonazzola et al (14) using a disk scatterer of 2 cm thickness and Whisnant et al (15) using a cylindrical geometry 2.54 cm high and 3.81 cm diameter. This angular distribution is also in good agreement with the data from ENDF-B4 (97). The data reported by Yuasa (13) using a disk-shape scatterer were mainly for high angles between 70^{o} to 170^{o}.

The aluminium differential elastic scattering cross-section data were fitted with the Legendre polynomial expansion of equation;

Table (5.13)

The differential elastic scattering cross-section data for 14.1 MeV neutrons scattered from thin sample of aluminium in the centre of mass system.

θ_c°	Present Work	ENDF-B4	Whisnant et al	Bonazolla et al	Yuasa
26°	-	-	-	290 ± 29	-
31° 4'	130 ± 10	118.7	145.3	-	-
36° 14'	46 ± 6	39.8	49.7	-	-
39°	-	-	-	18 ± 2	-
41° 23'	11 ± 6	9.8	9.6	-	-
46° 31	9 ± 3	10.6	7.5	-	-
47°	-	-	-	31 ± 3	-
51° 38'	19 ± 3	23.8	22.9	-	-
56° 45'	39 ± 6	36.7	39.6	-	-
57°	-	-	-	63 ± 1	-
61° 51'	43 ± 4	43.3	48.4	-	-
66° 56'	46 ± 5	42.8	47.6	-	-
68°	-	-	-	40 ± 2	-
72° 01'	42 ± 5	37.3	40.1	-	45 ± 4
76° 30'	-	-	-	25 ± 4	-
77° 04'	29 ± 5	29.4	30.4	-	-
82° 07'	23 ± 5	21.6	21.9	-	22 ± 4
87° 08'	15 ± 7	15.4	16.1	-	-
89° 30'	-	-	-	15 ± 2	-
92° 09'	15 ± 6	11.7	13.1	-	16 ± 5

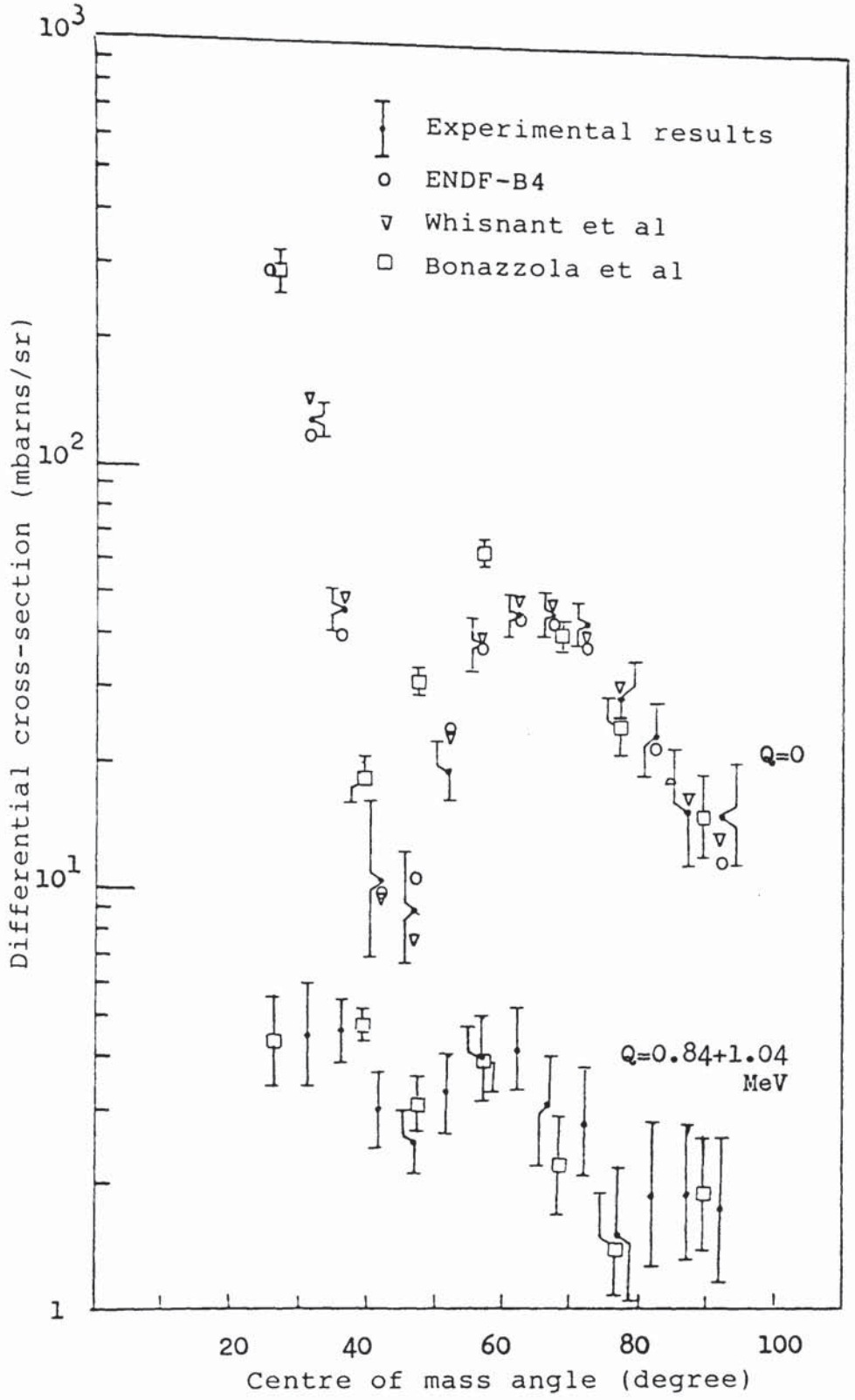

Figure (5.15):Comparison of the measurements of the differential scattering cross-section from aluminium for 14.1 MeV neutrons.

$$\frac{d\sigma}{d\Omega}(\theta_c) = \frac{\sigma_{int}}{4\pi} \sum_{l=0}^{l_{max}} [(2l+1).f_l.P_l(\text{Cos}\ \theta_c)] \qquad (5\text{-}10)$$

To keep the expression for the elastic cross-sections from blowing up at foward angles, a cross-section at 0° given by Wick's limit (2,98) was introduced, i.e

$$\frac{d\sigma}{d\Omega}(\theta_c = 0) \geqslant \left[\frac{\sigma_T}{4\pi.\lambda\!\!\!^{-}}\right]^2 \qquad (5\text{-}11)$$

where,

σ_T = the total cross-section,

$\lambda\!\!\!^{-}$ = De Broglie wavelength for neutron.

The wavelength of the neutron can be expressed as,

$$\lambda\!\!\!^{-2} = \frac{\hbar^2}{2\ \bar{m}\ \bar{E}} \qquad (5\text{-}12)$$

where,

$\bar{m} = \dfrac{M_1 \cdot M_2}{M_1 + M_2}$ = the reduced mass,

$\bar{E} = \dfrac{M_2}{M_1 + M_2} E_n$ = the energy of the reduced mass,

M_1 = mass of neutron,

M_2 = mass of the scatterer.

The calculation of Wick's limit was done using the total cross-section data taken from ENDF-B4 (97) and the calculated value was found as 1273 mbarns/sr.

The Legendre polynomial fitting was done using the

present experimental data together with the data reported by Yuasa (13) for scattering angles between 100^{o} to 170^{o} . The maximum coefficients of order l_{max} was obtained by choosing the minimum value of χ^{2} of equation (5-3) and the 0^{o} differential cross-section should agree with the Wick's limit calculated from equation (5-11).

The most suitable fitting was obtained with tenth order series of polynomial with $\chi^{2} < 0.4$ and the 0^{o} differential elastic cross-section was found as 1246 mbarns/sr . The Wick's limit value disagreed with the present data within only 2%.

The fit is shown as the solid line in figure (5.16) and the coefficients and the integrated elastic cross-section in the angular range 0^{o} to 180^{o} are given in table (5-14) together with the other data from ENDF-B4 (97) and Whisnant et al (15). The integrated cross-section was calculated as $4\pi a_{0}$ where a_{0} is the coefficient of 0 order of the polynomial.

Table (5.15) gives the comparison of the integrated elastic scattering cross-section with other published data (11,15,97,99,100).

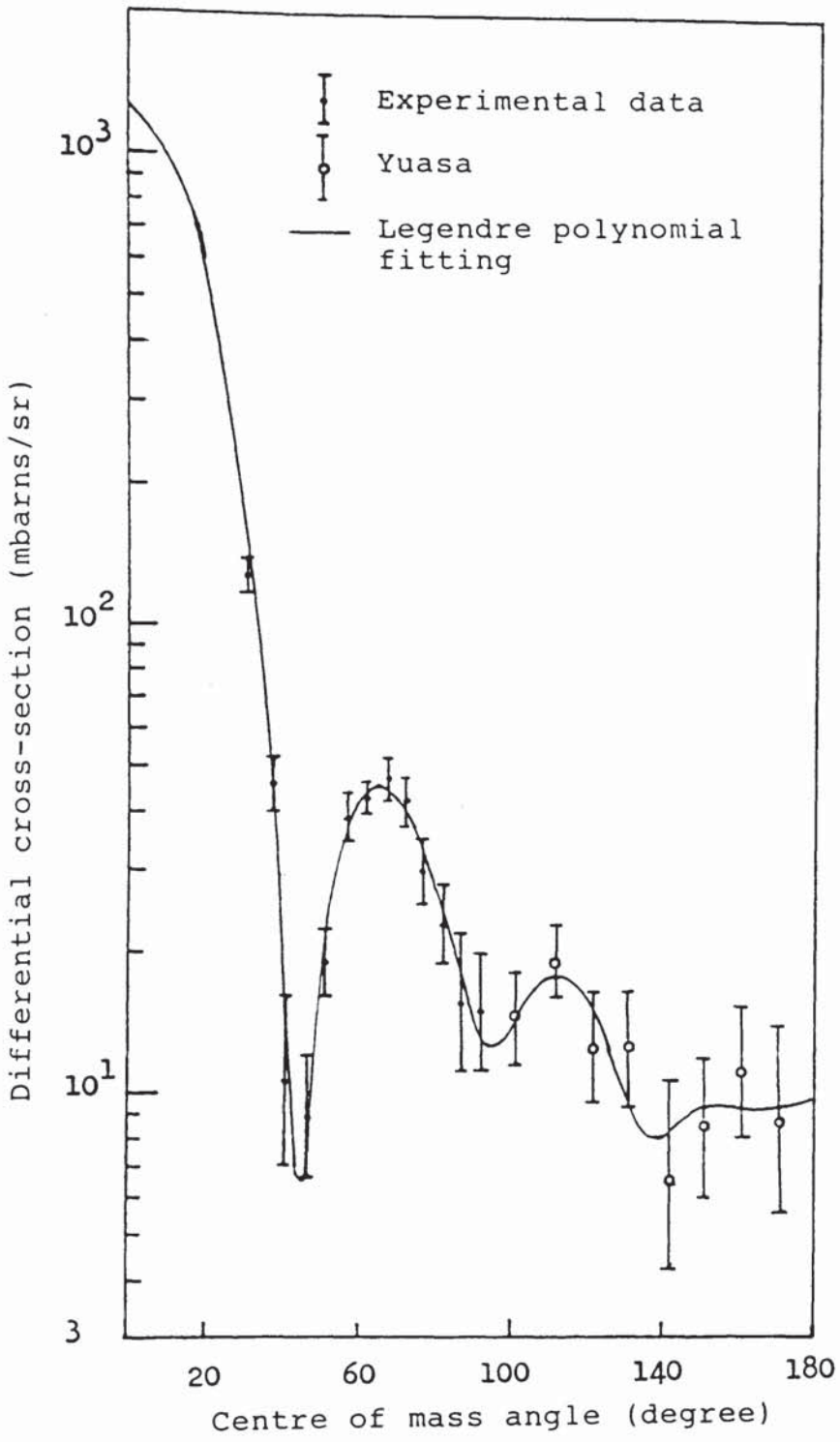

Figure (5.16):Legendre polynomial fits to the elastic scattering cross-section data for aluminium at 14.1 MeV neutrons.

Table (5.14)

Legendre polynomial coefficients and the integrated cross-section obtained from fits to the aluminium elastic scattering angular distribution for 14.1 MeV neutrons.

f_l	coefficients		
	Present work	ENDF-B4	Whisnant et al
f_0	1.000 ±0.020	1.000	1.000
f_1	0.686 ±0.017	0.690	0.687
f_2	0.535 ±0.015	0.527	0.539
f_3	0.451 ±0.014	0.435	0.434
f_4	0.377 ±0.012	0.366	0.363
f_5	0.299 ±0.011	0.296	0.292
f_6	0.213 ±0.009	0.210	0.199
f_7	0.114 ±0.007	0.111	0.100
f_8	0.045 ±0.005	0.045	0.037
f_9	0.019 ±0.005	0.017	0.007
f_{10}	0.007 ±0.004	0.005	-
σ_{int}	734 ±14 mbarns	651 mbarns	728 ± 36 mbarns

Table (5.15)

Comparison of the integrated elastic scattering cross-sections for aluminium at 14 MeV neutrons.

σ_{int} mbarns	Author
734 ± 14	Present work
651	ENDF-B4 (97)
728 ± 36	Whisnant et al (15)
742	UKNDL (99)
830 ± 40	Pierre et al (100)
670 ± 30	Coon et al (11)

5.6.1.2:RESULTS FOR DIFFERENTIAL INELASTIC SCATTERING CROSS-SECTION.

The results for the differential inelastic cross-section for combined groups of 0.844 MeV and 1.041 MeV states in aluminium were calculated for angular range 30^{o} to 90^{o} with 5^{o} increments and the data were converted in the centre of mass system. The data are tabulated in table (5-16) with the data reported by Bonazzola et al (14).

Table (5-16)

Aluminium differential inelastic cross-sections for combined groups of 0.844 MeV and 1.041 MeV in the centre of mass system.

θ_c°	Present work mbarns/sr	Bonazzola et al mbarns/sr
26°	-	4.4 ± 1.3
31°04'	4.5 ± 1.8	-
36°14'	4.6 ± 1.1	-
39°	-	4.8 ± 0.3
41°23'	3.0 ± 0.7	-
46°31'	2.5 ± 0.9	-
47°	-	3.1 ± 0.5
51°38'	3.4 ± 0.8	-
56°45'	4.0 ± 0.9	-
57°	-	3.9 ± 0.8
61°51'	4.2 ± 1.0	-
66°56'	3.1 ± 1.1	-
68°	-	2.2 ± 0.7
72°01'	2.8 ± 1.0	-
76°30'	-	1.4 ± 0.5
77°04'	1.6 ± 0.9	-
82°07'	1.9 ± 0.9	-
87°08'	1.9 ± 0.9	-
89°30'	-	1.9 ± 0.7
92°09'	1.8 ± 0.9	-

The cross-section data in the angular range 30° to 90° were fitted by Legendre polynomial expansion and the best fit was obtained by specifiying only even terms in the polynomial. The fit is shown as the solid line in figure (5.17) and the coefficients and the integrated inelastic cross-section in whole angular range are given in table (5-17).

Table (5.17)

Legendre polynomial coefficients obtained from fits to the thin sample of aluminium inelastic scattering angular distribution for combined groups of 0.844 MeV and 1.041 MeV states in the centre of mass system.

f_l	Coefficients
f_0	1.000 ± 0.223
f_2	0.449 ± 0.207
f_4	0.314 ± 0.176
f_6	0.271 ± 0.135
f_8	0.168 ± 0.093
f_{10}	0.107 ± 0.055
f_{12}	0.074 ± 0.027
f_{14}	0.023 ± 0.010
σ_{int}	67 ± 15

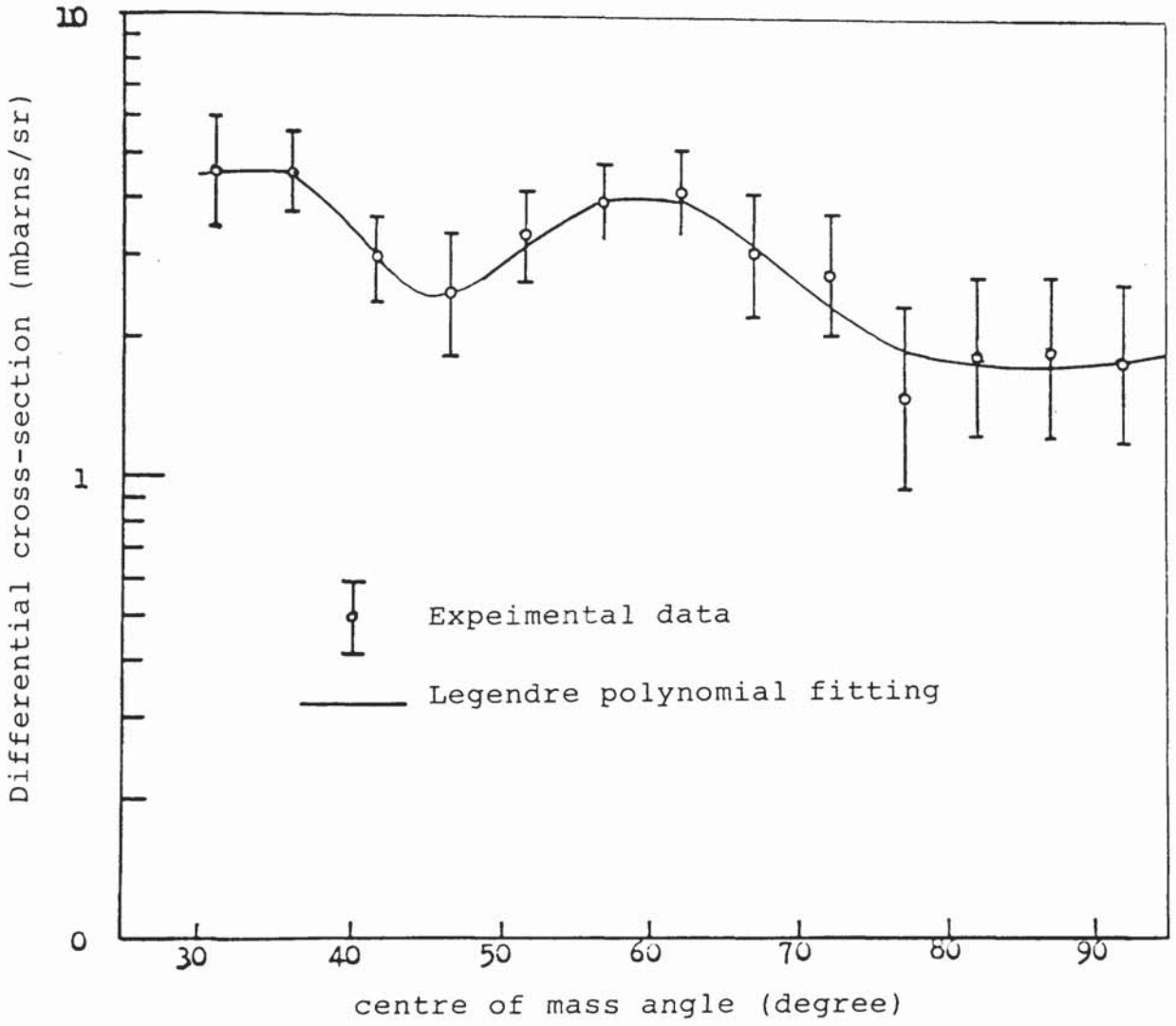

Figure (5.17):Legendre polynomial fits to the inelastic (0.84 + 1.04 MeV) scattering cross-section data for aluminium at 14.1 MeV neutrons.

The aluminium differential cross-sections for energy ranges E > 11 MeV, (11-8) MeV and (8-5) MeV are presented in table (5.18) and the data for each energy range were fitted by Legendre polynomial expansion as before. No such measurements have been done to compared with the present experimental results.

Table (5.18)

Aluminium differential cross-sections for energy ranges in the centre of mass system.

θ_c (deg)	$d\sigma/d\Omega(\theta)$ mbarns/sr		
	E > 11MeV	(11-8)MeV	(8-5)MeV
31°04'	154 ± 8	12 ± 3	17 ± 4
36°14'	57 ± 5	9 ± 2	15 ± 3
41°23'	16 ± 4	9 ± 3	12 ± 3
46°31'	13 ± 2	5 ± 2	8 ± 2
51°38'	25 ± 2	10 ± 2	11 ± 2
56°45'	47 ± 4	8 ± 2	14 ± 3
61°51'	51 ± 3	10 ± 1	13 ± 2
66°56'	55 ± 4	10 ± 2	16 ± 3
72°01'	49 ± 4	9 ± 2	15 ± 3
77°04'	34 ± 3	7 ± 2	13 ± 3
82°07'	28 ± 3	7 ± 2	11 ± 3
87°08'	21 ± 4	5 ± 2	9 ± 3
92°09'	19 ± 4	5 ± 3	6 ± 3

The results of the polynomial fitting for each energy range are presented in figure (5.18) as a smooth lines and the coefficients obtained are listed in table (5.19).

Table (5.19)

Legendre polynomial coefficients obtained from fits to the aluminium differential cross-sections for energy ranges at 14.1 MeV neutrons.

f_l	Coefficients		
	E > 11MeV	(11-8)MeV	(8-5)MeV
f_0	1.000 ± 0.019	1.000 ± 0.141	1.000 ± 0.038
f_2	0.567 ± 0.016	-0.249 ± 0.120	0.069 ± 0.029
f_4	0.379 ± 0.012	-0.284 ± 0.101	0.015 ± 0.023
f_6	0.204 ± 0.008	-0.161 ± 0.074	0.022 ± 0.017
f_8	0.032 ± 0.004	-0.163 ± 0.049	-0.045 ± 0.012
f_{10}	-	-0.048 ± 0.028	-

The integrated of elastic and inelastic scattering cross-sections in the centre of mass system were calculated in the angular range between 30° to 90° using equation (5-7). The results are tabulated in table (5-20) together with the results calculated from other measurements (14,15,97)

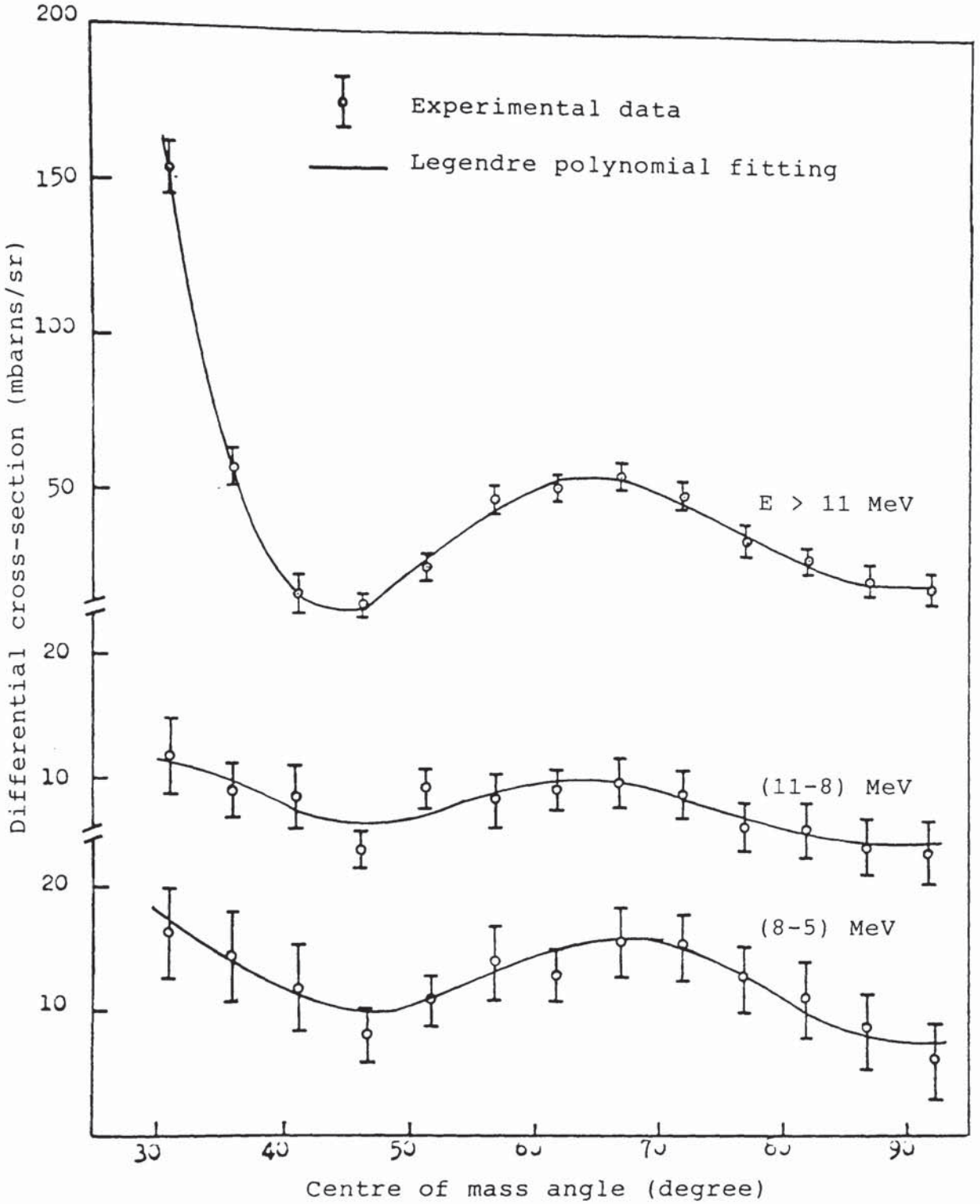

Figure (5.18):Legendre polynomial fits to the differential scattering cross-section data for the energy ranges in aluminium.

Table (5-20)

Integrated scattering cross-sections in the angular range 30° to 90° for 14.1 MeV neutrons from aluminium in the centre of mass system.

Reaction	$\sigma_{int} = \int_{\pi/6}^{\pi/2} d\sigma/d\Omega(\theta_c)\, d\Omega$ mbarns			
	Present work	Bonazzola et al	Whisnant et al	ENDF-B4
Elastic	182 ± 9	205.9	189.4	173.4
Inelastic	16 ± 2	15.9	-	-
E > 11MeV	220 ± 8	-	-	-
(11-8)MeV	43 ± 4	-	-	-
(8-5)MeV	68 ± 5	-	-	-

5.2:RESULTS FOR COPPER SAMPLE.

5.2.1:BACKGROUND OF THE SAMPLE.

Natural copper consists two stable isotopes of ^{63}Cu and ^{65}Cu with abundance of 69.1% and 30.9% respectively. In this differential cross-section measurements five different thicknesses of sample inform of flat plate geometry similar to those in aluminium samples were investigated. The dimensions and the thicknesses of the samples are listed in table (5.21).

Table (5.21)

Dimensions of the copper samples used in the present work.

Sample dimension (cm^2)	sample thickness	
	cm	m.f.p at 14 MeV
20 x 15	1.0	0.243
20 x 15	2.0	0.486
20 x 15	4.0	0.973
20 x 15	6.0	1.459
20 x 15	8.0	1.945

The experimental measurements of the differential cross-section were done using the similar procedures to those in the aluminium differential cross-section measurements. The sample-detector distance used in these

measurements was 129.5 cm.

Typical examples of the time of flight spectrum measured at 40° for sample thickness of 4 cm and 50° for sample thickness of 6 cm are given in figures (5.19) and (5.20) respectively. The errors indicated in each point in the spectrum are due to the statistical uncertainties in accumulations and background subtractions.

From each figure it is shown that the peaks due to excited states levels in ^{63}Cu and ^{65}Cu are unresolved individually and from the elastic peak because of the poor resolution of the spectrometer and very close separation between the ground state and the excited states of both isotopes. The energy level diagrams for ^{63}Cu and ^{65}Cu nuclei are presented in figures (5.21) (94). Using the similar technique to that in the aluminium spectra, the number of neutrons under the elastic peak of copper spectra can be determined.

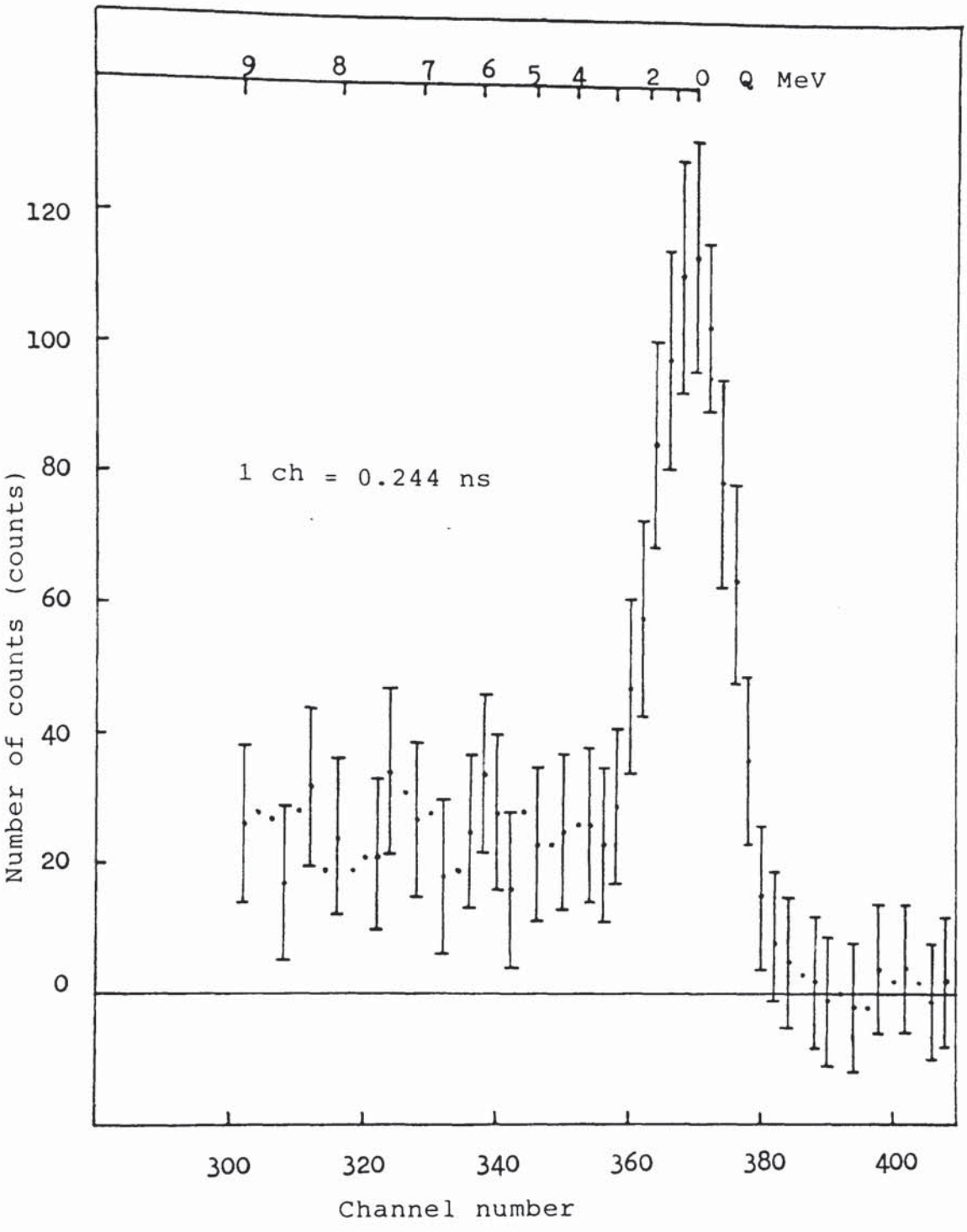

Figure (5.19):The time of flight spectrum of 14.1 MeV neutrons for scattering angle 40° scattered from 4 cm thickness of copper.

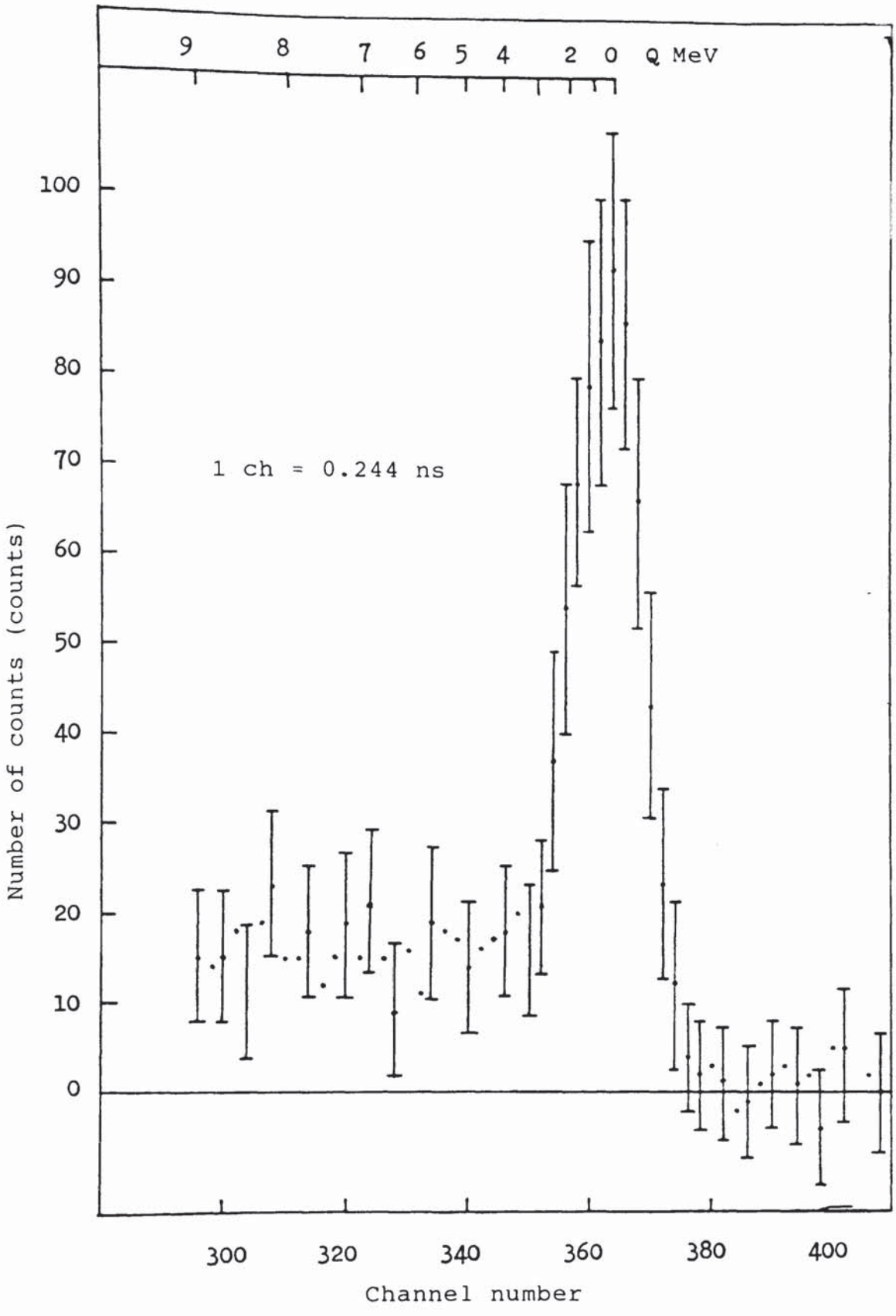

Figure (5.20):The time of flight spectrum of 14.1 MeV neutrons for scattering angle 50° scattered from 6 cm thickness of copper.

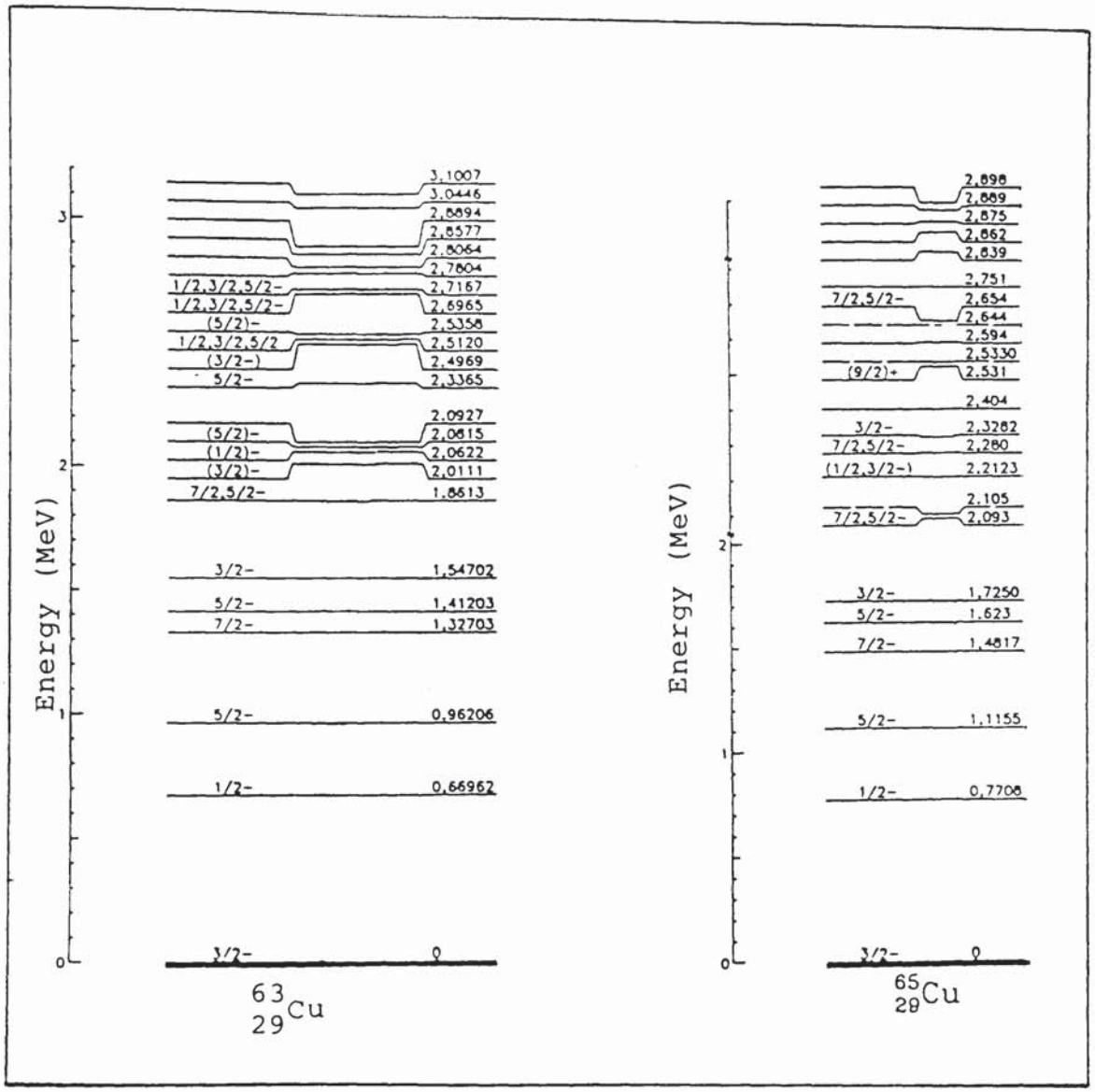

Figure (5.21):The energy level diagrams of Cu^{63} and Cu^{65}.

5.2.2:EXPERIMENTAL RESULTS FOR THE DIFFERENTIAL ELASTIC CROSS-SECTION.

The experimental results of the differential elastic scattering cross-section, calculated using equation (4-23) for five different thicknesses of copper sample are tabulated in table (5.22). The measurements were made for each laboratory angle between 30° to 90° with sample in the position and the sample was removed for background subtraction.

Table(5.22)

Copper differential elastic scattering cross-sections for 14.1 MeV neutrons in the laboratory system.

θ_L (deg)	x (cm)	λ (m.f.p)	$d\sigma/d\Omega(\theta_L)$ (mbarns/sr)
30	1.00	0.243	335 ± 22
	2.00	0.486	338 ± 19
	4.00	0.973	446 ± 23
	6.00	1.459	524 ± 29
	8.00	1.945	582 ± 35
40	1.00	0.243	54 ± 9
	2.00	0.486	55 ± 6
	4.00	0.973	62 ± 6
	6.00	1.459	72 ± 6
	8.00	1.945	88 ± 8
50	1.00	0.243	34 ± 7
	2.00	0.486	38 ± 5
	4.00	0.973	42 ± 5
	6.00	1.459	50 ± 6
	8.00	1.945	59 ± 6
60	1.00	0.243	11 ± 5
	2.00	0.486	11 ± 4
	4.00	0.973	14 ± 3
	6.00	1.459	17 ± 4
	8.00	1.945	20 ± 5

Table (5.22):Continued.

θ_L (deg)	x (cm)	λ (m.f.p)	$d\sigma/d\Omega(\theta_L)$ (mbarns/sr)
70	1.00	0.243	14 ± 5
	2.00	0.486	17 ± 4
	4.00	0.973	19 ± 4
	6.00	1.459	25 ± 4
	8.00	1.945	27 ± 5
80	1.00	0.243	33 ± 8
	2.00	0.486	35 ± 7
	4.00	0.973	38 ± 7
	6.00	1.459	44 ± 8
	8.00	1.945	51 ± 8
90	1.00	0.243	26 ± 17
	2.00	0.486	27 ± 11
	4.00	0.973	37 ± 9
	6.00	1.459	45 ± 8
	8.00	1.945	46 ± 8

The errors appear in the differential cross-sections were calculated by considering the errors in each term of equation (4-23) as listed in table (5.23).

Table (5.23)

Experimental errors in the calculations of the differential cross-sections in copper.

Factor	Estimated error (%)
F_1	0.4
F_2	0.3
$\Delta\Omega$	0.8
$\epsilon(E_n)$	3.0
$\bar{x}$	<1.0
$1 - \exp(-n\sigma_T x)$	1.4 - 4.2
N	$(A^2 + B^2)^{1/2}$
σ_T	2.1

Similar to those in the aluminium, the differential elastic scattering cross-sections data for each thickness of copper sample were fitted with Legendre polynomial expansion of equation (5-1). The fits are shown as the smooth curves in figure (5.22) and the coefficients are given in table (5.24).

Table (5.24)

Legendre polynomial coefficients for elastic neutrons scattering from copper.

a_l	sample thickness (cm)				
	1.00	2.00	4.00	6.00	8.00
a_0	281.13	254.37	318.05	373.94	415.55
a_2	1123.80	986.39	1238.20	1454.10	1612.00
a_4	1444.20	1240.80	1550.70	1822.30	2012.00
a_6	1185.60	980.42	1204.80	1416.30	1565.80
a_8	739.56	572.87	680.58	797.49	887.98
a_{10}	298.72	197.62	213.74	250.28	286.16
a_{12}	49.67	-	-	-	-

The integrated elastic scattering cross-sections for each sample thickness were calculated using equation (5-7) in the angular range between 30° to 90°. The results are presented in table (5.25).

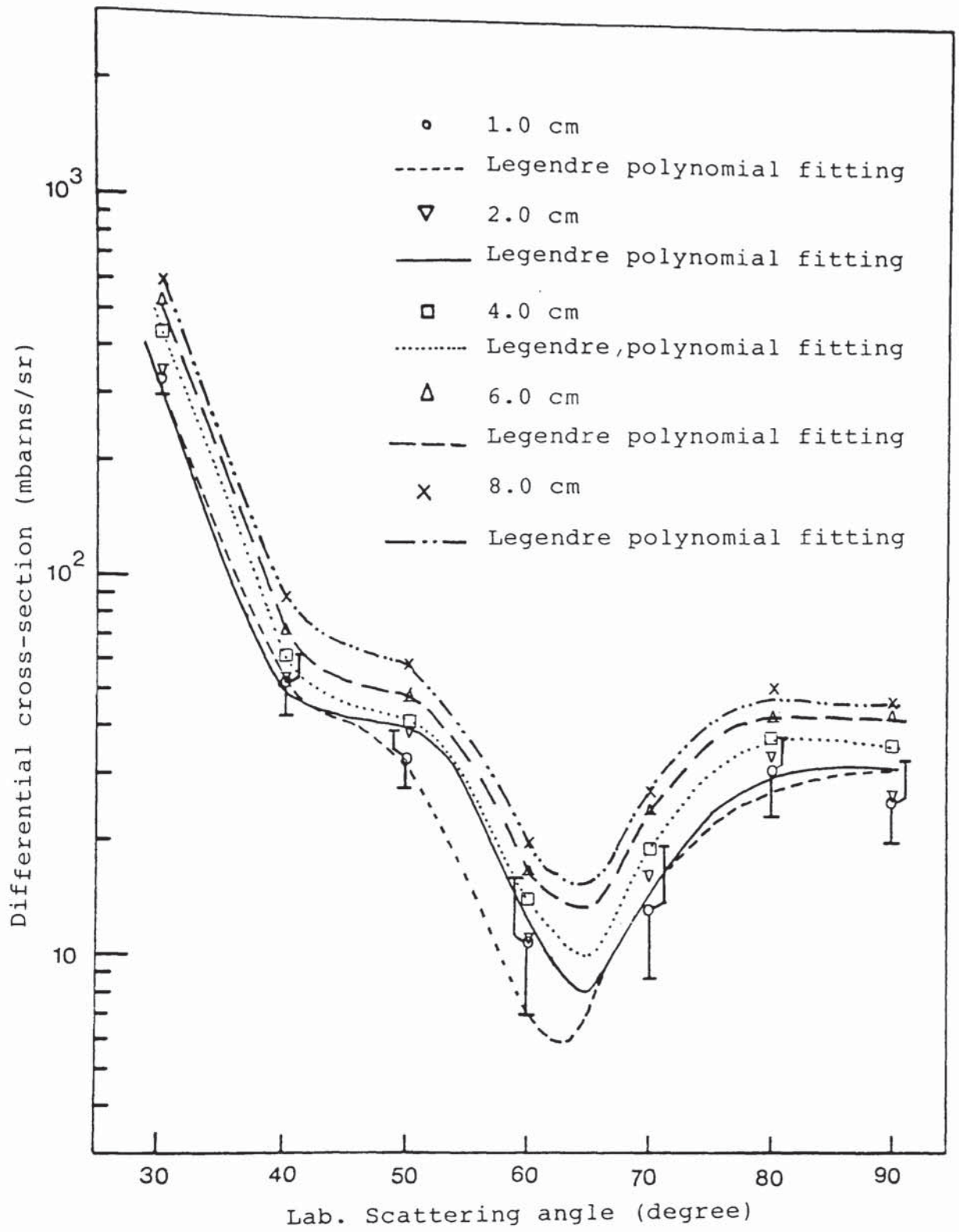

Figure (5.22):Angular distributions of neutron elastic scattering at 14.1 MeV neutron for different thicknesses of copper.

Table (5.25)

Integrated elastic scattering cross-sections in the angular range 30° to 90° for different thicknesses of copper in the laboratory system.

Sample thickness (cm)	$\sigma_{int} = \int_{\pi/6}^{\pi/2} d\sigma/d\Omega \cdot d\Omega$ mbarns
1.00	206 ± 17
2.00	222 ± 13
4.00	272 ± 13
6.00	321 ± 14
8.00	366 ± 16

5.2.3:EXPERIMENTAL RESULTS FOR THE DIFFERENTIAL INELASTIC CROSS-SECTION.

As shown in the neutron energy spectrum of copper (figures (5.19) and (5.20)), it was not possible to resolve the individual peaks of inelastic scattered neutrons. Therefore, only the angular distributions of scattered neutrons in different energy ranges were calculated. The experimental results for the differential scattering cross-sections in the enegy ranges E > 11 MeV, (11-8) MeV and (8-5) MeV for five different thicknesses of copper sample are presented in table (5.26).

Table (5.26)

Copper differential cross-sections for energy ranges E > 11 MeV, (11-8) MeV and (8-5) MeV for various sample thicknesses in the laboratory system.

θ_L°	Sample Thickness (cm)	$d\sigma/d\Omega(\theta_L)$ mbarns/sr		
		E > 11 (MeV)	(11-8) (MeV)	(8-5) (MeV)
30	1.00	404 ± 20	35 ± 7	56 ± 9
	2.00	383 ± 18	33 ± 5	45 ± 6
	4.00	513 ± 24	44 ± 4	78 ± 6
	6.00	617 ± 32	46 ± 4	85 ± 6
	8.00	658 ± 38	63 ± 5	109 ± 8
40	1.00	69 ± 7	18 ± 4	27 ± 5
	2.00	65 ± 5	18 ± 3	31 ± 4
	4.00	74 ± 5	22 ± 3	38 ± 4
	6.00	104 ± 7	27 ± 3	44 ± 4
	8.00	117 ± 8	32 ± 3	54 ± 5

Table (5.26):Continued

θ_L°	Sample thickness (cm)	$d\sigma/d\Omega(\theta_L)$ mbarns/sr		
		E > 11 (MeV)	(11-8) (MeV)	(8-5) (MeV)
50	1.00	42 ± 5	12 ± 4	21 ± 5
	2.00	47 ± 4	11 ± 3	19 ± 4
	4.00	55 ± 4	17 ± 3	31 ± 4
	6.00	64 ± 5	16 ± 3	28 ± 4
	8.00	73 ± 6	21 ± 3	38 ± 4
60	1.00	15 ± 3	7 ± 2	10 ± 3
	2.00	15 ± 3	7 ± 2	12 ± 3
	4.00	19 ± 3	9 ± 2	16 ± 2
	6.00	23 ± 3	12 ± 2	20 ± 3
	8.00	25 ± 3	13 ± 2	24 ± 3
70	1.00	18 ± 4	9 ± 3	17 ± 3
	2.00	20 ± 3	8 ± 2	14 ± 3
	4.00	23 ± 3	13 ± 3	24 ± 3
	6.00	28 ± 3	14 ± 3	24 ± 4
	8.00	34 ± 4	16 ± 3	26 ± 4
80	1.00	41 ± 6	13 ± 4	32 ± 6
	2.00	44 ± 5	14 ± 4	27 ± 5
	4.00	45 ± 5	16 ± 4	40 ± 5
	6.00	52 ± 6	19 ± 4	43 ± 6
	8.00	68 ± 7	21 ± 4	45 ± 6
90	1.00	40 ± 15	15 ± 9	33 ± 13
	2.00	38 ± 10	16 ± 6	35 ± 8
	4.00	51 ± 8	18 ± 4	40 ± 6
	6.00	67 ± 7	23 ± 4	38 ± 5
	8.00	68 ± 7	27 ± 4	45 ± 5

The errors appear in the differential cross-sections were calculated by considering the errors in each term of equation (4-23) as listed in table (5.23)

The angular distribution of scattered neutrons in the laboratory system for energy ranges E > 11 MeV, (11-8) MeV and (8-5) MeV corresponding to different sample thicknesses are plotted as shown in figures (5.23), (5.24)

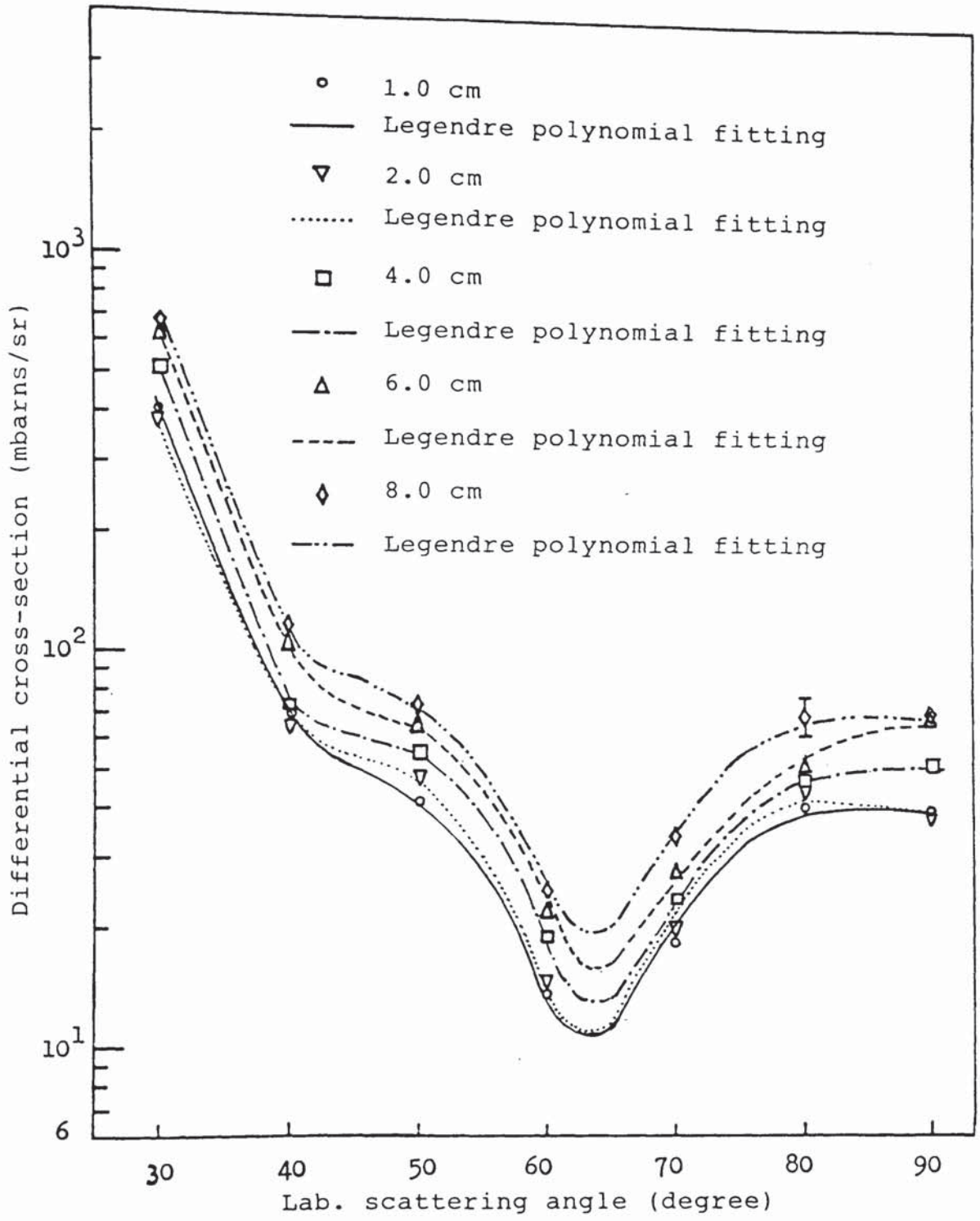

Figure (5.23):Angular distribution for the energy range E > 11 MeV at 14.1 MeV neutrons for different thicknesses of copper.

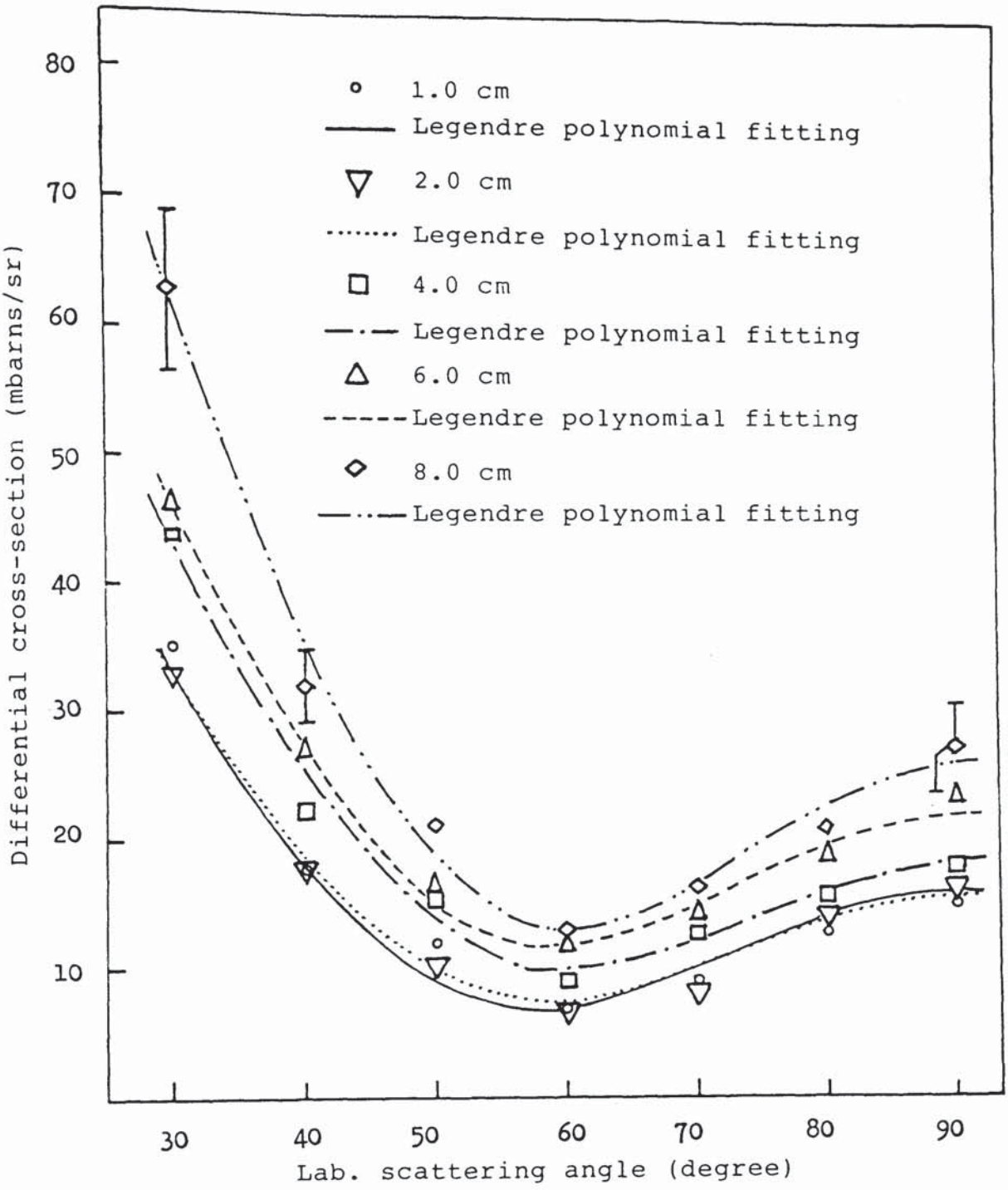

Figure (5.24):Angular distribution for the energy range (11-8) MeV at 14.1 MeV neutrons for different thicknesses of copper.

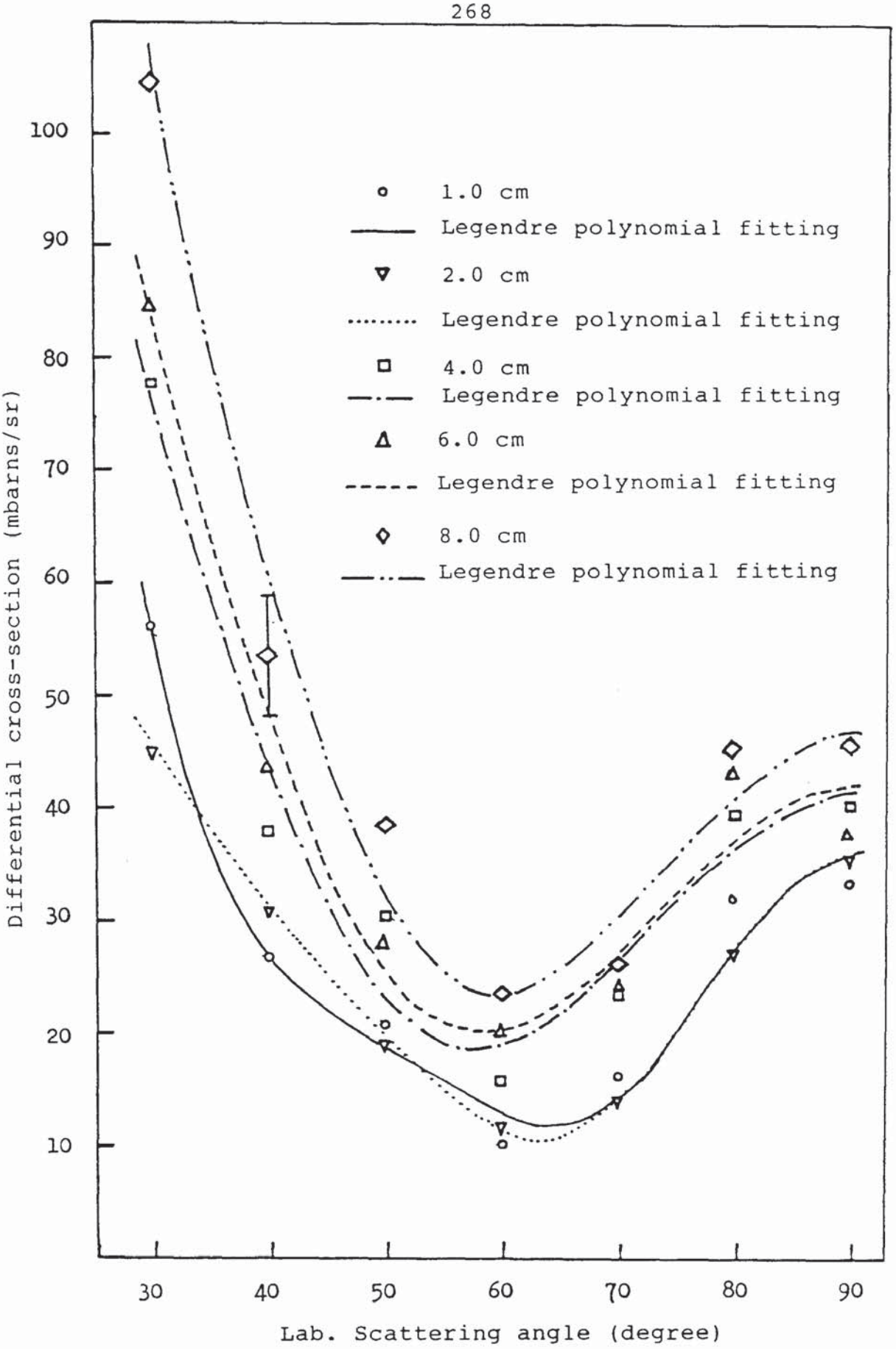

Figure (5.25):Angular distribution for the energy range (8-5) MeV at 14.1 MeV neutrons for different thicknesses of copper.

and (5.25) respectively. The smooth curves represent the Legendre polynomial fitting to the differential cross-section data using the similar procedure as before for different sample thicknesses.

The integrated cross-sections in the angular range 30° to 90° were calculated for each energy range and for each sample thickness using the similar procedure as before. The results in the laboratory system are tabulated in table (5.27).

Table (5.27)

Copper integrated cross-sections in the angular range 30° to 90° for different energy ranges and different sample thicknesses.

Sample thickness (cm)	$\sigma_{int} = \int_{\pi/6}^{\pi/2} d\sigma/d\Omega \cdot d\Omega$ mbarns		
	E > 11MeV	(11-8)MeV	(8-5)MeV
1.00	271 ± 13	69 ± 8	125 ± 11
2.00	272 ± 10	71 ± 6	125 ± 8
4.00	329 ± 11	90 ± 6	177 ± 8
6.00	410 ± 13	104 ± 6	187 ± 8
8.00	459 ± 15	125 ± 6	222 ± 9

5.2.4:THE VARIATION OF THE DIFFERENTIAL CROSS-SECTION WITH SAMPLE THICKNESS.

The experimental differential cross-sections for elastic scattered neutrons and for energy ranges E > 11 MeV, (11-8) MeV and (8-5) MeV for each scattering angle were fitted as a function of mean free path thickness using the least squares method discussed in section (5.1.3). The values of constant α obtained from the fitting for each angle and for each reaction are tabulated in table (5.28). Figures (5.26) through to (5.29) show the variation of the differential cross-section with thickness in term of mean free path. The solid lines appear in the figures were plotted using the average value of α .

Table (5.28)

The values of constant α obtained from least square fits to the experimental scattering cross-section data.

angle (deg)	Elastic Scattering	E > 11 MeV	(8-11) MeV	(5-8) MeV
30°	0.36 ± 0.04	0.34 ± 0.05	0.38 ± 0.09	0.45 ± 0.08
40°	0.31 ± 0.08	0.35 ± 0.07	0.39 ± 0.10	0.38 ± 0.08
50°	0.31 ± 0.10	0.32 ± 0.01	0.35 ± 0.14	0.35 ± 0.11
60°	0.37 ± 0.21	0.34 ± 0.03	0.39 ± 0.16	0.47 ± 0.13
70°	0.37 ± 0.16	0.36 ± 0.01	0.36 ± 0.15	0.39 ± 0.17
80°	0.27 ± 0.13	0.28 ± 0.05	0.29 ± 0.17	0.25 ± 0.11
90°	0.31 ± 0.21	0.38 ± 0.07	0.39 ± 0.20	0.15 ± 0.14
α_{av}	0.33 ± 0.14	0.34 ± 0.04	0.36 ± 0.15	0.35 ± 0.12

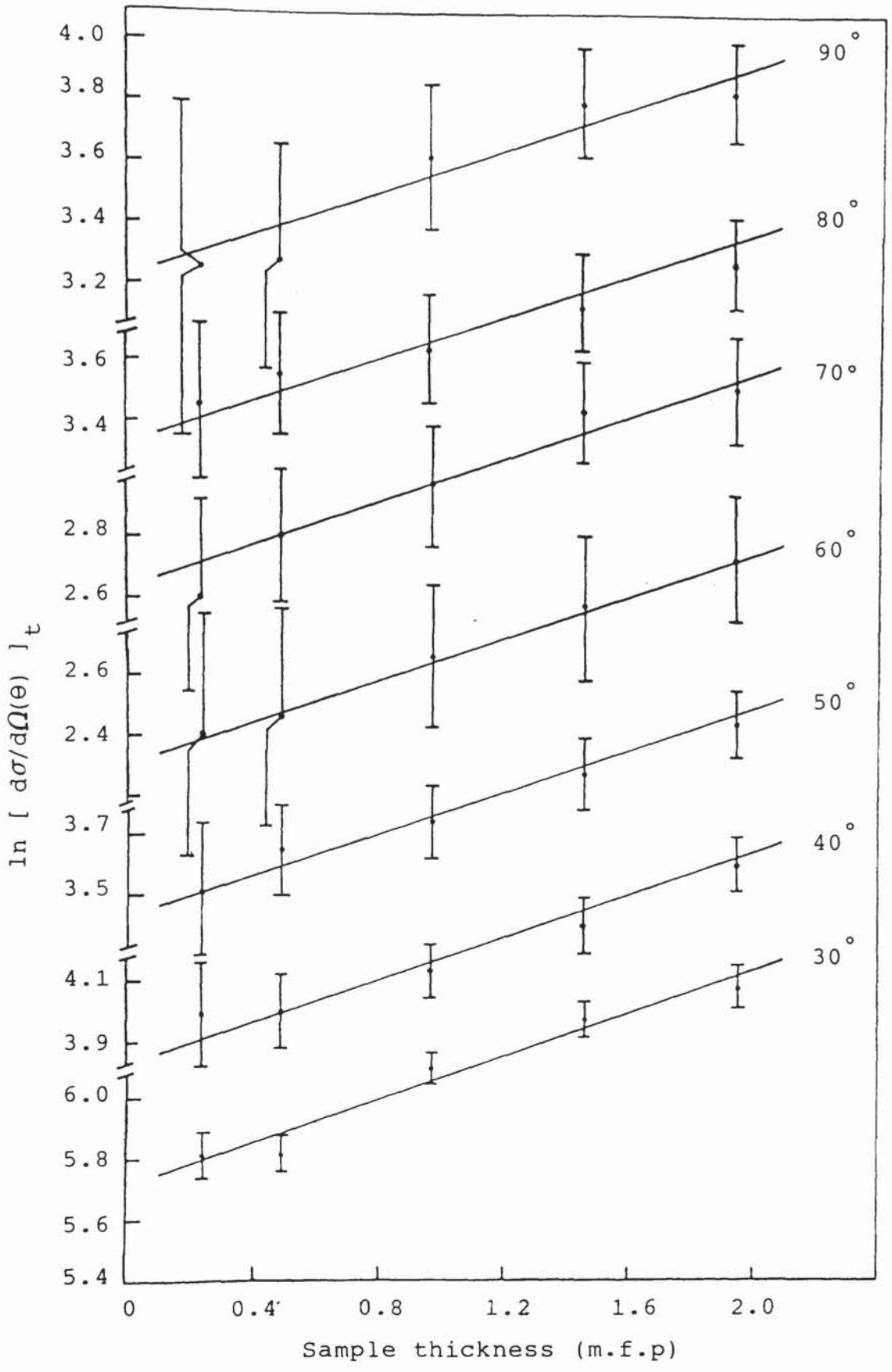

Figure (5.26): The variation of the copper differential elastic cross-section as a function of sample thickness at various scattering angles.

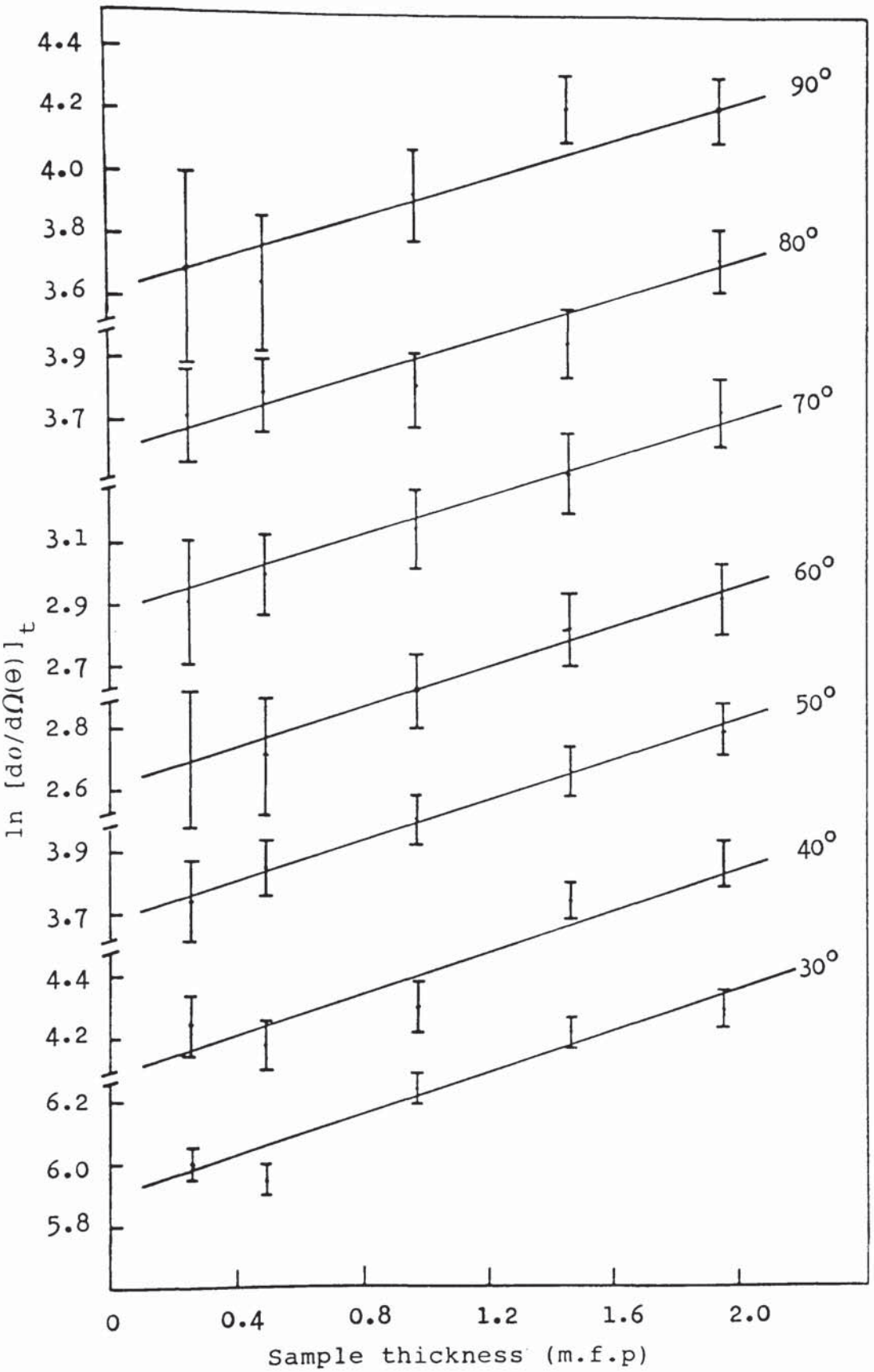

Figure (5.27): The variation of the copper differential cross-section for energy range E > 11 MeV as a function of sample thickness at various scattering angles.

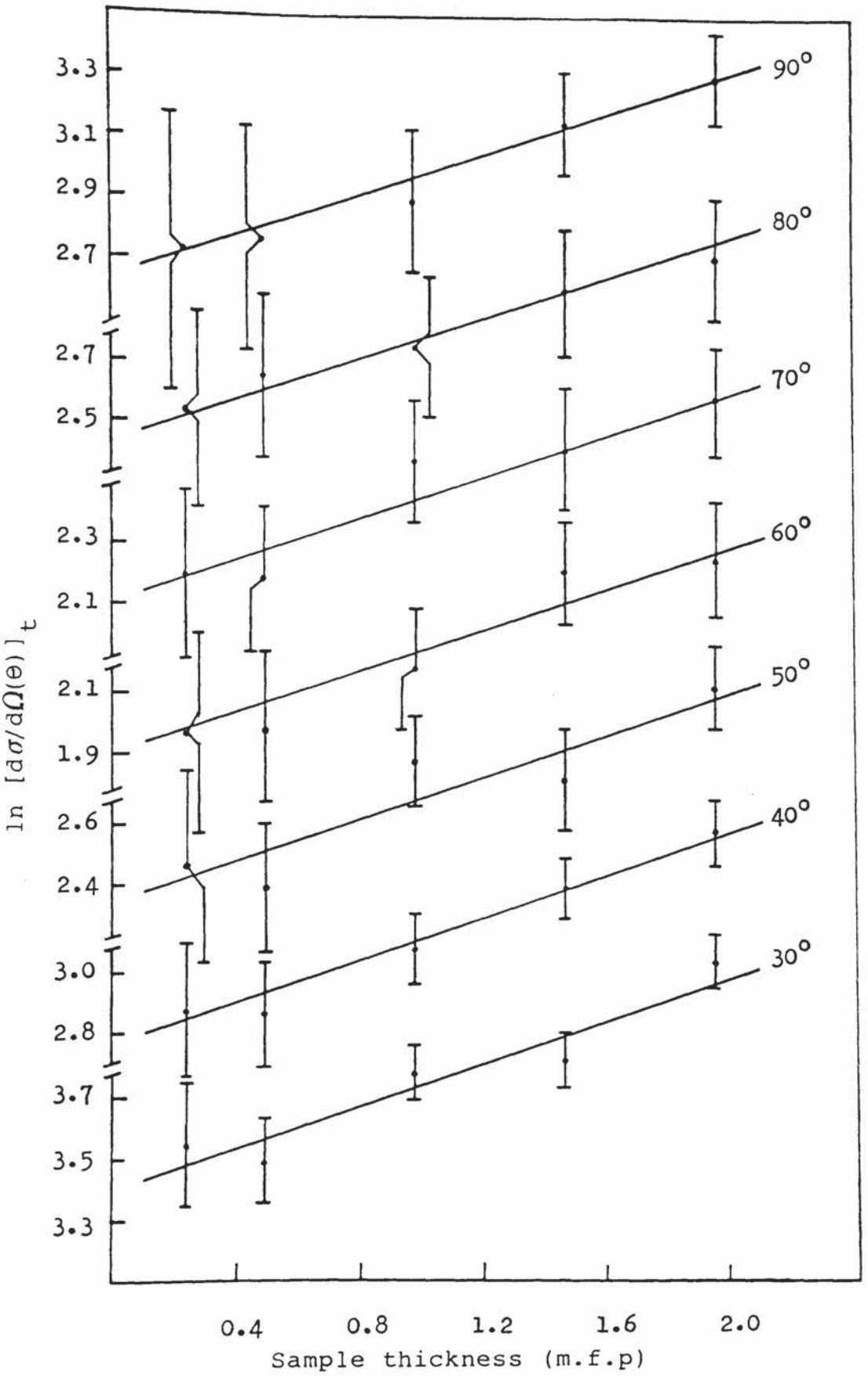

Figure (5.28): The variation of the copper differential cross-section for energy range (11-8) MeV as a function of sample thickness at various scattering angles.

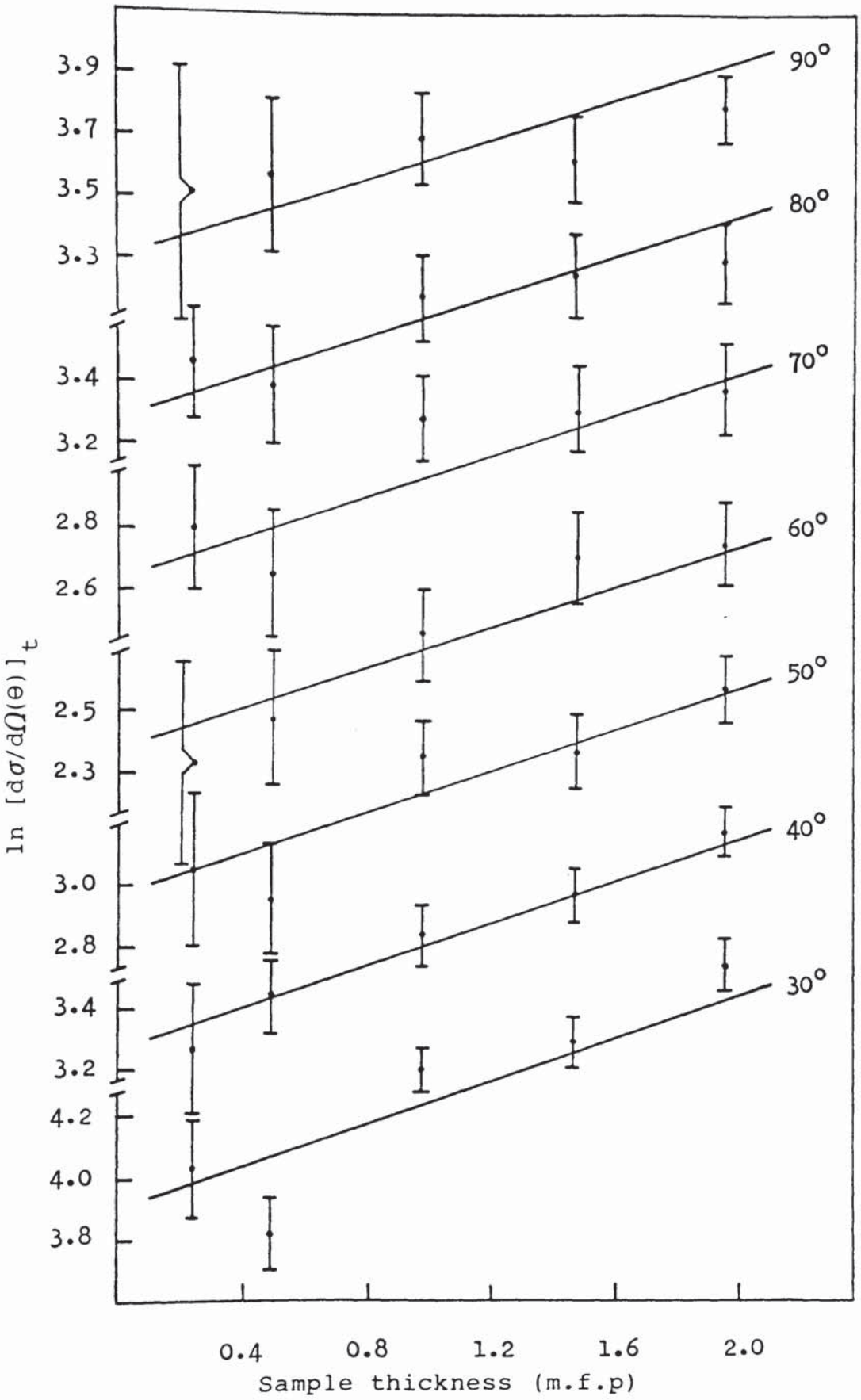

Figure (5.29):The variation of the copper differential cross-section for energy range (8-5) MeV as a function of sample thickness at various scattering angles.

The average value of constant α for copper sample was calculated as,

$$\alpha_{Cu} = 0.35 \pm 0.13 \ (m.f.p)^{-1}$$

The average value of constant α obtained from the present work for both aluminium and copper was found to be $(0.345 \pm 0.12) \ (m.f.p)^{-1}$. This value is in good agreement with the other measurements as listed in table (5.29) together with the present results.

Table (5.29)

The comparison of constant α obtained in the present work with other measurements.

Element	E_n (MeV)	$\alpha(m.f.p)^{-1}$	Reaction	Author
Al	14.1	0.36 ± 0.10	(n,n)	Present work
Al	14.1	0.35 ± 0.09	(n,n′)	Present work
Cu	14.1	0.33 ± 0.14	(n,n)	Present work
Cu	14.1	0.35 ± 0.12	(n,n′)	Present work
Concrete	14.1	0.45 ± 0.20	(n,n′γ)	Al-Shalabi(101)
Concrete	14.1	0.38 ± 0.14	(n,n)	Anvarian (102)
Fe	14.1	0.26 ± 0.10	(n,n)	Anvarian (102)
Fe	14.4	0.36 ± 0.13	(n,n′)	Anvarian (102)
Li	14.1	0.36 ± 0.11	(n,n)	Jasim (93)
Li	14.1	0.29 ± 0.11	(n,n′)	Jasim (93)
Li	14.4	0.45 ± 0.17	(n,n)	Jasim (93)
Pb	14.1	0.37 ± 0.12	(n,n)	Jasim (93)

5.2.5:EXPERIMENTAL RESULTS FOR THIN COPPER SAMPLE.

5.2.5.1:RESULTS FOR ELASTIC SCATTERING CROSS-SECTION.

Differential cross-sections for 14.1 MeV neutrons elastic scattering in copper have been measured at scattering angles between 30° to 90° with 5° increments . The results in the centre of mass system are tabulated in table (5.30).

Table (5.30)

Differential elastic scattering cross-sections for thin sample of copper in the centre of mass system at 14.1 MeV neutrons.

θ_c° (deg)	Present work mbarns/sr	ENDF-B4 mbarns/sr	Coon et al mbarns/sr
$30^{\circ}27'$	326 ± 21	309.1	300.2
$35^{\circ}31'$	115 ± 11	112.2	135.5
$40^{\circ}35'$	53 ± 9	51.9	50.1
$45^{\circ}39'$	42 ± 9	36.5	48.4
$50^{\circ}42'$	33 ± 7	24.2	31.5
$55^{\circ}45'$	13 ± 5	13.6	21.1
$60^{\circ}47'$	11 ± 4	7.7	10.6
$65^{\circ}49'$	8 ± 4	7.0	-
$68^{\circ}51'$	-	-	11.7
$70^{\circ}51'$	13 ± 4	12.4	-
$75^{\circ}53'$	19 ± 4	22.6	-
$78^{\circ}54'$	-	-	27.6
$80^{\circ}54'$	32 ± 8	30.4	-
$85^{\circ}54'$	33 ± 7	30.2	-
$90^{\circ}55'$	26 ± 16	24.2	-

The results of the differential elastic scattering cross-sections were plotted as a function of centre of mass scattering angle as shown in figure (5.30). From the

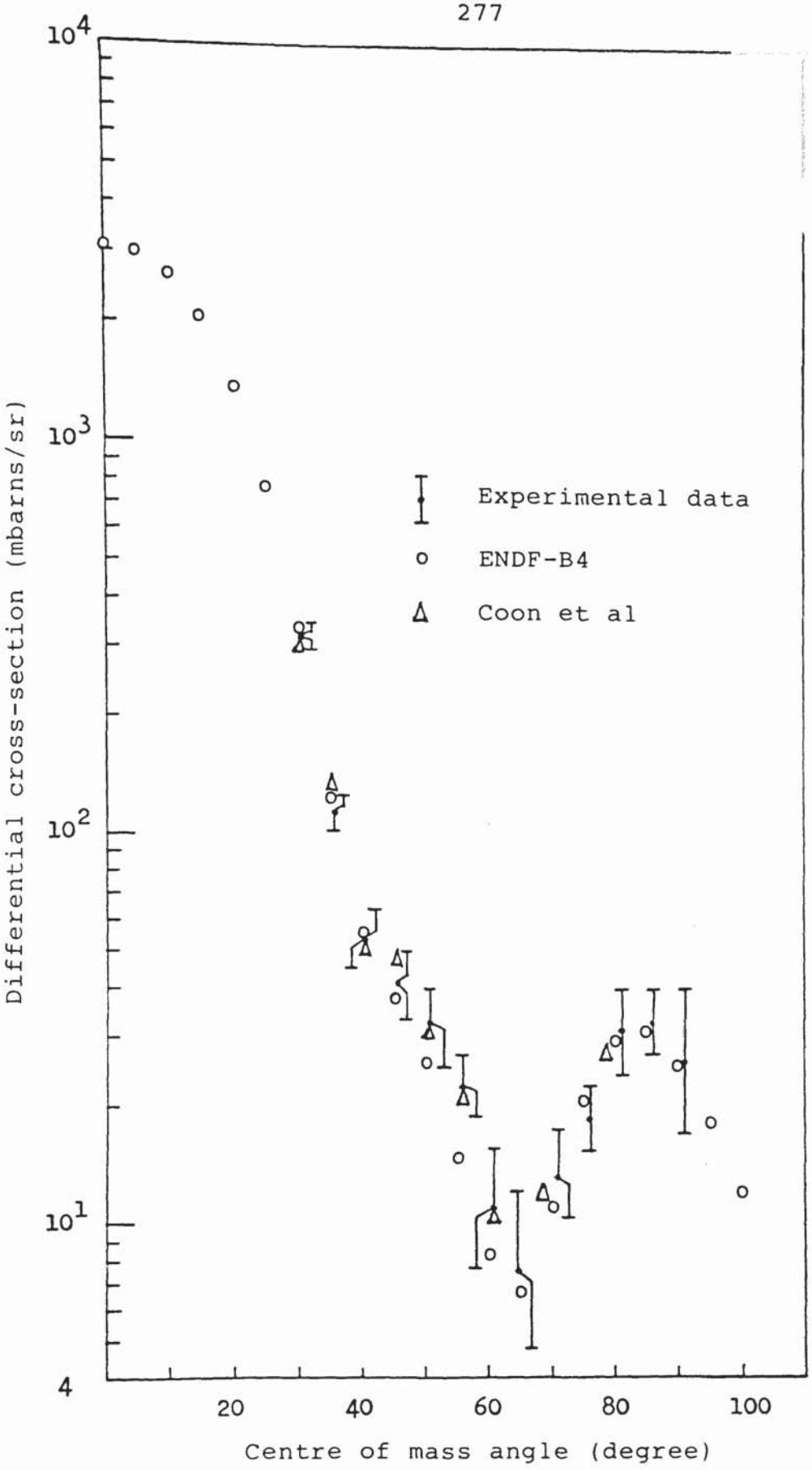

Figure (5.30):Comparison of the measurements of the differential elastic scattering cross-section from copper for 14.1 MeV neutrons.

figure, it appears that the present results are in reasonable agreement with the data from ENDF-B4 (103) and Coon et al (11) using ring Geometry.

The data of the differential elastic scattering cross-sections were fitted with Legendre polynomial expansion of equation (5.10). The fitting was done using the present experimental data together with the data from ENDF-B4 (103) for scattering angles above 100° . The maximum coefficients of order, l_{max} was determined using the same procedure to that in the thin sample of aluminium. The most suitable fitting was obtained with 11 th order series of polynomial with $\chi^2 < 0.8$. The Wick's limit for setting the lower limit of the differential elastic cross-section in the foward direction was calculated using equation (5.11) as σ_w = 3441 mbarns/sr. The 0° differential elastic cross-section obtained from the fitting was 3703 mbarns/sr and this value agrees with the value calculated from Wick's limit ($\frac{d\sigma}{d\Omega}(0^{\circ}) > \sigma_w$).

The Legendre polynomial fit is shown as the solid line in figure (5.31) and the coefficients and the integrated elastic cross-section are given in table (5.31) together with the data from ENDF-4 (103). The integrated cross section was calculated as $4\pi a_0$ where a_0 is the coefficient of zero order of the polynomial.

Table (5.31)

Legendre polynomial coefficients obtained from fits to the copper elastic scattering angular distributions at 14.1 MeV neutrons.

f_l	coefficients	
	Present work	ENDF-B4
f_0	1.000 ± 0.014	1.000
f_1	0.840 ± 0.012	0.835
f_2	0.732 ± 0.011	0.727
f_3	0.624 ± 0.011	0.617
f_4	0.506 ± 0.010	0.495
f_5	0.379 ± 0.008	0.366
f_6	0.262 ± 0.007	0.244
f_7	0.175 ± 0.006	0.155
f_8	0.115 ± 0.005	0.095
f_9	0.064 ± 0.004	0.046
f_{10}	0.025 ± 0.003	0.009
f_{11}	0.006 ± 0.002	-0.008
f_{12}	-	-0.012
f_{13}	-	-0.010
f_{14}	-	-0.007
f_{15}	-	-0.004
f_{16}	-	-0.001
σ_{int}	1544 ± 22 mb	1453 mb

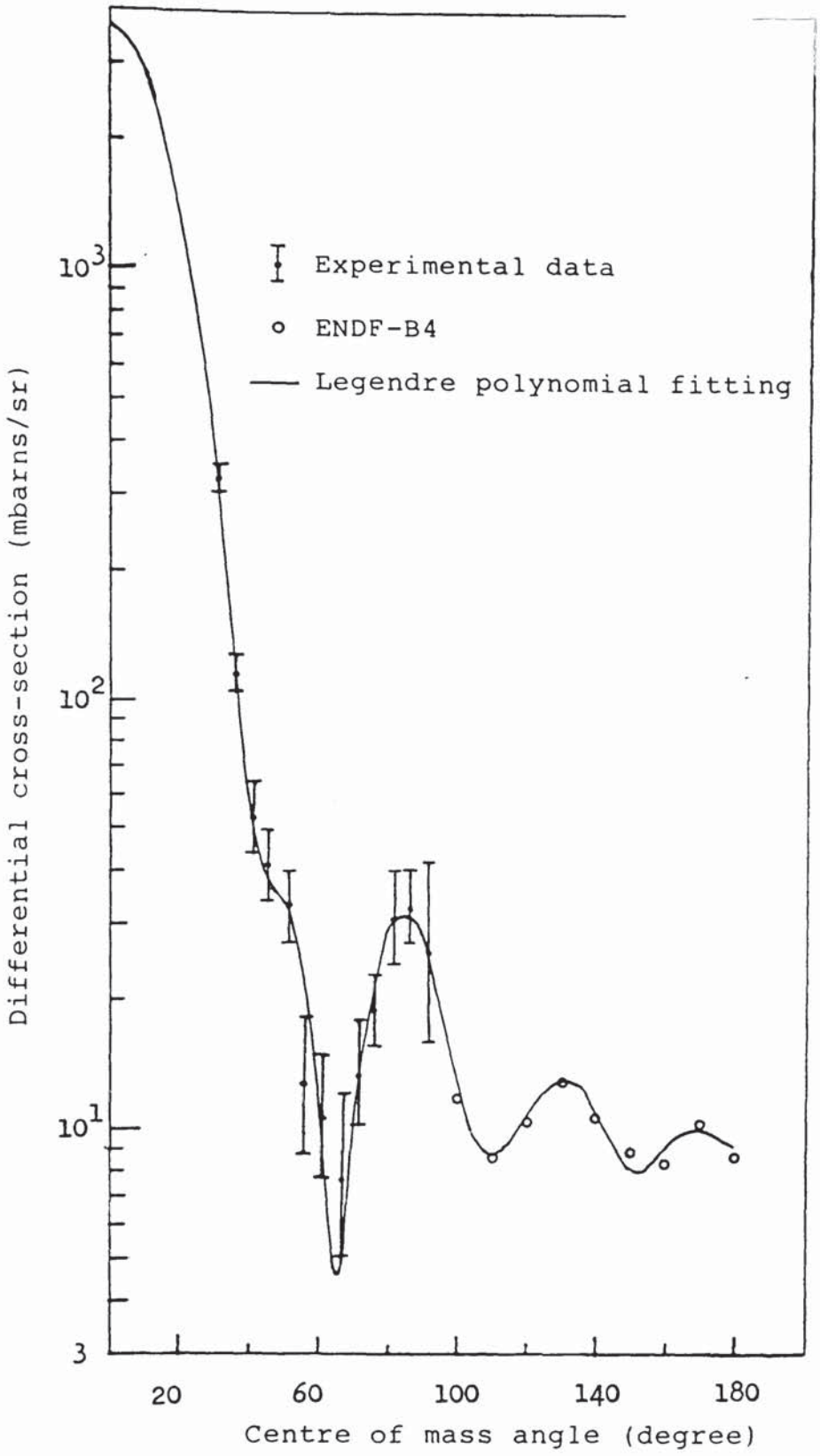

Figure (5.31): Legendre polynomial fits to the elastic scattering cross-section data for copper at 14.1 MeV neutrons.

Table (5.32) gives the comparison of the integrated elastic cross-section obtained in this work with the other published data (11,103,104).

Table (5.32)

Comparison of the integrated elastic cross-sections for copper at 14 MeV neutrons in the centre of mass system.

σ_{int} mbarns/sr	Author
1544 ± 22	Present work
1453	ENDF-B4 (103)
1510	UKNDL (104)
1450 ± 70	Coon et al (11)

5.2.5.2:RESULTS FOR DIFFERENTIAL CROSS-SECTION IN THE ENERGY RANGES.

The differential scattering cross-sections in the energy ranges E > 11 MeV, (11-8) MeV and (8-5) MeV for thin sample of copper are presented in table (5.33) in the centre of mass coordinate system.

Table (5.33)

Differential scattering cross-sections for energy ranges E > 11 MeV, (11-8) MeV and (8-5) MeV in thin sample of copper in the centre of mass system.

θ_c°	$d\sigma/d\Omega(\theta)$ mbarns/sr		
	E > 11MeV	(11-8)MeV	(8-5)MeV
30°27'	393 ± 20	33 ± 6	53 ± 8
35°31'	155 ± 10	19 ± 5	33 ± 7
40°35'	68 ± 6	17 ± 4	25 ± 5
45°39'	62 ± 7	12 ± 5	21 ± 6
50°42'	41 ± 5	11 ± 4	20 ± 5
55°45'	20 ± 5	8 ± 3	16 ± 5
60°47'	14 ± 3	7 ± 2	10 ± 3
65°51'	12 ± 4	5 ± 3	9 ± 4
70°51'	18 ± 4	9 ± 2	16 ± 3
75°53'	28 ± 5	11 ± 4	20 ± 3
80°54'	41 ± 6	13 ± 4	32 ± 6
85°54'	51 ± 14	20 ± 12	32 ± 16
90°55'	40 ± 14	15 ± 10	33 ± 13

Figure (5.32) shows the angular distributions of scattered neutrons for each energy range. The solid lines represent the Legendre polynomial fitting obtained using the same procedure as before. The results of the Legendre polynomial coefficients are tabulated in table (5.34) for each energy range. The best fit to the data in the angular range studied were obtained by specifiying only even terms in the polynomial.

Table (5.34)

Legendre polynomial coefficients obtained from fits to the copper differential cross-sections for energy ranges at 14.1 MeV neutrons.

	coefficients		
f_l	E > 11 MeV	(11-8)MeV	(8-5)MeV
f_0	1.000 ± 0.047	1.000 ± 0.046	1.000 ± 0.100
f_2	0.762 ± 0.041	0.264 ± 0.029	0.445 ± 0.089
f_4	0.523 ± 0.032	0.170 ± 0.021	0.341 ± 0.070
f_6	0.273 ± 0.021	-	0.141 ± 0.046
f_8	0.119 ± 0.011	-	0.087 ± 0.025
f_{10}	0.029 ± 0.005	-	0.016 ± 0.009

Table (5.35) gives the integrated cross-sections in the angular range 30° to 90° for thin sample of copper in the centre of mass system. The calculations were done

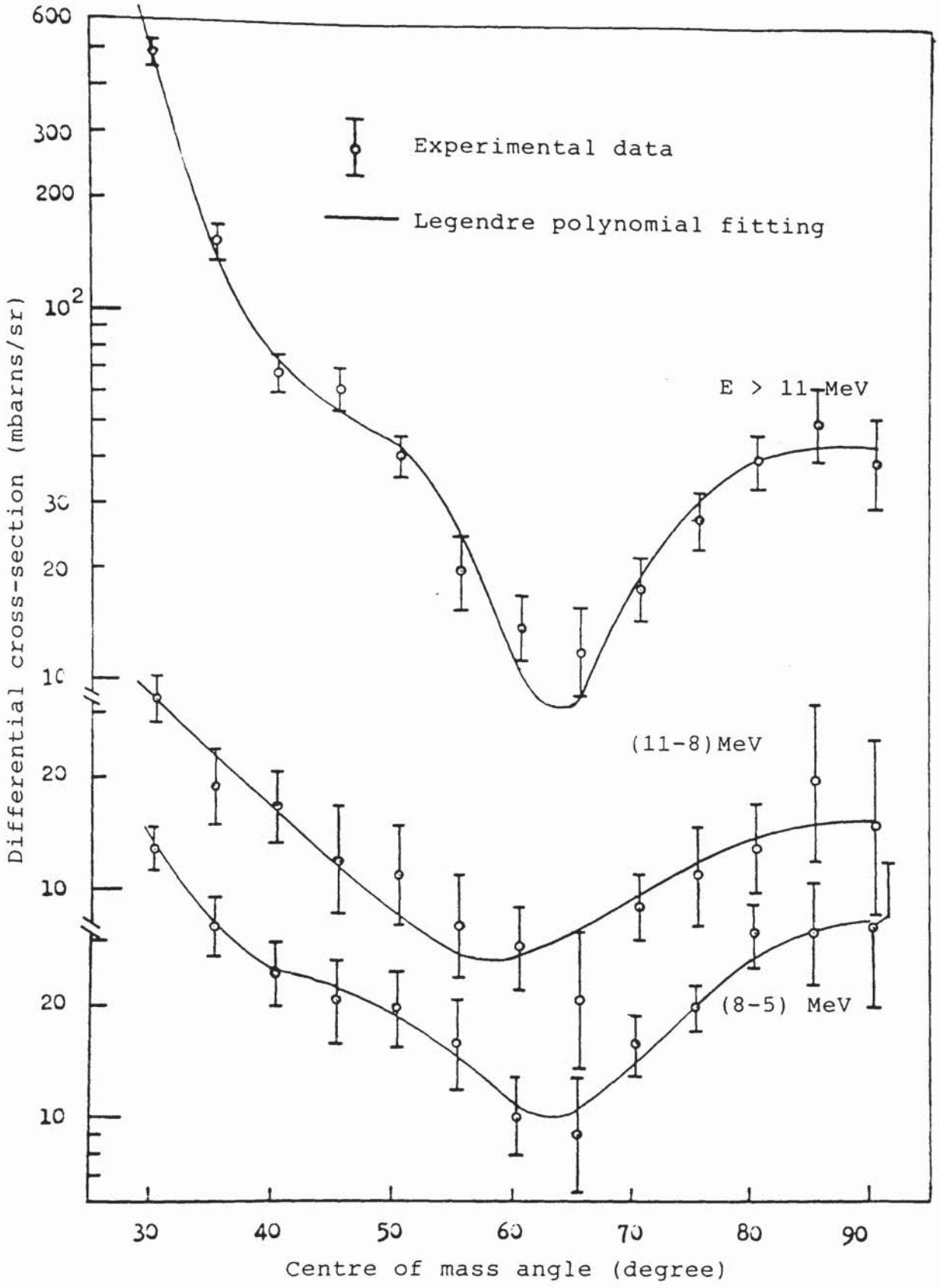

Figure (5.32):Legendre polynomial fits to the differential cross-section data for copper in the energy ranges.

using equation (5-7).

Table (5.35)

Integrated cross-sections in the angular range 30° to 90° for 14.1 MeV neutrons from thin copper sample in the centre of mass system.

Reaction	$\sigma_{int} = \int_{\pi/6}^{\pi/2} d\sigma/d\Omega . d\Omega$ mb	
	Present work	ENDF-B4
Elastic	213 ± 17	200.7
E > 11MeV	284 ± 13	-
(11-8)MeV	67 ± 8	-
(8-5)MeV	121 ± 11	-

5.3:RESULTS FOR MOLYBDENUM SAMPLE.

5.3.1:THE BACKGROUND OF THE SAMPLE.

The scattering sample used in this experiment was molybdenum powder, -100 mesh supplied by Aldrich Chemical Co. Ltd with 99+% purity. Natural molybdenum consists seven stable isotopes with the natural abundances given in table (5.36).

Table (5.36)

Natural abundances of molybdenum isotopes.

Isotope	Abundance (%)
^{92}Mo	15.84
^{94}Mo	9.04
^{95}Mo	15.72
^{96}Mo	16.53
^{97}Mo	9.46
^{98}Mo	23.78
^{100}Mo	9.63

Because of the limited amount of the sample, the measurements of the differential cross-section were made only for thin sample. The molybdenum power was canned in thin aluminium container in rectangular slab geometry with inside dimension of 15 cm x 20 cm and 3 cm thickness corresponding to 0.199 m.f.p of molybdenum at 14 MeV neutrons.

The differential cross-section measurements on molybdenum were made using the same procedure as used in aluminium measurements. An empty aluminium container was used for background subtraction. Alternate run were done with the molybdenum sample in the position and the empty aluminium container in the same position for the same number of alpha-counts. The sample-detector distance used in these measurements was 120.5 cm.

Typical examples of the time of flight spectrum of molybdenum measured at scattering angles 40° and 70° are presented in figure (5.33) and (5.34) respectively. In order to analyze the time of flight spectrum it is necessary to know the properties of the energy levels of molybdenum isotopes. The energy levels for all accuring isotopes of molybdenum are given in figures (5.35) through to (5.37) taken from reference (94).

The time of flight spectrum of molybdenum consists primary peak of neutrons elastic scattering with the secondary peaks of neutrons inelatic scattering are not resolved individually. The left hand side of the elastic peak was broadened by the contribution of the low energy inelastic peaks of the excited states. However, using the same procedure of Gaussian fitting as used in aluminium and copper samples, the contribution of inelastic peaks in the elastic peak can be eliminated.

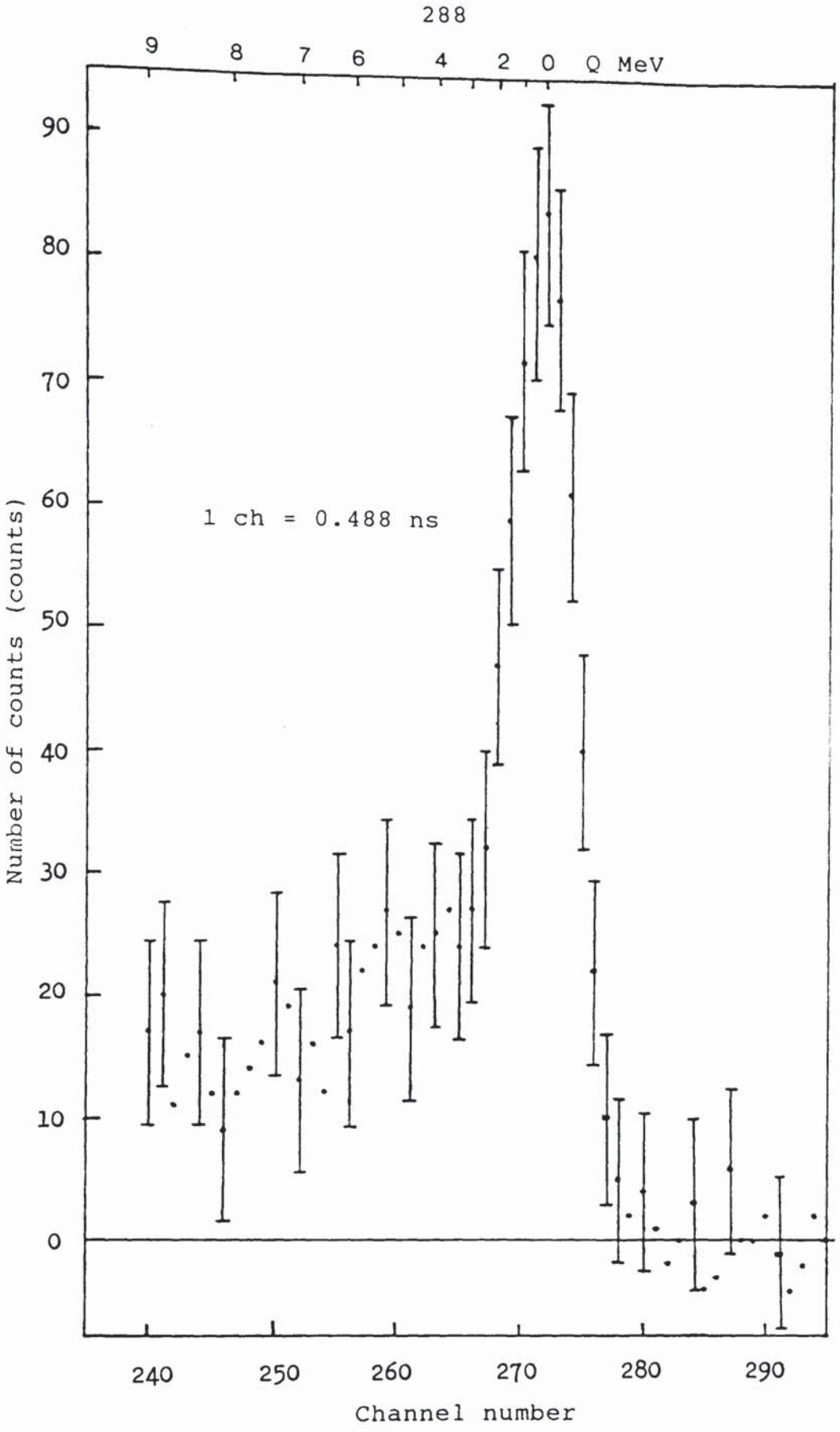

Figure (5.33):The time of flight spectrum of 14.1 MeV neutrons for scattering angle 40° scattered from 3 cm of molybdenum.

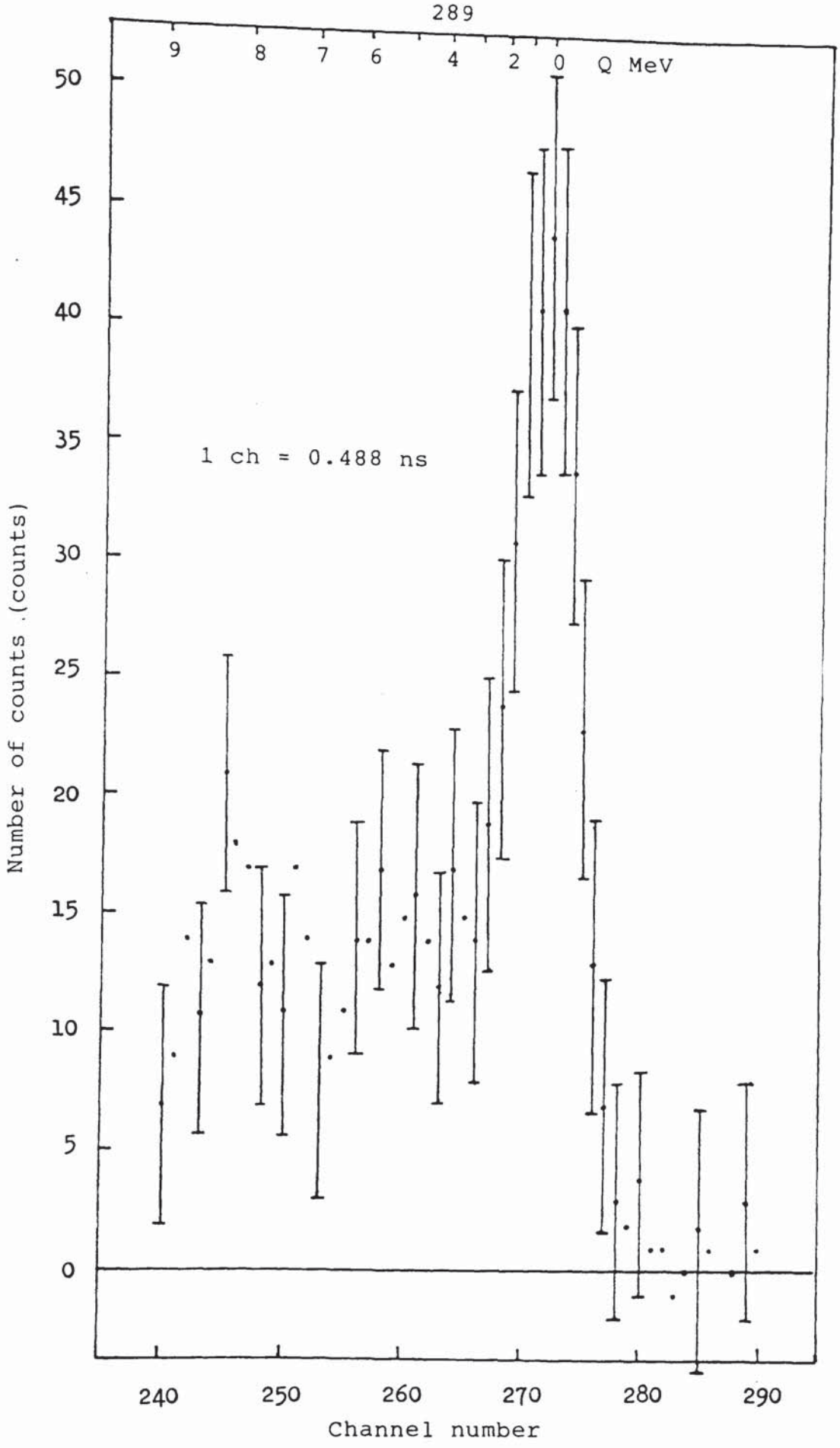

Figure (5.34):The time of flight spectrum of 14.1 MeV neutrons for scattering angle 70° scattered from 3 cm of molybdenum.

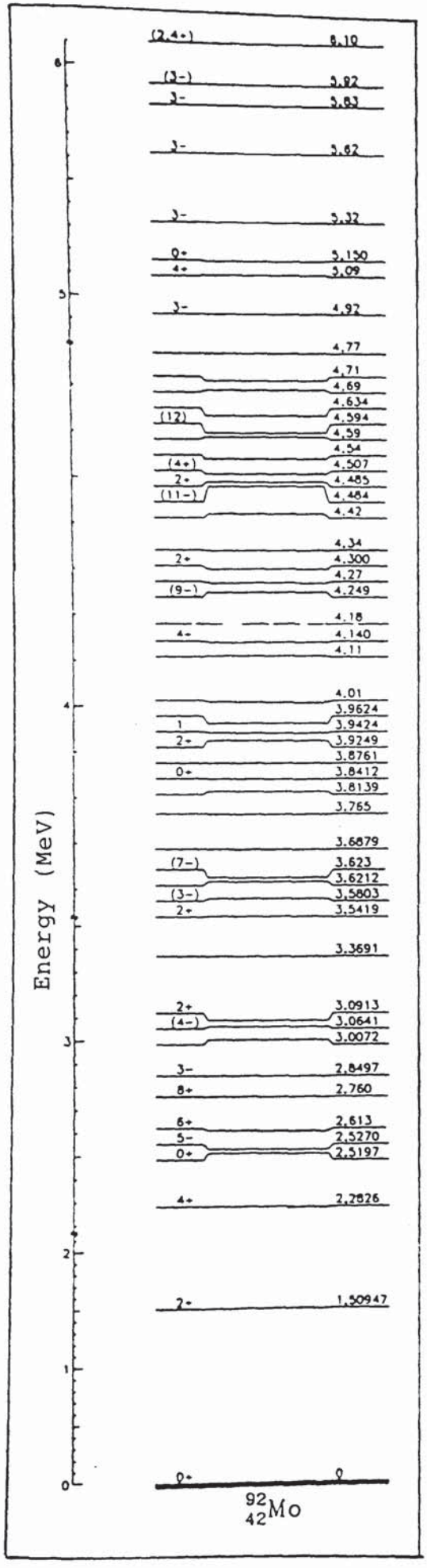

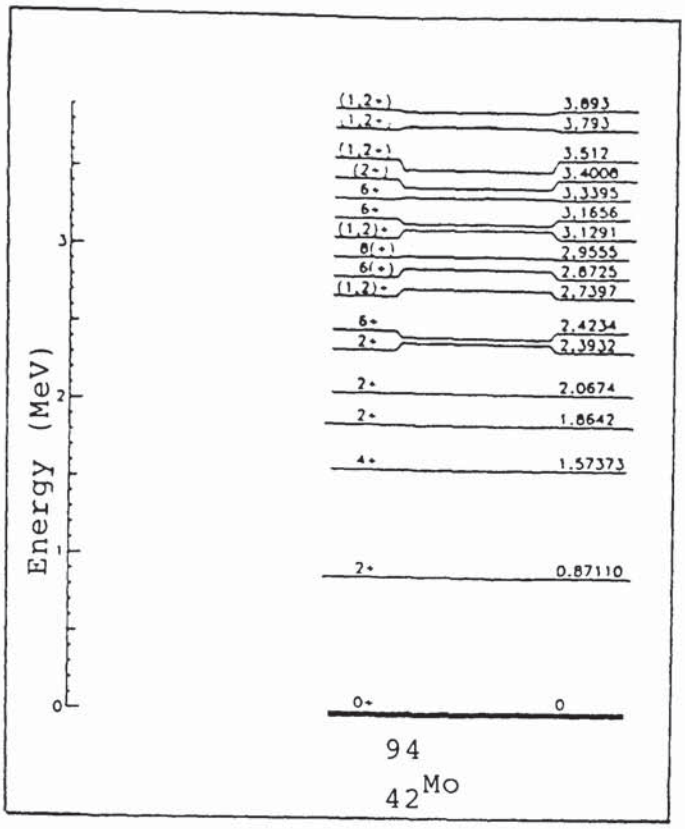

Figure (5.35):Energy level diagram of ^{92}Mo and ^{94}Mo.

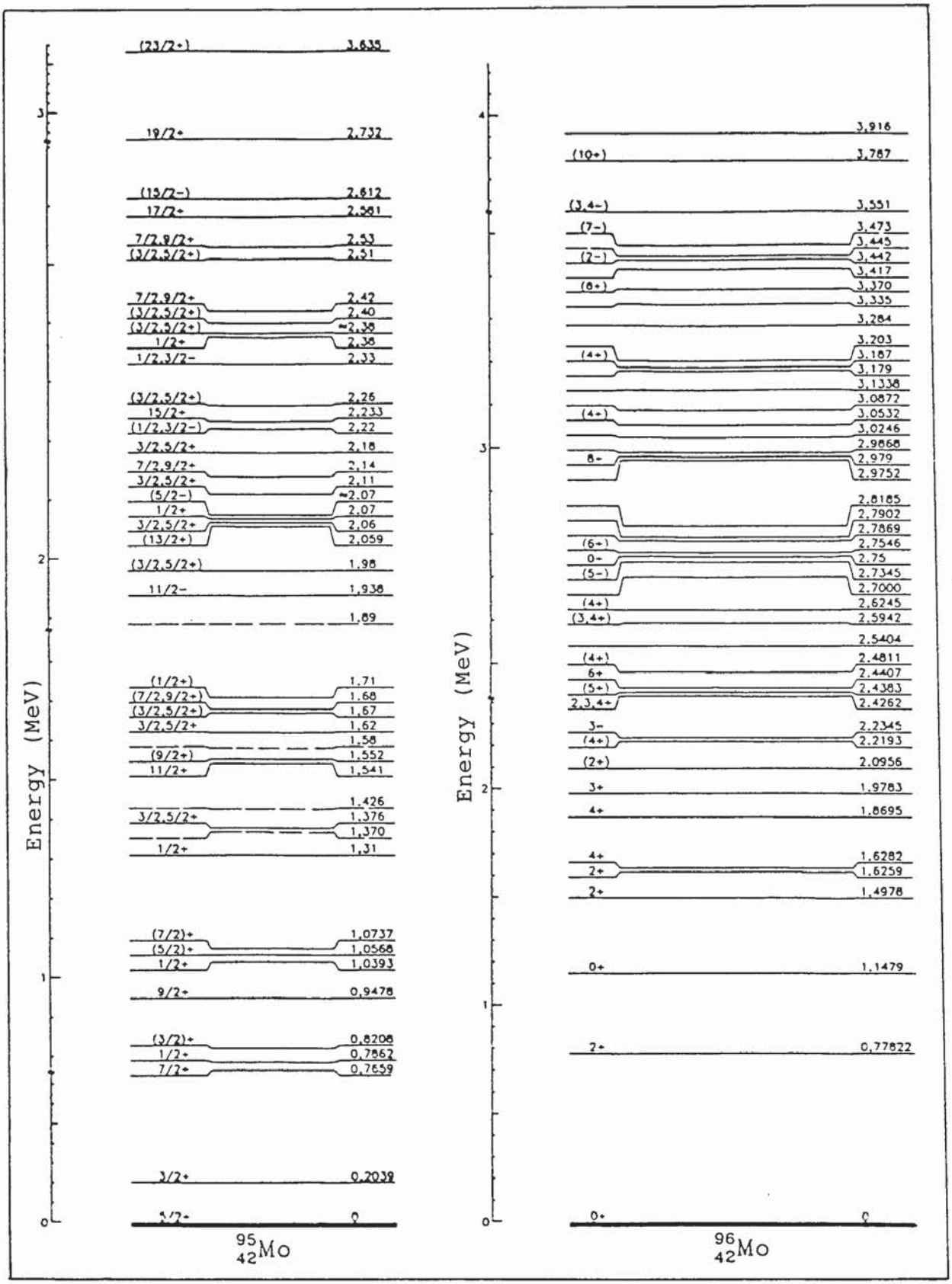

Figure (5.36):The energy level diagrams of Mo^{95} and Mo^{96}.

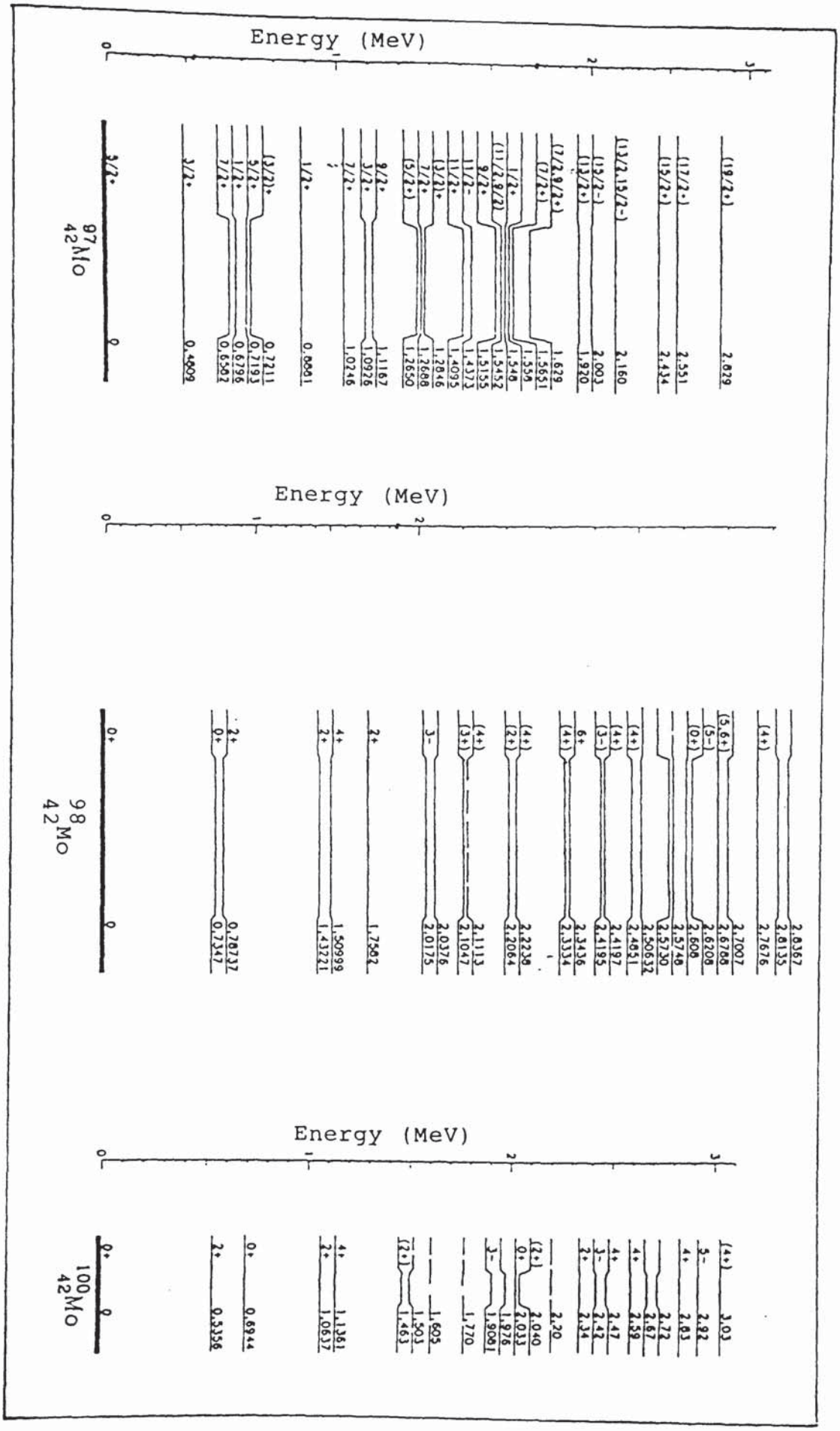

Figure (5.37): Energy level diagram of ^{97}Mo, ^{98}Mo and ^{100}Mo.

5.3.2:RESULTS FOR THIN SAMPLE OF MOLYBDENUM.

5.3.2.1:RESULTS FOR ELASTIC SCATTERING CROSS-SECTION.

The differential cross-sections for 14.1 MeV neutrons elastic scattering in molybdenum have been measured at scattering angles between 30° to 90° with 5° increments. The calculations of the differential cross-sections were done using equation (4-23) and the results after converted to the centre of mass system are tabulated in table (5.37) together with the results published by Strizhak et al (17).

Table (5.37)

Differential elastic scattering cross-sections of 14.1 MeV neutrons for thin sample of molybdenum in the centre of mass system.

θ_c°	Present work (mbarns/sr)	Strizhak et al (mbarns/sr)
$30^{\circ}18'$	376 ± 44	359.4
$35^{\circ}21'$	170 ± 22	133.4
$40^{\circ}23'$	51 ± 9	49.3
$45^{\circ}26'$	17 ± 5	17.0
$50^{\circ}28'$	33 ± 8	31.9
$55^{\circ}30'$	40 ± 8	35.8
$60^{\circ}31'$	35 ± 8	31.9
$65^{\circ}33'$	30 ± 8	34.0
$70^{\circ}34'$	34 ± 8	36.1
$75^{\circ}35'$	29 ± 7	25.0
$80^{\circ}36'$	25 ± 10	27.2
$85^{\circ}36'$	15 ± 6	19.1
$90^{\circ}36'$	11 ± 4	12.0

The errors indicated in the present experimental results were calculated by considering each term in equation (4-23) as listed in table (5.38).

Table (5.38)

Experimental errors in the calculations of the differential cross-sections in molybdenum.

Factor	Estimated error (%)
F_1	0.4
F_2	0.3
$\Delta\Omega$	0.8
$\bar{x}$	< 1.0
$1- \exp(-n\sigma_T x)$	11
$N_e(\theta)$	$\left[\Sigma(A_i^2 + B_i^2)\right]^{\frac{1}{2}}$
$\epsilon(E_n)$	3.0
σ_T	1.5

Figure (5.38) shows that the present results are in reasonable agreement with Strizhak at al (17) in this angular range. The data obtained by Strizhak et al (17) were made using toroidal scatterer and the measurements were done in the angular range 15° to 160° with 5° increments.

The data of the differential elastic scattering cross-sections were fitted with Legendre polynomial

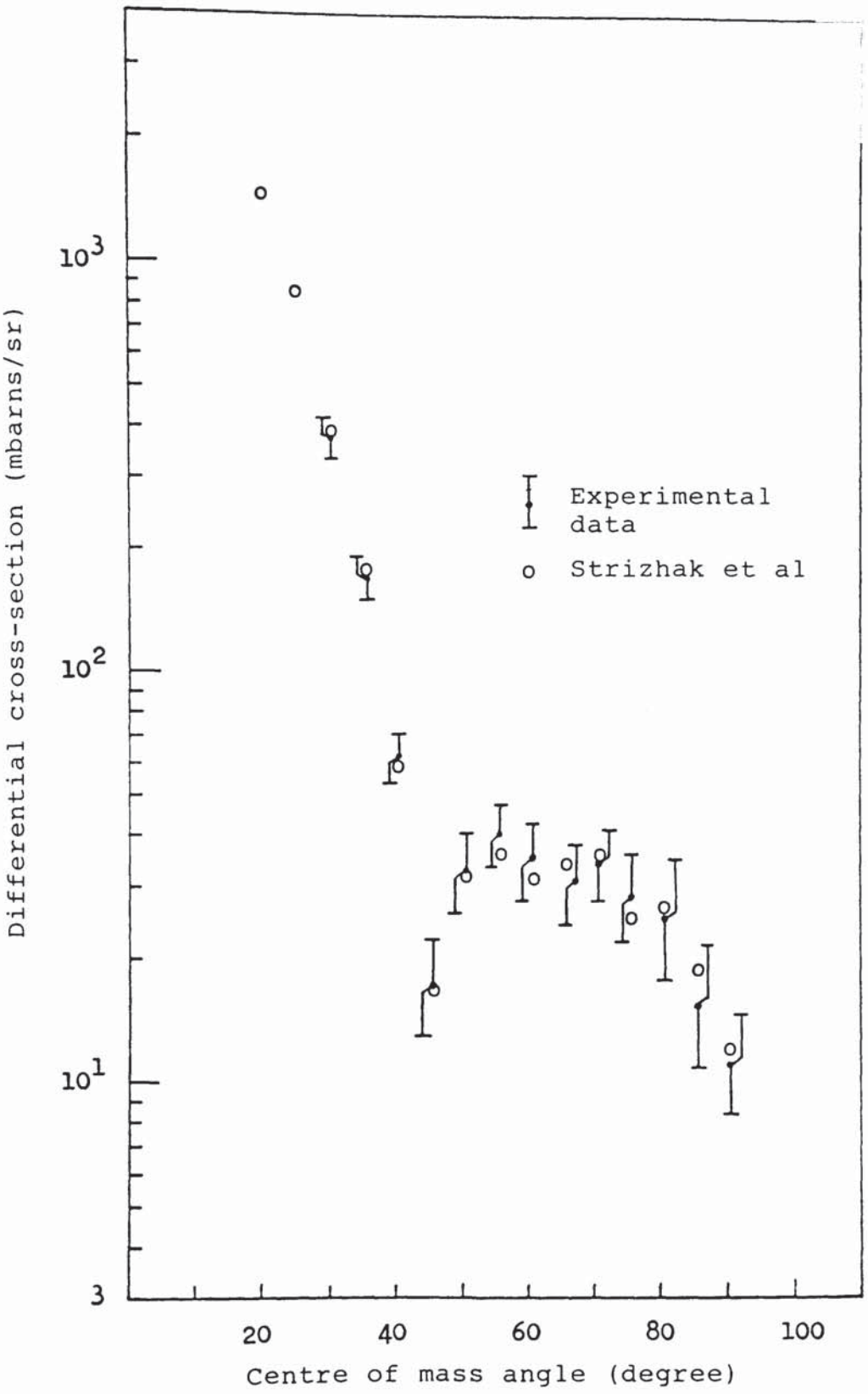

Figure (5.38):Molybdenum differential elastic cross-sections for 14.1 MeV neutrons in the centre of mass-system.

expansion of equation (5-10). The fitting was done using the present experimental data and the data from Strizhak et al (17) for scattering angles above 100°. Using the same procedure as in thin sample of aluminium and copper, the most suitable fitting for molybdenum data was obtained with 17 th order series of polynomial with $\chi^2 < 0.2$. The 0° differential elastic cross-section obtained from the fitting was 7495 mbarns/sr and this value agrees with the Wick's limit with the value of 6370 mbarns/sr calculated from equation (5-11).

The Legendre polynomial fit is shown as a solid line in figure (3.39) and the coefficients and integrated elastic scattering are given in table (5.39). The integrated cross-section was calculated as $4\pi a_0$ where a_0 is the coefficient of zero order of the polynomial.

Table (5.40) gives the comparison of the integrated elastic cross-section obtained in this work with other published data (105,106). The result obtained agrees well within the experimental error.

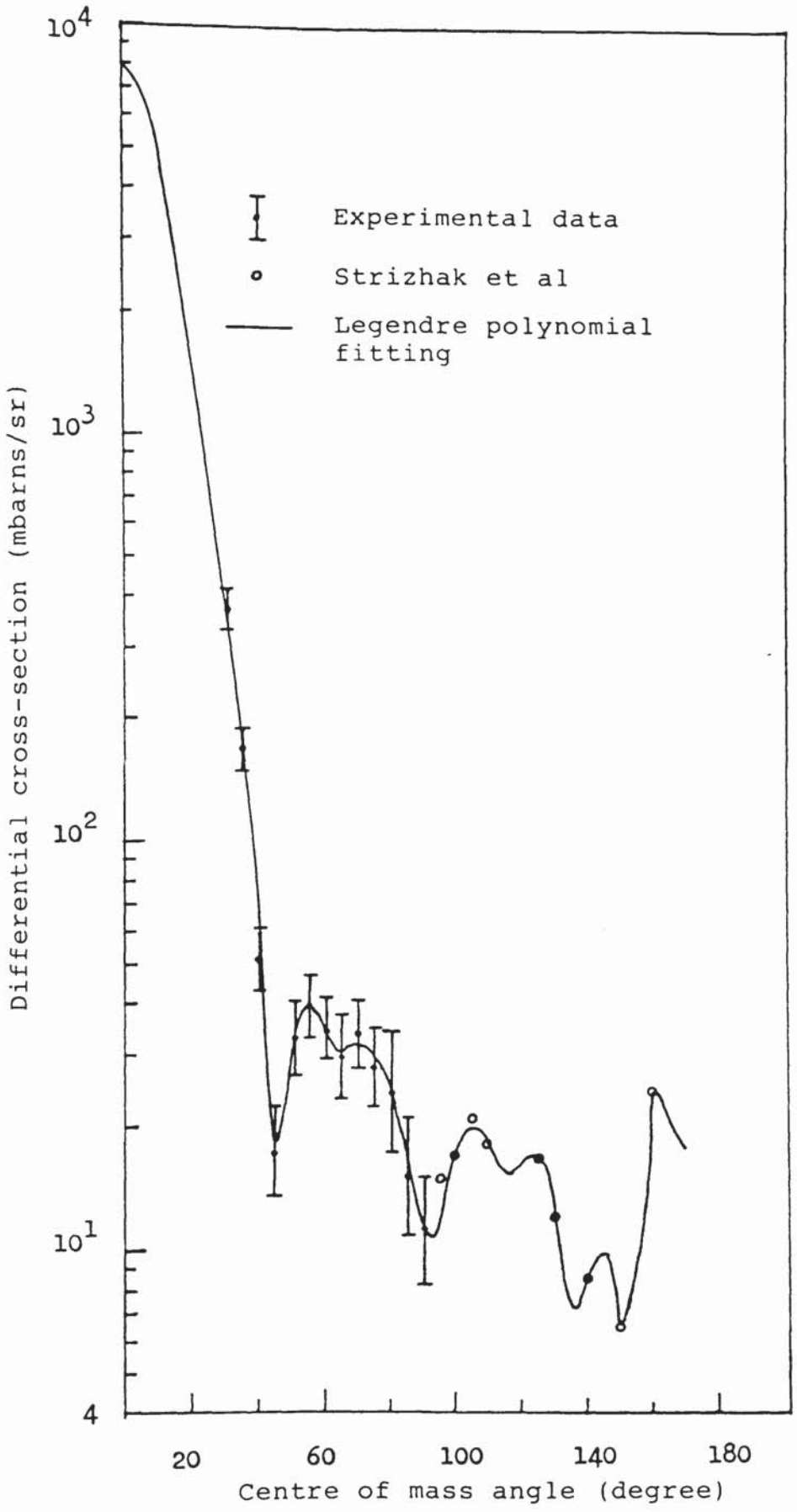

Figure (5.39):Legendre polynomial fits to the elastic cross-section data for molybdenum at 14.1 neutrons.

Table (5.39)

Legendre polynomial coefficients and integrated elastic scattering cross-section obtained from fits to the molybdenum elastic scattering angular distribution at 14.1 MeV neutrons.

f_l	Coefficient
f_0	1.000 ± 0.027
f_1	0.862 ± 0.038
f_2	0.763 ± 0.027
f_3	0.667 ± 0.035
f_4	0.561 ± 0.024
f_5	0.458 ± 0.032
f_6	0.360 ± 0.021
f_7	0.272 ± 0.027
f_8	0.196 ± 0.017
f_9	0.150 ± 0.020
f_{10}	0.108 ± 0.012
f_{11}	0.084 ± 0.014
f_{12}	0.057 ± 0.008
f_{13}	0.046 ± 0.009
f_{14}	0.029 ± 0.004
f_{15}	0.020 ± 0.004
f_{16}	0.007 ± 0.002
f_{17}	0.005 ± 0.002
σ_{int}	2055 ± 55 mbarns

Table (5.40)

Comparison of the integrated elastic cross-sections for molybdenum at 14.1 MeV neutrons.

(mbarns/sr)	Author
2055 ± 55	Present work
2088	UKNDL (106)
2050	ENDF-B4 (105)

5.3.2.2:RESULTS FOR THE DIFFERENTIAL CROSS-SECTION IN THE ENERGY RANGES.

Because of the difficulty of resolving the induvidual peaks of inelastic scattered neutrons, only differential cross-sections of molybdenum in different energy ranges were calculated. The results in the energy ranges E > 11 MeV, (11-8) MeV and (8-5) MeV are tabulated in table (5.41).

Table (5-41)

Differential cross-sections for energy ranges E > 11 MeV, (11-8) MeV and (8-5) MeV for molybdenum scattered from 14.1 MeV neutrons in the centre of mass system.

θ_c (deg)	$d\sigma/d\Omega(\theta_c)$ mbarns/sr		
	E > 11MeV	(11-8)MeV	(8-5) MeV
30° 18'	429 ± 50	32 ± 7	51 ± 10
35° 21'	203 ± 25	30 ± 6	42 ± 8
40° 23'	67 ± 10	23 ± 5	27 ± 7
45° 26'	25 ± 6	15 ± 5	27 ± 7
50° 28'	43 ± 8	20 ± 5	37 ± 8
55° 30'	52 ± 9	17 ± 5	36 ± 7
60° 31'	45 ± 9	21 ± 5	31 ± 7
65° 33'	41 ± 8	20 ± 5	26 ± 7
70° 34'	43 ± 8	16 ± 5	26 ± 7
75° 35'	37 ± 7	11 ± 4	23 ± 7
80° 36'	33 ± 7	11 ± 4	16 ± 6
85° 36'	20 ± 6	11 ± 4	10 ± 6
90° 36'	15 ± 4	4 ± 2	7 ± 3

The results of the differential cross-section in the energy ranges were fitted with Legendre polynomial expansion in the angular range 30° to 90° . The fits are presented in figure (5.40) and (5.41), and the coefficients are tabulated in table (5.42). The best fits for each energy range in the the angular range studied were obtained by specifiying only even terms in the polynomial.

Table (5.42)

Legendre polynomial coefficients obtained from fits to the molybdenum differential cross-sections in the energy ranges at 14.1 MeV neutrons.

f_l	coefficients		
	E > 11MeV	(11-8)MeV	(8-5)MeV
f_0	1.000 ± 0.035	1.000 ± 0.035	1.000 ± 0.096
f_2	0.695 ± 0.030	0.225 ± 0.019	0.324 ± 0.084
f_4	0.427 ± 0.022	0.071 ± 0.015	0.126 ± 0.062
f_6	0.200 ± 0.014	0.055 ± 0.013	0.108 ± 0.039
f_8	0.045 ± 0.007	-0.015 ± 0.001	0.014 ± 0.019

The integrated cross-sections in the angular range 30° to 90° for thin sample of molybdenum were calculated using equation (5-7). The results in the centre of mass syste are tabulated in table (5.43).

Table (5.43)

Integrated cross-sections in the angular range 30° to 90° for 14.1 MeV neutrons from molybdenum in the centre of mass system.

Reaction	$\sigma_{int} = \int_{\pi/6}^{\pi/2} d\sigma/d\Omega . d\Omega$ mbarns	
	Present work	Strizhak et al
Elastic	259 ± 12	237
E > 11MeV	332 ± 20	-
(11-8)MeV	90 ± 5	-
(8-5)MeV	142 ± 8	-

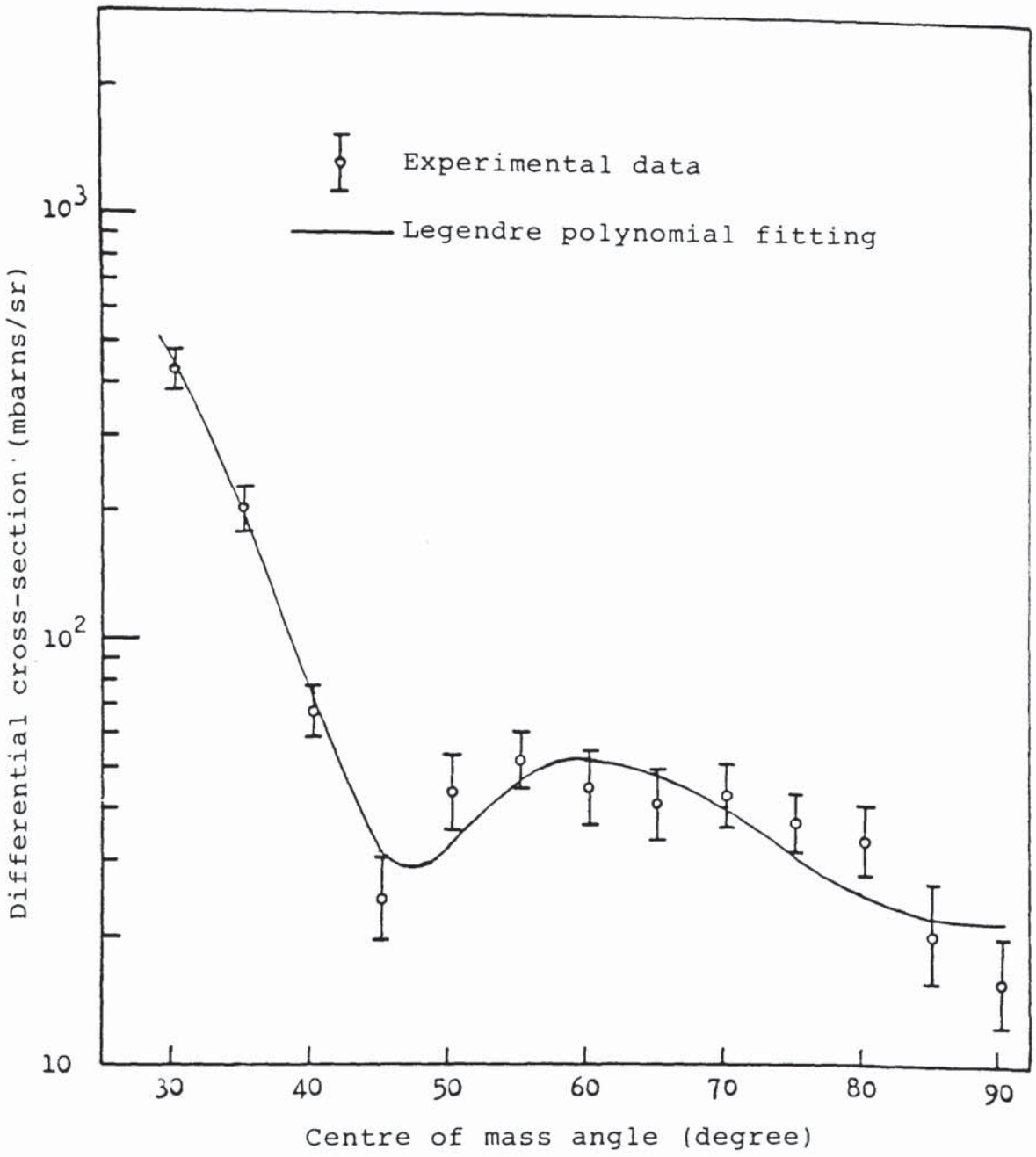

Figure (5.40):Legendre polynomial fits to the differential cross-section data in the energy range E > 11 MeV in molybdenum.

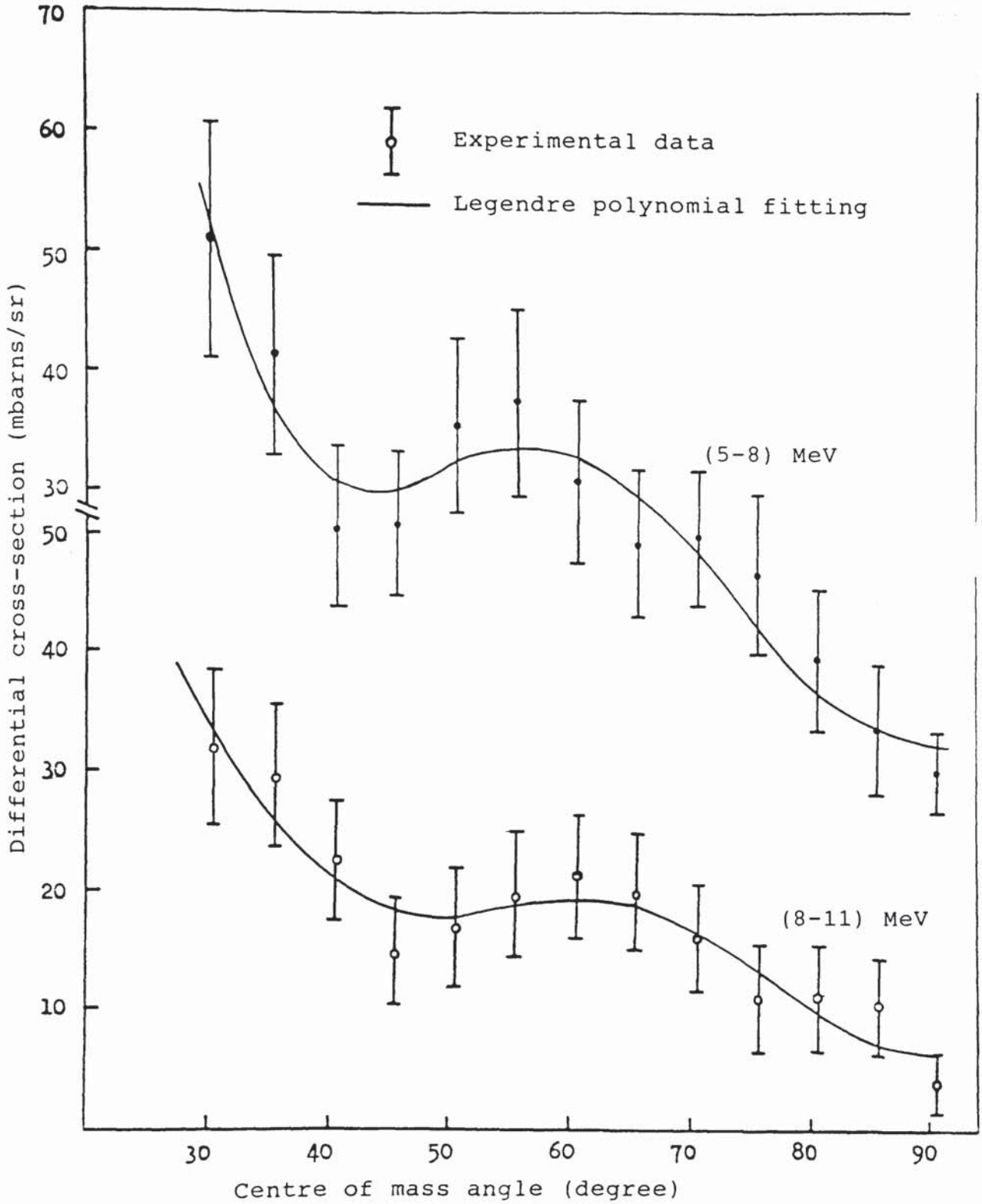

Figure (5.41):Legendre polynomial fits to the differential cross-section data in the energy ranges (11-8) MeV and (8-5) meV in molybdenum.

CHAPTER 6

THEORETICAL COMPARISON OF RESULTS

6.1:THE OPTICAL MODEL.

6.1.1:INTRODUCTION.

In this work the angular distributions of the elastic scattering of 14.1 MeV neutrons from thin sample of aluminium, copper and molybdenum were compared with Optical Model calculations. A number of global parameter sets resulting from fitting such data over a wide range in energy and mass number have been published. In this section the comparison of the present data to the predictions based on the four sets of the optical model parameters given by Wilmore and Hodgson (6), Becchetti and Greenlees (7), Ferrer, Carlson and Rapaport (107) and Cindro and Bersillon (108) were investigated. The calculations were done using a spherical optical model programme SCAT-2 from CEA-N-2227 (18). The programme was run at University of Manchester Regional Computer Centre on CDC 7600 computer via AMDAHL Computer.

The goodness of the data obtained from each set of the optical parameters compared with the present data for each sample was tested by the following expression,

$$\chi^2 = \frac{1}{N} \sum_{i=1}^{N} \left[\frac{\sigma_i^{exp} - \sigma_i^{th}}{\Delta \sigma_i^{exp}} \right]^2 \qquad (6\text{-}1)$$

where,

σ_i^{exp} = the experimental differential cross-section,

σ_i^{th} = the theoretical prediction of the differential cross-section,

$\Delta\sigma_i^{exp}$ = the experimental error of the differential cross-section,

N = the number of data fitted.

The minimum value of λ^2 represents the best agreement between calculated values and the experimental data.

6.1.2:THE OPTICAL POTENTIAL.

In general form, the optical model potential for neutron scattering is defined as a combination of Woods-Saxon volume and surface derivative form. It contains the real central potential, imaginary potential and spin-orbit potential. The complex optical potential can be written in general form as,

$$V(r) = V_o\, f(r) + i\, W(r) + U_{so}(r) \qquad (6\text{-}2)$$

The real central potential V_o is responsible for the shape elastic scattering and constitutes the energy dependent term. It has the volume distribution described typically by the Woods-Saxon form,

$$V_o f(r) = - V_o f(r, R_o, a_o) \qquad (6\text{-}3)$$

where $f(r, R_o, a_o)$ is the Woods-Saxon form factor

characterized by a radius parameter R_o and a diffuseness parameter a_o , that is a measured of the distance over which the potential falls from the maximum value to zero. The form factor $f(r,R_o,a_o)$ can be represented by (4),

$$f(r,R_o,a_o) = [1 + \exp (r-R_o)/a_o]^{-1} \qquad (6-4)$$

The imaginary part of the optical model potential is responsible for the absorption process in the nuclear reactions and contains surface and volume absorption potential, and is given by,

$$W(r) = - W_v f(r,R_v,a_v) + W_d . 4a_d \frac{d}{dr} f(r,R_d,a_d) \qquad (6-5)$$

where,

$$f(r,R_v,a_v) = [1 + \exp (r-R_v)/a_v]^{-1}$$

and

$$f(r,R_d,a_d) = [1 + \exp (r-R_d)/a_d]^{-1}$$

W_v is the imaginary volume-absorptive potential and has the same potential form as the real central potential.

W_d is the imaginary surface-absorptive potential and its form factor is taken to be the derivative woods-Saxon type defined by $-4a_d (d/dr)f(r,R_d,a_d)$. The normalization factor $(-4a_d)$ being includes in order to make the maximum value of the form factor equal to unity.

The imaginary volume-absorptive potential is responsible for absorption within the nuclear volume while the imaginary surface-absorptive potential is responsible

for absorption near the surface of the nucleus. It is well known that the phenomenological optical model potential analysis of neutron elastic scattering required only a surface-peaked absorption at low nucleon energies ($W_v = 0$) while at higher energies only volume absorption term is generally used ($W_d = 0$). At intermediate energies both terms are frequently used.

The spin-orbit potential U_{so} constitutes the complex attractive potential. This potential is considered if the incident particle has a spin and the interaction with target nucleus has the spin dependent component. It is given by usual Thomas form, i.e,

$$U_{so}(r) = -(V_{so} + iW_{so})\left(\frac{\hbar}{m_{\pi}c}\right)^2 \frac{1}{r}\frac{d}{dr} f(r,R_{so},a_{so})\hat{L}.\hat{S} \qquad (6\text{-}6)$$

where,

$$f(r,R_{so},a_{so}) = [1 + \exp(r-R_{so})/a_{so}]^{-1} \qquad (6\text{-}7)$$

$\hbar = h/2$, h = Planck constant

c = the velocity of light,

m_{π} = pion mass,

$(\hbar/m_{\pi}c)^2 = 2$ is the square of half the pion Compton wavelength which is applied to keep the dimension of the spin-orbit potential in correct value.

$\hat{L}.\hat{s}$ is the scalar product of the intrinsic and angular momentum operators. For the particles with spin 1/2 like proton and neutron, the total angular momentum is given by

$J = l \pm \frac{1}{2}$

The imaginary part of the spin-orbit potential is usually taken to be zero (109). This mean that the spin-orbit potential is taken to be purely real ($W_{so} = 0$).

6.1.3:THE OPTICAL MODEL CALCULATION.

A:WILMORE and HODGSON POTENTIAL.

These authors used the local potential equivalent to the non-local potential of Perey and Buck (5). The optical model potential is taken to have the form

$$- V(r) = V_o f(r) + iW_d g(r) \qquad (6\text{-}8)$$

where,

V_o = the real central potential,

W_d = the imaginary surface-absorptive potential,

$f(r)$ = the Woods-Saxon form factor,

$g(r)$ = the derivative Woods-Saxon (surface peaked) form factor.

Perey and Buck (5) showed that to a first approximation the local potential $V_L(r)$ equivalent to their non-local potential $V_N(r)$ is given by,

$$V_L(r) \exp\left[\frac{M\beta^2}{2\hbar^2}(E_n - V_L(r)\right] = V_N(r) \qquad (6\text{-}9)$$

where,

β = the range of non locality.

Wilmore and Hodgson (6) represented the equivalent local potentials $V_L(r)$ by functions with parameters depending on energy and mass number. The calculations were made for non-local potentials approprite to 1, 5, 10 and 15 MeV neutrons elastically scattered by nuclei of masses A = 50, 100, 150 and 200. The values obtained

could be fitted by the following expression,

$$V_o = 47.01 - 0.267\ E_n - 0.00118\ E_n^2 \quad \text{MeV} \qquad (6\text{-}10)$$

$$W_d = 9.52 - 0.53\ E_n \quad \text{MeV} \qquad (6\text{-}11)$$

$$R_o = 1.322 - 0.00076\ A + (4\times10^{-6})\ A^2 - (8\times10^{-9})\ A^3 \qquad (6\text{-}12)$$

$$R_d = 1.266 - 0.00037\ A + (2\times10^{-6})\ A^2 - (4\times10^{-9})\ A^3 \qquad (6\text{-}13)$$

$$a_o = 0.66 \text{ fm} \qquad (6\text{-}14)$$

$$a_d = 0.48 \text{ fm} \qquad (6\text{-}15)$$

The imaginary volume-absorptive potential W_v was considered to be zero. This is because their work mostly concerned on low energy neutron. Neutron total and differential cross-sections for Si, S, Ca, Ti, Fe, Ba, Pb and U were calculated from this optical potentials for neutron energies from 1 to 15 MeV and satisfactory agreement with experimental results were obtained.

The spin-orbit term was not included in the Wilmore-Hodgson (6) optical parameters. However, in the present calculations, the spin-orbit term was added to their potential with the following values,

$$V_{so} = 7.00 \text{ MeV} \qquad (6\text{-}16)$$

$$R_{so} = 1.3042 \text{ fm} \qquad (6\text{-}17)$$

$$a_{so} = 0.66 \text{ fm} \qquad (6\text{-}18)$$

Using the programme SCAT-2 , with the Wilmore-Hodgson parameters disccused above, the angular distributions of the elastic scattering of 14 MeV neutrons from aluminium, copper and molybdenum were calculated. The results for each sample are shown in figures (6.1) through to (6.3) as a smooth curve. For copper and molybdenum which consist of several isotopes, the differential cross-sections for each angle were obtained by averaging the differential cross-sections for each isotope based on the isotopic abundance of the element. The results obtained for each element were compared with the experimental results as indicated in the same graph.

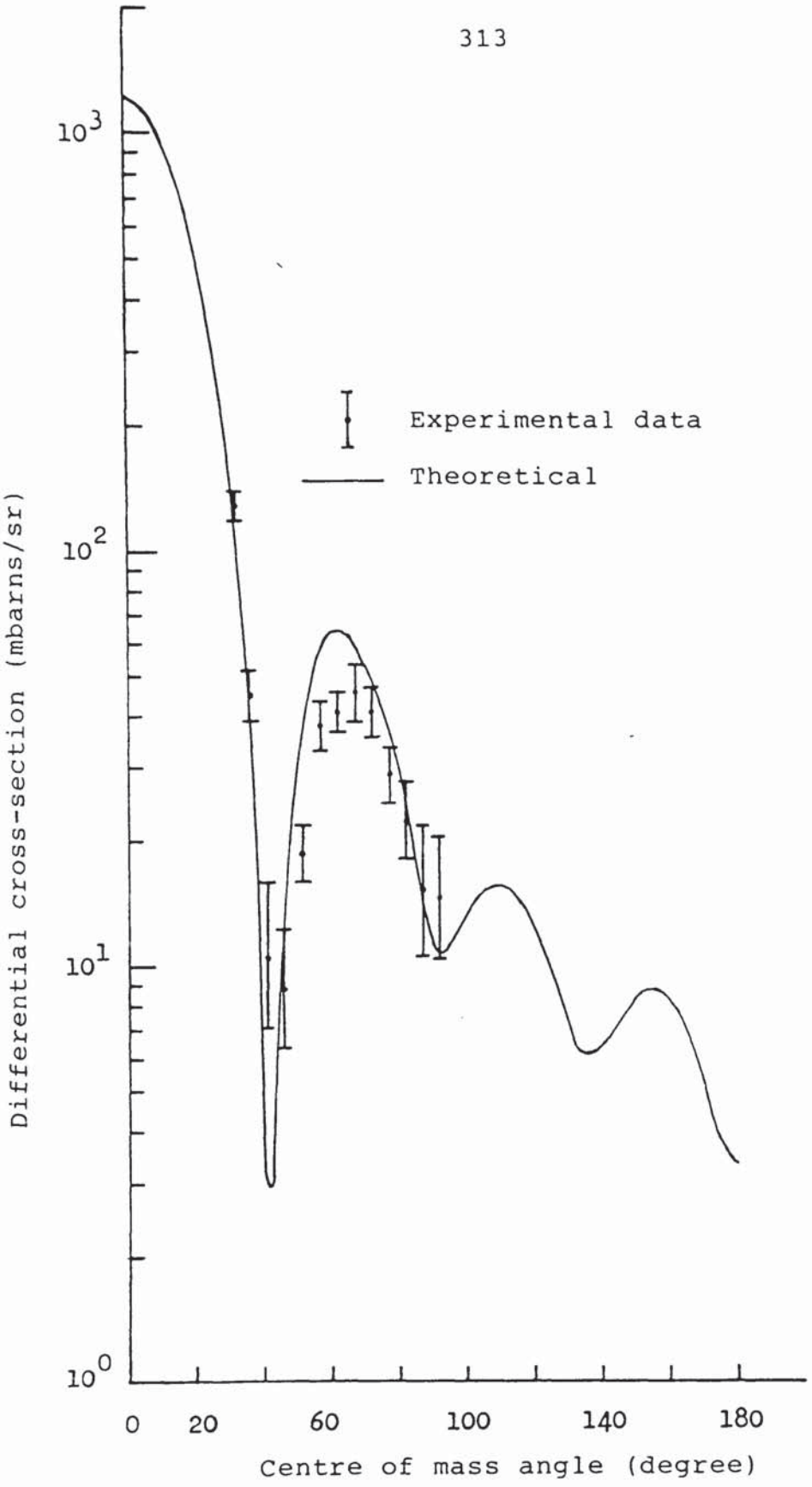

Figure (6.1): The angular distributions of elastic scattering of 14.1 MeV neutrons from aluminium calculated using Wilmore-Hodgson optical model parameters.

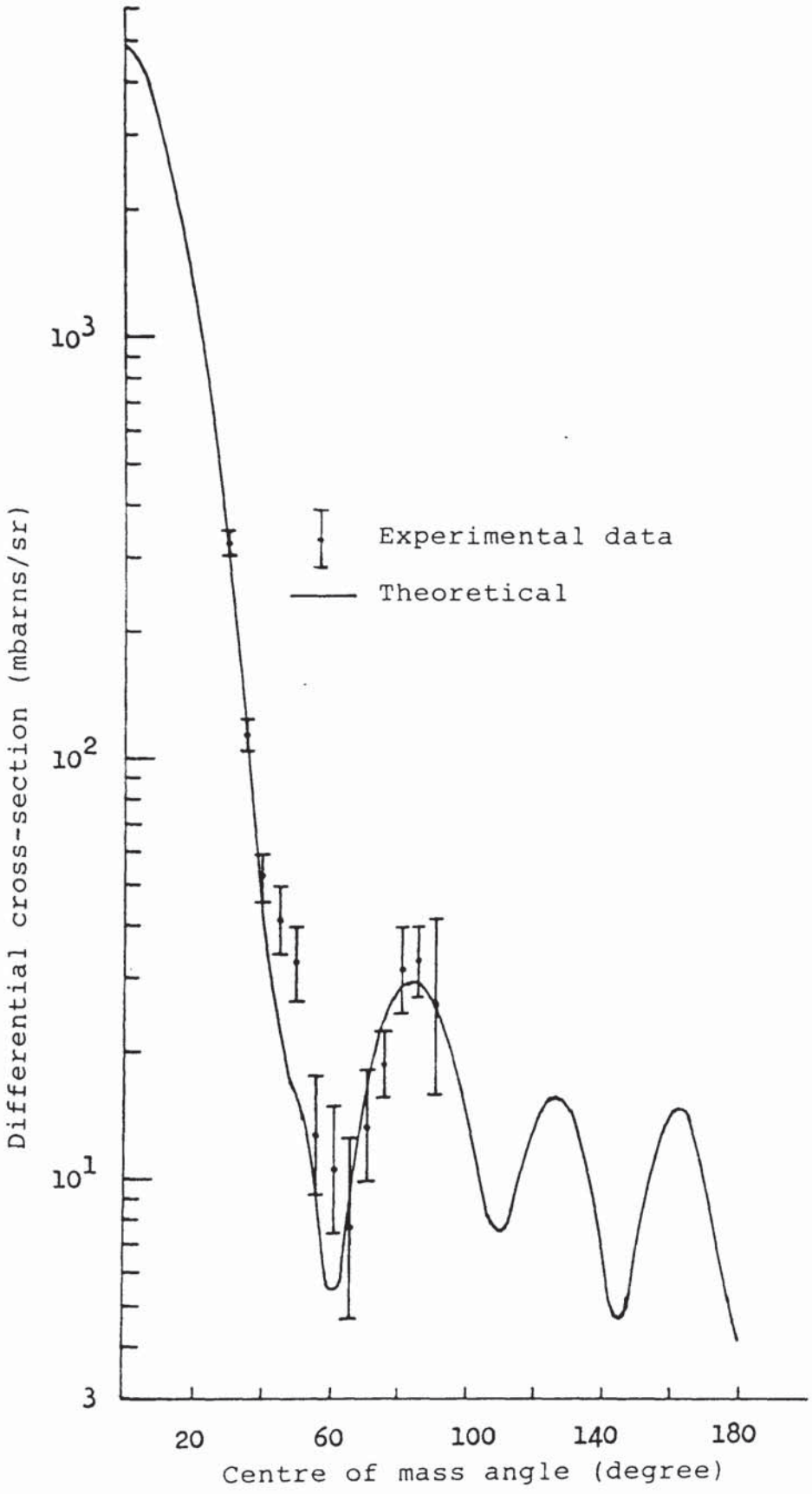

Figure (6.2):The angular distributions of elastic scattering of 14.1 MeV neutrons from copper calculated calculated using Wilmore-Hodgson optical model parameters.

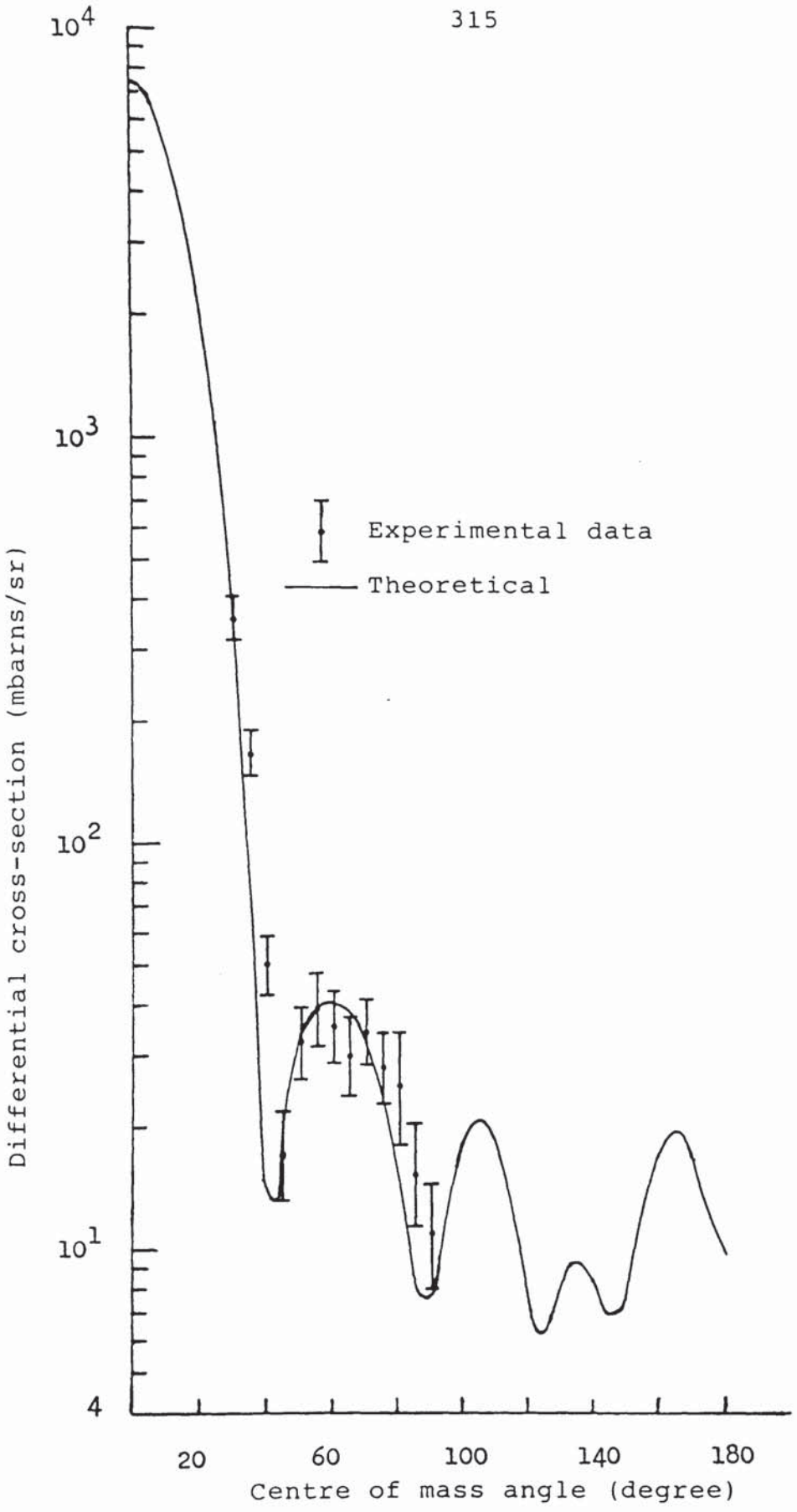

Figure (6.3):The angular distributions of elastic scattering of 14.1 MeV neutrons from molybdenum calculated using Wilmore-Hodgson optical model parameters.

B.BECCHETTI and GREENLEES POTENTIAL.

A wide range of neutron data for nuclei mostly with A > 90 and energies mostly between 1 to 7 MeV was analyzed by Becchetti and Greenlees (7). The analysis on neutron data were based on a global proton-nucleus analysis for proton data between 10 to 40 MeV.

The optical potential which was used is a combination of Woods-Saxon volume and surface derivative forms. The best fit to the neutron data, using energy and isospin dependence from the best fit to the proton data, was obtained using the following parameters,

$$V_o = 56.3 - 0.32\, E_n - 24.0\, \frac{(N-Z)}{A} \quad \text{MeV} \qquad (6\text{-}19)$$

$$R_o = 1.17 \quad \text{fm} \qquad (6\text{-}20)$$

$$a_o = 0.75 \quad \text{fm} \qquad (6\text{-}21)$$

$$W_d = 13.0 - 0.25\, E_n - 12.0\, \frac{(N-Z)}{A} \quad \text{MeV} \qquad (6\text{-}22)$$

or $= 0$, whichever is greater.

$$R_d = 1.26 \quad \text{fm} \qquad (6\text{-}23)$$

$$a_d = 1.26 \quad \text{fm} \qquad (6\text{-}24)$$

$$W_d = 0.22\, E_n - 1.56$$

or $= 0$, whichever is greater. (6-25)

$$R_v = R_d = 1.26 \quad fm \tag{6-26}$$

$$a_v = a_d = 0.58 \quad fm \tag{6-27}$$

$$V_{so} = 6.2 \text{ MeV} \tag{6-28}$$

$$R_{so} = 1.010 \quad fm \tag{6-29}$$

$$a_{so} = 0.75 \quad fm \tag{6-30}$$

where E_n is the energy of the incident neutrons in MeV in the laboratory system.

The results of the calculations are presented as a smooth curve in figures (6.4), (6.5) and (6.6) for Al, Cu and Mo respectively together with the present experimental data.

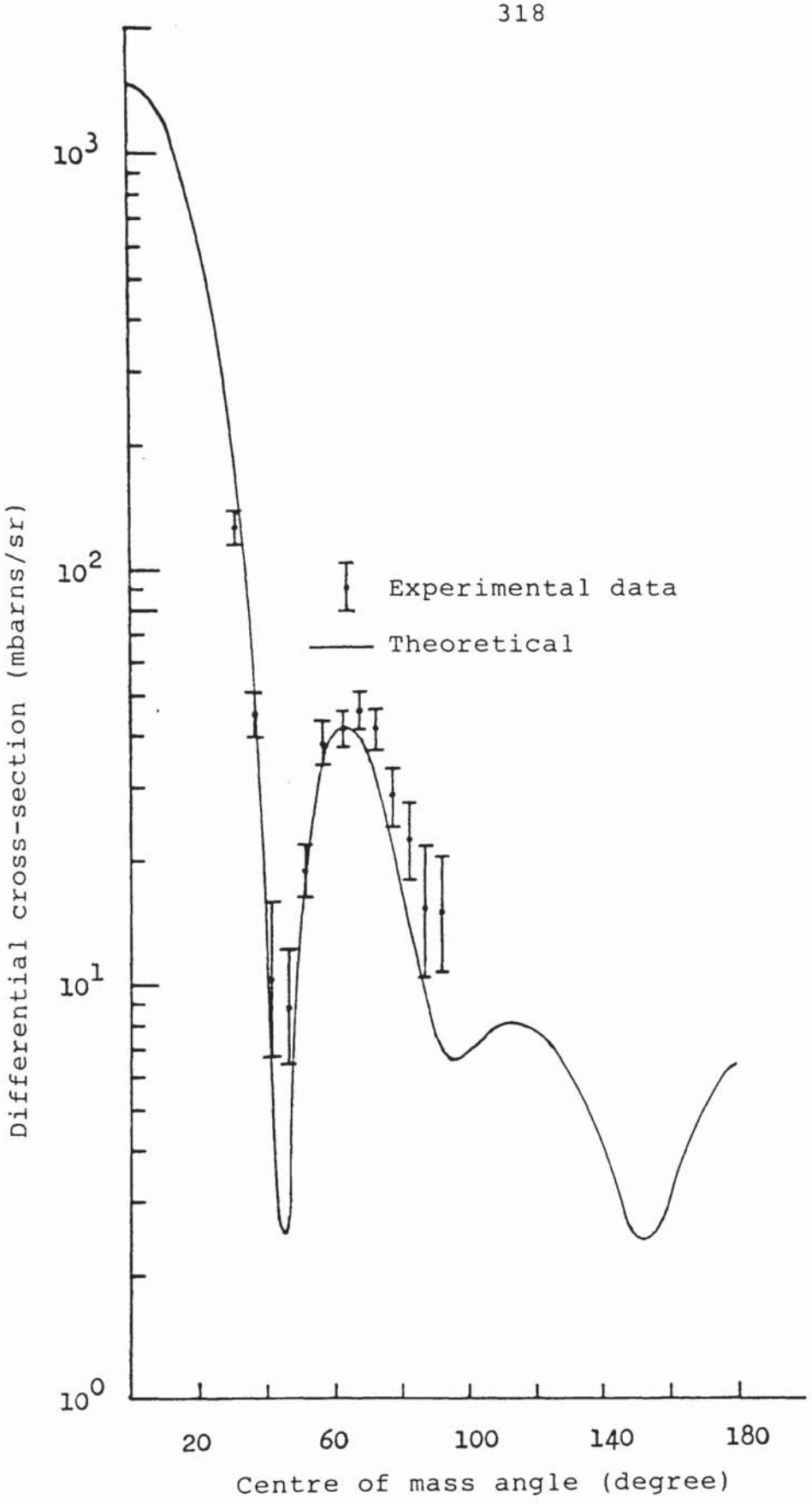

Figure (6.4):The angular distributions of elastic scattering of 14.1 MeV neutrons from aluminium calculated using Becchetti-Greenlees optical model parameters.

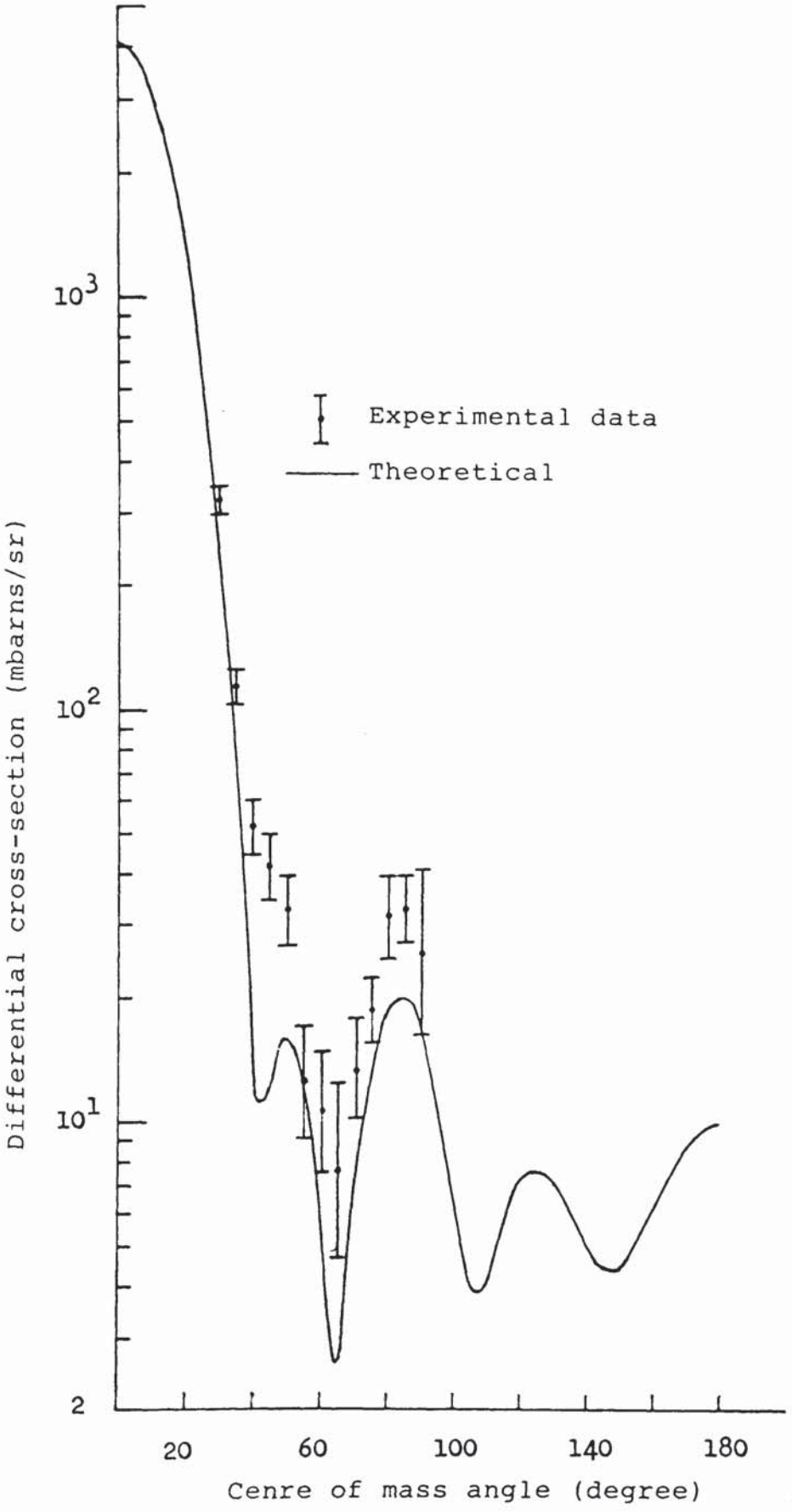

Figure (6.5):The angular distributions of elastic scattering of 14.1 MeV neutrons from copper calculated using Becchetti-Greenlees optical model parameters.

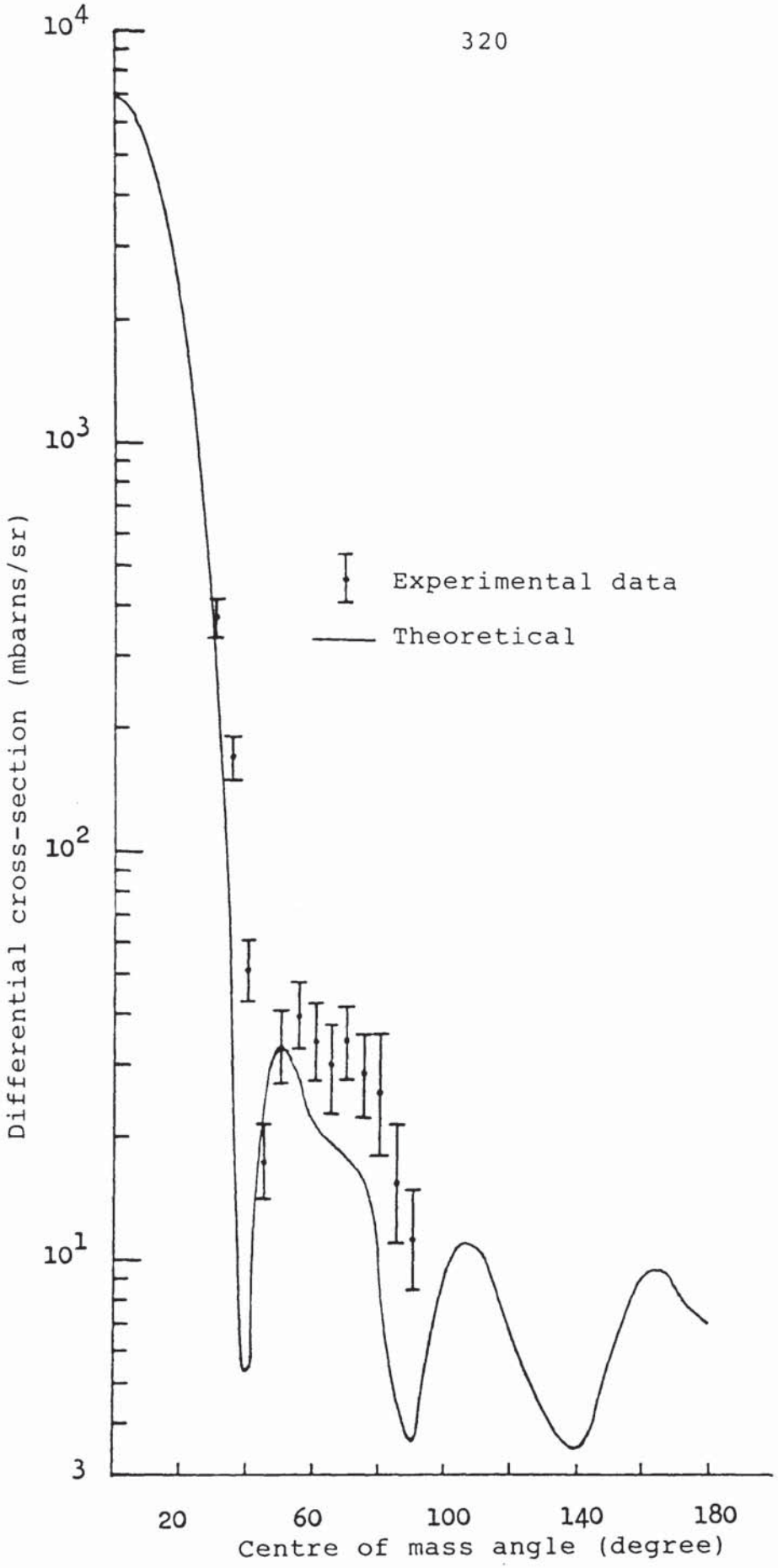

Figure (6.6):The angular distributions of elastic scattering of 14.1 MeV neutrons from molybdenum calculated using Becchetti-greenlees optical model parameters.

C.FERRER-RAPAPORT POTENTIAL.

Analysis of neutron elastic scattering data at 11 MeV neutrons scattered from Mg, Al, S, Ca, Mn, Fe, Co, Ni, Nb, $Mo^{92,96,98,100}$, In, Sn^{120}, Ho, Ta, Pb, Pb^{206} and Bi have been done by Ferrer et al (107). The optical potential based on the Becchetti and Greenlees (7) was used in their analysis. However, the imaginary volume-absorptive potential was not included in their calculation.

The best overall fit to the experimental data for above nuclei was obtained using the following parameters.

$$V_o = 47.14 - 22.50 \frac{(N-Z)}{A} \quad \text{MeV} \qquad (6\text{-}31)$$

$$R_o = 1.27 \text{ fm} \qquad (6\text{-}32)$$

$$a_o = 0.710 \text{ fm} \qquad (6\text{-}33)$$

$$W_d = 12.16 - 2.03 \frac{(N-Z)}{A} \quad \text{MeV} \qquad (6\text{-}34)$$

$$R_d = 1.27 \text{ fm} \qquad (6\text{-}35)$$

$$a_d = 0.434 \text{ fm} \qquad (6\text{-}36)$$

$$V_{so} = 4.55 \text{ MeV} \qquad (6\text{-}37)$$

$$R_{so} = 0.85 \text{ R} = 1.080 \text{ fm} \qquad (6\text{-}38)$$

$$a_{so} = a_o = 0.710 \text{ fm} \qquad (6\text{-}39)$$

The results of the calculations for Ferrer-Rapaport potential using programme SCAT-2 are presented as a smooth curve in figures (6.7), (6.8) and (6.9) for Al, Cu and Mo respectively together with the present experimental data.

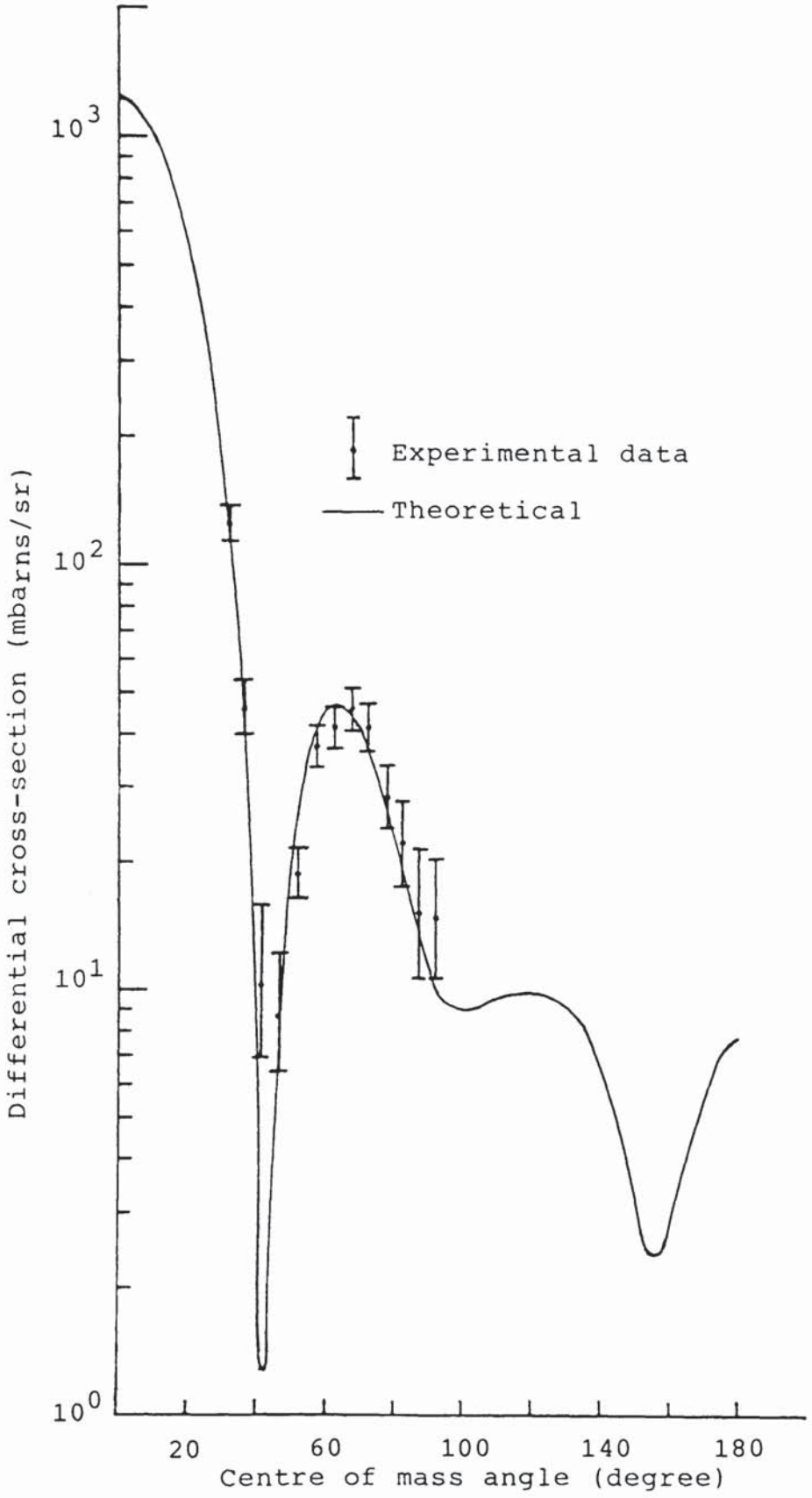

Figure (6.7): The angular distributions of elastic scattering of 14.1 MeV neutrons from aluminium calculated using Ferrer-Rapaport optical model parameters.

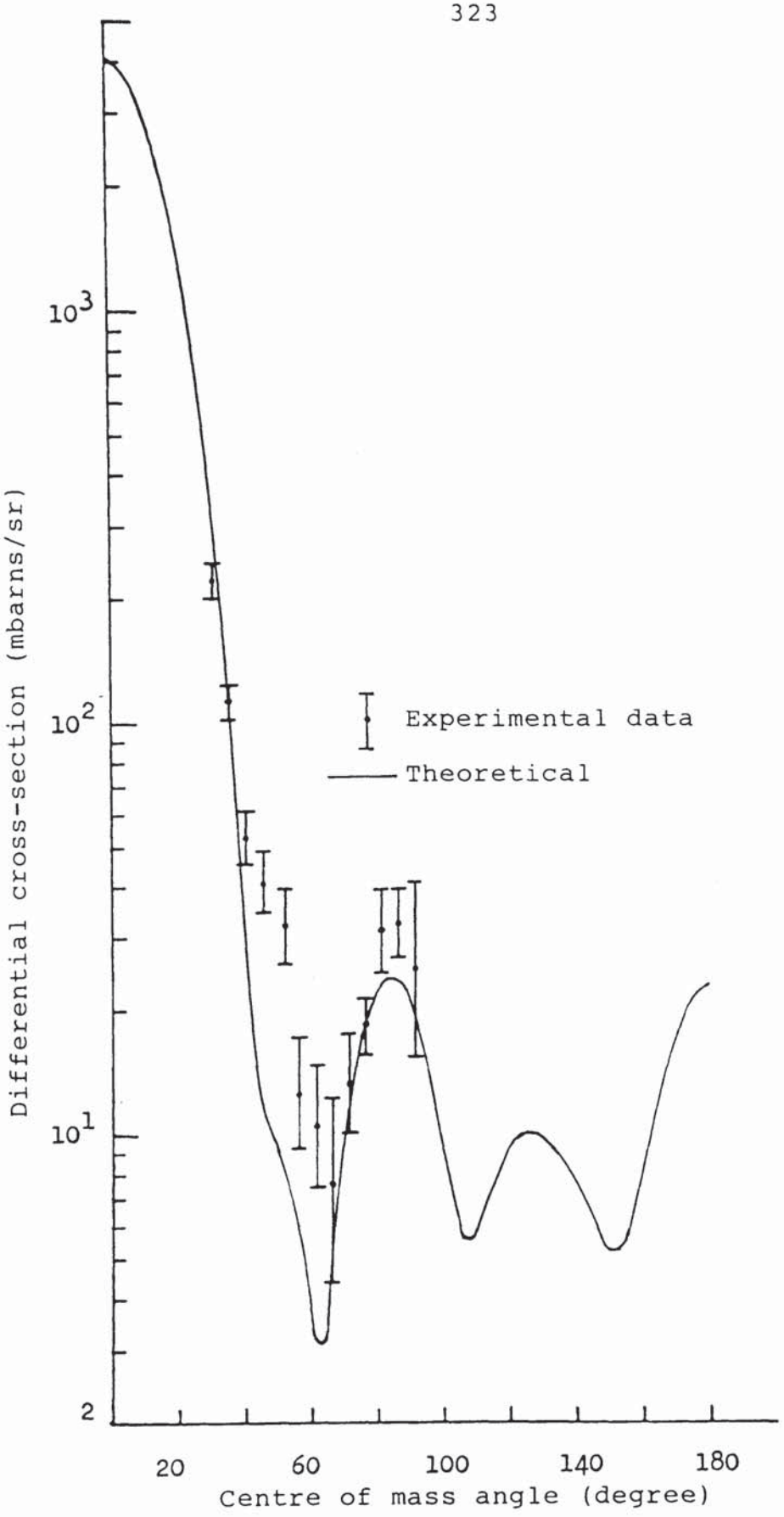

Figure (6.8):The angular distributions of elastic scattering of 14.1 MeV neutrons from copper calculated using Ferrer-Rapaport optical model parameters.

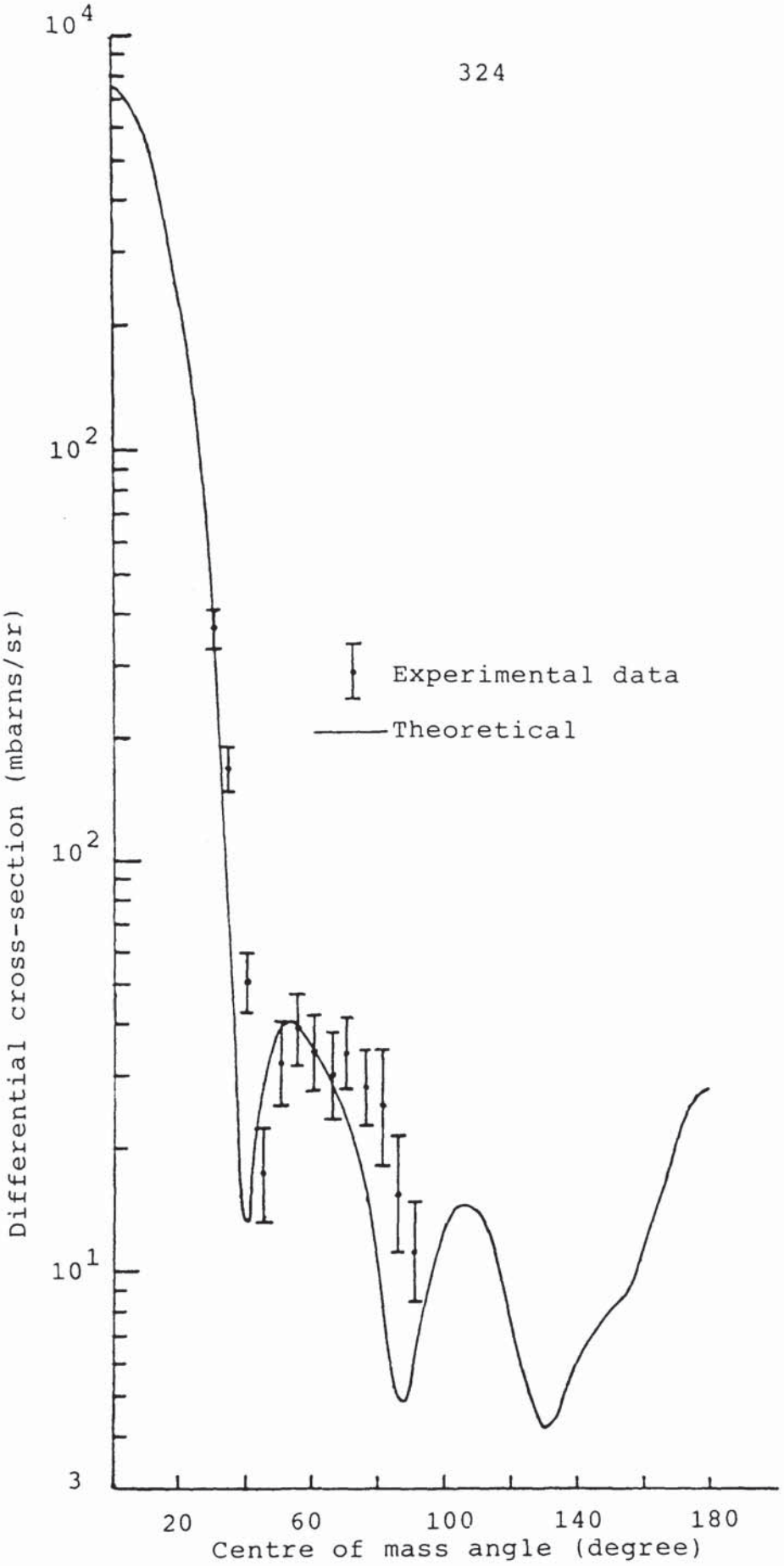

Figure (6.9):The angular distributions of elastic scattering of 14.1 MeV neutrons from molybdenum calculated using Ferrer-Rapaport optical model parameters.

D.CINDRO-BERSILLON POTENTIAL.

A local equivalent of a non-local potential with the Woods-Saxon form for the real and the Woods-Saxon derivative for the imaginary part of the potential was suggested by Cindro and Bersillon (108). The optical model parameters were the following,

$$V_o = 71.0 \text{ MeV} \quad (6\text{-}40)$$

$$R_o = 1.182 + 1.93 \times 10^{-4} A \text{ fm} \quad (6\text{-}41)$$

$$a_o = 0.65 \text{ fm} \quad (6\text{-}42)$$

$$\beta \text{ (non-locality)} = 0.85 \text{ fm} \quad (6\text{-}43)$$

$$W_d = 7.00 + 0.4 E_n \text{ MeV} \quad (6\text{-}44)$$

$$R_d = 1.21 \text{ fm} \quad (6\text{-}45)$$

$$a_d = 0.47 \text{ fm} \quad (6\text{-}46)$$

$$V_{so} = 7.00 \text{ MeV} \quad (6\text{-}47)$$

$$R_{so} = R_o = 1.182 + 1.93 \times 10^{-4} A \text{ fm} \quad (6\text{-}48)$$

$$a_{so} = a_o = 0.65 \text{ fm} \quad (6\text{-}49)$$

Using the above optical model parameters, the angular distributions of the elastic scattering of 14.1 MeV neutrons from Al, Cu and Mo were calculated using programme SCAT-2. The results are presented as a smooth curve in figures (6.10), (6.11) and (6.12) for Al, Cu and Mo respectively together with the present experimental data.

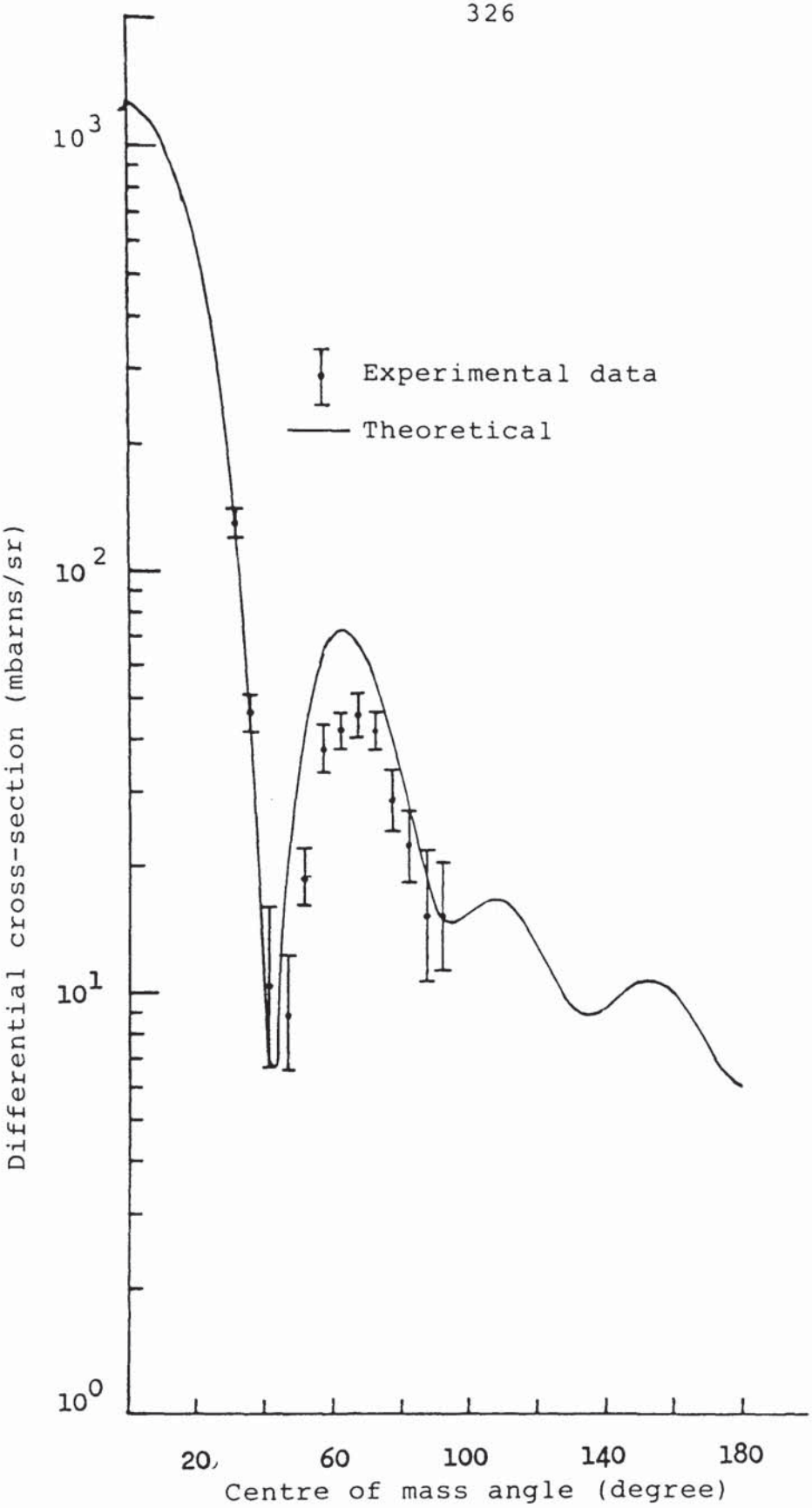

Figure (6.10):The angular distributions of elastic scattering of 14.1 MeV neutrons from aluminium calculated using Cindro-Bersillon optical model parameters.

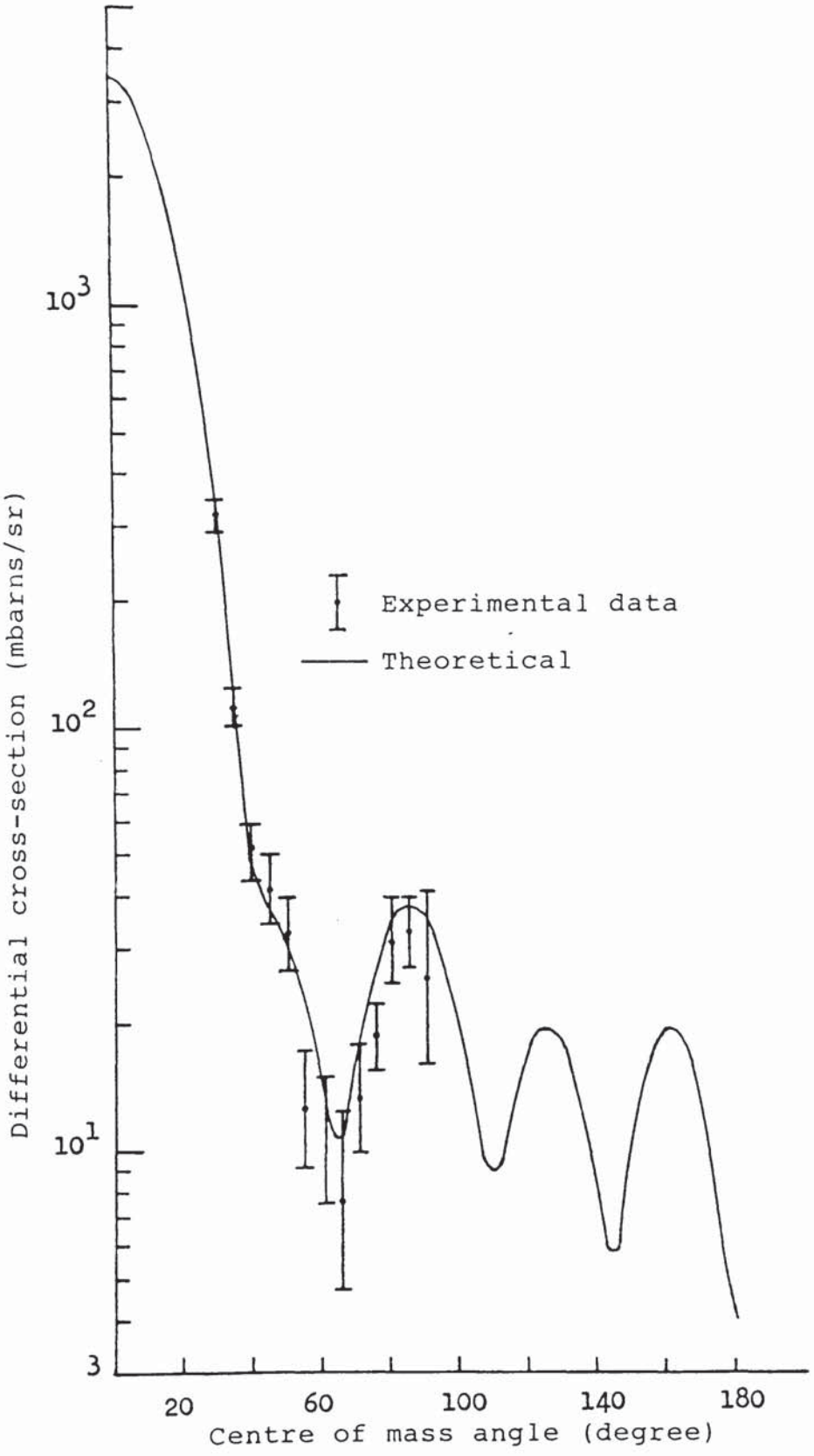

Figure (6.11):The angular distributions of elastic scattering of 14.1 MeV neutrons from copper calculated using Cindro-Bersillon optical model parameters.

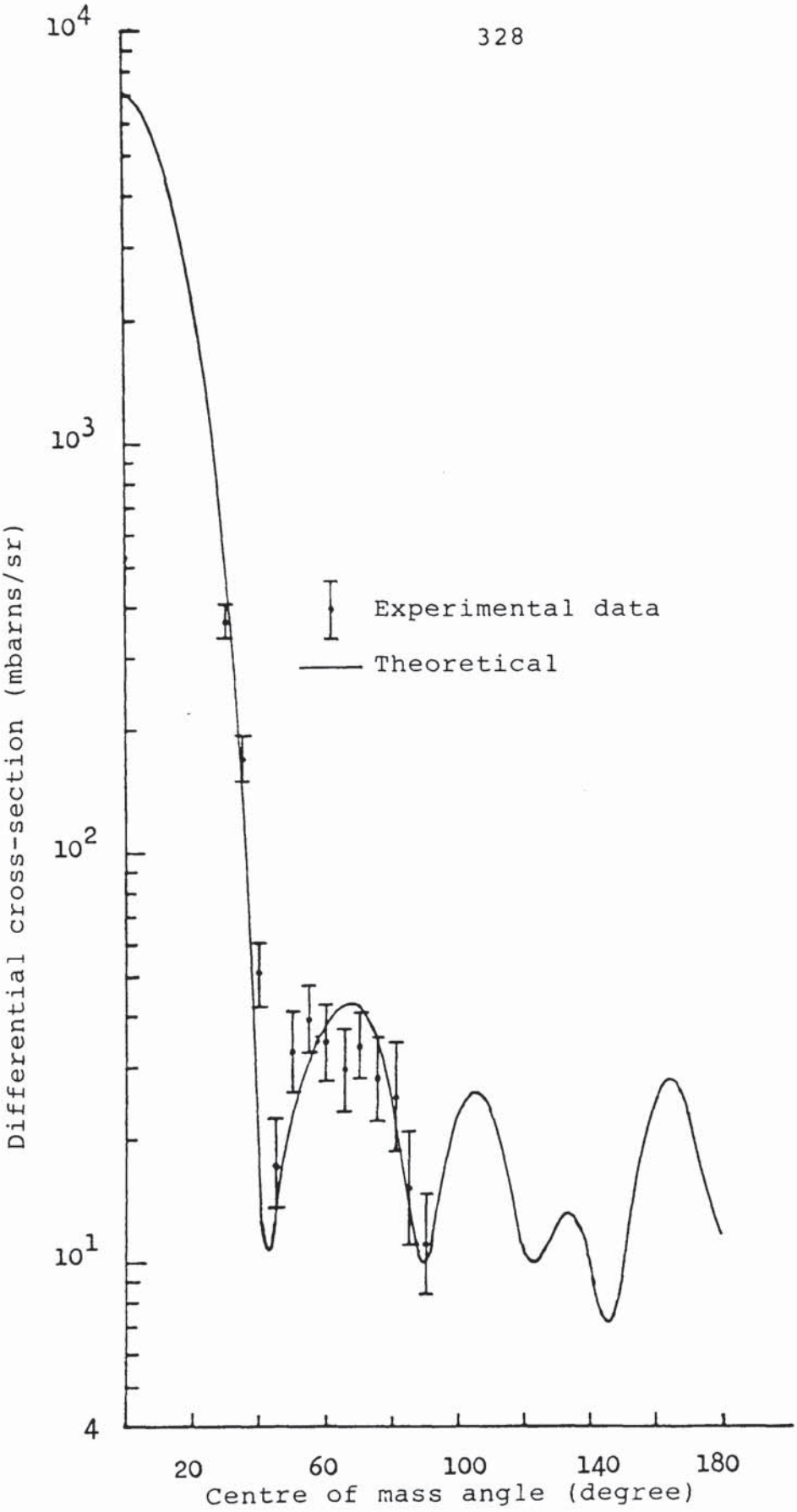

Figure (6.12): The angular distributions of elastic scattering of 14.1 MeV neutrons from molybdenum calculated using Cindro-Bersillon optical model parameters.

6.1.4:DISCUSSION OF RESULTS.

The results of the optical model calculations for various optical model potentials were compared with the present experimental data by calculating the value of χ^2 of equation (6-1). The results for each element are tabulated in table (6.1)

Table (6.1)

The value of χ^2 for Al, Cu and Mo obtained from optical model calculation for various optical parameters.

Element	Cindro-Bersillon	Wilmore-Hodgson	Ferrer-Rapaport	Becchetti-Greenlees
Al	15.5	9.4	1.6	0.5
Cu	1.8	2.3	4.3	7.2
Mo	2.9	3.5	5.5	8.8

From the table it is shown that except for Al the best agreement with the present experimental results were obtained from the calculations using Cindro-Bersillon potential. For Cu and Mo the best agreement which are found for the optical model potentials in order of merit are Cindro-Bersillon, Wilmore-Hodgson, Ferrer-Rapaport and Becchetti-Greenlees potential. This is infact because Becchetti-Greenlees model was heavily weighted to fit lower energies (1-7 MeV) neutron-nucleus data and

Ferrer-Rapaport model was obtained to fit only neutron-nucleus data with energy 11 MeV. These are different from the Wilmore-Hodgson model where the parameters were obtained to fit the cross-section data for medium and heavy nuclei for neutron energies between 1 to 15 MeV and the Cindro-Bersillon model was done to fit the neutron-nucleus data for 14 MeV neutrons.

For aluminium the best agreement with the present experimental data was found for optical model calculation based on the Becchetti-Greenlees parameters. Whisnant et al (15) reported a set of optical model parameters based on fitting 11 to 17 MeV neutron cross-section data for aluminium. The parameters obtained are in reasonable agreement with Becchetti-Greenlees parameters as shown in table (6.2).

The elastic scattering cross-sections for 14 MeV neutrons obtained from the optical model calculation at various optical model set parameters are presented in table (6.3). In general the results for Al, Cu and Mo are in reasonable agreement with the present experimental results calculated from the Legendre polynomial expansion.

Table (6.2)

Optical model parameters obtained from Whisnsnt et al (15) and Becchetti-Greenlees (7) for Al cross-sections data at 14 MeV neutrons.

Parameter	Becchetti-Greenlees	Whisnant et al
V_o	50.93 MeV	47.53 MeV
R_o	1.17 fm	1.18 fm
a_o	0.75 fm	0.64 fm
W_d	9.06 MeV	7.14 MeV
R_d	1.26 fm	1.26 fm
a_d	0.58 fm	0.58 fm
W_v	1.52 MeV	0.00 MeV
R_v	1.26 fm	-
a_v	0.58 fm	-
V_{so}	6.20 MeV	6.00 MeV
R_{so}	1.01 fm	1.01 fm
a_{so}	0.75 fm	0.50 fm

Table (6.3)

The elastic scattering cross-sections for Al, Cu and Mo calculated from optical model in barns.

Isotope	Cindro-Bersillon	Wilmore-Hodgson	Ferrer-Rapaport	Becchetti-Greenlees	Present Work
Al^{27}	0.788	0.720	0.667	0.739	0.734
Cu^{63}	1.401	1.464	1.506	1.430	
Cu^{65}	1.470	1.532	1.525	1.454	
Nat Cu	1.422	1.485	1.512	1.437	1.544
Mo^{92}	2.324	2.330	2.269	2.011	
Mo^{94}	2.381	2.381	2.291	2.041	
Mo^{95}	2.409	2.405	2.302	2.054	
Mo^{96}	2.437	2.429	2.313	2.069	
Mo^{97}	2.465	2.454	2.324	2.083	
Mo^{98}	2.492	2.475	2.355	2.094	
Mo^{100}	2.546	2.520	2.357	2.126	
Nat Mo	2.436	2.427	2.313	2.068	2.055

6.2:MONTE CARLO MODEL.

6.2.1:INTRODUCTION.

Information on the angular distribution of neutron elastic scattering is of considerable interest and can be obtained by the study of scattering of neutron in large sample. As the thickness of the sample will be extensive, multiple scattering will play an important role in the scattering of fast neutron in the materials. In the scattering proceses, the effect of multiple scattering is to cause an effective increase in the measured cross-sections due to increase on the probability of neutron scattering interactions in the sample. In detail, the probability of multiple scattering depends on the dimensions of the sample and the microscopic scattering cross-sections. Analysis of how the effective cross-section varies with thickness is very complicated due to the complicated sample geometries and the variation of the scattering cross-section with energy. The Monte Carlo method is one of the possible method for treating the multiple scattering processes in the extended sample. However, in using this method a lot of approximations have to be made and the accurate data of microscopic cross-sections are needed at various energies.

The Monte Carlo method requires the use of large computing facilities with the capability of random number generation and large virtual storage space. In this method, a number of source neutrons are considered to

travel through a system and the individual neutron histories are traced. Random numbers are used to determine the sequence of events in each neutron's life history in a particular manner.

In the present work, a Monte Carlo simulation programme suitable for a small computer was developed. The programme was capable to predict the number of neutrons scattered from various thicknesses of the sample at all possible angles between 0^{o} to 350^{o} with 10^{o} increments. In order to make the programme not too complicated and capable of being run on microcomputer with in reasonable time, the calculation was done in two dimension coordinate system. The programme was written in BASIC and run on the BBC microcomputer.

6.2.2:DESCRIPTION OF THE MODEL.

The Monte Carlo method which has been widely employed in neutron transport problems, is based on the simulation of the physical events which take place inside the material because an incident neutron. Random numbers are used to determine the sequence of events in each neutron life history in the material. In reaction between nuclei and neutron the sequence of events are determined by means of effective cross-sections.

Consider a monoenergetic neutrons with energy E and intensity n_o incident upon a sample of thickness x

as shown in figure (6.13). The problem of the neutron histories was traced by the following subsections.

6.2.2.1:CHOOSE POINT OF INTERACTION.

Assuming that neutrons enter the material with 0^{o} before first interaction occurs. The point of interaction was chosen based on the width of the sample irradiated by neutron beam. According to the neutron beam profile (section 2.5) the width of the sample irradiated by neutrons beam at horizontal direction was calculated as 4.2 cm. Therefore, the point of interaction was chosen by the following equation,

$$I = 4\ R + 8 \qquad (6\text{-}50)$$

where,

R = the random number generated (between 0 to 1).

6.2.2.2:CALCULATION OF DISTANCE TRAVEL.

The distance of travel of neutron in the material before first interaction occurs can be calculated by the following method.

Consider n_o neutrons incident into a block of material. The number of neutrons N remaining after passed through a thickness x is given by,

$$N = n_o\ e^{-\Sigma x} \qquad (6\text{-}51)$$

or

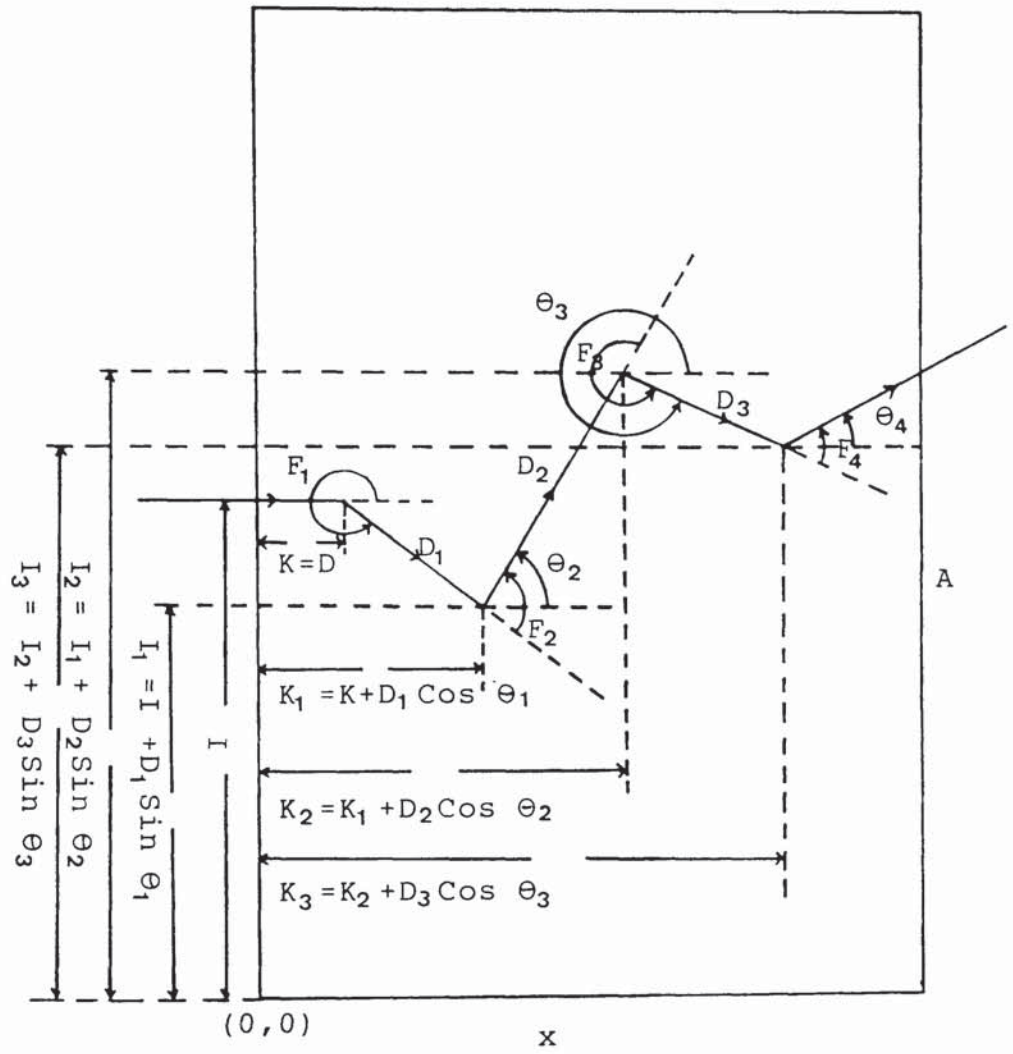

Figure (6.13):Model to calculate the passage of neutrons using Monte Carlo method.

$$N = n_o \, e^{-x/\lambda} \qquad (6.52)$$

where,

$\Sigma = 1/\lambda$ and λ is the mean free path.

The probability of a neutron being absorbed is $(1 - N/n_o)$ and the hence the probability of it not being absorbed is N/n_o. Therefore, by generating a random number P where $P = e^{-x/\lambda}$, the distance of neutron travel in the material can be calculated by the following equation,

$$x = \lambda \log_e \left(\frac{1}{P}\right) \qquad (6.53)$$

However, $0 \leqslant P < 1$, therefore if P=0, then x is infinite. Hence the expression,

$$x = \lambda \log_e \left(\frac{1}{1-P}\right) \qquad (6\text{-}54)$$

is used because P is never 1 and x can never infinite.

The value of x is then tested by the following conditions,

(i) If $x \geqslant a$ then the neutron has escaped from the material.

(ii) If $x < a$ then the neutron has interacted in the material,

where a is the distance to edge of sample from point of interaction.

If condition (i) is obeyed then the neutron history is terminated. If condition (ii) is obeyed then the history continues into the next section.

6.2.2.3:TYPE OF INTERACTION.

In neutron physics, reactions between nuclei and neutrons are ordinarily described by means of partial cross-sections. Since the cross-sections are of the form,

$$\Sigma_T = \Sigma_s + \Sigma_a \tag{6-55}$$

then the probabilities of scattering and absorption are $\frac{\Sigma_s}{\Sigma_T}$ and $\frac{\Sigma_a}{\Sigma_T}$ respectively, where,

Σ_T = the macroscopic total cross-section,

Σ_s = the macroscopic elastic scattering cross-section,

Σ_a = the macroscopic absorbtion cross-section.

These probabilities can be represented as lengths of a line of the following figure,

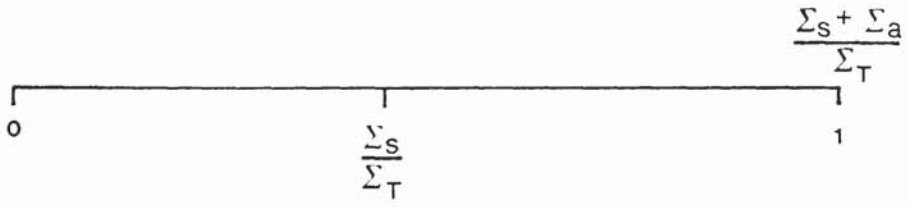

In order to determine the type of interaction, another random number, $\}'$ is generated and tested against the following conditions,

(i) If $\}' \geq \frac{\Sigma_a}{\Sigma_T}$, then absorbtion occurs.

(ii) If $\}' < \frac{\Sigma_s}{\Sigma_T}$, then scattering occurs.

If condition (i) is observed then the neutron history is terminated and the next neutron is allowed to pass through the sample. If condition (ii) is chosen the problem proceeds to the next section of the programme.

6.2.2.4:CHOICE OF SCATTERING ANGLE.

This Monte Carlo programme was capable to predict the number of neutrons scattered at all possible angles between 0^o to 350^o with 10^o increments. A similar approach to the method described in section (6.2.2.3) was used. The probabilities of the neutron being scattered through each angle can be considered as the lenght of each segment of the following figure,

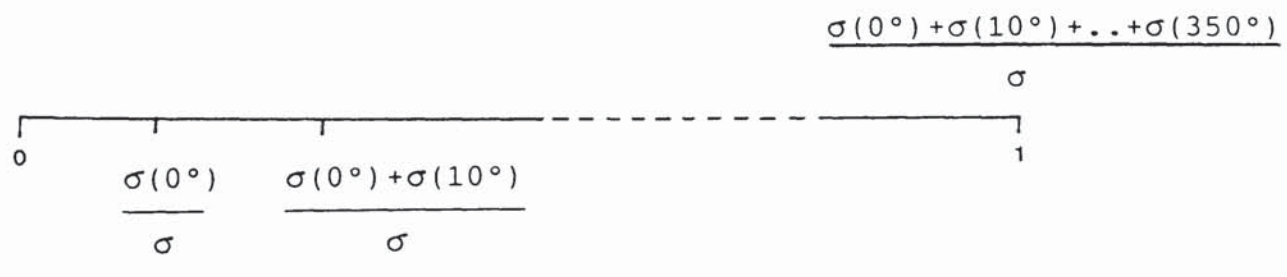

where,

$$\sigma(\Theta) = \frac{d\sigma}{d\Omega}(\Theta)\cdot\Delta\Omega \qquad (6\text{-}56)$$

$\frac{d\sigma}{d\Omega}$ = the differential elastic scattering cross-section,

$\Delta\Omega$ = the solid angle,

$\sigma = \sigma(0^\circ) + \sigma(10^\circ) + \sigma(20^\circ) + \ldots\ldots + \sigma(350^\circ)$

= the integrated elastic scattering cross-section.

The computer then generate a random number R, and tests by the following conditions.

If $R < \sigma(0^\circ)/\sigma$, then $\Theta = 0^\circ$, else

If $R < [\sigma(0^\circ) + \sigma(10^\circ)]/\sigma$, then $\Theta = 10^\circ$, else

.....

.....

If $R < [\sigma(0^\circ) + \sigma(10^\circ) + \ldots\ldots + \sigma(340^\circ)]/\sigma$, then $\Theta = 340^\circ$

Else , then $\Theta = 350^\circ$.

The computer goes through each comparison in order to choose the scattering angle for each interaction.

6.2.2.5:CALCULATION OF ENERGY AND MEAN FREE PATH.

As we are concerned only on the elastic scattering process, the fraction of energy retained at each interaction can be calculated from the conservation of momentum and energy in the center of mass system and laboratory system. It gives (110),

$$Q(\varphi) = \frac{E'}{E_o} = \frac{A^2 + 2A\,\mathrm{Cos}\,\varphi + 1}{(A+1)^2} \qquad (6\text{-}57)$$

and,

$$\mathrm{Cos}\,\Theta = \frac{A\,\mathrm{Cos}\,\varphi + 1}{(A^2 + 2A\,\mathrm{Cos}\,\varphi + 1)^{1/2}} \qquad (6\text{-}58)$$

where,

A = the mass of nuclei,

φ = center of mass scattering angle,

Θ = laboratory scattering angle.

In term of laboratory scattering angle, equation (6-57) can be written as,

$$Q(\Theta) = \left[\frac{\mathrm{Cos}\Theta + (\mathrm{Cos}^2\Theta + A^2 - 1)^{1/2}}{1 + A}\right]^2 \qquad (6\text{-}59)$$

The new mean free path of scattered neutrons was calculated by the following simplification.

As the probability of an interaction occuring is propotional to the time the neutron spends near the nucleus, therefore,

$$\sigma \propto \frac{1}{v} \qquad (6\text{-}60)$$

where,

v = the velocity of neutron.

The kinetic energy of neutron is given by,

$$E = \frac{1}{2} m v^2 \qquad (6\text{-}61)$$

therefore equation (6-60) can be written as,

$$\sigma \propto \frac{1}{E^{1/2}} \tag{6-62}$$

The mean free path of neutron is,

$$\lambda = \frac{1}{\Sigma} = \frac{1}{n\sigma} \tag{6-63}$$

therefore,

$$\lambda \propto E^{1/2} \tag{6-64}$$

Hence,

$$\lambda_n = \lambda_o \sqrt{Q(\Theta)} \tag{6-65}$$

λ_n = mean free path after interaction,

λ_o = mean free path before interaction,

$Q(\Theta)$ = the fraction of energy retained.

6.2.3:RESULTS AND DISCUSSION.

The aim of the Monte Carlo calculation is to predict the angular distributions of elastic scattered neutrons from various thicknesses of aluminium and copper samples. The thicknesses up to 2 mean free path were investigated for both samples. The differentiial elastic scattering cross-sections used in this calculation were taken from ENDF B-IV (97,103).

In order to obtain greater accuracy, the programme was run for 10^6 neutrons for each thickness for both samples. The programme was written in BBC BASIC as shown in Appendix E.

Figures (6.14) and (6.15) show the angular distributions of the number of elastic scattered neutrons at various thicknesses of aluminium and copper samples. The figures show that the number of elastic scattered neutrons predicted by this model for each thickness are in reasonable agreement with the experimental results.

In the present calculation, neutrons are assumed to enter the material at 0° direction before first interaction occure. From the calculation, the results showed that the number of neutrons scattered at 0° decrease as the thickness of the sample increase. This is because the thicker the sample, the greater the chance of neutron is deflected from straight ahead direction. Because of this, the number of neutrons scattered at angles between 10° to 180° increase as the thickness

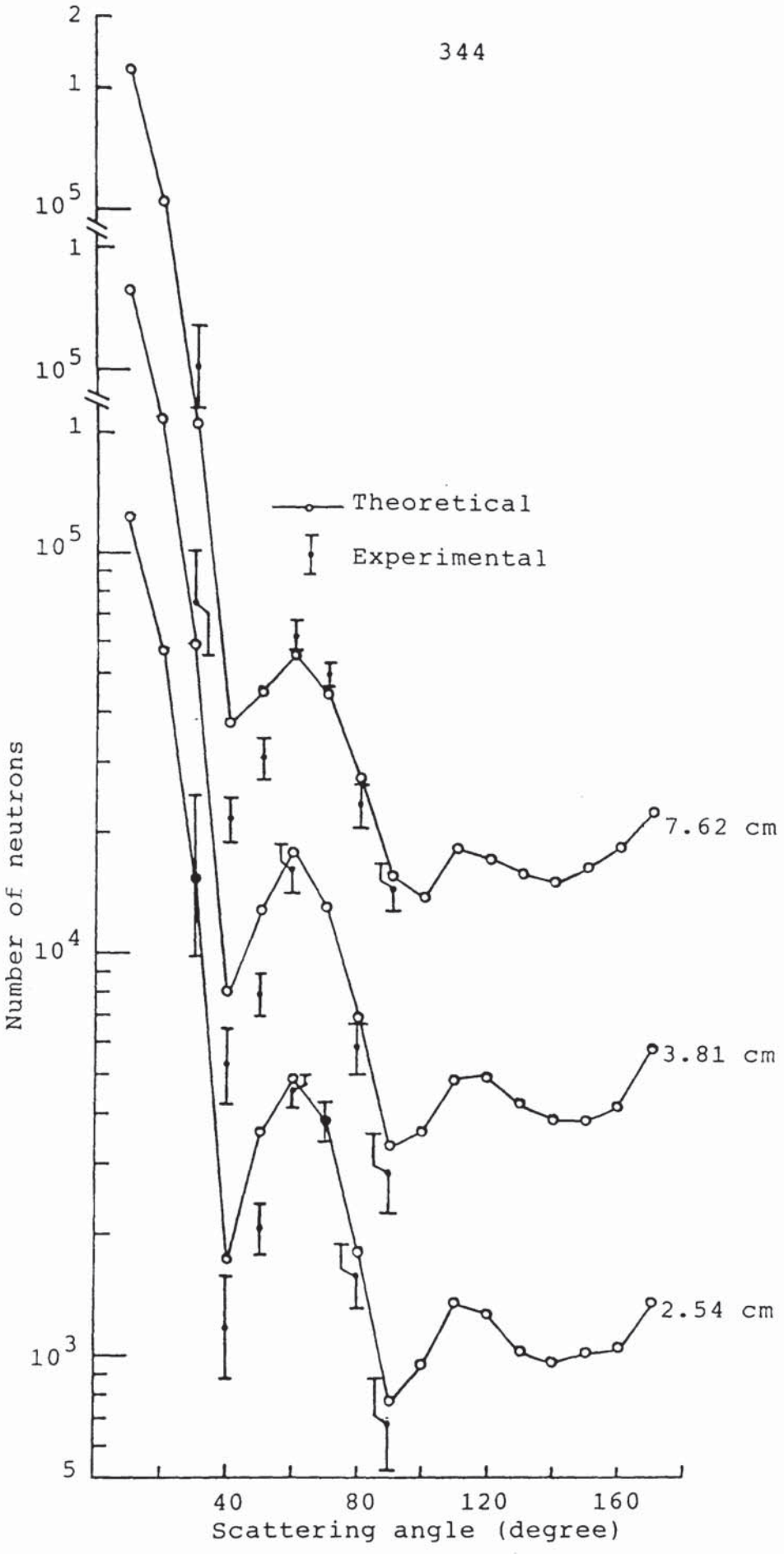

Figure (6.14): The angular distributions of the number of scattered neutrons from various thicknesses of aluminium calculated from Monte carlo method.

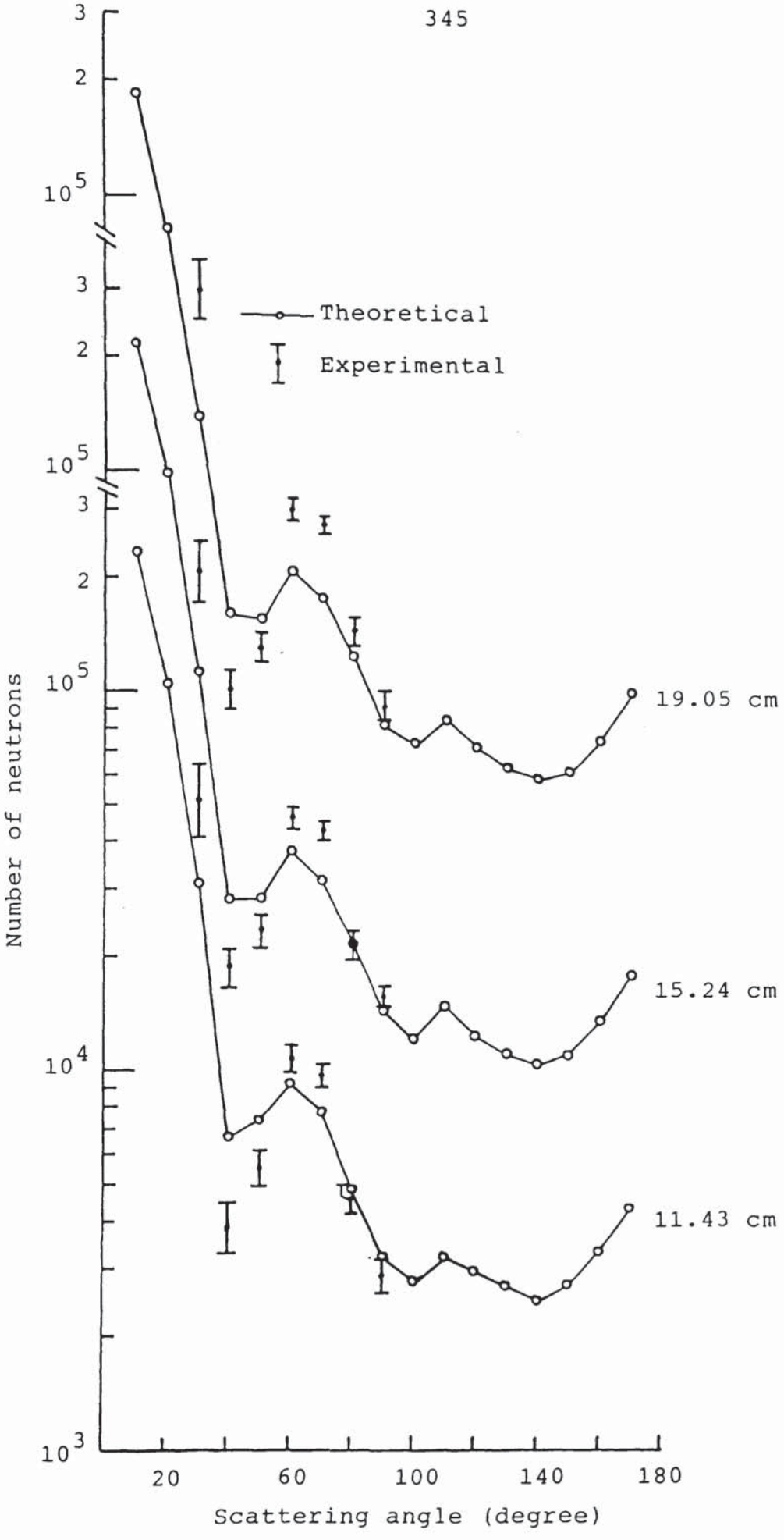

Figure (6.14):Continued.

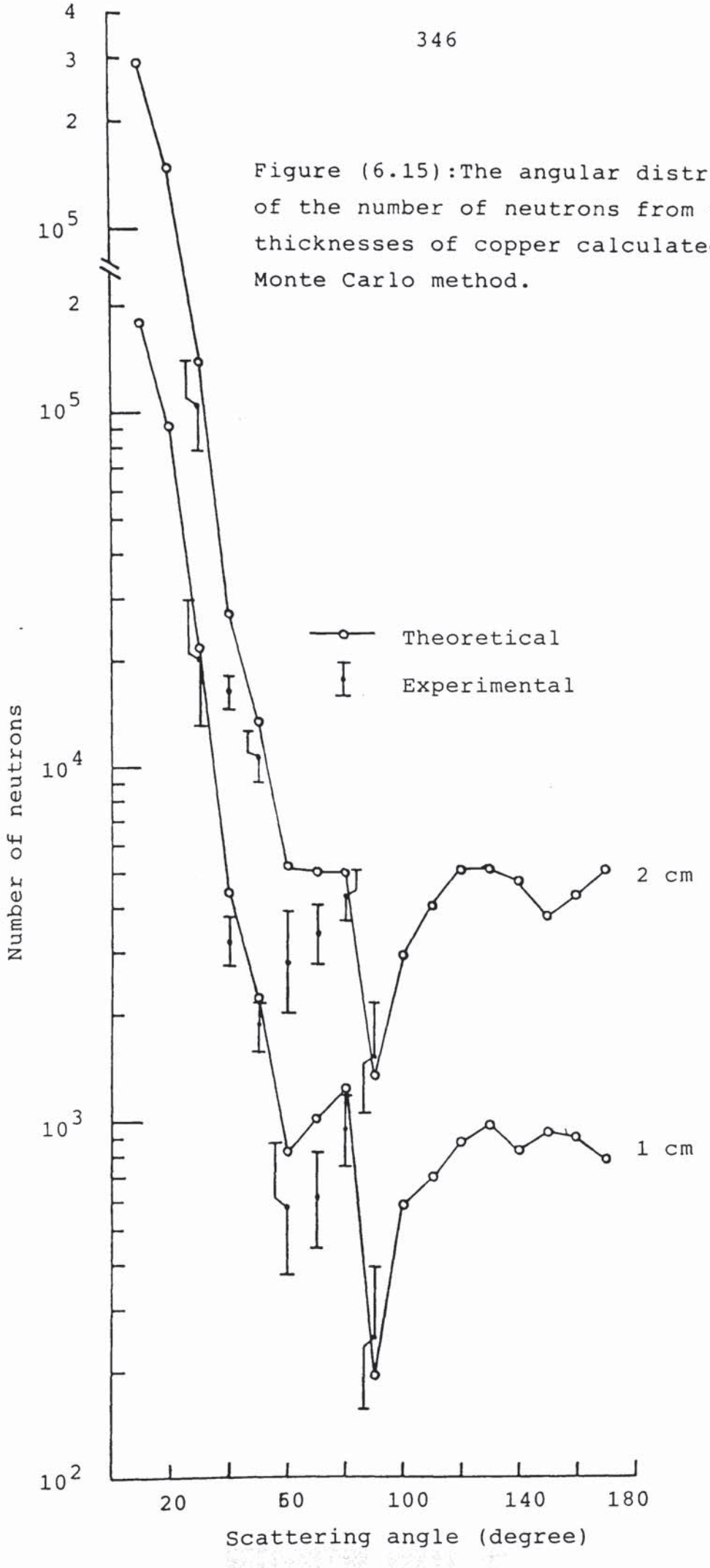

Figure (6.15):The angular distributions of the number of neutrons from various thicknesses of copper calculated from Monte Carlo method.

Figure (6.15):Continued.

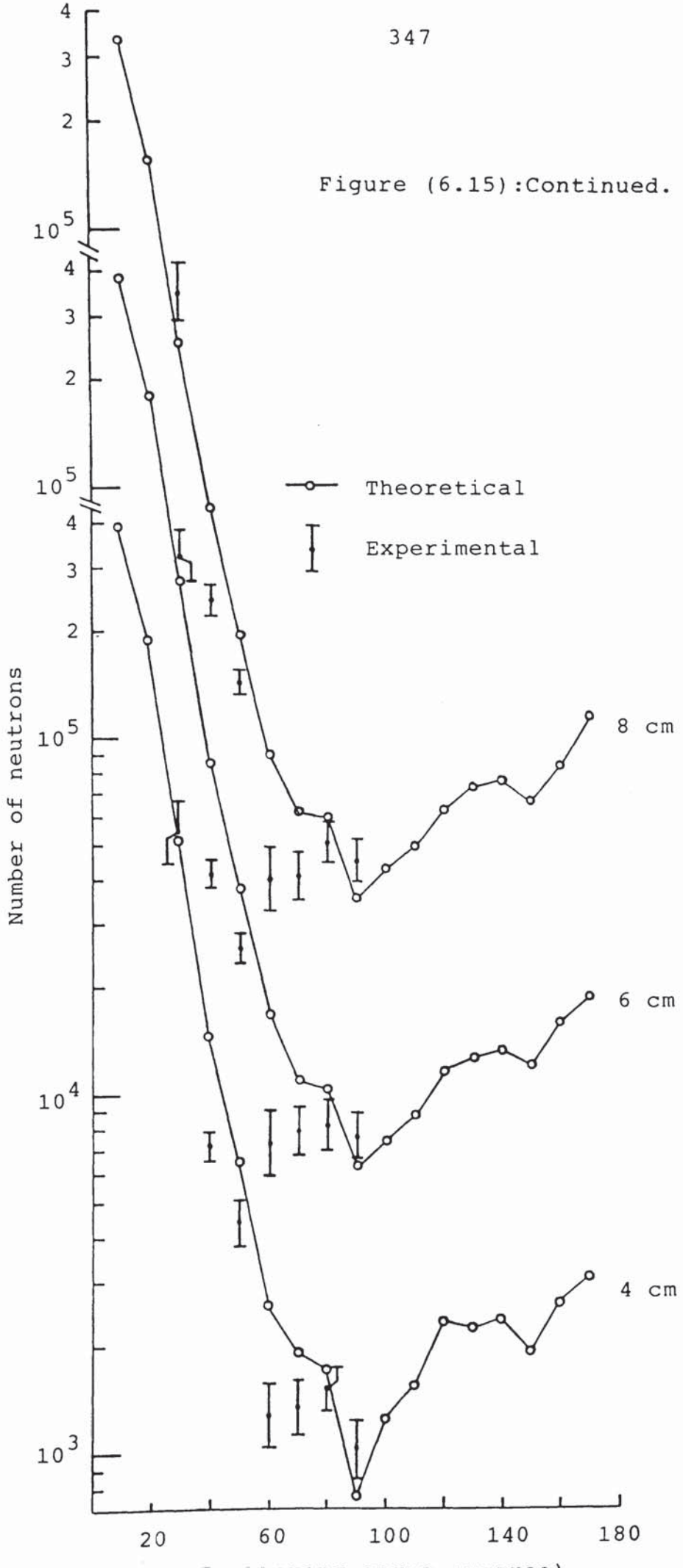

increase especially at higher angles.

From the calculation it was shown that the number of neutron scattered at angles greater than 180° have a similar behaviour. Figure (6.16) shows an example of the symmetric behaviour of the angular distribution of the scattered neutrons at angles from 0° to 350° from 3.81 cm thickness of aluminium.

From the calculation, it was predicted that the number of neutrons absorbed in the sample increases as the thickness increases. Table (6.4) shows the percentage of the neutrons absorb at different thicknesses for both aluminium and copper samples.

Table (6.4):The percentage of the neutrons absorbed at various thicknesses of aluminium and copper samples.

Aluminium		Copper	
Thickness m.f.p at 14 MeV	% absorbed	Thickness m.f.p at 14 MeV	% absorbed
0.267	15.6	0.243	12.1
0.400	22.6	0.486	23.0
0.800	40.3	0.973	40.9
1.200	53.6	1.459	54.8
1.600	63.6	1.945	65.4
2.000	71.1		

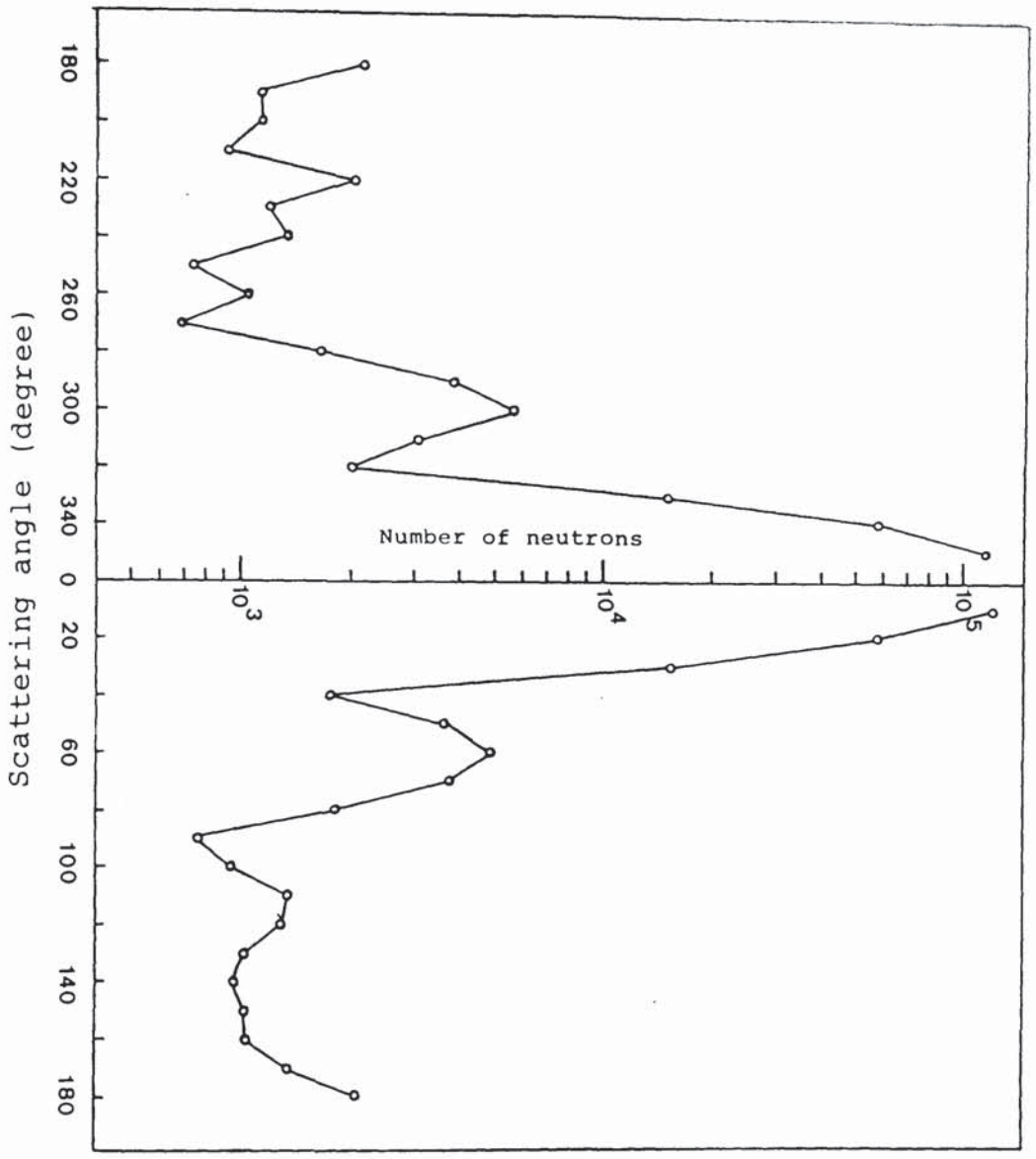

Figure (6.16):The symetric behaviour of the angular distribution of the scattered neutrons at angles between 0° to 350° from 3.81 cm thickness of Al.

6.2.4:THE VALIDATION OF THE MODEL.

In order to check the validation of the model, the differential scattering cross-sections were calculated from the number of neutrons predicted by this model. The differential elastic scattering cross-sections were calculated from the following formula,

$$\frac{d\sigma}{d\Omega}(\theta) = \frac{N_e(\theta).\sigma}{n_o[1 - \exp(-n\sigma x)]\Delta\Omega} \qquad (6\text{-}57)$$

where,

$N_e(\theta)$ = the number of scattered neutrons predicted from the model,

$\Delta\Omega$ = the solid angle,

n_o = the total number of incident neutrons,

σ = the total cross-section,

x = the thickness of the sample,

n = the number of nuclei per cm^3.

The differential elastic scattering cross-sections calculated by the above formula were then compared with the input data of ENDF-BIV (97,103). As for examples figures (6.17) and (6.18) show the results for aluminium and copper scattered from 3.81 cm and 2 cm thickness respectively. The solid line that appears in each figure is the differential elastic scattering cross-section from ENDF-BIV (97,103).

For both aluminium and copper samples, the differential cross-sections predicted by this model are in reasonable agreement with the input data. However, the

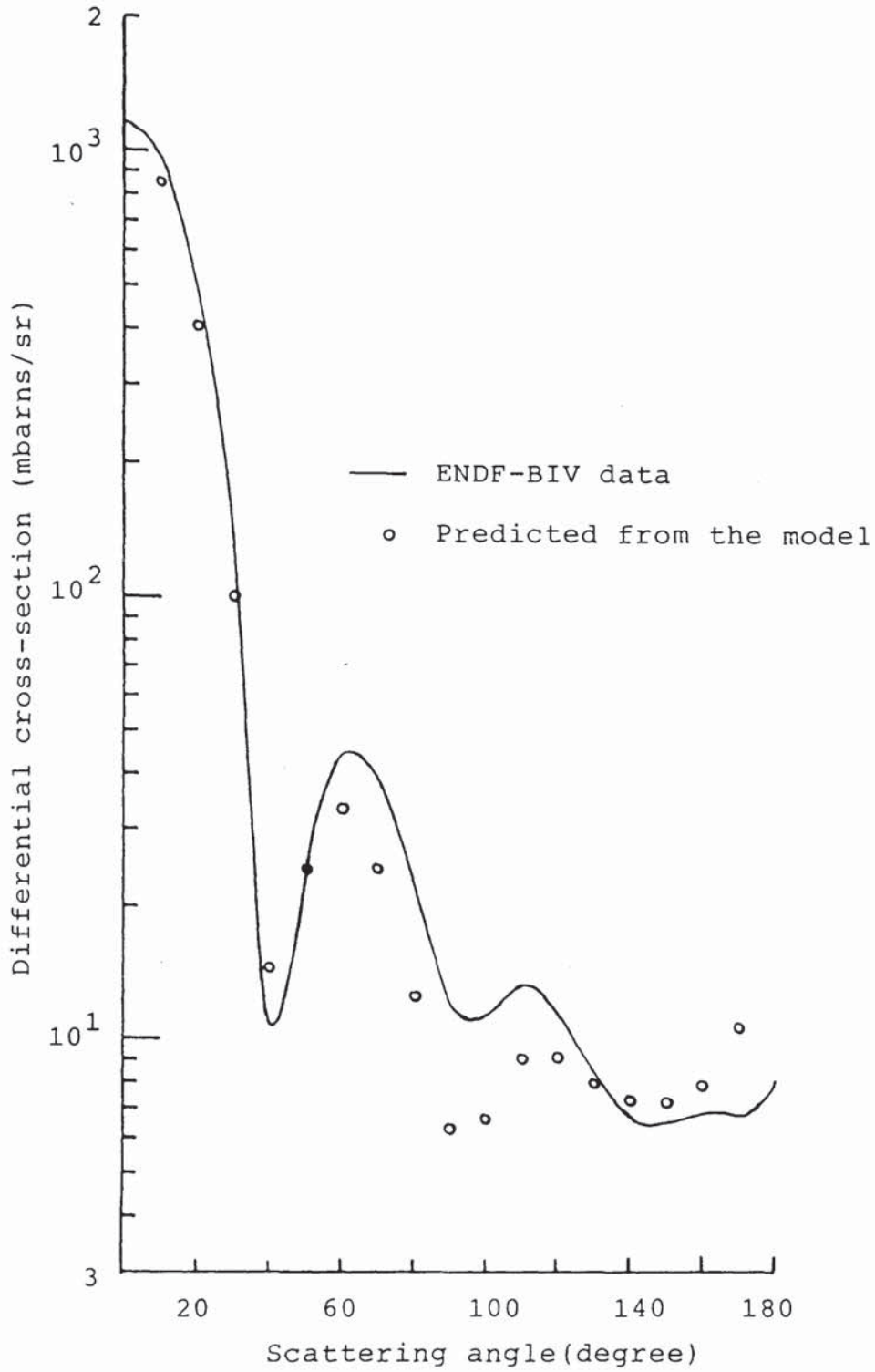

Figure (6.17):The angular distribution of the differential elastic scattering cross-section calculated from Monte Carlo model for 3.81 cm thickness of aluminium

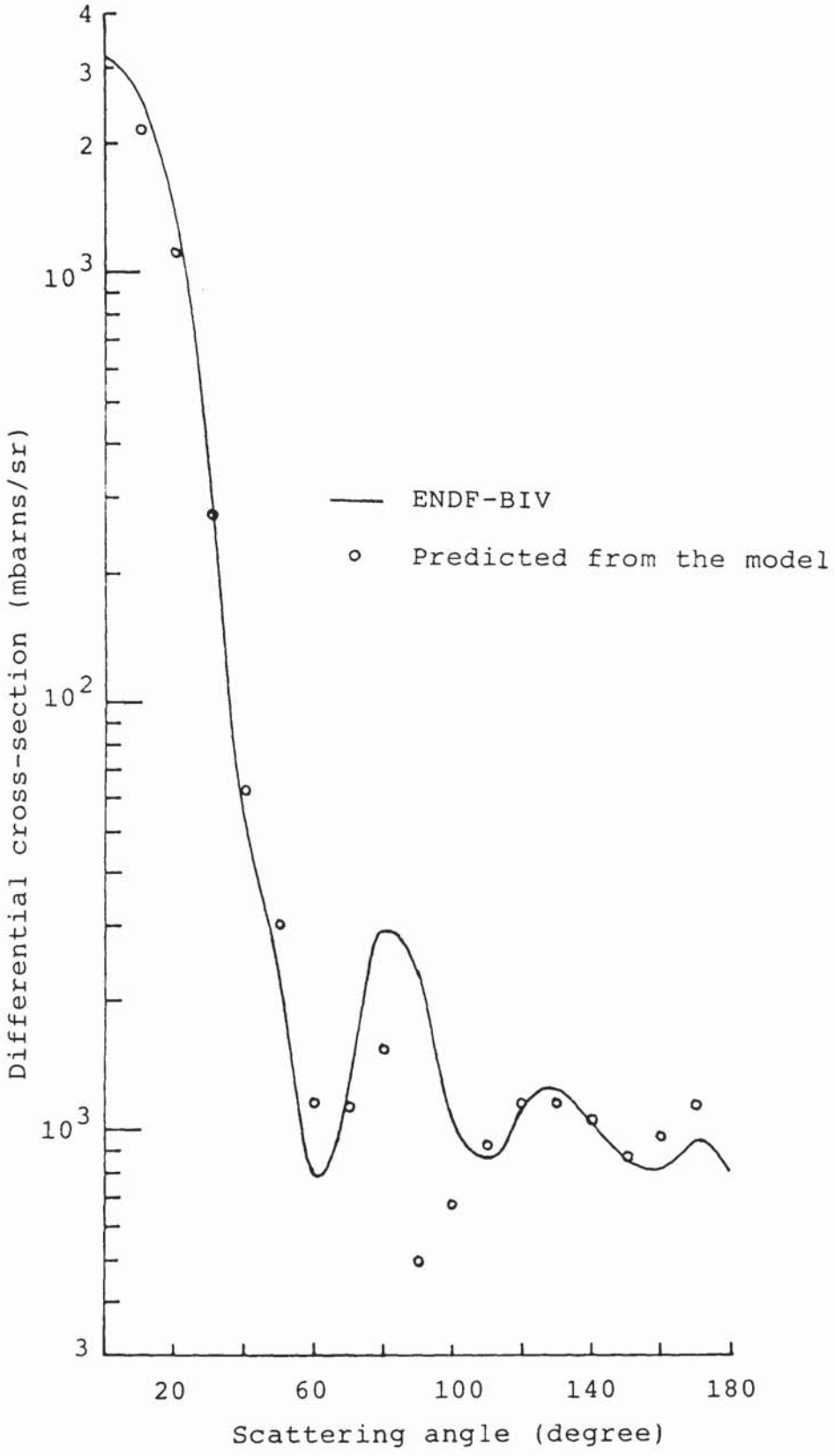

Figure (6.18):The angular distribution of the differential elastic scattering cross-section calculated from Monte Carlo model for 2 cm thickness of copper.

results predicted at angles between 80° to 100° are much lower than the ENDF-BIV data. The reason for this is that, at these angles neutrons have maximum thickness to penetrate into the sample because of the rectangular shape of the sample geometry. Because of this, the chance of neutrons escape from the sample at these angles is less compared to other angles.

The results also show that the agreement becomes less as the thickness of the sample increase especially at lower angles.

CHAPTER 7

CONCLUSION

The associated particle time of flight technique has been used in the present work to measure the differential scattering cross-sections of 14.1 MeV neutrons scattered from D-T fusion reactor blanket materials, aluminium, copper and molybdenum. The 14.1 MeV neutron flux was generated from $T(d,n)He^4$ reaction by accelerating the deuteron beam up to 140 keV on to tritiated titanium target using S.A.M.E.S type J electrostatic accelerator.

According to the kinematics of the $T(d,n)He^4$ reaction discussed in chapter 2, the most intense neutrons with energy 14.1 MeV was found at 83.5° to the deuteron beam direction associated with alpha particle angle at 90° to the deuteron beam direction. This angle was chosen as the 0° neutron scattering angle in the practical arrangement.

The performance of the time of flight spectrometer was tested by observing the time spectrum taken from the direct neutron beam i.e at $\theta_n = 83.5^{\circ}$. By choosing the flight path of 1.29 m, the time resolution of the spectrometer was obtained as 2.2 ± 0.2 ns FWHM and the full width at 1/10 maximum was found to be 4.1 ± 0.4 ns. It is

possible to improve the time resolution by choosing large sample-to-detector distance. However, this will increase the background counts and the accumulation time of the spectrum.

The time resolution of the spectrometer was limited mainly by the contributions of the time uncertainty of the neutron detector and photomultiplier tube. It is noted that the plastic scintillator NE102A employed in the present work was 50.8 mm radius and 50.8 mm thickness, resulting in an appreciable amount of time fluctuation due to the transit time of neutron through the large volume of the scintillator. Using smaller dimensions of the scintillator, it is expected that there would be an improvement of time resolution. However, using thin scintillator would cause a reduction in the efficiency of the detector and consequently reduce the signal-to-background ratio in the neutron channel. The presence of a light guide in the neutron detector system can further decrease the performance of the spectrometer. The used of light guide will increase the time spread in response time due to the fluctuation of the photon collection time on the photocathode.

In the present work, the photomultiplier tube employed in the neutron detector was Philip 56 AVP which had a rise time of 2 ns. Therefore, most of the limitation in the time resolution arises from the fluctuations in the transit time of neutrons in the

scintillator.

Due to the limitation of the time resolution of the spectrometer, it was not possible to resolve the elastic and inelastic components of the scattered neutrons from aluminium, copper and molybdenum isotopes. However, as discussed in chapter 4, using the Gaussian shape of the elastic peak, it was possible to strip off the contribution of the inelastic scattered neutrons in the elastic peak. The present method is applicable to small computer, reasonably accurate and requires only minimal input information.

The associated particle time of flight technique constructed in the present work was used to measure the differential scattering cross-sections of 14.1 MeV neutrons for D-T fusion reactor blanket materials, aluminium, copper and molybdenum, at different thicknesses of slab geometry. The differential scattering cross-sections were measured at several scattering angles between 30° to 90° by rotating the neutron detector through different angles with respect to the sample position.

The results of the differential elastic scattering cross-sections for 14.1 MeV neutrons for the thin aluminium sample using slab geometry with thickness of 2.54 cm were in agreement within the experimental error with the data obtained by Bonazzola et al (14) using a disk scatterer of 2 cm thickness and Whisnant et al (15)

using a cylindrical geometry 2.54 cm high and 3.81 cm diameter. This angular distribution is also in good agreement with the data from ENDF-BIV (97) and the data reported by Yuasa (13) using a disk scatterer.

The differential elastic scattering cross-section data were fitted by a Legendre polynomial expansion and the optimum coefficients were obtained by minimizing the value of χ^2 . The result of the integrated elastic scattering cross-section obtained from the fit is compatible with the data of ENDF-BIV (97) and others (11,15,99,100). The lower limit of the differential elastic cross-section in the foward direction i.e $d\sigma/d\Omega$ ($\theta_{cm}=0^\circ$) obtained from the fit disagrees with the value calculated from the Wick's limit by only 2%.

The differential inelastic scattering cross-sections for combined group of 0.84 MeV and 1.04 MeV states in the thin sample of aluminium were measured over the angular range between 30° to 90° . The results obtained show reasonable agreement with the data measured by Bonazzola et al (14). The non-elastic differential cross-sections (n,n') and (n,2n), for neutron in the energy range (5-14) MeV in 3 MeV intervals were measured. No similar measurements were found in the published literature to compare with the present work.

The results of the differential elastic scattering cross-sections for 14.1 MeV neutrons for the thin copper sample with 1 cm thickness were in good agreement within

the experimental error with the data of Coon et al (11) using ring geometry and the data from ENDF-BIV (103). Legendre polynomial fits were produced and the optimum coefficients obtained were compared to the ENDF-BIV data (103). The result of the integrated elastic scattering cross-section obtained from the fitting is in agreement within the experimental error with the data of ENDF-BIV (103) and others (11,104). The 0° differential cross-section obtained from the fit was found to be 7.6% higher than the predicted Wick's limit.

The individual peak of neutron inelastic scattering in copper could not be resolved individually because of the poor resolution of the spectrometer and very close separation between the ground state and the excited states of the copper isotopes. Therefore, only the non-elastic differential cross-sections in the energy range (5-14) MeV in 3 MeV intervals were measured. No similar measurements have been found to compare with the present work.

The differential elastic scattering cross-sections for thin sample of molybdenum were measured in the angular range between 30° to 90°. The results obtained are in reasonable agreement with the published data by Strizhak et al (17). The integrated elastic scattering cross-section obtained from the Legendre polynomial fit is in good agreement with the data of ENDF-BIV (105) and UKNDL (106). The 0° differential elastic cross-section obtained from the fit was found to be 17.6% higher than

the predicted Wick's limit. The non-elastic differential cross-sections of 14.1 MeV neutrons in the energy range (5-14) MeV in 3 MeV intervals were also presented in the present work.

The differential scattering cross-sections of 14.1 MeV neutrons for thick samples of aluminium and copper were measured at various thicknesses up to 2 Mean free path. No such measurements have so far been done for these samples and it is hoped that these results will be useful as a source of data to study the multiple scattering process in the extended sample.

The variation of the differential elastic and non-elastic scattering cross-sections with the sample thicknesses for both samples is predicted by the relation $\sigma_x = \sigma_o \exp (\alpha x)$. The average value of constant α obtained is in good agreement with the results for iron and concrete measured by Anvarian (102) and Jasim (93) for lithium and lead samples. It seems this relationship can be used in general for all elements with extended thickness.

The results of the differential elastic scattering cross-sections of 14.1 MeV neutrons for thin samples of aluminium, copper and molybdenum were compared with the results predicted by optical model calculation using the computer programme SCAT-2 (18). The comparisons of the present data were investigated based on the prediction of four sets of the optical model parameters given by Wilmore

and Hodgson (6), Becchetti and Greenlees (7), Ferrer et al (107) and Cindro and Bersillon (108). For copper and molybdenum, the theoretical results show that the best agreement with the experimental results were found using the Cindro and Bersillon (108) optical model parameters. This is because the Cindro and Bersillon parameters were already used to fit the neutron-nucleus data for 14 MeV neutron especially for medium and heavy nuclei. For aluminium, the best agreement was found using the prediction of the optical model parameters given by Becchetti and Greenlees (7). This feature agrees with the work done by Whisnant et al (15) where their experimental measurements were also in good agreement with the results predicted based on the Becchetti and Greenlees optical model parameters.

The integrated elastic scattering cross-sections for aluminium, copper and molybdenum obtained in the present work are also in reasonable agreement with the values predicted by the optical model calculations.

In conclusion, these comparisons indicates that the optical model analysis can give a good description of the general features of neutron scattering from medium and heavy nuclei.

In order to investigate the multiple scattering processes in the extended sample, a Monte Carlo simulation model was developed. The model was capable of predicting the number of scattered neutrons at all possible angles

from 0° to 350° for various sample thicknesses. The effective differential elastic cross-sections predicted by this model are in reasonable agreement with the input data of ENDF-BIV (97,103) at low angles and show departures at higher angles.

APPENDIX A

KINEMATICS OF THE T(d,n)He^4 REACTION

```
100 OPEN 1,4
120 PRINT£1,SPC(4)"KINEMATIC OF T(D,N)HE4 REACTION"
130 PRINT£1
160 M1=2.014102
170 M2=3.016049
180 M3=1.008665
190 M4=4.002604
200 Q=(M1+M2-M3-M4)*931.375
290 FOR E1=.00000000000000000001 TO .14 STEP 0.01
300 PRINT£1,SPC(4)"DEUTERON ENERGY=";E1
310 PRINT£1,SPC(4)"********************"
315 PRINT
320 PRINT£1,SPC(4)"NEUTRON ANG"SPC(3)"ALPHA ANG"SPC(7)"NEUTRON ENERGY"
330 PRINT£1,SPC(4)"==========="SPC(3)"========="SPC(7)"=============="
350 FOR ANG=76 TO 100 STEP 1
360 IF ANG=180 THEN 620
370 PSI=ANG* /180
380 K=SQR(M1*M3*E1)/(M4+M3)*COS(PSI)
390 L=(M4-M1)/(M4+M3)*E1+Q*M4/(M4+M3)
400 A1=(M1*M3*E1)/(M4+M3)↑2*COS(PSI)*COS(PSI)
410 B1=SQR(A1+L)
420 EN=(K+B1)↑2
430 E3=INT(EN*1000+.5)/1000
450 EH=E1+Q-E3
460 E4=INT(EH*1000+.5)/1000
480 A=(M4/M3)*((M1+M2)/M1)
490 B=A*((M2/(M1+M2))+(Q/E1))
500 C=SQR((B-(SIN(PSI)*SIN(PSI))))
510 C1=.5*SIN(2*PSI)+SIN(PSI)*C
520 C2=COS(PSI)*C-(SIN(PSI)*SIN(PSI))-(M4/M3)
530 D=(180/3.1415926)*ATN(C1/C2)
550 FI=INT(D*1000+.5)/1000
560 IF FI<0 THEN GO TO 610
570 FI=180-FI
580 PRINT£1,SPC(6);ANG;SPC(7);FI;SPC(12);E3
590 NEXT ANG
600 NEXT E1
610 FI=FI*(-1) :GO TO 630
620 FI=0
630 PRINT£1,SPC(69;ANG;SPC(7);FI;SPC(12);E3
640 NEXT ANG
645 PRINT
650 NEXT E1
660 CLOSE 1,4
670 END

READY.
```

APPENDIX B

DETERMINATION OF THE NUMBER OF COUNTS IN THE NEUTRON PEAK.

In nuclear spectroscopy, the energy spectrum obtained with a multi-channel pulse height analyzer contains a peak which can be represented by a Gaussian function;

$$Y(x) = Y_o \exp [- (x - x_o)^2 / 2\sigma^2] \qquad (B-1)$$

where,

$Y(x)$ = the amplitud of the Gaussian at channel x,

Y_o = the peak height,

x_o = the peak position,

σ = the standard deviation.

Using the property of the Gaussian function, we obtained,

$$Q(x) = \frac{Y(x - 1)}{Y(x + 1)} = \exp [2 (x - x_o)/\sigma^2] \qquad (B-2)$$

The logarithm of equation (B-2) is written by,

$$\log_e Q(x) = 2 (x - x_o)/\sigma^2 \qquad (B-3)$$

The quantity of $\log_e Q(x)$ is a linear function of x and can be fitted to a straight line by the least squares method. The standard deviation σ and the centroid x_o of the Gaussian can be obtained from the slope m and the intercept c of this linear fit, i.e

$$\sigma = (2/m)^{\frac{1}{2}} \qquad \text{(B-4)}$$

and $$x_o = - c/m \qquad \text{(B-5)}$$

In this fitting, the weights associated to $\log_e Q(x)$ are chosen as,

$$W = \left[\frac{1}{N_i + 1} + \frac{1}{N_i - 1}\right]^{-1} \qquad \text{(B-6)}$$

The peak height Y_o is then evaluated from the weighted mean,

$$\log_e Y_o = \frac{\sum_i^N W_i' \left[\log_e N_i + (x_i - x_o)^2 / 2\sigma^2\right]}{\sum_i W_i'} \qquad \text{(B-7)}$$

where the weighting factors are chosen (91) as,

$$W_i = \left[\frac{1}{N_i} + \frac{(x_i - x_o)^2}{\sigma^2}\left\{(\Delta x_o)^2 + \frac{(x_i - x_o)^2}{\sigma^2}(\Delta\sigma)^2\right\}\right]^{-1} \qquad \text{(B-8)}$$

and Δx_o = the standard deviation of x_o,

$\Delta\sigma$ = the estimated standard deviation of .

The total area under the peak A can be calculated from the value of Y_o i.e

$$A = (2\pi)^{\frac{1}{2}} Y_o \qquad \text{(B-9)}$$

and its full width at half maximum is

$$\text{FWHM} = 2 (2 \log_e 2)^{\frac{1}{2}} . \sigma = 2.355\sigma \qquad \text{(B-10)}$$

GAUSSIAN DISTRIBUTION

```
100 OPEN 1,4
110 PRINT£1,SPC(3)"DETERMINATION OF THE NUMBER OF COUNTS"
120 PRINT£1
130 PRINT£1,SPC(3)"CARBON SAMPLE 30 DEG"
140 PRINT£1
170 INPUT N
180 DIM X(N),Y(N),Q(N),U(N),W(N)
190 A1=0
200 B1=0
210 C1=0
220 D1=0
230 E=0
240 FOR I=1 TO N STEP 1
250 READ X(I):NEXT
260 FOR I=1 TO N STEP 1
270 READ Y(I):NEXT
280 FOR I=2 TO N
290 PRINT£1,TAB(4);X(I);TAB(10);Y(I):NEXT
300 FOR I=2 TO N-1 STEP 1
310 K=I-1
320 J=I+1
330 L=N-2
340 Q(I)=LOG(Y(K)/Y(J))
350 U(I)=(1/Y(J)+1/Y(K))
360 U(I)=1/U(I)
370 A1=A1+X(I)*U(I)
380 B1=B1+Q(I)*U(I)
390 C1=C1+X(I)*Q(I)*U(I)
400 D1=D1+X(I)*X(I)*U(I)
410 E=E+U(I)
420 NEXT I
430 M=(E*C1-A1*B1)/(E*D1-A1*A1)
440 B=(B1*D1-A1*C1)/(E*D1-A1*A1)
450 PRINT£1,"M=";M
460 PRINT£1,"B=";B
480 S=SQR(2.0/M)
500 X0=-(B)/M
510 PRINT£1,"PEAK POSITION=";X0
530 PRINT£1,"SIGMA=";S
560 A2=0
570 D2=0
580 A2=A2+X(I)
590 D2=D2+X(I)*X(I)
600 S2=(L*D2)-(A2)↑2
610 D3=0
620 FOR I=2 TO N-1 STEP 1
630 Z=2*(X(I)-X0)/S↑2
640 D=(Q(I)-Z)↑2
650 R=D3+D
```

```
660 NEXT I
680 P=(R)/(L-2)
690 T0=SQR((L*P)/(S2))
700 S1=(0.7071*T0)/(M)↑1.5
720 S3=SQR((P*D)/S2)
730 S4=SQR((S3/M)↑2+(B*T0/M↑2)↑2)
750 REM S=S+S1
770 Z3=0
780 G=0
790 FOR I=1 TO N STEP 1
800 V=(S4)↑2+((X(I)-X0)↑2)*((S1)↑2)/(S↑2)
810 W(I)=1/Y(I)+(((X(I)-X0)↑2)*V)/(S↑4)
820 W(I)=1/W(I)
840 T1=((X(I)-X0)↑2)/(2*(S)↑2)
850 H1=(W(I)*(LOG(Y(I))+T1))
860 H2=H1/W(I)
870 H=H2+Z3
880 NEXT I
900 Y0=EXP(H)
910 PRINT£1,"PEAK HEIGHT=";Y0
920 A=2.507*S*Y0
930 PRINT£1,"PEAK AREA=";A
940 FW=2.355*S
950 PRINT£1,"FWHM=";FW
960 FOR X=360 TO 410 STEP 1
970 T1=((X-X0)↑2)/(2*(S)↑2)
980 T1=-T1
990 Y1=Y0*EXP (T1)
1000 PRINT£1 ,X,Y1
1010 NEXT X
1015 CLOSE 1
1020 END
1030 DATA 251,252,253,254,255,256,257,258,259,260,261,262,263,264
1040 DATA 117,158,205,216,279,314,329,312,288,268,227,202,148,111

READY.
```

APPENDIX C

LEGENDRE POLYNOMIAL FIT

The Legendre polynomial expansion is expressed by the equation,

$$y = a_o P_o(x) + a_1 P_1(x) + ... + a_n P_n(x)$$

$$= \sum_{l=0}^{n} a_l P_l(x) \qquad (C-1)$$

where, $x = \text{Cos } \Theta$ (C-2)

$$P_o(x) = 1 \qquad (C-3)$$

$$P_1(x) = x \qquad (C-4)$$

and higher order terms are given by,

$$P_l(x) = \frac{1}{l}\,(2l - 1)x\, P_{l-1}(x) - (l - 1)P_{l-2}(x) \qquad (C-5)$$

Legendre polynomial are orthogonal when averaged over all values of $x = \text{Cos } \Theta$,

$$\int_{-1}^{+1} P_l(x)\, P_m(x)\, dx = \begin{cases} 1 & \text{if } l = m \\ 0 & \text{if } l \neq m \end{cases} \qquad (C-6)$$

METHOD OF LEAST SQUARES.

Let us developed the method of least squares for an arbitrary function of order n,

$$y(x) = a_o X_o(x) + a_1 X_1(x) + ... + a_n X_n(x)$$

$$= \sum_{j=0}^{n} a_j X_j(x) \qquad (C-7)$$

The method of least squares is done by minimizing the quantity called χ^2 defined as,

$$\chi^2 = \sum_{i=1}^{N} \left\{ \frac{1}{\sigma^2} \left[y_i - y(x_i) \right]^2 \right\} \qquad \text{(C-8)}$$

where,

σ_i = the standard deviation for the experimental data $y(x_i)$,

y_i = the predicted data.

In order to minimize the value of χ^2, as a set of (n+1) equations

$$\frac{\delta}{\delta a_k} \sum_{i=1}^{N} [y_i - y(x_i)]^2 = \frac{\delta}{\delta a_k} \sum_{i=1}^{N} \left\{ y_i - \sum_{j=0}^{n} [a_i X_i(x_i)] \right\}^2 = 0 \qquad \text{(C-9)}$$

where k takes on all values from 0 to n.

The solution of these equations yields the values for the coefficients a_j for which χ^2 is a minimum. The yields for a set of (n+1) simultaneous equations become,

$$\Sigma y_i X_o(x_i) = a_o \Sigma X_o^2(x_i) + a_1 \Sigma X_1^2(x_i) X_o(x_i) + \ldots\ldots + a_n \Sigma X_n(x_i) X_o(x_i)$$

$$\Sigma y_i X_1(x_i) = a_o \Sigma X_o(x_i) X_1(x_i) + a_1 \Sigma X_1^2(x_i) + \ldots\ldots + a_n \Sigma X_n(x_i) X_1(x_i)$$

$$\ldots\ldots\ldots\ldots\ldots\ldots\ldots\ldots\ldots\ldots\ldots\ldots\ldots\ldots\ldots\ldots$$

$$\Sigma y_i X_n(x_i) = a_o \Sigma X_o(x_i) X_n(x_i) + a_1 \Sigma X_1(x_i) X_n(x_i) + \ldots\ldots + a_n \Sigma X_n^2(x_i)$$

which can be expressed as,

the inverse of the curvature matrix $\epsilon = \alpha^{-1}$, the result gives the solution for the coefficient matrix a directly since $\alpha\,\alpha^{-1} = I$

$$\alpha = \beta\,\alpha^{-1} \tag{C-15}$$

Equation (C-15) can be expressed in more conventional notation as,

$$a_j = \sum_{k=0}^{n} (\epsilon_{jk}\,\beta_k) = \sum_{k=0}^{n} \left\{ \epsilon_{jk} \sum \left[\frac{1}{\sigma^2} y_i X_k(x_i) \right] \right\} \tag{C-16}$$

ESTIMATION OF ERROR.

The uncertainties in the coefficients a_j can be estimated by considering the standard deviation σ_{aj},

$$\sigma_{aj}^2 = \sum \left[\sigma_i^2 \left(\frac{\delta a_j}{\delta y_i} \right) \right] \tag{C-17}$$

from equation (C-16) gives the derivetives,

$$\frac{\delta a_j}{\delta y_i} = \sum_{k=0}^{n} \left[\epsilon_{jk} \frac{1}{\sigma_i^2} X_k(x_i) \right] \tag{C-18}$$

and the weighted sum of the squares of the derivatives can be reduced to,

$$\sum \left[\sigma_i^2 \left(\frac{\delta a_j}{\delta y_i} \right)^2 \right] = \sum_{k=0}^{n} \sum_{m=0}^{n} \left\{ \epsilon_{jk}\,\epsilon_{jm} \sum \left[\frac{1}{\sigma_i^2} X_k(x_i) X_m(x_i) \right] \right\}$$

$$= \sum_{k=0}^{n} \sum_{m=0}^{n} (\epsilon_{jk}\,\epsilon_{jm}\,\alpha_{km}) = \epsilon_{jj} \tag{C-19}$$

The inverse matrix $\epsilon = \alpha^{-1}$ is called the error matrix because it contains most of the information needed

to estimated the error.

$$\sigma_{aj}^2 = \epsilon_{jj} \qquad \text{(C-20)}$$

If the uncertainties in the data point are not known, the uncertainty can be approximated as,

$$\sigma_i^2 = \sigma^2 = s^2 = \frac{1}{N-n-1} \sum \left\{ y_i - \sum_{j=0}^{n} [a_j X_j (x_i)] \right\}^2 \qquad \text{(C-21)}$$

where ^{2} is the sample variance for the fit.

$\nu = N-n-1$ is the number of degrees of freedom after fitting N data points with n+1 parameters. Combining equations (C-17) and (C-21), the uncertainty in the coefficient a is given by,

$$\sigma_{aj} \simeq s^2 \epsilon_{jj} \ (\sigma_i = 1) \qquad \text{(C-22)}$$

where $\epsilon_{jj} \ (\sigma_i = 1)$ is the error matrix evaluated with $\sigma_i = 1$.

LEGENDRE POLYNOMIAL FIT PROGRAMME

```
C       LEGENDRE POLYNOMIAL PROGRAM < LEGFIT >
C
C        PURPOSE
C           MAKE A LEAST-SQUARES FIT TO DATA WITH A LEGINDRE POLYNOMIAL
C             Y = A(1) + A(2)*X + A(3)*(3X**2-1)/2 +.........
C               = B(1) + (1.  + B(2)*X +B(3)*(3X**2-1)/2 +.....)
C                 WHERE X = COS(THETA)
C
C       DESCRRIBTION OF PARAMETERS
C       --------------------------
C
C         INPUT PARAMETERS
C         ****************
C
C         THETA -  ARRAY  OF ANGLES (IN DEGREES) OF THE DATA POINTS
C         Y     -  ARRAY  OF DATA POINTS FOR DEPENDENT VARIABLE
C         SIGMAY-  ARRAY OF STANDARD DEVIATIONS FOR Y DATA POINTS
C         NPTS  -  NUMBER OF PAIRS OF DATA POINTS
C         NORDER-  HIGHEST ORDER OF POLYNOMIAL ( NUMBER OF TERMS - 1 )
C         FTEST -  ARRAY OF VALUES OF F(L) FOR AN F-TEST
C
C
C         OUTPUT PARAMETERS
C         *****************
C
C         YFIT  -  ARRAY OF CALCULATED VALUES OF Y
C         A     -  ARRAY OF COEFFICENTS OF POLYNOMIAL
C         SIGMAA-  ARRAY OF STANDARD DEVIATIONS CEOFFICIENTS
C         B     -  ARRAY OF NORMALIZED RELATIVE CEOFFICIENTS
C         SIGMAB-  ARRAY OF STANDARD DEVIATIONS FOR RELATIVE COEIFFICENTS
C         CHISQR-  REDUCED CHI SQUAREE FOR FIT
C
C         SUBROUTINES AND FUNCTION SUBPROGRAMS REQUIRED
C                 MATINV (ARRAY, NTERMS, DET )
C                   INVERS A SYMMETRIC TWO-DIMENSIONAL MATRIX OF DEGREE N
C                   AND CALCULATES ITS DETERMINANT
C
C
      DOUBLE PRECISION COSINE , P, BETA, ALPHA, CHISQ
      DIMENSION WEIGHT(500), P(500,24)
      DIMENSION THETA(22), Y(22), SIGMAY(22),YFIT(22),A(22),B(22)
      DIMENSION SIGMAB(22),SIGMAA(22),FTEST(22)
      DIMENSION BETA(20), ALPHA(20,20)
C
C      ACCUMLATE WEIGHT AND LEGENDRE POLYNOMIAL
C
      READ(12,*)NPTS
      DO 2 I= 1, NPTS
      READ(12,*)THETA(I),Y(I),SIGMAY(I),FTEST(I)
```

```
  2    CONTINUE
       DO 1000 NORDER =0,20,1
 11    NTERMS = 1
       NCOEFF=1
       NEVEN=0
       MODE = 0
       WRITE(13,'("NORDER=",I3)') NORDER
       WRITE(13,'("MODE=",I3)') MODE
       WRITE(13,'("NEVEN=",I3)') NEVEN
       JMAX=NORDER+1
 20    DO 40 I = 1, NPTS
 21    IF ( MODE ) 22, 27, 29
 22    IF ( Y(I) ) 25, 27, 23
 23    WEIGHT(I) = 1. / Y(I)
       GO TO 31
 25    WEIGHT(I) = 1. / (-Y(I))
       GO TO 31
 27    WEIGHT(I) = 1.
       GO TO 31
 29    WEIGHT(I) = 1. / SIGMAY(I)**2
 31    COSINE = COS(.01745329252 * THETA(I))
       P(I,1) = 1.
       P(I,2) = COSINE
       DO 36 L = 2, NORDER
       FL = L
 36    P(I,L+1)=((2.0*FL-1.0)*COSINE*P(I,L)-(FL-1.0)*P(I,L-1))/FL
C
C        ACCUMULATE MATRICES ALPHA AND BETA
C
 40    CONTINUE
 51    DO 54 J = 1, NTERMS
       BETA(J) = 0.
       DO 54 K = 1, NTERMS
 54    ALPHA(J,K) = 0.
 61    DO 66 I = 1, NPTS
       DO 66 J = 1, NTERMS
       BETA(J) = BETA(J) + P(I,J)*Y(I)*WEIGHT(I)
       DO 66 K = J , NTERMS
       ALPHA(J,K) = ALPHA(J,K) + P(I,J)*P(I,K)*WEIGHT(I)
 66    ALPHA(K,J) = ALPHA(J,K)
C
C        DELETE FIXED COEFFICIENTS
C
 70    IF (NEVEN) 71, 91, 81
 71    DO 76 J = 3, NTERMS, 2
       BETA(J) = 0.0
       DO 75 K = 1, NTERMS
       ALPHA(J,K) = 0.0
 75    ALPHA(K,J) = 0.0
 76    ALPHA(J,J) = 1.0
       GO TO 91
 81    DO 86 J = 2, NTERMS, 2
       BETA(J) = 0.0
       DO 85 K = 1, NTERMS
       ALPHA(J,K) = 0.0
 85    ALPHA(K,J) = 0.0
 86    ALPHA(J,J) = 1.0
C
C        INVERT CURVATURE MATRIX ALPHA
C
```

```
   91  DO 95 J = 1, JMAX
       A(J) = 0.0
       SIGMAA(J) = 0.0
       B(J) = 0.0
   95  SIGMAB(J) = 0.0
       DO 97 I = 1, NPTS
   97  YFIT(I) = 0.0
  101  CALL MATINV (ALPHA,NTERMS,DET)
C
C       CALCULATE COEFFICIENTS,FIT , AND, CHI SQURES
C
       IF (DET) 111, 103, 111
  103  CHISQR = 0.0
       GO TO 170
  111  DO 115 J = 1, NTERMS
       DO 113 K = 1, NTERMS
  113  A(J) = A(J) + BETA(K)*ALPHA(J,K)
       DO 115 I = 1, NPTS
  115  YFIT(I) = YFIT(I) + A(J)*P(I,J)
  121  CHISQ = 0.0
       DO 123 I = 1, NPTS
       CHISQ = CHISQ + (Y(I) - YFIT(I))**2 * WEIGHT(I)
  123  CONTINUE
       FREE = NPTS - NCOEFF
       CHISQR = CHISQ / FREE
C
C       TEST FOR END OF FIT
C
  131    IF ( NTERMS - JMAX) 132, 151, 151
  132    IF ( NCOEFF - 2) 133, 134, 141
  133    IF (NEVEN) 137,137,135
  134    IF (NEVEN) 135, 137, 135
  135    NTERMS = NTERMS + 2
         GO TO 138
  137    NTERMS = NTERMS + 1
  138    NCOEFF = NCOEFF + 1
         CHISQ1 = CHISQ
         GO TO 51
  141    FVALUE = ( CHISQ1 - CHISQ) / CHISQR
         IF ( FTEST(NTERMS) -    FVALUE ) 134, 143, 143
  143    IF (NEVEN) 144, 146, 144
  144    NTERMS = NTERMS - 2
         GO TO 147
  146    NTERMS = NTERMS - 1
  147    NCOEFF = NCOEFF - 1
         JMAX = NTERMS
  149    GO TO 51
C
C       CALCULATE REMINDER OF OUTPUT
C
  151    IF (MODE) 152, 154, 152
  152    VARNCE = 1.0
         GO TO 155
  154    VARNCE = CHISQR
  155 WRITE(13,*)" COEFFICIENTS FOR LEAST SQUARE FIT TO A LEGENDRE POL
       WRITE(13,*)"-------------------------------------------"
       WRITE(13,*)"           "
       DO 156 J = 1, NTERMS
      IF(ALPHA(J,J) .LE. 0.0 ) ALPHA(J,J)=0.009
       SIGMAA(J) =DSQRT(VARNCE*ALPHA(J,J))
```

```
      WRITE(13,*)"A(J)=",A(J) , "SIGMAA(J)=",SIGMAA(J)
  156   CONTINUE
  100  IF (A(1)) 162, 170, 162
  162   WRITE(13,*)"           "
        WRITE(13,*)" NORMALIZED LEGENDRE POLYNOMIAL "
        WRITE(13,*)"--------------------------------"
         DO 166 J = 2, NTERMS
         IF (A(J)) 164, 166, 164
  164    B(J) = A(J) / A(1)
  165  SIGMAB(J) = B(J)* DSQRT((SIGMAA(J)/A(J))**2 + (SIGMAA(1)/A(1))**2
     1  - 2.0 * VARNCE*ALPHA(J,1)/(A(J)*A(1)))


      WRITE(13,*)"B(J)=",B(J)      ,"SIGMAB(J)=",SIGMAB(J)
  166   CONTINUE
        B(1) = 1.0
       WRITE(13,*)"
       WRITE(13,*)"RESULT OF FITTING"
       WRITE(13,*)"-----------------"
       WRITE(13,*)"                 "
       WRITE(13,*)"ANGLE(THETA)","YEXP","YFIT"
       WRITE(13,*)"============","====","===="
        DO 989 I=1, NPTS
       WRITE(13,*)THETA(I),Y(I),YFIT(I)
  989   CONTINUE

       WRITE(13,*)"CHISQR=",CHISQR
       WRITE(13,*)"                 "
       WRITE(13,*)"************NEXT DEGREE**************************"
  1000 CONTINUE
   170 STOP
       END
C
C
C       SUBROUTINE MATINV
C
C
C         PURPOSE
C           INVERT A SYMMETRIC MATRIX AND CALCULATE ITS DETERMINANT
C
C         DESCRIBTION OF PARAMETERS
C           ARRAY    -  INPUT MATRIX WHICH IS REPLACED BY ITS INVERS
C           NORDER   -  DEGREE OF MATRIX (ORDER OF DETERMINANT)
C           DET      -  DETERMINANT OF INPUT MATRIX
C
       SUBROUTINE MATINV (ARRAY, NORDER, DET)
       DOUBLE PRECISION ARRAY, AMAX, SAVE
       DIMENSION ARRAY(20,20), IK(20), JK(20)
   10        DET = 1.
   11        DO 100 K = 1, NORDER
C
C        FIND LARGEST ELEMENT ARRAY(I,J) IN REST OF MATRIX
C
             AMAX = 0.0
   21        DO 30 I = K, NORDER
             DO 30 J = K, NORDER
   23        IF (ABS(AMAX) - ABS(ARRAY(I,J))) 24, 24, 30
   24        AMAX = ARRAY(I,J)
             IK(K) = I
             JK(K) = J
```

```
 30          CONTINUE
C
C         INTERCHANGE THE ROWS AND COLUMNS TO PUT AMAX IN ARRAY(K,K)
C
 31          IF (AMAX) 41, 32, 41
 32          DET = 0.0
             GO TO 140
 41          I = IK(K)
             IF ( I - K ) 21, 51, 43
 43          DO 50 J = 1, NORDER
              SAVE = ARRAY(K,J)
         ARRAY(K,J) = ARRAY(I,J)
 50           ARRAY(I,J) = -SAVE
 51           J = JK(K)
              IF (J-K) 21, 61, 53
 53           DO 60 I=1, NORDER
              SAVE = ARRAY(I,K)
              ARRAY(I,K) = ARRAY(I,J)
 60           ARRAY(I,J) = -SAVE
C
C         ACCUMULATE ELEMENTS OF INVERSE MATRIX
C
 61           DO 70 I = 1, NORDER
               IF (I-K) 63, 70, 63
 63           ARRAY(I,K) = -ARRAY(I,K) / AMAX
 70           CONTINUE
 71           DO 80 I = 1, NORDER
              DO 80 J = 1, NORDER
              IF (I-K) 74, 80, 74
 74           IF (J-K) 75, 80, 75
 75           ARRAY(I,J) = ARRAY(I,J)+ ARRAY(I,K)*ARRAY(K,J)
 80           CONTINUE
 81           DO 90 J = 1, NORDER
              IF (J-K) 83, 90, 83
 83           ARRAY(K,J) = ARRAY(K,J) / AMAX
 90           CONTINUE
              ARRAY(K,K) = 1.0/AMAX
 100          DET = DET*AMAX
C
C         RESTORE ORDERING OF MATRIX
C
 101          DO 130 L = 1, NORDER
              K = NORDER - L +1
              J = IK(K)
              IF (J-K) 111, 111, 105
 105          DO 110 I = 1, NORDER
              SAVE = ARRAY(I,K)
              ARRAY(I,K) = - ARRAY(I,J)
 110          ARRAY(I,J) = SAVE
 111          I = JK(K)
              IF ( I - K ) 130, 130, 113
 113          DO 120 J = 1, NORDER
              SAVE = ARRAY(K,J)
              ARRAY(K,J) = - ARRAY(I,J)
 120          ARRAY(I,J) = SAVE
 130          CONTINUE
 140          RETURN
         END
```

APPENDIX D

LEAST-SQUARES FIT

```
50 OPEN 1,4
100 PRINT£1,SPC(4)"A LEAST SQUARES FIT TO A STRAIGHT LINE Y=A+B*X"
110 PRINT£1
120 PRINT£1,SPC(4)"DIFFERENTIAL ELASTIC SCATTERING X-SECTION"
150 PRINT£1
180 PRINT£1,SPC(4)"ALUMINIUM SAMPLE 40 DEG"
200 PRINT£1
220 INPUT MOD
230 PRINT£1
235 PRINT£1,SPC(4)"MODE=";MOD
237 PRINT£1
240 S=0
250 S0=0
260 T0=0
270 S1=0
280 S2=0
290 T1=0
295 PRINT£1,SPC(4)"FITTING DATA"
297 PRINT£1
300 N=6
301 PRINT£1,SPC(4)"NUMBER OF POINTS=";N
302 PRINT£1
303 PRINT£1,SPC(4)"X(I)"SPC(7)"Y(I)"SPC(7)"C(I)"
304 PRINT£1,SPC(4)"============================"
308 PRINT£1
310 FOR I=1 TO N
320 READ X(I),Y(I),C(I)
330 PRINT£1,SPC(4);X(I);SPC(4);Y(I);SPC(4);C(I)
340 NEXT I
345 FOR I=1 TO N
360 IF MOD =0 GOTO 390
370 IF MOD =1 GOTO 380
380 W=1/C(I)↑2
385 GOTO400
390 W=1
400 S=S+W
410 S0=S0+(W*X(I))
420 T0=T0+W*Y(I)
430 S1=S1+W*X(I)*X(I)
440 S2=S2+W*X(I)*Y(I)
450 T1=T1+W*Y(I)*Y(I)
460 NEXT I
465 PRINT£1
470 D=S*S1-S0*S0
480 A=((S1*T0)-(S0*S2))/D
485 B=(S2*S-S0*T0)/D
486 PRINT£1,SPC(4)"============================"
487 PRINT£1
488 PRINT£1,SPC(4)"BEST FITTING"
490 PRINT£1
```

```
491 PRINT£1,SPC(4)"X(I)"SPC(7)"Y(I)"
492 PRINT£1,SPC(4)"================"
493 PRINT£1
494 FOR I=1 TO N
495 Z(I)=A+B*X(I)
498 Z(I)=INT(Z(I)*1000+.5)/1000
500 PRINT£1,SPC(4);X(I);SPC(4);Z(I)
505 NEXT I
510 PRINT£1
520 PRINT£1,SPC(4)"================"
523 PRINT£1
525 PRINT£1,SPC(4)"A=";A
526 PRINT£1
527 PRINT£1,SPC(4)"B=";B
529 PRINT£1
530 IF MODE=0 GOTO 570
540 IF MODE=1 GOTO 560
560 V=1
565 GOTO 600
570 C=N-2
580 V=(T1+A*A*S+B*B*S1-2*(A*T0+B*S2-A*B*S0))/C
600 SA=SQR(V*S1/D)
605 SA=INT(SA*10000+.5)/10000
610 SB=SQR(V*S/D)
620 SB=INT(SB*10000+.5)/10000
630 R=(S*S2-S0*T0)/SQR(D*(S*T1-T0*T0))
640 R=INT(R*10000+.5)/10000
650 PRINT£1,SPC(4)"SA="SA
660 PRINT£1
670 PRINT£1,SPC(4)"SB=";SB
680 PRINT£1
690 PRINT£1,SPC(4)"R=";R
693 CLOSE 1
695 END
700 DATA .2667,2.412,.335
710 DATA .4,2.881,.224
720 DATA .8,3.044,.146
730 DATA 1.2,3.145,.140
740 DATA 1.6,3.341,.124
750 DATA 2,3.402,.121

READY.
```

APPENDIX E

```
10 PRINT"STORE X-SECTION DATA ON FILE":INPUTS$:IF S$="Y" THEN GOTO 3330
20 DIM D(36)
30 PRINT"ENTER X,Y DIMENSION OF THE CRYSTAL (CM)":INPUT A,B
40 GOSUB 2420:REM READ DIRECTION
50 DIM Q(36),B(36,14),X(36),C(36,14),Z(20,2),P(14),I(14),W(14)
60 SP=0:REM NO OF STOPPED PARTICLES
70 PRINT"ENTER ATOMIC NO":INPUT ANO
80 GOSUB 2690:REM CALCULATE ENERGY AND M.F.P
90 GOSUB 2970:REM READ DIFFERENTIAL CROSS SECTION
100 PRINT"DO YOU READ RESULTS OF A FILE":INPUT F$
110 IF F$="Y" THEN GOSUB 2980:GOTO 140
120 PRINT"DO YOU WANT SOME RESULTS TO TYPE IN Y/N":INPUT A$
130 IF A$="Y" THEN GOSUB 2200:REM READ RESULT
140 PRINT"HOW MANY NEUTRONS":INPUT NN
150 PRINT
160 GOSUB 340:REM CALCULATE PASSAGE OF NEUTRONS
170 PRINT
180 T1=X(0)+X(1)+X(2)+X(3)+X(4)+X(5)+X(6)+X(7)+X(8)+X(9)+X(10)+X(11)+X(12)
190 T2=X(13)+X(14)+X(15)+X(16)+X(17)+X(18)+X(19)+X(20)+X(21)+X(22)+X(23)
200 T3=X(24)+X(25)+X(26)+X(27)+X(28)+X(29)+X(30)+X(31)+X(32)+X(33)+X(34)+X(35)
210 TT=T1+T2+T3
220 GOSUB 2450
230 PRINT"MORE NEUTRONS Y/N":INPUT A$
240 IF A$="Y" THEN GOTO 140
250 PRINT "DO YOU WANT A COPPY Y/N":INPUT B$
260 IF B$="Y" THEN GOSUB 2450
270 PRINT"STORE RESULT ON FILE":INPUT Z$
280 IF Z$="Y" THEN GOSUB 3140
290 END
300 I=RND(1)*4.0 + 8.0
310 GOSUB 2660
320 K=D
330 RETURN
340 FOR N=1 TO NN:PRINT "NO OF PARTICLE=";N
350 FK=0:REM NO OF INTERRECTIONS
360 H=0:REM HAS PARTICLE BEEN ABSORBED
370 AL=0:J=JO:JB=13
380 F=0
390 GOSUB 300:REM CHOOSE POINT OF INTERACTION
400 REMPRINT"F=";F;"K=";K;"I=";I
410 IF K>B THEN GOTO 1350
420 C1=C(0,JB)+C(1,JB)+C(2,JB)+C(3,JB)+C(4,JB)+C(5,JB)
430 C2=C(6,JB)+C(7,JB)+C(8,JB)+C(9,JB)+C(10,JB)
440 C3=C(11,JB)+C(12,JB)+C(13,JB)+C(14,JB)
450 C4=C(15,JB)+C(16,JB)+C(17,JB)+C(18,JB)
460 C5=2*(C(15,JB)+C(16,JB)+C(17,JB))+C(18,JB)
470 C6= C1+C2+2*C3+C5
480 C7=C1+2*(C2+C3)+C5
490 REMPRINT"F=";F;"K=";K;"I=";I
500 PP=RND(1):REM CHOOSE CHANGE IN DIRECTION
510 REMPRINT"PP=";PP
520 IF J<SQR(0.001)*JO THEN SP=SP+1:GOSUB 2990
530 IF PP<C(0,JB)/P(JB) THEN Z=0:GOTO 890
540 IF PP<(C(0,JB)+C(1,JB))/P(JB) THEN Z=1:GOTO 890
550 IF PP<(C(0,JB)+C(1,JB)+C(2,JB))/P(JB) THEN Z=2:GOTO 890
```

```
560 IF PP<(C(0,JB)+C(1,JB)+C(2,JB)+C(3,JB))/P(JB) THEN Z=3:GOTO 890
570 IF PP<(C(0,JB)+C(1,JB)+C(2,JB)+C(3,JB)+C(4,JB))/P(JB) THEN Z=4:GOTO 890
580 IF PP<C1/P(JB)THEN Z=5:GOTO 890
590 IF PP<(C1+C(6,JB))/P(JB) THEN Z=6:GOTO 890
600 IF PP<(C1+C(6,JB)+C(7,JB))/P(JB) THEN Z=7:GOTO 890
610 IF PP<(C1+C(6,JB)+C(7,JB)+C(8,JB))/P(JB) THEN Z=8:GOTO 890
620 IF PP<(C1+C(6,JB)+C(7,JB)+C(8,JB)+C(9,JB))/P(JB) THEN Z=9:GOTO 890
630 IF PP<(C1+C2)/P(JB) THEN Z=10:GOTO 890
640 IF PP<(C1+C2+C(11,JB))/P(JB) THEN Z=11:GOTO 890
650 IF PP<(C1+C2+C(11,JB)+C(12,JB))/P(JB) THEN Z=12:GOTO 890
660 IF PP<(C1+C2+C(11,JB)+C(12,JB)+C(13,JB))/P(JB) THEN Z=13:GOTO 890
670 IF PP<(C1+C2+C3)/P(JB) THEN Z=14:GOTO 890
680 IF PP<(C1+C2+C3+C(15,JB))/P(JB) THEN Z=15:GOTO 890
690 IF PP<(C1+C2+C3+C(15,JB)+C(16,JB))/P(JB) THEN Z=16:GOTO 890
700 IF PP<(C1+C2+C3+C(15,JB)+C(16,JB)+C(17,JB))/P(JB) THEN Z=17:GOTO 890
710 IF PP<(C1+C2+C3+C4)/P(JB) THEN Z=18:GOTO 890
720 IF PP<(C1+C2+C3+C4+C(17,JB))/P(JB) THEN Z=19:GOTO 890
730 IF PP<(C1+C2+C3+C4+C(17,JB)+C(16,JB))/P(JB) THEN Z=20:GOTO 890
740 IF PP<(C1+C2+C3+C4+C(17,JB)+C(16,JB)+C(15,JB))/P(JB) THEN Z=21:GOTO 890
750 IF PP<(C1+C2+C3+C4+C5+C(14,JB))/P(JB) THEN Z=22:GOTO 890
760 IF PP<(C1+C2+C3+C4+C5+C(14,JB)+C(13,JB))/P(JB) THEN Z=23:GOTO 890
770 IF PP<(C1+C2+C3+C4+C5+C(14,JB)+C(13,JB)+C(12,JB))/P(JB) THEN Z=24:GOTO 890
780 IF PP<C6/P(JB) THEN Z=25:GOTO 890
790 IF PP<(C6+C(10,JB))/P(JB) THEN Z=26:GOTO 890
800 IF PP<(C6+C(10,JB)+C(9,JB))/P(JB) THEN Z=27:GOTO 890
810 IF PP<(C6+C(10,JB)+C(9,JB)+C(8,JB))/P(JB) THEN Z=28:GOTO 890
820 IF PP<(C6+C(10,JB)+C(9,JB)+C(8,JB)+C(7,JB))/P(JB) THEN Z=29:GOTO 890
830 IF PP<C7/P(JB) THEN Z=30:GOTO 890
840 IF PP<(C7+C(5,JB))/P(JB) THEN Z=31:GOTO 890
850 IF PP<(C7+C(5,JB)+C(4,JB))/P(JB) THEN Z=32:GOTO 890
860 IF PP<(C7+C(5,JB)+C(4,JB)+C(3,JB))/P(JB) THEN Z=33:GOTO 890
870 IF PP<(C7+C(5,JB)+C(4,JB)+C(3,JB)+C(2,JB))/P(JB) THEN Z=34:GOTO 890
880 Z=35
890 FK=FK+1
900 GOSUB 2780:IF H=1 GOTO 2400
910 J=J*SQR(Q(Z)):REMCALCULATE NEW MFP
920 REMPRINT "Z=";Z
930 GOSUB 2660:REM DISTANCE TRAVELED
940 JB=INT(J*J*14/(JO*JO)):IF JB=14 THEN JB=13
950 F=Z+AL
960 REMPRINT "F=";F
970 IF F>35 THEN F=F-36:REM SET NEW CO-ORDS
980 G=(22/7)/180
990 IF F=0 THEN K=K+D:I=I:GOTO 1350
1000 IF F=1 THEN K=K+D*COS(10*G):I=I+D*SIN(10*G):GOTO 1370
1010 IF F=2 THEN K=K+D*COS(20*G):I=I+D*SIN(20*G):GOTO 1400
1020 IF F=3 THEN K=K+D*COS(30*G):I=I+D*SIN(30*G):GOTO 1430
1030 IF F=4 THEN K=K+D*COS(40*G):I=I+D*SIN(40*G):GOTO 1460
1040 IF F=5 THEN K=K+D*COS(50*G):I=I+D*SIN(50*G):GOTO 1490
1050 IF F=6 THEN K=K+D*COS(60*G):I=I+D*SIN(60*G):GOTO 1520
1060 IF F=7 THEN K=K+D*COS(70*G):I=I+D*SIN(70*G):GOTO 1550
1070 IF F=8 THEN K=K+D*COS(80*G):I=I+D*SIN(80*G):GOTO 1580
1080 IF F=9 THEN K=K:I=I+D:GOTO 1610
1090 IF F=10 THEN K=K+D*COS(100*G):I=I+D*SIN(100*G):GOTO 1630
1100 IF F=11 THEN K=K+D*COS(110*G):I=I+D*SIN(110*G):GOTO 1660
```

```
1110 IF F=12 THEN K=K+D*COS(120*G):I=I+D*SIN(120*G):GOTO 1690
1120 IF F=13 THEN K=K+D*COS(130*G):I=I+D*SIN(130*G):GOTO 1720
1130 IF F=14 THEN K=K+D*COS(140*G):I=I+D*SIN(140*G):GOTO 1750
1140 IF F=15 THEN K=K+D*COS(150*G):I=I+D*SIN(150*G):GOTO 1780
1150 IF F=16 THEN K=K+D*COS(160*G):I=I+D*SIN(160*G):GOTO 1810
1160 IF F=17 THEN K=K+D*COS(170*G):I=I+D*SIN(170*G):GOTO 1840
1170 IF F=18 THEN K=K-D:I=I:GOTO 1870
1180 IF F=19 THEN K=K+D*COS(190*G):I=I+D*SIN(190*G):GOTO 1890
1190 IF F=20 THEN K=K+D*COS(200*G):I=I+D*SIN(200*G):GOTO 1920
1200 IF F=21 THEN K=K+D*COS(210*G):I=I+D*SIN(210*G):GOTO 1950
1210 IF F=22 THEN K=K+D*COS(220*G):I=I+D*SIN(220*G):GOTO 1980
1220 IF F=23 THEN K=K+D*COS(230*G):I=I+D*SIN(230*G):GOTO 2010
1230 IF F=24 THEN K=K+D*COS(240*G):I=I+D*SIN(240*G):GOTO 2040
1240 IF F=25 THEN K=K+D*COS(250*G):I=I+D*SIN(250*G):GOTO 2070
1250 IF F=26 THEN K=K+D*COS(260*G):I=I+D*SIN(260*G):GOTO 2100
1260 IF F=27 THEN K=K:I=I-D:GOTO 2130
1270 IF F=28 THEN K=K+D*COS(280*G):I=I+D*SIN(280*G):GOTO 2150
1280 IF F=29 THEN K=K+D*COS(290*G):I=I+D*SIN(290*G):GOTO 2180
1290 IF F=30 THEN K=K+D*COS(300*G):I=I+D*SIN(300*G):GOTO 2210
1300 IF F=31 THEN K=K+D*COS(310*G):I=I+D*SIN(310*G):GOTO 2240
1310 IF F=32 THEN K=K+D*COS(320*G):I=I+D*SIN(320*G):GOTO 2270
1320 IF F=33 THEN K=K+D*COS(330*G):I=I+D*SIN(330*G):GOTO 2300
1330 IF F=34 THEN K=K+D*COS(340*G):I=I+D*SIN(340*G):GOTO 2330
1340 IF F=35 THEN K=K+D*COS(350*G):I=I+D*SIN(350*G):GOTO 2360
1350 IF K>B THEN X(0)=X(0)+1:B(0,JB)=B(0,JB)+1:GOTO 2390
1360 AL=F:GOTO 420
1370 IF K>B THEN X(1)=X(1)+1:B(1,JB)=B(1,JB)+1:GOTO 2390
1380 IF I>A THEN X(1)=X(1)+1:B(1,JB)=B(1,JB)+1:GOTO 2390
1390 AL=F:GOTO 420
1400 IF K>B THEN X(2)=X(2)+1:B(2,JB)=B(2,JB)+1:GOTO 2390
1410 IF I>A THEN X(2)=X(2)+1:B(2,JB)=B(2,JB)+1:GOTO 2390
1420 AL=F:GOTO 420
1430 IF K>B THEN X(3)=X(3)+1:B(3,JB)=B(3,JB)+1:GOTO 2390
1440 IF I>A THEN X(3)=X(3)+1:B(3,JB)=B(3,JB)+1:GOTO 2390
1450 AL=F:GOTO 420
1460 IF K>B THEN X(4)=X(4)+1:B(4,JB)=B(4,JB)+1:GOTO 2390
1470 IF I>A THEN X(4)=X(4)+1:B(4,JB)=B(4,JB)+1:GOTO 2390
1480 AL=F:GOTO 420
1490 IF K>B THEN X(5)=X(5)+1:B(5,JB)=B(5,JB)+1:GOTO 2390
1500 IF I>A THEN X(5)=X(5)+1:B(5,JB)=B(5,JB)+1:GOTO 2390
1510 AL=F:GOTO 420
1520 IF K>B THEN X(6)=X(6)+1:B(6,JB)=B(6,JB)+1:GOTO 2390
1530 IF I>A THEN X(6)=X(6)+1:B(6,JB)=B(6,JB)+1:GOTO 2390
1540 AL=F:GOTO 420
1550 IF K>B THEN X(7)=X(7)+1:B(7,JB)=B(7,JB)+1:GOTO 2390
1560 IF I>A THEN X(7)=X(7)+1:B(7,JB)=B(7,JB)+1:GOTO 2390
1570 AL=F:GOTO 420
1580 IF K>B THEN X(8)=X(8)+1:B(8,JB)=B(8,JB)+1:GOTO 2390
1590 IF I>A THEN X(8)=X(8)+1:B(8,JB)=B(8,JB)+1:GOTO 2390
1600 AL=F:GOTO 420
1610 IF I>A THEN X(9)=X(9)+1:B(9,JB)=B(9,JB)+1:GOTO 2390
1620 AL=F:GOTO 420
1630 IF I>A THEN X(10)=X(10)+1:B(10,JB)=B(10,JB)+1:GOTO 2390
1640 IF K<0 THEN X(10)=X(10)+1:B(10,JB)=B(10,JB)+1:GOTO 2390
1650 AL=F:GOTO 420
```

```
1660 IF I>A THEN X(11)=X(11)+1:B(11,JB)=B(11,JB)+1:GOTO 2390
1670 IF K<0 THEN X(11)=X(11)+1:B(11,JB)=B(11,JB)+1:GOTO 2390
1680 AL=F:GOTO 420
1690 IF I>A THEN X(12)=X(12)+1:B(12,JB)=B(12,JB)+1:GOTO 2390
1700 IF K<0 THEN X(12)=X(12)+1:B(12,JB)=B(12,JB)+1:GOTO 2390
1710 AL=F:GOTO 420
1720 IF I>A THEN X(13)=X(13)+1:B(13,JB)=B(13,JB)+1:GOTO 2390
1730 IF K<0 THEN X(13)=X(13)+1:B(13,JB)=B(13,JB)+1:GOTO 2390
1740 AL=F:GOTO 420
1750 IF I>A THEN X(14)=X(14)+1:B(14,JB)=B(14,JB)+1:GOTO 2390
1760 IF K<0 THEN X(14)=X(14)+1:B(14,JB)=B(14,JB)+1:GOTO 2390
1770 AL=F:GOTO 420
1780 IF I>A THEN X(15)=X(15)+1:B(15,JB)=B(15,JB)+1:GOTO 2390
1790 IF K<0 THEN X(15)=X(15)+1:B(15,JB)=B(15,JB)+1:GOTO 2390
1800 AL=F:GOTO 420
1810 IF I>A THEN X(16)=X(16)+1:B(16,JB)=B(16,JB)+1:GOTO 2390
1820 IF K<0 THEN X(16)=X(16)+1:B(16,JB)=B(16,JB)+1:GOTO 2390
1830 AL=F:GOTO 420
1840 IF I>A THEN X(17)=X(17)+1:B(17,JB)=B(17,JB)+1:GOTO 2390
1850 IF K<0 THEN X(17)=X(17)+1:B(17,JB)=B(17,JB)+1:GOTO 2390
1860 AL=F:GOTO 420
1870 IF K<0 THEN X(18)=X(18)+1:B(18,JB)=B(18,JB)+1:GOTO 2390
1880 AL=F:GOTO 420
1890 IF K<0 THEN X(19)=X(19)+1:B(19,JB)=B(19,JB)+1:GOTO 2390
1900 IF I<0 THEN X(19)=X(19)+1:B(19,JB)=B(19,JB)+1:GOTO 2390
1910 AL=F:GOTO 420
1920 IF K<0 THEN X(20)=X(20)+1:B(20,JB)=B(20,JB)+1:GOTO 2390
1930 IF I<0 THEN X(20)=X(20)+1:B(20,JB)=B(20,JB)+1:GOTO 2390
1940 AL=F:GOTO 420
1950 IF K<0 THEN X(21)=X(21)+1:B(21,JB)=B(21,JB)+1:GOTO 2390
1960 IF I<0 THEN X(21)=X(21)+1:B(21,JB)=B(21,JB)+1:GOTO 2390
1970 AL=F:GOTO 420
1980 IF K<0 THEN X(22)=X(22)+1:B(22,JB)=B(22,JB)+1:GOTO 2390
1990 IF I<0 THEN X(22)=X(22)+1:B(22,JB)=B(22,JB)+1:GOTO 2390
2000 AL=F:GOTO 420
2010 IF K<0 THEN X(23)=X(23)+1:B(23,JB)=B(23,JB)+1:GOTO 2390
2020 IF I<0 THEN X(23)=X(23)+1:B(23,JB)=B(23,JB)+1:GOTO 2390
2030 AL=F:GOTO 420
2040 IF K<0 THEN X(24)=X(24)+1:B(24,JB)=B(24,JB)+1:GOTO 2390
2050 IF I<0 THEN X(24)=X(24)+1:B(24,JB)=B(24,JB)+1:GOTO 2390
2060 AL=F:GOTO 420
2070 IF K<0 THEN X(25)=X(25)+1:B(25,JB)=B(25,JB)+1:GOTO 2390
2080 IF I<0 THEN X(25)=X(25)+1:B(25,JB)=B(25,JB)+1:GOTO 2390
2090 AL=F:GOTO 420
2100 IF K<0 THEN X(26)=X(26)+1:B(26,JB)=B(26,JB)+1:GOTO 2390
2110 IF I<0 THEN X(26)=X(26)+1:B(26,JB)=B(26,JB)+1:GOTO 2390
2120 AL=F:GOTO 420
2130 IF I<0 THEN X(27)=X(27)+1:B(27,JB)=B(27,JB)+1:GOTO 2390
2140 AL=F:GOTO 420
2150 IF I<0 THEN X(28)=X(28)+1:B(28,JB)=B(28,JB)+1:GOTO 2390
2160 IF K>B THEN X(28)=X(28)+1:B(28,JB)=B(28,JB)+1:GOTO 2390
2170 AL=F:GOTO 420
2180 IF I<0 THEN X(29)=X(29)+1:B(29,JB)=B(29,JB)+1:GOTO 2390
2190 IF K>B THEN X(29)=X(29)+1:B(29,JB)=B(29,JB)+1:GOTO 2390
2200 AL=F:GOTO 420
```

```
2210 IF I<0 THEN X(30)=X(30)+1:B(30,JB)=B(30,JB)+1:GOTO 2390
2220 IF K>B THEN X(30)=X(30)+1:B(30,JB)=B(30,JB)+1:GOTO 2390
2230 AL=F:GOTO 420
2240 IF I<0 THEN X(31)=X(31)+1:B(31,JB)=B(31,JB)+1:GOTO 2390
2250 IF K>B THEN X(31)=X(31)+1:B(31,JB)=B(31,JB)+1:GOTO 2390
2260 AL=F:GOTO 420
2270 IF I<0 THEN X(32)=X(32)+1:B(32,JB)=B(32,JB)+1:GOTO 2390
2280 IF K>B THEN X(32)=X(32)+1:B(32,JB)=B(32,JB)+1:GOTO 2390
2290 AL=F:GOTO 420
2300 IF I<0 THEN X(33)=X(33)+1:B(33,JB)=B(33,JB)+1:GOTO 2390
2310 IF K>B THEN X(33)=X(33)+1:B(33,JB)=B(33,JB)+1:GOTO 2390
2320 AL=F:GOTO 420
2330 IF I<0 THEN X(34)=X(34)+1:B(34,JB)=B(34,JB)+1:GOTO 2390
2340 IF K>B THEN X(34)=X(34)+1:B(34,JB)=B(34,JB)+1:GOTO 2390
2350 AL=F:GOTO 420
2360 IF I<0 THEN X(35)=X(35)+1:B(35,JB)=B(35,JB)+1:GOTO 2390
2370 IF K>B THEN X(35)=X(35)+1:B(35,JB)=B(35,JB)+1:GOTO 2390
2380 AL=F:GOTO 420
2390 REMPRINT"F=";F;"K=";K;"I=";I
2400 NEXT N
2410 RETURN
2420 FOR N= 0 TO 35 :D(N)=10*N
2430 NEXT N
2440 RETURN
2450 FOR N=0 TO 35
2460 REM PROCprint
2470 PRINT D(N):PRINT
2480 T=X(N)
2490 PRINT"NO OF PARTICLES=";T:PRINT
2500 FOR M=0 TO 13
2510 T=B(N,M)
2520 PRINT "FOR E= ";M;" MEV TO  ";M+1;" MEV,   N= ";T
2530 NEXT M
2540 PRINT
2550 NEXT N
2560 PRINT "NO DETECTED =";TT
2570 PRINT "NO STOPPED =";SP:PRINT "NO ABSORBED =";AB
2580 PRINT "DIMENSION OF CRYSTAL =";A;"BY";B;"(CM)"
2590 PRINT "ATOMIC WEIGHT OF SCATTERER =";MASS
2600 PRINT "ATOMIC NUMBER OF SCATTERER =";ANO
2610 VDU3
2620 RETURN
2630 GET G$:IF G$="" THEN GOTO 1760
2640 PRINT
2650 RETURN
2660 PR=1-RND(1)
2670 D=J*LN(1/PR)
2680 RETURN
2690 REM FRACTION OF ENERGY RETAINED IN INTERECTION
2700 PRINT"WHAT IS THE MASS OF THE TARGET NUCLEUS" :INPUT MASS
2710 DEF FND(S)=SQR(COS(S)*COS(S)+MASS*MASS-1)
2720 FOR N=0 TO 35:S=10*N*(22/7)/180
2730 Q(N)=(COS(S)+FND(S))/(1+MASS)
2740 Q(N)=Q(N)*Q(N)
2750 NEXT N
```

```
2760 FOR N=0 TO 35
2770 RETURN
2780 PP=RND(1):REM CHOOSE TYPE OF REACTION
2790 CT=I(JB)+P(JB)
2800 B=P(JB)/CT
2810 IF PP<R THEN RETURN
2820 FR=FR-1
2830 H=1:AB=AB+1
2840 RETURN
2850 Y=OPENIN"DATA"
2860 FOR L=0 TO 13
2870 FOR N=0 TO 18
2880 INPUT£Y,A$
2890 C(N,L)=VAL(A$)
2900 NEXT N
2910 P(L)=C(0,L)+2*C(1,L)+2*C(2,L)+2*C(3,L)+2*C(4,L)+2*C(5,L)+2*C(6,L)
2920 P(L)=P(L)+2*C(7,L)+2*C(8,L)+2*C(9,L)+2*C(10,L)+2*C(11,L)+2*C(12,L)
2930 P(L)=P(L)+2*C(13,L)+2*C(14,L)+2*C(15,L)+2*C(16,L)+2*C(17,L)+C(18,L)
2940 INPUT£Y,A$
2950 I(L)=VAL(A$)
2960 NEXT L:CLOSE£Y:JO=4.0:RETURN
2970 IF ANO=29 AND MASS=63 THEN GOSUB 2850:RETURN
2980 PRINT"INPUT NAME OF FILE":INPUT F$
2990 U=OPENIN(F$)
3000 FOR N=0 TO 35
3010 INPUT£U,A$:X(N)=VAL(A$)
3020 NEXT N
3030 FOR N=0 TO 35
3040 FOR M=0 TO 13
3050 INPUT£U,A$
3060 B(N,M)=VAL(A$)
3070 NEXT M
3080 NEXT N
3090 INPUT£U,A$:TT=VAL(A$)
3100 INPUT£U,A$:SP=VAL(A$)
3110 INPUT£U,A$:AB=VAL(A$)
3120 CLOSE£U
3130 RETURN
3140 INPUT"THE NAME OF FILE",B$
3150 PRINT"IS IT A NEW FILE":INPUT C$
3160 IF C$="Y" THEN GOTO 3170
3170 P%=OPENOUT(B$)
3180 FOR N=0 TO 35
3190 A$=STR$(X(N))
3200 PRINT£P%,A$
3210 NEXT N
3220 FOR N=0 TO 35
3230 FOR M=0 TO 13
3240 A$=STR$(B(N,M))
3250 PRINT£P%,A$
3260 NEXT M
3270 NEXT N
3280 PRINT£P%,STR$(TT)
3290 PRINT£P%,STR$(SP)
3300 PRINT£P%,STR$(AB)
```

```
3310 CLOSE£PX
3320 RETURN
3330 X=OPENOUT"DATA"
3340 FOR N=0 TO 13
3350 FOR L=0 TO 19
3360 READ VL
3370 A$=STR$(VL)
3380 PRINT£X,A$
3390 NEXT L
3400 NEXT N
3410 CLOSE£X
3420 DATA 87.72,286.28,319.03,197.94,83.26,17.59,6.72,13.77,13.54,14.42,8.74
3430 DATA 3.59,4.49,1.28,2.00,5.23,4.38,4.13,1.51,1650
3440 DATA 87.72,286.28,319.03,197.94,83.26,17.59,6.72,13.77,13.54,14.42,8.74
3450 DATA 3.59,4.49,1.28,2.00,5.23,4.38,4.13,1.51,1650
3460 DATA 87.72,286.28,319.03,197.94,83.26,17.59,6.72,13.77,13.54,14.42,8.74
3470 DATA 3.59,4.49,1.28,2.00,5.23,4.38,4.13,1.51,1650
3480 DATA 87.72,286.28,319.03,197.94,83.26,17.59,6.72,13.77,13.54,14.42,8.74
3490 DATA 3.59,4.49,1.28,2.00,5.23,4.38,4.13,1.51,1650
3500 DATA 87.72,286.28,319.03,197.94,83.26,17.59,6.72,13.77,13.54,14.42,8.74
3510 DATA 3.59,4.49,1.28,2.00,5.23,4.38,4.13,1.51,1650
3520 DATA 87.72,286.28,319.03,197.94,83.26,17.59,6.72,13.77,13.54,14.42,8.74
3530 DATA 3.59,4.49,1.28,2.00,5.23,4.38,4.13,1.51,1650
3540 DATA 87.72,286.28,319.03,197.94,83.26,17.59,6.72,13.77,13.54,14.42,8.74
3550 DATA 3.59,4.49,1.28,2.00,5.23,4.38,4.13,1.51,1650
3560 DATA 87.72,286.28,319.03,197.94,83.26,17.59,6.72,13.77,13.54,14.42,8.74
3570 DATA 3.59,4.49,1.28,2.00,5.23,4.38,4.13,1.51,1650
3580 DATA 77.94,265.57,320.70,190.04,55.29,7.41,1.89,1.60,8.68,13.28,8.76,4.80
3590 DATA 3.13,2.46,3.70,3.12,1.49,1.36,.51,1640
3600 DATA 77.94,265.57,320.70,190.04,55.29,7.41,1.89,1.60,8.68,13.28,8.76,4.80
3610 DATA 3.13,2.46,3.70,3.12,1.49,1.36,.51,1640
3620 DATA 82.27,269.02,286.83,137.64,31.47,6.59,1.20,1.75,10.62,12.92,7.71
3630 DATA 4.37,3.46,4.40,5.03,3.18,1.25,1.03,.37,1570
3640 DATA 82.27,269.02,286.83,137.64,31.47,6.59,1.20,1.75,10.62,12.92,7.71
3650 DATA 4.37,3.46,4.40,5.03,3.18,1.25,1.03,.37,1570
3660 DATA 77.14,256.1,258.0,86.95,18.75,10.36,3.69,6.45,16.49,13.22,5.87,4.49
3670 DATA 5.44,5.27,3.56,2.38,1.53,.94,.19,1504
3680 DATA 77.14,256.1,258.0,86.95,18.75,10.36,3.69,6.45,16.49,13.22,5.87,4.49
3690 DATA 5.44,5.27,3.56,2.38,1.53,.94,.19,1504
3700 REM DBPPROCprint
3710 REM VDU2:VDU1,27,1,33,1,4:*italic
3720 REM ENDPROC
```

REFERENCES.

1.Garber D.I and Kinsey R.R
Neutron Cross-sections, Volume II, Curves
BNL 325 (1976).

2.Foderaro A.
The Elements of Neutron Interaction Theory,
The MIT Press (1971) 395.

3.Fernbach S, Serber R and Taylor T.B,
Phys. Rev. 75 no. 9 (1949) 1352.

4.Woods R.D and Saxon D.S,
Phys. Rev. 95 (1954) 577.

5.Perey F and Buck B,
Nucl. Phys. 32 (1962) 353.

6.Wilmore D and Hudgson P.E,
Nucl. Phys. 55 (1964) 673.

7.Becchetti F.D and Greenlees G.W,
Phys. Rev. 182 no. 4 (1969) 1190.

8.El-Kadi S.M, Nelson C.E, Purser F.O, and Walter R.1
Nucl. Phys. A390 (1982) 509.

9.Rapaport J, Kulkarni V and Finlay R.W,
Nucl. Phys. A330 (1979) 15.

10.Janicki M.C and Cox A.J,
Int. J. Appl. Rad. Isot. 30(1979) 439.

11.Coon J.H, Davis R.W, Feithauser H.E and Nicodemus B.D
Phys. Rev. 111 (1958) 250.

12.Claude st. Pierre, Machwe M.K and Lorrain P,
Phys. Rev. 115 (1959) 999.

13.Yuasa K,
Journal of the Physical Society of Japan 13(1958) 1248

14.Bonazzola G.C and Chiavassa E,
Phys. Rev. B140 (1965) 838.

15.Whisnant C.S, Dave J.H and Gould C.R,
Phys. Rev. 30 no. 5 (1984) 1435.

16.Coon J.H,
Phys. Rev. 94 (1954) 785.

17.Strizhak V.I, Bobyr' V.V and Grona L.Ya,
Soviet Phys. JEPT 14 no. 2 (1962) 225.

18.Bersillon O,
SCAT-2:Un Programme de Modele Optique Spherique,
CEA-N-2227, (1981).

19.Finckh E,
Advances in measurements of neutron spectra,
Nuclear Spectroscopy and Reaction Part B,
Edited by Cerney, (1974) 586.

20.Cranberg L and Levin J.S,
Phys. Rev. 100 (1955) 434.

21.Molbey R.C,
Phys. Rev. 88 (1952) 360.

22.Smith A.B, Guenther P, Larsen R, Nelson C, Walker P and Whalen J.F,
Nucl. Instr. and Meth. 50 (1967) 277.

23.Stelson P.H, Robinson R.L, Kin H.J, Raparport J and Satchler G.R,
Nucl. Phys. 68 (1965) 97.

24.O'Niell G.K,
Phys. Rev. 92 (1953) 853.

25.Benveniste J and Zenger J,
URCL-4266 (1954).

26.Allen D.L and Poole M.J,
Proc. Roy. Soc. (london) 204 (1951) 500.

27.Argo H.V, Taschek R.F, Agnew H.M, Hemmendinger A and Leland W.T,
Phys. ReV. 87 (1952) 612.

28.Gunnersen E.M and James G,
Nucl. Instr. and Meth. 8 (1960) 173.

29.Conner J.P, Bonner T.W and Smith J.B,
Phys. Rev. 88 (1952) 468.

30.Arnold W.R, Philip J.A, Sawyer G.A, Stovall E.J.J.R and Tuck J.L,
Phys. Rev. 93 (1954) 483.

31.Poulsen A and Liskin H,
Nucl. Data Table, 11 (1972) 569.

32.Warshaw S.D,
Phys. Rev. 76 (1949) 1759.

33.Reynolds H.K, Dunber D.N, Wanzel W.A and Whaling W,
Phys. Rev. 92 (1953) 742.

34.Phillips J.A,
Phys. ReV. 90 (1953) 532.

35.Benveniste J, Mitchel A.C, Schrader C.D and Zenger J.H
Nucl. Instr. and meth. 7 (1960) 306.

36.Connel K.A,
PhD Thesis University of Aston (1972).

37.Atam P. Arya,
Fundemental of Nuclear Physics,
Allyn and Bacon, Inc. (1966).

38.Swartz C.D, Owen G.E and Ames O,
AEC Report no. NYO 2053 (1957).

39.Bame S.J, Haddad E, Perry J.E and Smith R.K,
Rev. Sci. Instr. 28 (1957) 997.

40.Marion J.B and Fowler J.L,
Fast Neutron Physics,
Interscience, New York, Part II (1963) 2209.

41.Del Guerra A,
Nucl. Instr. and Meth. 135 (1976) 337.

42.Marion J.B and Young F.C,
Nuclear Reaction Analysis,
North Holland Pub., Amsterdam (1968).

43.Jackson W.R, Divatia A.S, Bonner B.E, Joseph C,
Emerson S.T, Chen Y.S, Taylor M.C, Simpson W.D,
Valcovic C, Poul E.B and Phillips G.C,
Nucl. Instr. and Meth. 55 (1967) 349.

44.Hunt J.B, baker C.A, Batty C.J, Ford P, Friedman
and William L.E,
Nucl. Instr. and Meth. 85 (1970) 269.

45.Mc Naugton M.W, Brady F.T, Broste W.B, Sagle A.L
and Johnsen S.W,
Nucl. Instr. and Meth. 116 (1974) 25.

46.Fajer V and Alvarez W,
nucl. Instr. and meth. 184 (1981) 515.

47.Baccaccio P, Gramegna F, Viesti G and Augustyniak W,
Nucl. Instr. and meth. 184 (1981) 445.

48.Fowler J.L, Cookson J.A, Hussain M, Schwartz R.B,
Swinhoe M.T, Wise C and Uttley C.A,
Nucl. Instr. and Meth. 175 (1980) 449.

49.Gul K,
Nucl. Instr. and Meth. 176 (1980) 549.

50.Abdel-Wahab M.S, Bialy J and Schmidt F.K,
Nucl. Instr. and Meth. 200 (1982) 291.

51.Batchelor R, Gilboy W.B, Parker J.B and Towle J.H,
Nucl. Instr. and Meth. 13 (1961) 70.

52.Swartz C.D and Owen G.E,
Fast Neutron Physics,
Interscience, New York Vol.I (1960) 211.

53.Bailey C.L, Bennett W.E, Bergstralh T, Nuckolls R.G,
Richards H.T and William J.H,
Phys. Rev. 70 (1946) 583.

54.Nereson N and Darden S,
Physics. Rev. 89 (1953) 775.

55.Swartz C.D,
Phys. Let. B30 (1969) 36.

56.Foster D.G and Galsgow D.W,
Phys. Rev. c3 (1971) 576.

57.Bashter I.I.A and Cooper P.N,
Nucl. Instr. and Meth. A252 (1986) 113.

58.Gammel J.L,
Fast Neutron Physics,
Interscience, New York, Vol. IV Part II (1963).

59.Neutron-carban Cross-Section,
ENDF-BIV (1974).

60.Brooks F.D,
Nucl. Instr. and Meth. 162 (1979) 477.

61.Tome M.E,
Nucl. Instr. and Meth. 92 (1971) 61.

62.Segel, Swartz C.D and Owen G.E,
Rev. Sc. Instr. 25 (1954) 140.

63.Birks J.B,
The Theory and Practice of Scintillation Counting,
Mac Millan, New York (1964).

64.Smith D.L, Polk R.G and Miller T.G,
Nucl. Instr. and Meth. 64 (1968) 157.

65.Croun R.L and Smith D.L,
Nucl. Instr. and meth. 80 (1979) 239.

66.Wright T.G,
Phys. Rev. 91 (1953) 1282.

67.Gooding T.J and Pugh H.G,
Nucl. Instr. and meth. 7 (1960) 189.

68.Chou C.N,
Phys. rev. 87 81952) 904.

69.Wright T.G,
Phys. Rev. 100 (1955) 587.

70.Wright T.G,
Proc. Phys. Soc. B69 (1956) 358.

71.Kallman H and Brucker G.J,
Phys. Rev. 108 (1957) 1122.

72.Rich and Madey,
Range-energy Curves
URCL 2301 (1954).

73.Hirschfelder J.O and Magee J.L,
Phys. Rev. 73 (1948) 207.

74.Evans H.C and Bellamy E.H,
Proc. Phys. Soc. 31 (1960) 450.

75.Gettner M and Selove W,
Rev. Sc. Instr. 31 (1960) 450.

76.Mubarakmand S and Anwar M,
Nucl. Instr. and Meth. 93 (1971) 515.

77.Flynn L.E, Glendenin L.E, Steinbert E.P and Wright P.M
Nucl. Instr. and Meth. 27 (1964) 13.

78.Meadows,
Nucl. Sci. Eng. 9 (1961) 132.

79.Knoll G.F,
Radiation Detection and Measurement,
John Wiley and Son, New York (1979) 521.

80.Kreger W.E and Mathur R.L,
Scintillation Spectroscopy and Gamma Radiation,
Ed. S.M Shafroth, Gordon and Breach.

81.Hopkins J.C, Martin J.T and Shagrave J.D,
Nucl. Instr. and Meth. 56 (1967) 175.

82.Dearnaley G and Whitehead A.B,
nucl. Instr. and Meth. 12 (1961) 205.

83.Baynham D.E,
PhD Thesis, University of Aston, (1971).

84.Verbinski V.V, Burus W.R, Love T.A, Zobel W and Hill N.W,
Nucl. Instr. and Meth. 65 (1968) 8.

85.Knox H.H and Miller T.G,
Nucl. Instr. and Meth. 101 (1972) 519.

86.Moszynski M and Bengtson B,
Nucl. Instr. and Meth. 158 (1979) 1.

87.Cocchi M and Rota A,
Nucl. Instr. and Meth. 55 (1967) 365.

88.Moszynki M,
Nucl. Instr. and Meth. 134 (1976) 77.

89.Vervier J.F and Martegani A,
Nucl. Phys. 6 (1958) 260.

90.Kokta L,
Nucl. Instr. and Meth. 112 (1973) 245.

91.Mukoyama T,
Nucl. Instr. and Meth. 125 (1975) 289.

92.Bouchez R, Duclos J and Perrin P,
Nucl. Phys. 43 (1963) 628.

93.Jasim M,
PhD. Thesis University of Aston in Birmingham (1985).

94.Lederer C.M and Shirley V.S,
Table of Isotopes,
Seventh Edition, John Wiley and Sons (1978).

95.Bevington P.R,
Data Reduction and Error Analysis for the Physical Science,
Mc. Graw Hill (1969).

96.Anvarian S.T.P and Cox A.J,
Nucl. Instr. and Meth. 217 (1983) 483.

97.Neutron-Aluminium Cross-section,
ENDF-BIV (1974).

98.Wick, G.C,
Phys. Rev. 75 (1949) 1459.

99.Cross-section Data for Aluminium,
UKNDL (1981).

100.Pierre C.S,Machwe M.K and Lorrain P,
Phys. Rev. 115 (1959) 999.

101.Al-Shalabi
PhD. Thesis university of Aston in Birmingham (1982).

102.Anvarian S.T.P,
PhD. Thesis University of Aston in Birmingham (1983).

103.Neutron-Copper Cross-sections,
ENDF-BIV (1974).

104.Cross-section Data for Copper,
UKNDL (1981).

105.Neutron-Molybdenum Cross-sections,
ENDF-BIV (1974).

106.Cross-section Data for Molybdenum,
UKNDL (1981).

107.Ferrer J.C, Carlson J.D and Raparport J,
Nucl. Phys. A275 (1977) 325.

108.Cindro N and Bersillon O,
"Contribution to the 5th International Symposium on
Interaction of Fast Neutron with Nuclei"
Gaussig, DDR, 17-21 Nov.,1975.

109.Greenlees G.W, Pyle G.J and Tang Y.C,
Phys. Rev. 171 no4 (1968) 1115.

110.Yu.A.Shreider,
The Monte Carlo Method,
Pergamon Press, 1966.